Coherent Higher-Order Spectroscopy: Investigating Multi-Exciton Interaction

Dissertation zur Erlangung
des naturwissenschaftlichen Doktorgrades (Dr. rer. nat.)
an der Fakultät für Chemie und Pharmazie
der Julius-Maximilians-Universität Würzburg

vorgelegt von
Julian Konstantin Lüttig
aus Frankfurt am Main

Würzburg, 2022

Eingereicht bei der Fakultät für Chemie und Pharmazie am

28. September 2022

Gutachter der schriftlichen Arbeit

1. Gutachter: Prof. Dr. Tobias Brixner

2. Gutachter: Prof. Dr. Christoph Lambert

Prüfer des öffentlichen Promotionskolloquiums

1. Prüfer: Prof. Dr. Tobias Brixner

2. Prüfer: Prof. Dr. Christoph Lambert

3. Prüferin: Prof. Dr. Claudia Höbartner

4. Prüfer: Prof. Dr. Tobias Hertel

5. Prüfer: Prof. Dr. Volker Engel

Datum des öffentlichen Promotionskolloquiums

9. November 2022

Doktorurkunde ausgehändigt am

_____

List of Own Publications

[1] D. Ranaan*, J. Lüttig*, Y. Silberberg, and D. Oron.
Vibrational spectroscopy via stimulated Raman induced Kerr lensing.
APL Photonics **3**, 092501 (2018).

[2] B. Huber, S. Pres, E. Wittmann, L. Dietrich, J. Lüttig, D. Fersch, E. Krauss,
D. Friedrich, J. Kern, V. Lisinetskii, M. Hensen, B. Hecht, R. Bratschitsch, E.
Riedle and T. Brixner.
*Space- and time-resolved UV-to-NIR surface spectroscopy and 2D nanoscopy at
1 MHz repetition rate.*
Review of Scientific Instruments **90**, 113103 (2019).

[3] M. Hensen, B. Huber, D. Friedrich, E. Krauss, S. Pres, P. Grimm, D. Fersch,
J. Lüttig, V. Lisinetskii, B. Hecht, and T. Brixner.
*Spatial variations in femtosecond field dynamics within a plasmonic nanores-
onator mode.*
Nano Letters **19**, 4651–4558 (2019).

[4] B. Kriete, J. Lüttig, T. Kunsel, P. Malý, T. L. C. Jansen, J. Knoester, T. Brixner,
and M. S. Pshenichnikov.
*Interplay between structural hierarchy and exciton diffusion in artificial light har-
vesting.*
Nature Communications **10**, 4615 (2019).

[5] S. Mueller, J. Lüttig, P. Malý, L. Ji, J. Han, M. Moos, T. B. Marder, U. H. F.
Bunz, A. Dreuw, C. Lambert, and T. Brixner.
*Rapid multiple-quantum three-dimensional fluorescence spectroscopy disentangles
quantum pathways.*
Nature Communications **10**, 4735 (2019).

[6] B. Huber, M. Hensen, S. Pres, V. Lisinetskii, J. Lüttig, E. Wittmann, E. Krauss,
D. Friedrich, B. Hecht, E. Riedle, and T. Brixner.
*Time-resolved photoemission electron microscopy of a plasmonic slit resonator
using 1 MHz, 25 fs, UV-to-NIR-tunable pulses.*
EPJ Web of conferences **205**, 08002 (2019).

---

* = contributed equally.

[7] P. Malý, J. Lüttig, A. Turkin, J. Dostál, C. Lambert, and T. Brixner.
From wavelike to sub-diffusive motion: Exciton dynamics and interaction in squaraine copolymers of varying length.
Chemical Science **11**, 456–466 (2020).

P. Malý, J. Lüttig, A. Turkin, J. Dostál, C. Lambert, and T. Brixner.
Correction: From wavelike to sub-diffusive motion: Exciton dynamics and interaction in squaraine copolymers of varying length.
Chemical Science **11**, 11352–11352 (2020).

[8] P. Malý, J. Lüttig, S. Mueller, M. H. Schreck, C. Lambert, and T. Brixner.
Coherently and fluorescence-detected two-dimensional electronic spectroscopy: Direct comparison on squaraine dimers.
Physical Chemistry Chemical Physics **22**, 21222–21237 (2020).

[9] P. Malý, S. Mueller, J. Lüttig, C. Lambert, and T. Brixner.
Signatures of exciton dynamics and interaction in coherently and fluorescence-detected four- and six-wave-mixing two-dimensional electronic spectroscopy.
Journal of Chemical Physics **153**, 144204 (2020).

[10] J. Lüttig, P. Malý, A. Turkin, K. Mayershofer, S. Büttner, C. Lambert, and T. Brixner.
Probing exciton transport in squaraine polymers using fifth-order two-dimensional spectroscopy.
The 22nd International Conference on Ultrafast Phenomena 2020, F. Kärtner, M. Khalil, R. Li, F. Légaré, and T. Tahara, eds., OSA Technical Digest (Optica Publishing Group), paper Th2A.3 (2020).

[11] P. Malý, S. Mueller, J. Lüttig, M. Schreck, C. Lambert, and T. Brixner.
Coherently and fluorescence-detected four- and six-wave-mixing two-dimensional electronic spectroscopy: Measuring multi-exciton dynamics and delocalization.
The 22nd International Conference on Ultrafast Phenomena 2020, F. Kärtner, M. Khalil, R. Li, F. Légaré, and T. Tahara, eds., OSA Technical Digest (Optica Publishing Group), paper Tu4A.4 (2020).

[12] J. Lüttig, T. Brixner, and P. Malý.
Anisotropy in fifth-order exciton–exciton-interaction two-dimensional spectroscopy.
Journal of Chemical Physics **154**, 154202 (2021).

[13] S. Mueller, J. Lüttig, L. Brenneis, and T. Brixner.
Observing multiexciton correlations in colloidal semiconductor quantum dots via multiple-quantum two-dimensional fluorescence spectroscopy.
ACS Nano **15**, 4647–4657 (2021).

[14] P. Malý, J. Lüttig, P. A. Rose, A. Turkin, C. Lambert, J. J. Krich, and T. Brixner.
Highly nonlinear transient absorption spectroscopy.
The International Conference on Ultrafast Phenomena (UP) 2022, F. Légaré, T. Tahara, J. Biegert, T. Brixner, and N. Dudovich, eds., Technical Digest Series (Optica Publishing Group, 2022), paper W2A.6 (2022).

[15] P. A. Rose, J. Lüttig, P. Malý, J. J. Krich, and T. Brixner.
Isolating nonlinear orders of transient grating spectra from a single 2D spectrum.
The International Conference on Ultrafast Phenomena (UP) 2022, F. Légaré, T. Tahara, J. Biegert, T. Brixner, and N. Dudovich, eds., Technical Digest Series (Optica Publishing Group, 2022), paper Th4A.14 (2022).

[16] P. Malý, J. Lüttig, P. A. Rose, A. Turkin, C. Lambert, J. J. Krich, and T. Brixner.
Separating single- from multi-particle dynamics in nonlinear spectroscopy.
submitted (2022).

[17] J. Lüttig, P. Malý, S. Mueller, T. Brixner.
Higher-order multidimensional and pump–probe spectroscopy.
in preparation (2022).

[18] J. Lüttig, P. Malý, P. A. Rose, A. Turkin, M. Bühler, C. Lambert, J. J. Krich, T. Brixner.
High-order pump–probe and high-order two-dimensional spectroscopy on the example of squaraine oligomers.
in preparation (2022).

[19] Romain Rouxel, J. Lüttig, Michael R. Jones, and Donatas Zigmantas.
Tracking light harvesting in purple bacteria in vivo.
in preparation (2022).

Parts of this thesis have been published in some of the peer-reviewed journal articles or are prepared for publication as listed above. An overview of reprinted and adapted passages and the corresponding page numbers can be found in the tables below. The sources of adapted figures are additionally indicated at the end of the corresponding figure captions. For all reproduced material the permission for reprint was granted by the respective publishing company holding the copyright of the articles, or the authors were copyright owners. In cases where the only modification were style corrections due to different journals' publishing styles, the text is considered as reproduced only.

Publication	Use in Dissertation	Page Number
[13][1] pp. 4 and pp. 6	figures adapted	pp. 64
[20][2] pp. 5	figure adapted	pp. 66
[9][3] pp. 5 and pp. 11	figures adapted	pp. 71
[16]	figure adapted	pp. 75
[17]	text, figures, charts, and schemes will (partly) be used and modified in the publication currently in preparation	pp. 51–82
[12][4]	text and figures reproduced	pp. 83–133
[18]	text, figures, charts, and schemes will (partly) be used and modified in the publication currently in preparation	pp. 135–195
[16]	figure adapted	pp. 167

---

[1]Adapted with permission form the American Chemical Society. Copyright © (2021) American Chemical Society.

[2]Reproduced under the terms of the Creative Commons CC BY license 4.0 (http://creativecommons.org/licenses/by/4.0/)

[3]Reprinted with permission from AIP Publishing. Copyright © (2020) AIP Publishing.

[4]Reprinted with permission from AIP Publishing. Copyright © (2021) AIP Publishing.

Contents

CHAPTER 1

Introduction

In the beginning of photosynthetic research, Theodor Engelmann wanted to understand for which wavelength of the sun light photosynthetic organisms produce oxygen [21, 22]. To answer this question, he built a simple experiment. He took a long fiber of algae and split the white light of the sun with an apparatus that Carl Zeiss constructed so that different colors of the light were absorbed at different spatial positions of the algae. He added bacteria that gather around wherever oxygen is produced. From the mass of bacteria at different positions of the algae he came to the conclusion that most oxygen is produced for the red and blue wavelengths of the sunlight.

Since this experiment of Engelmann 140 years ago, the field of spectroscopy has made great progress. With the development of ultrashort laser pulses, the investigation of processes on the femtosecond timescale have become accessible. In order to measure fast processes in molecular systems such as the excited-state dynamics, different techniques employing ultrashort laser pulses have been developed. In one of the well-established techniques, a pump pulse excites the system and another pulse after some specific delay probes the system. With such kind of techniques, "snapshots" of the molecular processes can be taken and, for example, chemical reactions can be observed. More advanced techniques such as two-dimensional (2D) spectroscopy allows one to observe the flow of energy through the photosynthetic apparatus. Over the past two decades several 2D spectroscopic techniques have been developed allowing to study a variety of phenomena in biology, chemistry and physics.

Theoder Engelmann used a simple method to understand one specific aspect of photosynthesis. The development of new spectroscopic methods allows scientists to explore different phenomena that would be difficult to observe otherwise. In some sense new developed techniques are like a lens which shed light on one specific aspect. This thesis adds new pump–probe (PP) and 2D techniques to the toolkit of ultrafast spectroscopists.

The methods of 2D and PP measure a nonlinear polarization which occurs due to multiple interactions with the electric field. Measuring a nonlinear polarization allows one to observe specific phenomena such as the interaction of the system with the environment by lineshapes in the 2D spectrum, energy transfer on the femtosecond timescale and coherent superpositions between excited states. So far, most of the 2D and PP experiments focused on the lowest orders of the nonlinear response, i.e., third-order signals for coherently detected techniques and the fourth-order signals for action-based techniques in terms of perturbation theory. In recent years, the concept of 2D spectroscopy was extended to the detection of higher-order signals. Such higher-

order techniques measure in general a nonlinear signal that is higher than three for coherently detected techniques and higher than four for action-based techniques. The higher-order techniques enables one to observe higher terms of the perturbation theory and the connected effects.

The starting point of this thesis was the further development of such a higher-order spectroscopic technique: fifth-order exciton–exciton interaction (EEI) 2D spectroscopy which was demonstrated four years ago [20]. The technique of EEI2D spectroscopy allows one to directly observe exciton–exciton annihilation (EEA) which is not possible with other spectroscopic techniques. In EEA, the energy of two excitons is transferred to a higher excited state followed by rapid relaxation to the single-exciton manifold. The process of EEA can only occur if the excitons are in close proximity to each other. The direct observation of annihilation is crucial because its dynamics can be used as a probe to characterize the exciton diffusion in extended systems such as polymers and aggregates. Since the exciton diffusion in such systems is not connected to a change in the absorption spectrum, PP and lower-order 2D spectroscopy fail to characterize the exciton diffusion. Fifth-order EEI2D spectroscopy is an example of a newly developed spectroscopic technique that enables one to directly probe one specific property (in this case EEA) of the system.

The main aspect of this thesis is to develop a deeper understanding of higher-order spectroscopy and apply it to different systems. The motivation for this thesis can be summarized in several questions that initiated the different projects and were inspired by the first experiments of EEI2D spectroscopy: Can the anisotropy in fifth-order EEI2D spectroscopy be used to gain additional information about annihilation and exciton transport? What are the theoretical and technical differences between fluorescence-detected and coherently detected higher-order multidimensional spectroscopy? Is it possible to isolate higher-order signals in PP spectroscopy and if so, what are the differences between higher-order PP and 2D spectroscopy? Can the higher-order signals be used to obtain clean nonlinear signals and measure directly increasing orders in perturbation theory?

Before these questions can be answered, the theoretical and experimental basics are discussed. The thesis is structured as follows: After a brief description of the theoretical aspects of nonlinear spectroscopy such as double-sided Feynman diagrams in Chapter 2, Chapter 3 reviews the main aspects of 2D spectroscopy. The discussion starts with PP spectroscopy as a technique to study ultrafast processes. However, PP spectroscopy is not sufficient to study phenomena such as energy transfer between states that are energetically close to each other. This problem is solved by 2D spectroscopy as an extension of PP spectroscopy. The various technical implementations of 2D spectroscopy are discussed such as coherently detected and action-detected 2D spectroscopy the latter of which uses fluorescence, photoelectrons and photocurrent as an observable. The chapter closes with a brief discussion about the setup that was used during this thesis to measure PP as well as 2D spectra.

Chapter 4 focuses on the description of excitons. The theory of exctions is demonstrated on the example of a molecular dimer. Coupling between the states of the two monomers results in new eigenstates. The new excited states of the coupled system are called excitons. Due to the coupling, the excitonic states are no longer localized at the monomeric subunits but are rather delocalized over the dimer. Additionally, an introduction about excitons in extended systems such as molecular aggregates is provided. The chapter closes with the description of EEA as an interaction process between two excitons.

Chapter 5 combines the obtained knowledge about excitons, double-sided Feynman diagrams, and 2D spectroscopy. The double-sided Feynman diagrams of coherently detected 2D spectroscopy are analyzed and used to predict 2D spectra of a coupled dimer. In the case of coherently detected 2D spectroscopy the cross peaks in the 2D spectra are a direct indicator of delocalization. Furthermore, dynamical processes can be analyzed in terms of double-sided Feynman diagrams which is demonstrated on the example of energy transfer. The chapter ends with a discussion about the potential pitfalls if double-sided Feynman diagrams are used to analyze 2D spectra.

Chapter 6 discusses the recent developments in higher-order spectroscopy focusing on the new techniques that were developed as part of this thesis. The technique of phase cycling is discussed in detail. Phase cycling can be used to extract higher-order fluorescence-detected 2D spectra that correlate different coherences with each other. The higher-order signals can be used to study a variety of phenomena such as highly excited states in molecules, multi-exciton correlation in nanocrystals or EEA in a molecular dimer. Furthermore, fifth-order coherently detected EEI2D spectroscopy in the context of molecular aggregates and polymers is discussed. The technique of EEI2D spectroscopy is well-suited to track exciton diffusion by utilizing EEA as a probe. Both techniques, fluorescence-detected 2D spectroscopy as well as coherently detected EEI2D spectroscopy, are directly compared by measuring annihilation in a dimer. The chapter closes with the recent developments in higher-order PP spectroscopy that will be further discussed in Chapter 8.

Chapter 7 features the question if the anisotropy in fifth-order EEI2D spectroscopy can be used to obtain additional information about exciton transport. The general expressions for the calculation of the anisotropy in EEI2D spectroscopy are derived by rotational averaging. The expressions are used to demonstrate that the magic angle used to obtain isotropic signals and known from third-order experiments, is still valid in fifth-order EEI2D spectroscopy. The anisotropy in EEI2D spectroscopy can be used to determine a variety of different phenomena in polymers such as kinks, energetic and geometric disorder, and geometric domains within one polymer as demonstrated by simulations.

Chapter 8 begins with the extension of EEI2D spectroscopy to measure seventh-order signals. In coherently detected 2D spectroscopy in the PP geometry the higher-order signals are isolated by their spectral position along the excitation axis. Chapter 8 answers the question if higher-order signals can be measured in PP spectroscopy. A measurement protocol is introduced which uses the specific power dependence of

the higher-order signals in PP spectroscopy. Combining measurements at different excitation intensities with specific weighting factors allows one to isolate the higher-order PP signals. The obtained signals from both techniques, 2D as well as PP, can be utilized to eliminate contaminations by higher-order contributions at different signals. The procedure is a simple method that allows one to isolate the different terms of the perturbation theory and can be easily extended systematically to higher-order terms. Using this correction in PP as well as in 2D spectroscopy, annihilation-free third-order signals can be obtained even at high excitation intensities. Both techniques of separating different signal contributions, either by their spectral position along the excitation axis in 2D spectroscopy or by their power dependence in PP spectroscopy, are directly compared by measuring the third-, fifth-, and seventh-order nonlinear signals of squaraine oligomers. The higher-order signals can be used to study multi-(quasi)particle interaction of different systems as it is demonstrated on squaraine copolymers by measuring multi-exciton interaction of up to six excitons.

The final chapter summarizes all the previous chapters and provides an outlook on future experiments. In particular, measurement of higher-order PP spectroscopy on complete cells of green sulfur bacteria allows one to disentangle the exciton transport along the complex as well as the exciton diffusion within the antenna complex. Measurements at specific excitation intensities results in clean third- and fifth-order signals. The single-exciton dynamics can be studied by the third-order signal while the fifth-order signal characterizes the exciton diffusion within the antenna complex. Using both signals, a comprehensive picture of the exciton dynamics in light-harvesting systems can be achieved from one single experiment. Furthermore, two-color higher-order spectroscopy is discussed in order to observe the vibrational signatures of highly excited states. As a third example the combination of higher-order PP spectroscopy with microscopy is shown providing a platform to measure spatially resolved higher-order signals. Using this technique, local differences of the exciton diffusion can be studied which allows one to characterize thin films and interfaces.

Density Matrix Formalism

2.1. Time Evolution of the Density Matrix

Our starting point to describe the system dynamics in the case of light–matter interaction is the time-dependent Schrödinger equation [23] which is [1]

$$\frac{\partial}{\partial t} |\Psi(t)\rangle = -\frac{i}{\hbar} H(t) |\Psi(t)\rangle , \qquad (2.1)$$

with the Hamiltonian of the system $H(t)$.[2] The wavefunction $\Psi(t)$ describes the microscopic system, for example, an isolated molecule. We expand the wavefunction in the basis of the molecular eigenstates $|n\rangle$ by

$$|\Psi(t)\rangle = \sum_n c_n(t) |n\rangle \qquad (2.2)$$

with the coefficients $c_n(t)$ [23]. The energies of the states E_n are defined by the time-independent Hamilton operator H_0 with

$$H_0 |n\rangle = E_n |n\rangle . \qquad (2.3)$$

We introduce now the density matrix $\rho(t)$ as an alternative to describe the system by

$$\rho(t) \equiv |\Psi(t)\rangle \langle \Psi(t)| = \sum_m \sum_n c_m^*(t) c_n(t) |n\rangle \langle m| . \qquad (2.4)$$

In order to find the equivalent to the Schrödinger equation for the density matrix, we calculate its derivative with respect to time:

$$\frac{\partial}{\partial t}\rho(t) = \frac{\partial}{\partial t} \left(|\Psi(t)\rangle \langle \Psi(t)| \right) = \left(\frac{\partial}{\partial t} |\Psi(t)\rangle \right) \langle \Psi(t)| + |\Psi(t)\rangle \left(\frac{\partial}{\partial t} \langle \Psi(t)| \right) . \qquad (2.5)$$

Using Eq. (2.1) and its complex conjugate

$$\frac{\partial}{\partial t} \langle \Psi(t)| = \frac{i}{\hbar} \langle \Psi(t)| H(t), \qquad (2.6)$$

---

[1]$\hbar = 1.055 \times 10^{-34}$ Js
[2]The operator notation by a "hat" is discarded throughout this work, i.e., $\hat{H}$ is expressed by H etc.

we can simplify Eq. (2.5) to [23]

$$
\begin{aligned}
\frac{\partial}{\partial t}\rho(t) &= -\frac{i}{\hbar}H(t)\left|\Psi(t)\right\rangle\left\langle\Psi(t)\right| + \frac{i}{\hbar}\left|\Psi(t)\right\rangle\left\langle\Psi(t)\right|H(t) \\
&= -\frac{i}{\hbar}H(t)\rho + \frac{i}{\hbar}\rho H(t) \\
&= -\frac{i}{\hbar}\left[H,\rho\right].
\end{aligned}
\tag{2.7}
$$

Equation (2.7) is known as the Liouville–von Neumann equation. Note that for the state of a single molecule, i.e., a pure state, the density matrix formalism and the wavefunction formalism are identical and the Liouville–von Neumann equation replaces the time-dependent Schrödinger equation. The diagonal elements of the density matrix ρ_{nn} are interpreted as the probability to find the system in state n. Therefore, the elements are non-negative and the sum, i.e., the trace of the density matrix, is $\mathrm{Tr}(\rho) = 1$ [23]. In that sense, the diagonal elements of the density matrix correspond to populations. The off-diagonal elements ρ_{mn} correspond to coherences, i.e., coherent superpositions between the corresponding states. The density matrix formalism can also be used to describe a statistical ensemble which is not possible using wavefunctions [23, 24]. The expectation value of any operator A is calculated by taking the trace of the product of the density matrix and the operator:

$$
\langle A\rangle = \mathrm{Tr}\left\{\rho A\right\}.
\tag{2.8}
$$

The density matrix is also well suited to describe the interaction with light and can be used to study different aspects of spectroscopy [23, 25]. For this purpose, we switch to the interaction picture. The interaction picture separates the dynamics that are induced by the interaction with the light field from the dynamics of the system when the light field is not present. The wavefunction in the interaction picture $\Psi_I(t)$ is defined as

$$
\left|\Psi(t)\right\rangle \equiv e^{-\frac{i}{\hbar}H_0(t-t_0)}\left|\Psi_I(t)\right\rangle
\tag{2.9}
$$

with t_0 as an arbitrary reference point in time [23]. We further separate the Hamiltonian in a time-independent part H_0 and the external time-dependent perturbation

$$
H(t) = H_0 + V(t) = H_0 - \mu E(t).
\tag{2.10}
$$

Here, the time-dependent part contains the electric field $E(t)$ and the transition dipole operator μ.

An operator $\mathscr{O}(t)$ can be transferred into the interaction picture by $U^\dagger(t,t_0)\mathscr{O}(t)(t,t_0)$ with $U(t,t_0)$ as the evolution operator defined as

$$U(t,t_0) = e^{-\frac{i}{\hbar}H_0(t-t_0)} \tag{2.11}$$

and the dagger represents the hermitian conjugate. Based on this, we define the density matrix in the interaction picture $\rho_I(t)$ by

$$\rho(t) \equiv e^{-\frac{i}{\hbar}H_0(t-t_0)}\rho_I(t)e^{\frac{i}{\hbar}H_0(t-t_0)}. \tag{2.12}$$

We can extend the density matrix into a power series in terms of the interaction with the electric field. For n interactions, we achieve [23]

$$\begin{aligned}
\rho_I(t) = \rho_I(t_0) + \sum_{n=1}^{\infty} \left(-\frac{i}{\hbar}\right)^n \int_{t_0}^{t} \mathrm{d}t_n \int_{t_0}^{t_n} \mathrm{d}t_{n-1}... \int_{t_0}^{t_2} \mathrm{d}t_1 \\
\times \left[V_I(t_n), \left[V_I(t_{n-1}), ... \left[V_I(t_1), \rho_I(t_0)\right]...\right]\right].
\end{aligned} \tag{2.13}$$

Switching back from the interaction picture to the Schrödinger picture results in

$$\begin{aligned}
\rho(t) &= \rho^{(0)}(t) + \sum_{n=1}^{\infty} \rho^{(n)}(t) \\
&= \rho^{(0)}(t) + \sum_{n=1}^{\infty} \left(-\frac{i}{\hbar}\right)^n \int_{t_0}^{t} \mathrm{d}t_n \int_{t_0}^{t_n} \mathrm{d}t_{n-1}... \int_{t_0}^{t_2} \mathrm{d}t_1 \\
&\quad \times e^{-\frac{i}{\hbar}H_0(t-t_0)} \left[V_I(t_n), \left[V_I(t_{n-1}), ... \left[V_I(t_1), \rho(t_0)\right]...\right]\right] e^{+\frac{i}{\hbar}H_0(t-t_0)}.
\end{aligned} \tag{2.14}$$

Discarding the density matrix without any perturbation $\rho^{(0)}(t)$ and writing the perturbation explicitly for $\rho^{(n)}$ results in

$$\begin{aligned}
\rho^{(n)}(t) &= \left(\frac{i}{\hbar}\right)^n \int_{t_0}^{t} \mathrm{d}t_n \int_{t_0}^{t_n} \mathrm{d}t_{n-1}... \int_{t_0}^{t_2} \mathrm{d}t_1 E(t_n)E(t_{n-1})...E(t_1) \\
&\quad \times e^{-\frac{i}{\hbar}H_0(t-t_0)} \left[\mu_I(t_n), \left[\mu_I(t_{n-1}), ... \left[\mu_I(t_1), \rho(t_0)\right]...\right]\right] e^{+\frac{i}{\hbar}H_0(t-t_0)}.
\end{aligned} \tag{2.15}$$

This expression[3] contains the information how a system evolves under the interactions with n perturbations induced by the electric field. In the next section we will evaluate how the different excitation pathways can be measured.

---

[3] Note that the prefactor is now $\left(\frac{i}{\hbar}\right)^n$ instead of $\left(-\frac{i}{\hbar}\right)^n$ because each of the n interactions carry an additional negative sign.

2.2. Nonlinear Polarization and Double-Sided Feynman Diagrams

In a nonlinear optical experiment, the macroscopic polarization $P^{(n)}(t)$ is measured which can be expressed with the dipole operator μ by [23]

$$P^{(n)}(t) = \text{Tr}\left\{\mu\rho^{(n)}(t)\right\}. \tag{2.16}$$

We switch to relative time delays instead of absolute times by substituting $\tau_n \equiv t - t_n$, $\tau_{n-1} \equiv t_n - t_{n-1}$, ..., $\tau_1 = t_2 - t_1$. The reason for relative time delays is that relative time delays rather than absolute times are controlled in an experiment. The absolute and relative time delays are shown in Fig. 2.1a. Furthermore, we consider that the density matrix is in equilibrium before the interactions take place. We take this into account by setting $t_0 \rightarrow -\infty$ and therefore $\rho(-\infty)$. We can now write the general n-th order polarization $P^{(n)}(t)$ as

$$\begin{aligned} P^{(n)}(t) = \int_{-\infty}^{\infty} \mathrm{d}\tau_n \int_{-\infty}^{\infty} \mathrm{d}\tau_{n-1}... \int_{-\infty}^{\infty} \mathrm{d}\tau_1 E(t - \tau_n) \\ \times E(t - \tau_n - \tau_{n-1})...E(t - \tau_n - \tau_{n-1} - ... - \tau_1)Q^{(n)}(\tau_n, ..., \tau_1) \end{aligned} \tag{2.17}$$

containing the n-th order response function [9]

$$\begin{aligned} Q^{(n)}(\tau_n, ..., \tau_1) = \left(\frac{i}{\hbar}\right)^n \Theta(\tau_n)...\Theta(\tau_1) \\ \times \text{Tr}\left\{\mu U(\tau_n)\left[\mu, U(\tau_{n-1})\left[\mu, U(\tau_{n-2}), ... \left[\mu, U(\tau_1)\left[\mu, \rho(-\infty)\right]\right]...\right]\right]\right\}. \end{aligned} \tag{2.18}$$

where the Heaviside functions Θ are reflecting the causality of the response. Equation (2.18) corresponds to 2^n different excitation pathways because the dipole operator interacts from the left as well as from the right on the density matrix due to the commutator. Some of these excitation pathways are the complex conjugate of each other so it is enough to consider only 2^{n-1} pathways [23]. The different excitation pathways can be expressed by double-sided Feynman diagrams as shown in Fig. 2.1b [9, 25–28]. In these diagrams the temporal evolution of the density matrix including the interaction with light is illustrated. Time flows from bottom to top and interaction with the light field is represented by an arrow pointing towards or away of the density matrix. An arrow pointing to the density matrix corresponds to an excitation of the bra or the ket of the density matrix while an arrow pointing away corresponds to a de-excitation of the bra or the ket of the density matrix. The electric field can be written as

$$E(t) = E_0(t)\left(e^{-i\omega_0 t + i\mathbf{k}\cdot\mathbf{r} + i\phi} + e^{+i\omega_0 t - i\mathbf{k}\cdot\mathbf{r} - i\phi}\right) \tag{2.19}$$

with the pulse envelope $E_0(t)$, the carrier frequency ω_0, wavevector $\mathbf{k}$, and the phase factor ϕ [23]. An arrow pointing to the right in the double-sided Feynman diagrams cor-

responds to $e^{-i\omega t + i\mathbf{k}\cdot\mathbf{r} + i\phi}$ while an arrow pointing to the left corresponds to $e^{+i\omega t - i\mathbf{k}\cdot\mathbf{r} - i\phi}$. The emission of the signal is denoted by a dashed arrow to demonstrate that this
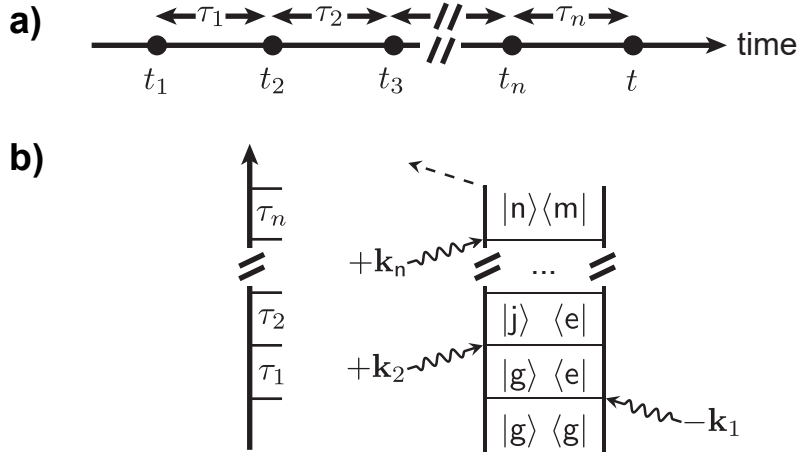
Figure 2.1.: Graphical expression of the nonlinear polarization with double-sided Feynman diagrams. (a) The times for the interactions can be defined at absolute times shown as points or as relative time delays shown as arrows. (b) The different excitation pathways of the nonlinear polarization correspond can be expressed as double-sided Feynman diagrams. In these diagrams, time is flowing from bottom to top and interactions with the density matrix are shown as arrows with the wavevector $\mathbf{k}$ that either excite or de-excite the system. The last dashed arrow corresponds to the emission of the signal. The ground state is labeled $|g\rangle$ and the other states ($|e\rangle$, $|j\rangle$, $|m\rangle$, $|n\rangle$) represent excited states.

process is different to the other interactions with the electric field. Note that each interaction from the right results in an additional multiplication of -1 of the response function $Q^{(n)}$ [23]. However, care has to be taken of the overall sign of diagrams since also an additional factor of -1 is sometimes included reflecting the specific experimental definition of signals [20]. The total number of diagrams that has to be considered in an experiment can be drastically reduced by the rotating-wave approximation (RWA), time ordering of the pulses, phase-matching condition, and phase cycling [23].

We have seen how the interaction of light with a system leads to a nonlinear polarization and how this polarization can be described in terms of double-sided Feynman diagrams. We now want to focus on the experimental side and discuss different ultrafast spectroscopic techniques.

Coherent Two-Dimensional Spectroscopy

Two-dimensional spectroscopy is a technique which combines high spectral resolution with high temporal resolution [23, 29–34]. Various ultrafast phenomena in physical [35–38], biological [39–42], and chemical systems [43–46] can be studied with 2D spectroscopy. Examples include, but are not limited to investigation of exciton transport in light-harvesting complexes [47], chemical reactions [48], and polaritons [49]. Depending on the employed spectral region, specific molecular properties can be investigated. For example, using 2D spectroscopy in the infrared region allows one to study molecular vibrations while visible light can be used to investigate electronically excited states. Since the experiments that were carried out in this thesis used visible light, we restrict our discussion mostly on this spectral region. The present chapter is intended to provide the reader with an overview of the state of 2D spectroscopy and will help the reader to better understand the different experiments in this thesis. The chapter is structured as follows: First we focus on the advantages of 2D spectroscopy compared to common PP techniques such as transient absorption (TA). After this, various implementations of 2D spectroscopy with their specific advantages as well as examples of experiments are discussed. The chapter closes with a detailed description of the experimental setup that was used during this thesis.

3.1. From Pump–Probe to Coherent Two-Dimensional Spectroscopy

With the availability of ultrashort laser pulses it is possible to investigate phenomena which occur on femtosecond timescales including molecular processes such as internal conversion (IC), vibrational relaxation, and photochemical reactions. One of the most common techniques in the ultrafast community is PP spectroscopy [50–57]. In terms of perturbation theory, PP spectroscopy is a technique that detects a third-order polarization, i.e., three interactions with the electric fields take place. In PP spectroscopy the system is first excited by one laser pulse, i.e., the pump pulse with the wavevector $\mathbf{k}_{\mathrm{pu}}$. After a waiting time T usually called population time, a second laser pulse, i.e., the probe pulse, with wavevector $\mathbf{k}_{\mathrm{pr}}$ interacts with the sample and probes the excited system. By changing the population time T, the dynamics of the excited states can be tracked. In TA measurements, the induced absorption by the pump pulse is mea-

sured by the probe pulse. In order to isolate this transient change, the probe spectra with and without the pump pulse have to be measured separately. This can be easily achieved by modulating the pump beam with a chopper. A schematic setup depicting a PP setup is shown in Fig. 3.1a. In this thesis we define the TA signal as a change in absorbance by

$$\text{Signal}_{\text{TA}}(T, \omega) = -\log_{10} \frac{I_{\text{pumped}}(T, \omega)}{I_{\text{unpumped}}(\omega)} \tag{3.1}$$

with $I_{\text{pumped}}(\omega)$ and $I_{\text{unpumped}}(\omega)$ as the intensities of the probe spectrum after passing the sample with and without the pump, respectively. The third-order TA signal is emitted in the direction of the probe with the phase-matching direction of $\pm\mathbf{k}_{\text{pu}} \mp \mathbf{k}_{\text{pu}} + \mathbf{k}_{\text{pr}}$. In TA techniques different signals can be distinguished: the loss of ground state absorption [ground-state bleach (GSB)], stimulated emission from the excited state (SE), and the excitation of the first-excited state to even higher excited states [excited-state absorption (ESA)].[1] Since the difference in absorption with and without the pump pulse is measured, the sign of GSB and SE is the same while the ESA has an opposite sign compared to GSB and SE. The absolute sign of the different signals depends on the particular definition of the TA signal. With the definition of Eq. (3.1) the GSB and SE contributions have a negative sign while the ESA has a positive sign. Note that the particular shape of the probe spectrum is not imprinted into the signal because the signal is calculated by dividing the probe spectrum with excitation by the probe spectrum without excitation and therefore any spectral shape of the probe spectrum cancels. However, if the probe spectrum contains spectral regions with low intensity the signal-to-noise ratio (SNR) of the TA signal is decreasing at this region. A schematic TA map is shown in Fig. 3.1b. Different positive and negative features with their individual amplitudes and lifetimes can be distinguished. Positive and negative features can cancel each other in the TA map which results in a complex interplay of different signals that can be disentangled by global analysis [60]. The technique of PP spectroscopy is nowadays a standard tool for the investigation of ultrafast phenomena such as the primary processes of vision which includes a photoisomerization on the femtosecond timescale [58]. However, the short excitation pulses lead to a problem: Since the pulse length of a spectrum is connected to its temporal length via Fourier transformation an ultrashort laser pulse has a broad spectrum and vice versa. If the observed time scales become shorter, a shorter pump pulse is needed resulting in a broader spectrum. This is especially a problem if an absorption spectrum contains spectral features which are not well separated. In such a case a short pump pulse excites several transitions and the different contributions are difficult to disentangle. An example for such a system with several energetically close transitions is the Fenna–Matthews–Olson (FMO) complex in green sulfur bacteria [61, 62].

---

[1]Another type of signal that is disregarded in the following discussion is the product absorption that occurs due to the formation of a photoproduct [58, 59].
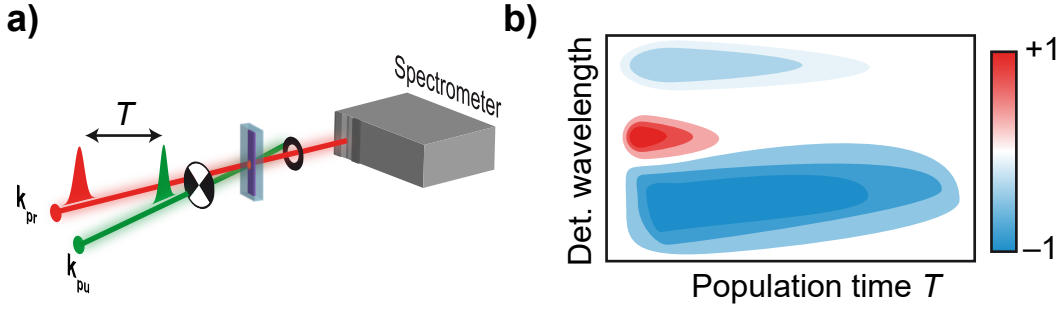
Figure 3.1.: Principle of transient absorption spectroscopy. (a) The first pulse, i.e., the pump pulse, excites the system and after a time delay T another pulse probes the system. After passing the sample the pump beam is blocked by an iris and the probe spectrum is measured. The pump beam is chopped and the transient absorption spectrum is constructed from the probe spectrum with and without the excitation beam. (b) For each population time a TA spectrum is measured and these TA spectra can be plotted as a map as shown here. The TA signal is negative for GSB and SE contributions and positive for an ESA.

The FMO complex contains eight different pigments. The absorption bands of this system are spectrally close to each other and the individual dynamics as well as the energy transport from the different subunits to each other is difficult to resolve in a PP experiment.

The problem was solved with the development of 2D spectroscopy. The technique of 2D spectroscopy was theoretically suggested [63] based on similar concepts in NMR spectroscopy [64], first developed in terms of nonlinear optics [65] and then used in near-infrared [66] and the infrared region [67]. Nowadays it is used in all the spectral regions reaching from X-Rays [68] and ultraviolet [69, 70] over the visible [71, 72], infrared [23, 66] into the Terahertz [36] regime. Let us take a closer look at 2D spectroscopy measured in the PP geometry. In this geometry the close correspondence between PP and 2D spectroscopy becomes visible [73]. In a 2D experiment in this configuration the pump pulse is split into two replica with the time delay τ which is also called coherence time (Fig. 3.2a). The first two pulses act now as the pump pulses while the third pulse is the probe pulse. For each population time step T, the coherence time τ is scanned and for each set of delays, the TA signal is measured. The signal is emitted in the same phase-matching direction as in a PP experiment ($\pm\mathbf{k}_{pu} \mp \mathbf{k}_{pu} + \mathbf{k}_{pr}$) since both pump pulses have the same wavevector $\mathbf{k}_{pu}$. By performing Fourier transformation over the coherence time τ, a 2D map is obtained with the probe frequency on one axis and the excitation frequency on the other axis (Fig. 3.2b). The detection axis can be directly obtained by measuring the probe with a spectrometer. Due to the Fourier transformation, the missing spectral resolution in the excitation process from PP spectroscopy is recovered. What is the physical picture behind the spectral resolution of the excitation in 2D spectroscopy?

In a PP experiment the pump spectrum is constant during the whole experiment. In a 2D experiment the pump spectrum is modulated depending on the time delay τ. For different delays certain frequencies interfere destructively while other frequency components interfere constructively. As a consequence, for each delay τ different parts of the absorption spectrum are excited. The Fourier transformation over the coherence time extracts the information of the specific excitation. Imperfections such as jittering in the coherence time lead to a loss of spectral resolution. Therefore, phase stability of the coherence time is necessary which leads to additional experimental requirements. The phase stabilization can either be realized by passive stabilization building a robust setup and using common path optics [71, 72] or the phase can be actively stabilized [74, 75]. Note that if the 2D spectrum is integrated along the excitation axis, the PP signal is recovered which demonstrates the close correspondence between the two techniques [23].
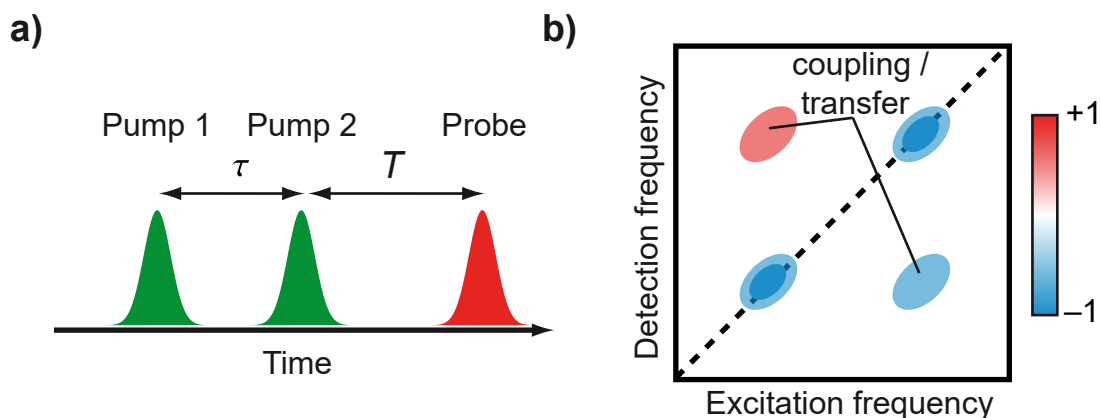
Figure 3.2.: Coherently detected 2D spectroscopy in PP geometry. (a) A double pulse with a variable delay τ excites the sample first followed by a probe pulse after the delay T. (b) In the 2D map, cross peaks and diagonal peaks can be distinguished. The cross peaks are a sign of coupling or energy transfer.

2D spectroscopy is in principle a spectroscopic method that correlates transitions with each other. In a 2D spectrum two different kinds of peaks can be distinguished: diagonal peaks and off-diagonal peaks which are also called cross peaks [23, 76]. Diagonal peaks correspond to excitation and probing of the same transitions while in coherently detected 2D spectroscopy cross peaks reflect coupling or energy transfer. 2D spectroscopy is a useful tool to investigate energy transfer in a complex system with many transitions because the transfer can be followed by observation of the amplitude of the cross peaks for different population times T [77]. It was theoretically demonstrated that under certain conditions the state-to-state population transfer-rate model can be completely and uniquely recovered from 2D spectroscopy which is not possible with normal TA spectroscopy [78]. The power of 2D spectroscopy can be demonstrated in natural light-harvesting complexes. Here, the energy is transferred after absorption over several parts of the photosynthetic complex with specific spectral signatures.

With the help of 2D spectroscopy the time constants for the transport between the different parts of the light-harvesting complex were identified [79]. Further examples of phenomena that can be studied with 2D spectroscopy are delocalization [80], inhomogeneous and homogenous lineshapes [81], and lifetimes [8]. 2D spectroscopy can also be used to study coherences which manifest as oscillations during the population time T. In order to focus on the coherences, the population dynamics are subtracted by fitting the dynamics of the peaks with a series of exponentials which leaves only the oscillating contribution. Additional Fourier transformation over T allows one to extract specific frequencies which can be analyzed in the form of beating maps [82]. The approach was applied to reveal the electronic structures of molecules [83] or nanocrystals [84].

3.2. Implementations of Two-Dimensional Spectroscopy

Two-dimensional spectroscopy has gained popularity during the last decades and nowadays a variety of different methods and experimental implementations are known. In general, the different techniques can be separated according to their detection scheme such as action-based spectroscopy [85, 86] and coherently detected spectroscopy [87, 88] or according to their geometry such as collinear [89–91], partially collinear (PP geometry) [73, 92–94], or noncollinear [71, 87, 88, 95]. In this section some of the experimental realizations of multidimensional spectroscopy are discussed.

One of the possible implementations of 2D spectroscopy is the noncollinear geometry as shown in Fig. 3.3a [66, 71, 72]. Here, four beams are used with four different wavevectors. The pulses 1 and 2 act as the pump pulses with the wavectors $\mathbf{k_1}$ and $\mathbf{k_2}$, respectively, while the third pulse 3 is the probe pulse with the wavevector $\mathbf{k_3}$. Different signal contributions such as the rephasing and non-rephasing signals are isolated by their phase matching conditions which reflects the conservation of momentum [23]. The corresponding third-order signals are emitted in the phase matching directions $+\mathbf{k_1} - \mathbf{k_2} + \mathbf{k_3}$ for the non-rephasing signal contribution and $-\mathbf{k_1} + \mathbf{k_2} + \mathbf{k_3}$ for the rephasing signal contributions. The signal is then heterodyne detected by the fourth beam which is often called local oscillator (LO) with the wavevector $\mathbf{k}_{\mathrm{LO}}$. The LO interferes with the third-order signal with a fixed delay and the spectral interference is measured by a spectrometer. Such an experiment is called coherently detected 2D spectroscopy [8]. Different geometries for the two pump beams and the probe beam can be realized. Note that the chosen geometry dictates the location of the LO. One geometry is the equilateral triangle. In this geometry, the two pump beams and the probe beam are located at the corners of a regular triangle. In the box-CARS geometry, the three beams are located at the corners of a square. In both geometries, box-CARS as well as the equilateral triangle, the rephasing and non-rephasing parts of the signal can be measured by changing the location of the LO. However, in practice it is much easier to simply change the time ordering between pulse 1 and pulse 2 and leave the

position, i.e., the wavevector of the LO constant [87, 96]. The population time T can be scanned via a mechanical stage which allows to measure long population times. Since all four beams have different beam paths, the polarization of each beam can be set independently as indicated in Fig. 3.3a. Polarization-controlled experiments are used to suppress different contributions such as specific coherences or peaks in the 2D spectrum [97–99]. If the signal is heterodyne detected by a LO, the phase between the LO and the signal has to be determined for each experiment individually. For this purpose an additional PP experiment is performed and the integrated 2D spectrum and the PP spectrum are compared to determine the phase [71, 100]. If the phasing procedure is not done correctly, the absorptive and dispersive parts of the 2D spectrum are mixing which lead to a distortion of the lineshapes [23]. One of the first 2D experiments in the visible spectral region using a noncollinear geometry was the already mentioned investigation of the FMO complex of green sulfur bacteria [47]. The 2D spectra determined the state-to-state transfer as well as the delocalization of the excitons within the photosynthetic antenna complex. A more recent example of 2D spectroscopy in the noncollinear geometry investigated the coherences that occur in the FMO complex which were part of an ongoing discussion concerning coherent superpositions between excitonic states and their significance in photosynthesis [101–104]. Combining a noncollinear setup with polarization control identified the nature and timescales of the underlying coherences and demonstrated that the origin of the long-lived coherences are vibrational coherences and not excitonic coherences [105].

Coherently detected 2D spectroscopy can be realized in a PP geometry as well. A setup for 2D experiments in the PP geometry is schematically shown in Fig. 3.3b. Here a double pulse excites the system and a third pulse probes the system. The signal is isolated for example by using choppers which allows one to obtain the TA signal for each coherence time step τ and population time step T [73, 92, 106]. The probe pulse also acts as the LO, i.e., the signal is self-heterodyne detected [23]. Therefore, no further phasing procedure is needed. Since the first two pulses, i.e., the two pump pulses, have the same wavevector $\mathbf{k}_{pu}$, the rephasing and the non-rephasing part of the signal are emitted in the same direction. Therefore, the absorptive 2D spectrum, i.e., the sum of the rephasing and non-rephasing, is directly measured. Additional experimental procedures such as phase cycling can be used to separate the rephasing and non-rephasing contributions [107, 108]. 2D spectroscopy in the PP geometry can be realized by inserting an interferometer or pulse shaper into the excitation beam of an ordinary PP experiment [73]. We will discuss a setup in PP geometry in more detail at the end of this chapter.

In the past fifteen years, multidimensional spectroscopy using incoherent observables such as photoelectrons [109], photoions [91], fluorescence [110, 111], and photocurrents [112] have been realized. All the techniques have in common that a signal which is proportional to the excited state population of the sample, is measured after excitation with a set of pulses. Therefore, instead of a third-order signal, a fourth-order signal is measured. Techniques that use an incoherent observable are also often called action-based or population-detected techniques. In contrast to coherently detected tech-

a) Noncollinear geometry   **b)** Pump–probe geometry
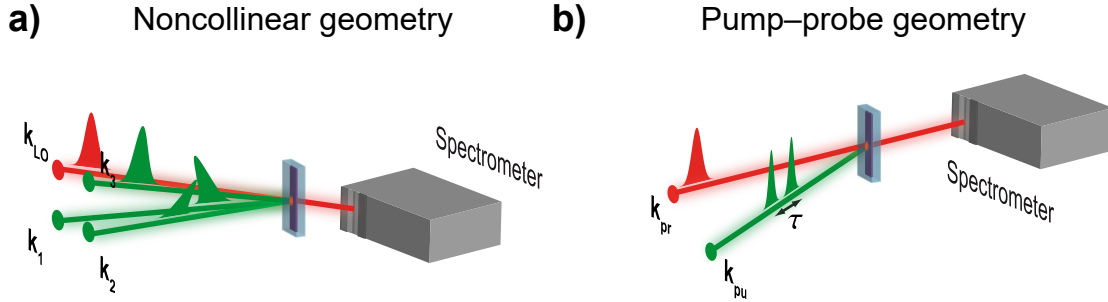
Figure 3.3.: Two examples of experimental implementations of coherently detected 2D spectroscopy. (a) In the noncollinear geometry, three beams with different wavevectors $\mathbf{k}_i$ with $i = 1, 2, 3$ interact with the sample. The fourth beam acts as the local oscillator (LO) with the wavevector $\mathbf{k}_{\mathrm{LO}}$. The polarizations of the pulses can be changed as demonstrated with pulse one and two. (b) In the PP geometry the first two pulses act as the excitation pulses and share the same wavevector $\mathbf{k}_{\mathrm{pu}}$. The probe beam interacts with a different wavevector with the sample and is a also used as a LO.

niques, the nonlinear signal in action-detected spectroscopy cannot be distinguished by its specific phase-matching condition and therefore several procedures have been established to extract the nonlinear signal from measurements using an incoherent observable. Phase cycling is one of these techniques. In phase cycling, the phases of the pulses (φ_i with $i = 1, 2, 3, 4$) are changed systematically in addition to the time delays [5, 26, 90, 113–115]. The different phase combination are imprinted into the incoherent observable and for each set of delays and phases, the intensity of, e.g., the fluorescence is measured. The so obtained raw data is weighted to extract different contributions such as the rephasing spectrum. Fourier transformation over the delay τ provides the excitation axis while the detection axis is achieved by Fourier transformation over the delay t between pulse 3 and pulse 4. Another technique to extract nonlinear signals from an incoherent observable is phase modulation. In this approach, the relative phase of each of the pulses is modulated with a specific frequency (Ω_i with $i = 1, 2, 3, 4$) by an acuosto-optic modulator (AOM) [37, 110, 111, 116–118]. Phase modulation is also named dynamic phase cycling [117, 119]. The modulation frequency replaces the wavevector from the noncollinear geometry. Therefore, each interaction with these pulses can be tracked by its specific modulation frequency that is imprinted on the signal. The signal is then for example isolated by lock-in detection on combinations of these modulation frequencies [111, 118]. Note that phase cycling and phase modulation are not exclusively used in action-detected spectroscopy but can also be used in coherently detected experiments. For example phase cycling can be used to suppress scattering contributions in coherently detected spectroscopy [23]. We will discuss both techniques in more detail in Chapter 6.

Special care has to be taken in the interpretation of action-based multidimensional spectroscopy. Especially the interpretation of fluorescence-detected 2D spectroscopy

was thoroughly discussed in recent years [120–122]. In contrast to coherently detected signals, additional double-sided Feynman diagrams contribute to the action-detected signal. Interestingly, there is a set of double-sided Feynman diagrams that does not end in a singly excited state but in a doubly excited state. We discuss briefly the impact of these additional pathways in the context of 2D spectroscopy using fluorescence detection. In fluorescence-detected 2D spectroscopy each diagram is weighted by the yield of the final population state Φ [122]. A diagram which ends up in a doubly excited state can have in principle a yield of $\Phi = 2$, i.e., it can contribute twice as strong to the signal as a diagram that ends in a singly excited state. This can be easily demonstrated on the example of two independent monomers. Such a system can be described in the basis of collective states [123]. The doubly excited state consists of the first excited state of both monomers. Since each monomer is excited and they do not interact, also fluorescence from each monomer is possible and in principle two photons can be emitted. In the case of interaction between the monomers the yield of the diagrams ending in a population of a doubly excited state can be reduced by processes such as EEA or IC. Then cancellation of different diagrams takes place which leads to fundamental differences in fluorescence-detected and coherently detected 2D spectra. As one of the most surprising consequences, cross peaks in fluorescence-detected 2D spectroscopy in a molecular dimer can occur due to EEA in the system [120]. Recent studies directly compared fluorescence-detected and coherently detected methods both experimentally and theoretically, and pointed to the technical as well as fundamental differences [8, 120, 121]. One big advantage of fluorescence-detected 2D spectroscopy as well as other action-detected spectroscopic techniques compared to coherently detected methods is that non-resonant solvent contributions are not mixing into the signal. This allows to measure the early time dynamics close to $T = 0$ without solvent contributions. Note that other contributions such as different time ordering of the pulses can still distort the signal at early population times as previously shown in coherently detected 2D spectroscopy [124]. A detailed analysis of the non-time-ordered diagrams in the context of action-detected 2D spectroscopy is missing.

Fluorescence detection allows to measure spatially resolved multidimensional spectra using a microscope. In Fig. 3.4a, a setup for fluorescence-detected 2D microspectroscopy based on phase cycling is shown. Phase cycling can be achieved by an acuosto-optic programmable dispersive filter (AOPDF) [89] or by a pulse shaper in 4f-geometry [125]. Signal extraction with phase cycling as well as with phase modulation combined with fluorescence microscopy has been demonstrated [126–129]. Such an experiment allows one to measure a 2D spectrum at different spatial positions which can be used in the case of heterogeneous samples to characterize the spatial variation of physical properties. In one of the examples, fluorescence-detected 2D microspectroscopy was applied to a structured film [130]. The spatially resolved 2D spectra determined the structural differences within the film. Combining the experiments with simulations allowed to determine the optical coherence length and local structure. In another example, spatially resolved 2D spectroscopy was used to characterize the variations in the excitonic structure of bacteria that were grown under different conditions [127].

Note that also coherently detected 2D setups can be combined with microscopy as in a recent example which demonstrated the combination of confocal microscopy, atomic force microscopy and broadband multidimensional spectroscopy [131]. The technique was used to investigate the morphology in (6,13-bis(triisopropylsilylethynyl)(TIPS)-pentacene microcrystals and to observe a low-energy singlet state at the edges of the microcrystals as well as at defects [132].
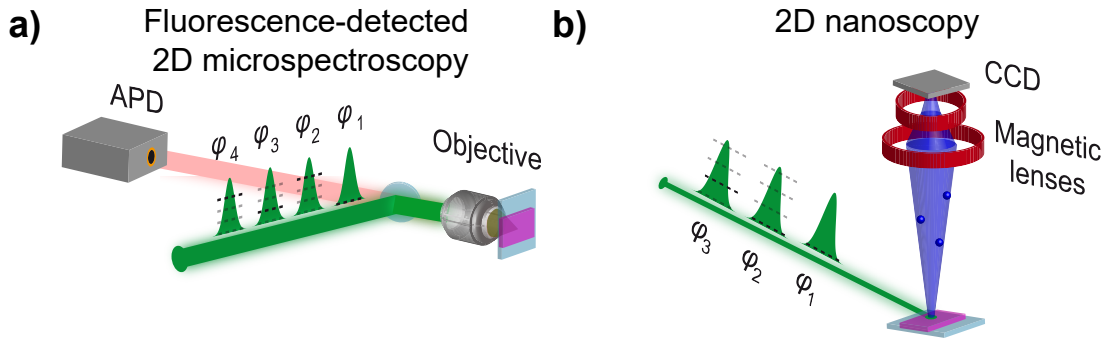
Figure 3.4.: Multidimensional spectroscopy combined with spatially resolved microscopy. (a) In this example of fluorescence-detected microscopy the sample is illuminated by a four-pulse sequence with variable time delays. The fluorescence is collected by the same objective that is used for focusing the pulses onto the sample. The fluorescence is isolated by a dichroic mirror from the excitation light and then measured via an avalanche photodiode (APD). The nonlinear signals are separated by phase cycling indicated by the phases of the pulses φ_i with $i = 1, 2, 3, 4$ that are systematically varied in the experiment. (b) Instead of collecting fluorescence, in 2D nanoscopy, photoelectrons are detected. The electrons are emitted from the sample via multiphoton ionization by the pulse sequence and then detected by magnetic lenses combined with a CCD. The signal can be isolated by phase cycling analogously to fluorescence-detected microspectroscopy.

Another technique which allows spatially resolved 2D spectroscopy on the nanometer scale is 2D nanoscopy. In this approach the spatial resolution is obtained by a photoemission electron microscope (PEEM) [6, 133, 134]. Such an experiment is schematically shown in Fig. 3.4b. The photoelectrons are emitted from the sample by multiphoton ionization via the pulse sequence itself [135]. In principle also a UV pulse could be used for the photoionization. Recent experimental approaches demonstrated the generation of short UV pulses [6, 136, 137]. In the same way as in fluorescence-detected 2D spectroscopy phase cycling is used to extract the signal but instead of the fluorescence intensity the photoelectron yield is measured for each set of phases and delays. Due to the imaging of photoelectrons the spatial resolution is not limited by the diffraction limit of the excitation light and a spatial resolution of around several nanometers depending on the sample conditions can be realized [3]. Not all samples are suited for a PEEM experiment since the sample has to withstand the ultrahigh vacuum conditions and additionally the sample has to be electrically conductive because a high voltage is applied to accelerate the photoelectrons away from the sample into

the imaging system [138]. For high electron densities the Coulomb interaction between the electrons become relevant. This effect is known as space charge and can lead to distorted images in PEEM experiments [139]. In order to avoid space charge the laser intensity has to be reduced to keep the electron density per laser pulse low. However, reducing the laser intensity also decreases the SNR. Therefore, usually laser systems with high repetition rates of 200 kHz or higher are used in PEEM experiments to reduce the acquisition time per image [6, 140]. The technique of 2D nanoscopy allows one to obtain 2D spectra on the nanometer length scale which makes this method extremely powerful to investigate plasmonic and surface phenomena. In the first demonstration of 2D nanoscopy, a silver surface was investigated and the coherence lifetimes at a local hotspot were determined [133]. In another experiment the interface formed between tris(8-hydroxyquinolinato)aluminium (Alq_3) and a Cobalt surfaces was investigated. [135]. The experiments combined 2D nanoscopy with energy filtering of the photoelectrons' kinetic energy and revealed long-lived optical coherences within the disordered molecular film.
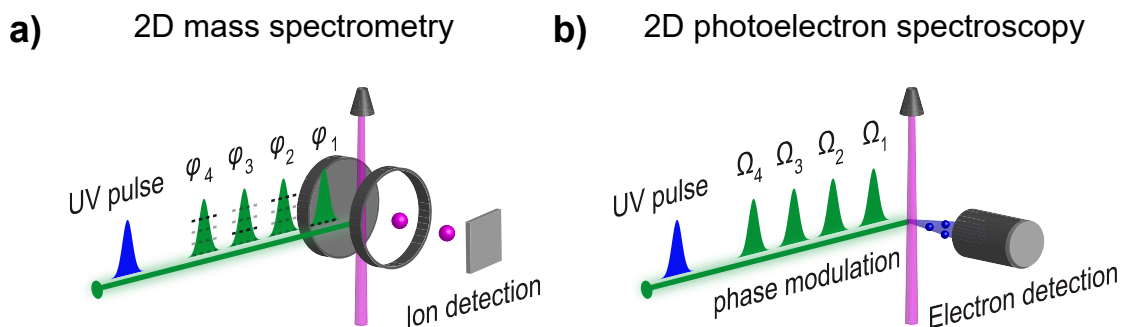
Figure 3.5.: Multidimensional spectroscopy in the gas phase. (a) A molecular beam is combined with mass spectrometry. A four-pulse sequence excites the system and a fifth pulse is used for ionization. The nonlinear signal contribution is then isolated via phase cycling. (b) Another experiment in the gas phase detects photoelectrons instead of ions. In this example the signal extraction is performed via phase modulation indicated by the modulation frequencies Ω_i with $i = 1, 2, 3, 4$.

Molecular gas beams allow one to investigate a sample in the gas phase without the interaction to any solvent. In recent experiments, multidimensional spectroscopy was combined with gas-phase experiments [141]. The sample is ionized followed by detection of either the photoelectrons or the mass ions. The ionization can occur by multiphoton ionization or by the interaction with an additional UV pulse [91]. A schematic setup, in which the mass ions are selected and measured by a mass spectrometer, is shown in Fig. 3.5a. Here the ionization is achieved by an additional UV pulse and signal extraction takes place via phase cycling (indicated by φ_i with $i = 1, 2, 3, 4$). Instead of the mass ions also photoelectrons that are emitted from a molecular beam can be detected as shown in Fig. 3.5b. In this example the signal is extracted via phase modulation (indicated by Ω_i with $i = 1, 2, 3, 4$). Ionization is a step

that is possible for most of the samples in contrast to fluorescence detection which is not feasible for some samples because of their low quantum yields. Therefore, gas-phase 2D experiments could in principle be applied to a broad range of samples. However, the sample has to be suitable for a molecular beam which reduces the samples that can be used in such an experiment. The first ion-detected multidimensional spectroscopy experiment applied an effusive gas beam and studied the ionization pathways of NO_2 [91]. Another experiment demonstrated the capability to study Rubidium molecules (Rb_2 and Rb_3) in helium droplets [37]. In the experiment, a dynamic Stokes shift in the Rb_3 molecules induced by the Helium matrix as well as coherent oscillations in Rb_2 reflecting vibrational wave packets could be observed. A recent study compared the dynamics of azulene in fluorescence-detected 2D spectroscopy in the liquid phase with ion-detected 2D spectroscopy in the gas phase [142]. This experiment investigated the influence of the solvent bath on the molecular dynamics.

Besides fluorescence, photoelectron and ion detection, it is also possible to measure a 2D spectrum using photocurrent as an incoherent observable (Fig. 3.6a) [112, 143].[2] The first demonstration of photocurrent-detected 2D spectroscopy was performed on a nanostructure using a phase-modulation approach [119]. The photocurrent is directly associated with the function of solar cells and is therefore a direct way to study the dynamics of such an optoelectronic device. Following this argumentation, the technique of photocurrent-detected 2D spectroscopy was used to investigate the multi-exciton generation in quantum-dot-based solar cells [144]. In this experiment direct comparison between photocurrent detection and fluorescence detection has been realized. Thorough analysis revealed that the difference in the 2D spectra for fluorescence and photocurrent detection can be explained by the yield of the pathways ending in a population of a doubly excited state that we discussed above. For photocurrent detection, these pathways are contributing more to the signal, i.e., the yield is higher than for fluorescence detection. For fluorescence measurement, the quantum yield of this doubly excited state is significantly reduced due to Auger recombination.

A different approach for multidimensional spectroscopy is based on multiple repetition frequency-stabilized mode-locked lasers [145, 146]. Closely related to this technique is the usage of multiple frequency combs combining stabilization of the repetition rate as well as the carrier-envelope-offset frequencies [147–149]. One experimental setup for 2D spectroscopy based on asynchronous optical sampling, i.e., combining two repetition frequency-stabilized mode-locked lasers, is schematically shown in Fig. 3.6b. The two oscillators have both stabilized repetition frequencies f_r that are slightly different. The time delay between the pump pulses and the probe pulse, i.e., the population time T, is continuously changed from pulse to pulse because of the mismatch between the two repetition rates. The different beams are focused into the sample (focusing optics are not shown in Fig. 3.6b) and the signal is emitted in the corresponding phase-matching direction. A LO is used to interfere with the signal and the intensity of the LO is detected by a photodiode. Scanning the delay t followed by Fourier transforma-

---

[2]Note that 2D nanoscopy measures photoelectrons which can be viewed as an "external" photocurrent while the photocurrent mentioned could be labeled as an "internal" photocurrent.

a) 2D photocurrent spectroscopy   **b)**   2D spectroscopy using
                                                   multiple mode-locked lasers
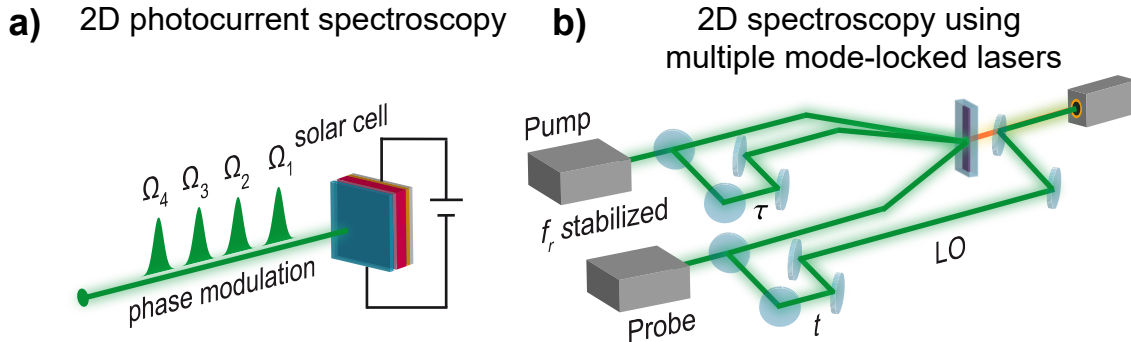
Figure 3.6.: Two different approaches to multidimensional spectroscopy: photocurrent spectroscopy and applying multiple mode-locked lasers. (a) In one variant of 2D spectroscopy the photocurrent is used as an incoherent observable. In this example, a four pulse sequence interacts with a solar cell and the resulting photocurrent is detected. The nonlinear signal is isolated by phase modulation of the pulses indicated by Ω_i with $i = 1, 2, 3, 4$. (b) In a different approach multiple mode-locked lasers with stabilized repetition frequencies f_r are used. In this example the repetition rate of the pump and probe are both stabilized. The coherence time τ as well as the time delay t between probe and LO are scanned via mechanical stages.

tion results in the detection axis. Note that in this setup two mechanical stages are used to scan the coherence time τ and the time delay t between probe and LO. The technique using two repetition frequency-stabilized mode-locked lasers was applied to bacteriochlorophyll a [145]. Due to scanning of the delays by the different repetition rates, the dynamics can be followed from the femtosecond to the nanosecond regime within one experiment enabling to study simultaneously vibrational coherences as well as lifetime dynamics. Another setup uses three frequency combs in order to obtain a 2D spectrum. The method was demonstrated on Rubidium atoms and allowed one to measure a 2D spectrum on the order of milliseconds because no mechanical stages are needed at all [150].

3.3. Experimental Setup

This section provides a detailed description of the setup that was used to measure PP as well as 2D spectroscopy during this thesis [4, 7–11, 16, 18]. We will discuss the hollow-core fiber as a source for ultrashort, broadband pulses as well as the chopping scheme that was used to isolate the nonlinear signal in PP and 2D measurements. The experimental setup is drawn schematically in Fig. 3.7.
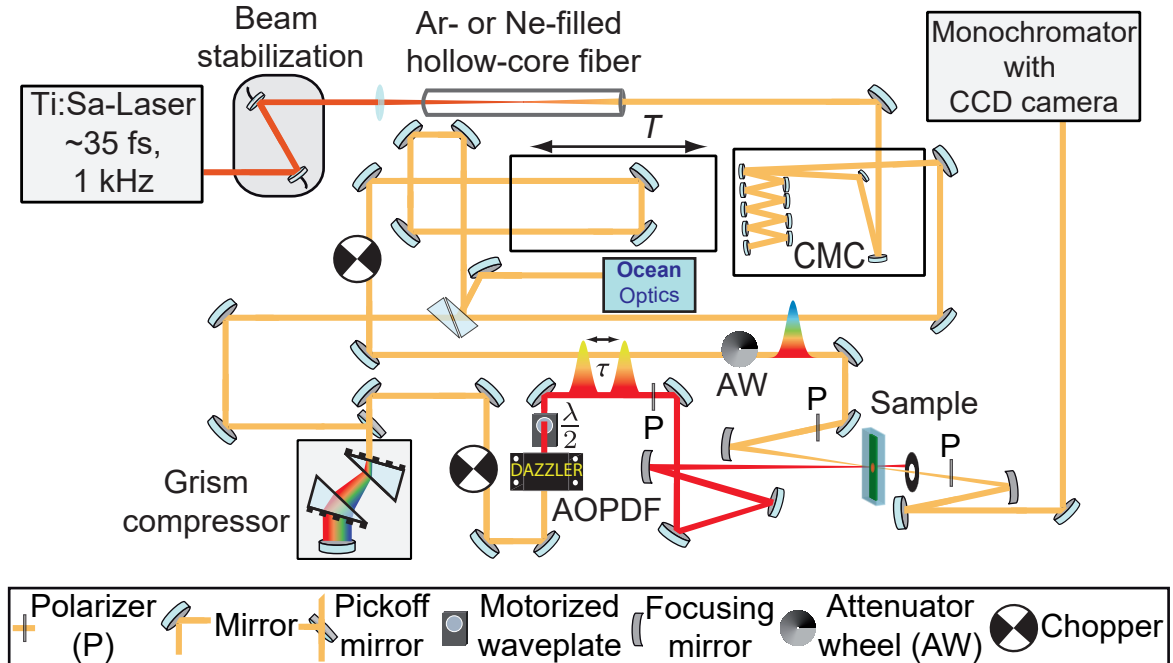
Figure 3.7.: Broadband 2D setup in PP geometry for the measurements of PP as well as 2D spectroscopy. The output of an amplified laser system is broadened by a noble gas filled hollow-core fiber. After compression with a chirped mirror compressor (CMC) the beam is split by a pair of wedges. One beam acts as a probe beam while the other beam is the pump beam. The pump passes a prism compressor with engraved gratings ("grism") before it enters an acuosto-optic programmable dispersive filter (AOPDF). The AOPDF is used to compress the pump pulses to their Fourier transform limit and is also used to create a double pulse with variable delay τ. The pump and the probe beam are both focused into the sample. The probe spectrum is measured with a monochromator which is combined with a CCD camera. The time delay between pump and probe (the population time T) is controlled by a linear translation stage acting on the probe beam. The pump and probe beams are modulated by choppers which allows one to construct the transient absorption signal.

The output of a commercial Ti:Sa-Laser (Spitfire Pro, SpectraPhysics) with a repetition rate of 1 kHz is attenuated by a beam splitter to ~1 W and then focused into a hollow-core fiber. A beam stabilization (Aligna, TEM) ensures that the position of the focused beam stays constant at the entrance of the fiber. The hollow-core

fiber is filled with argon or neon, or a mixture of both. Focusing the beam in the filled hollow-core fiber results in self-phase modulation and a broadband white-light continuum is achieved after the fiber [151]. Using argon, a spectrum with more blue components is obtained while at the same pressure, the spectrum resulting from white-light generation with neon is more centered around the fundamental of the input laser ($\lambda_0 = 800\,\text{nm}$). The pressure of the hollow-core fiber varied between 1–1.5 bar. Depending on the experimental requirements, the spectrum can be tuned by the gas pressure [151, 152]. An exemplary spectrum measured directly after the hollow-core fiber is shown in Fig. 3.8a. This spectrum corresponds to the spectrum of the probe. The red part of the spectrum is usually cut by interference filters because of the strong modulations of the spectrum around 800 nm.
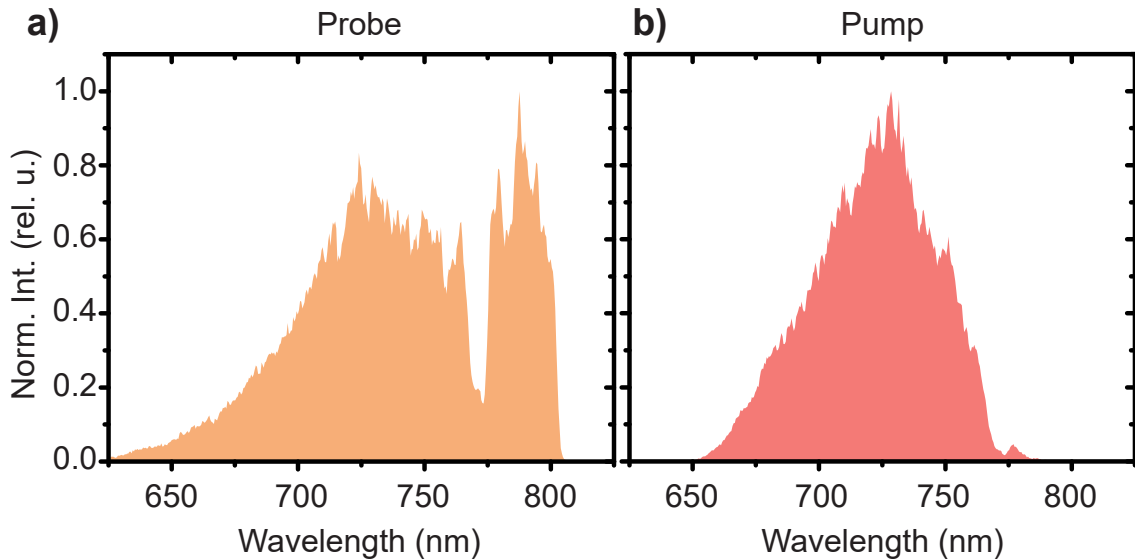
Figure 3.8.: Exemplary pump and probe spectra resulting from white-light generation via the hollow-core fiber. (a) As a probe spectrum, the unshaped output of the hollow-core fiber is used. The spectrum is cut by a shortpass filter at around 800 nm. (b) The spectrum of the pump pulse is shaped by an AOPDF.

The output of the hollow-core fiber is first compressed by a set of chirped mirrors (Ultrafast Innovations). After that, a pair of wedges separate the incident beam into the pump and the probe beam. The reflection on the first surface of the first wedge is used as a probe beam while the transmitted beam is the pump beam. One of the other reflections of the wedge pair is coupled into a fiber-based spectrometer (HR-2000+, Ocean Optics) to monitor the white-light continuum, i.e., the probe spectrum throughout the experiment. The pump beam is further compressed by a prism compressor with engraved gratings on the prisms. This allows better and more flexible dispersion management as with a normal prism compressor. The pump beam is guided through an AOPDF (Dazzler, Fastlite). A telescope consisting of two focusing mirrors (not shown

in Fig. 3.7) before the compressor is used to adjust the beam size to the aperture of the AOPDF. The AOPDF cuts out the desired pump spectrum and compresses the pulse to its Fourier transform limit. The compression is achieved by the combination of the prism compressor and the AOPDF. The pump spectrum is usually shaped at a full width at half maximum (FWHM) of around 80–120 nm and has a super-Gaussian-like shape. A smooth spectrum is necessary for 2D spectroscopy because otherwise the modulations will be directly visible in the 2D map [8]. An exemplary spectrum for the pump pulse is shown in Fig. 3.8b. The AOPDF is also used to create a double pulse with a variable delay τ for 2D measurements. After the wedge pair, the probe beam passes a delay line (M-IMS600LM, Newport) which controls the population time T. Both beams, the pump as well as the probe, are focused into the sample by focusing mirrors. The power of the probe is adjusted by an optical attenuator wheel. In the PP geometry, the pump and the probe beam excite the sample from different directions, i.e., with different wavevectors $\mathbf{k}$. The pump beam is blocked by an iris after the sample while the probe beam is recollimated by another focusing mirror. Polarizers are used before and after the sample to achieve a clean probe polarization (parallel to each other and to the axis of the probe polarization). The polarization of the pump beam is adjusted by a motorized half-wave plate and passes an additional polarizer to achieve a clean polarization. Using the polarizer and the half-wave plate the polarization between the pump and probe beam can be set to the magic angle of 54.7°

The pump pulse is characterized by collinear frequency-resolved optical gating (c-FROG) [153]. For such a measurement, the sample is replaced by a 10 μm thick β-barium borate crystal. The thus created second harmonic is coupled into a fiber-based spectrometer (HR-2000+, Ocean Optics). The delay of a double pulse is scanned and for each time step the spectrum of the second harmonic is measured. The fundamental is blocked by a polarizer or a color filter. The pulse shape in the time domain as well as in the spectral domain is reconstructed by a commercial software package. The probe pulse is measured by cross-correlation frequency-resolved optical gating (X-FROG). For this measurement, the characterized pump pulse is overlapped with the probe pulse and the spectrum of the sum frequency is measured for different delays between pump and probe pulse [153]. For PP and 2D measurements, the probe beam is focused into a monochromator with an attached CCD camera (Acton SpectraPro 2558i assembled with camera Pixis 2 K, Princeton Instruments). Both beams are modulated by choppers (MC2000, Thorlabs). Since both beams are modulated, four different combinations of the pump and the probe beam can be measured in total (see Fig. 3.9): both beams are blocked (background contribution, I_B), the probe is open and the pump is blocked (reference spectrum, I_Pr), the probe is blocked and the pump is open (scattering contribution, I_Pu), and both beams are open (excited spectrum, $I_\mathrm{Pu\text{-}Pr}$). By using the four combinations, the TA signal, i.e., the transient change in absorption (ΔOD) is calculated by

$$\Delta\mathrm{OD} = -\log_{10}\left(\frac{I_\mathrm{Pu\text{-}Pr} - I_\mathrm{Pu}}{I_\mathrm{Pr} - I_\mathrm{B}}\right). \tag{3.2}$$

Laser after HCF

Probe

Pump

Excited spectrum | Scattering | Reference spectrum | Background
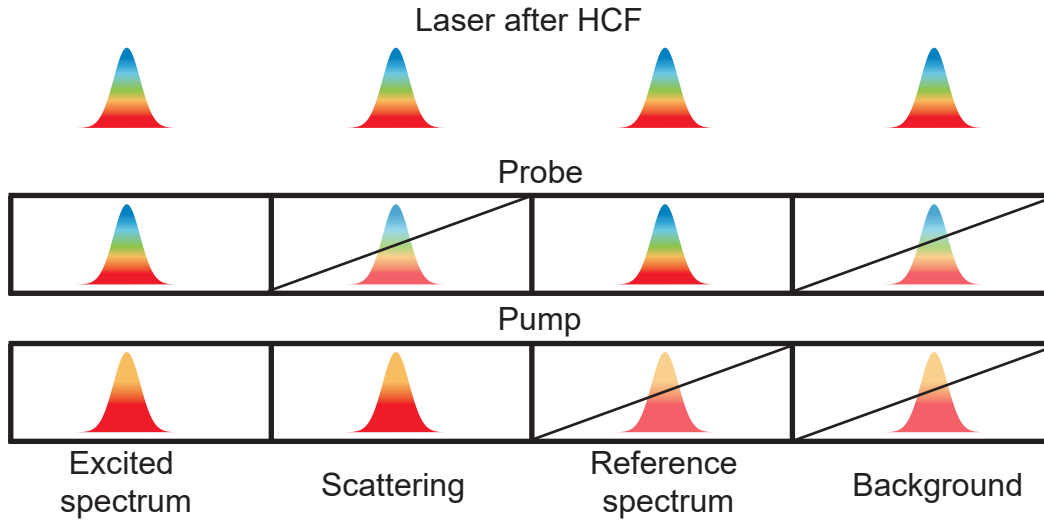
Figure 3.9.: Double-chopping scheme for the measurements of 2D spectra in PP geometry. The 1 kHz repetition rate of the laser (top) is modulated by choppers. For the probe beam, every second pulse is blocked (indicated by a diagonal line) while for the pump beam, two consecutive pulses are blocked. The different colors of the pump pulse compared to the probe pulse reflects shaping of the pulse by the AOPDF. Due to the modulation of the pump as well as the probe beam four different contributions can be separated.

The advantage of such a double-chopping scheme is that the scattering can be minimized which results in an overall better SNR. It is possible to measure each contribution for only one laser shot by chopping the pump at 500 Hz and the probe at 250 Hz. For lower modulation frequencies, each contribution is averaged over several laser pulses. Spectral modulations of the probe spectrum are not visible in the 2D maps because the excited probe spectrum is divided by the reference probe spectrum. Note that strong modulations such as the strong change in intensity at around 780 nm in the probe spectrum shown in Fig. 3.8a will be usually visible in a 2D spectrum as a region with increased noise due to the low intensity of I_{Pr} on the detector. The 2D spectrum is much more sensitive to the pump spectrum than to the probe spectrum. Strong modulations in the pump spectrum can distort the 2D spectrum as previously shown [8].

Excitons and Exciton Dynamics

The systems that were investigated during this thesis have in common that the excited states can be described in the framework of exciton theory [154–156]. An exciton is the excited state of a coupled system such as a molecular aggregate or a dimer [24, 157]. It can be thought as an electron–hole pair, i.e., a quasiparticle. In literature two classes of excitons are known: Frenkel excitons [158] and Wannier–Mott excitons [24]. The former is an electron–hole pair with a small radius. i.e., electron and hole are tightly bound while the latter has a much bigger radius. Frenkel excitons can be found in molecular systems [157]. In this thesis only molecular systems were investigated and therefore we will restrict this chapter on the description of Frenkel excitons. The following chapter provides an overview of exciton theory starting with a molecular dimer. After the discussion of excitons in molecular aggregates we will discuss the interaction of excitons in the form of EEA which is one of the main phenomena investigated in this thesis.

4.1. Dimer

One of the simplest systems in which excitons can be observed is a molecular dimer. The electronic properties of a dimer in terms of exciton theory are described in literature, [24, 123, 159] and here we only review the main points. A dimer consists of two coupled monomeric units. The coupling does not mean that the monomers are necessarily chemically bonded. It rather means that the interaction is strong enough that the excited states cannot be described anymore as the excited states of the individual monomers. A simple model system for a dimer consists of two monomers and each monomer is described as a two-level systems. The two monomers have a fixed distance R_{ab} and a fixed orientation to each other. The Hamilton operator of a dimer H_{site} in the so called site basis can be described in terms of the collective states by [123]

$$
\begin{aligned}
H_{\mathrm{site}} = {} & (H_{\mathrm{a}}^{\mathrm{g}} + H_{\mathrm{b}}^{\mathrm{g}}) \left| \mathrm{g} \right\rangle \left\langle \mathrm{g} \right| + H_{\mathrm{a}}^{\mathrm{e}} \left| \mathrm{a} \right\rangle \left\langle \mathrm{a} \right| \\
& + H_{\mathrm{b}}^{\mathrm{e}} \left| \mathrm{b} \right\rangle \left\langle \mathrm{b} \right| + J \left(\left| \mathrm{a} \right\rangle \left\langle \mathrm{b} \right| + \left| \mathrm{a} \right\rangle \left\langle \mathrm{b} \right| \right) + (H_{\mathrm{a}}^{\mathrm{e}} + H_{\mathrm{b}}^{\mathrm{e}}) \left| \mathrm{ab} \right\rangle \left\langle \mathrm{ab} \right|.
\end{aligned}
\tag{4.1}
$$

Here H_i^{g} and H_i^{e} are the Hamilton operators of the ground and excited states of the ith molecule. The state $\left| \mathrm{g} \right\rangle$ corresponds to the state in which both molecules are in the ground state, $\left| \mathrm{a} \right\rangle$ ($\left| \mathrm{b} \right\rangle$) in which molecule a (molecule b) is in the excited state and the other molecule is in the ground state, and the state $\left| \mathrm{ab} \right\rangle \left\langle \mathrm{ab} \right|$ in which both

molecules are excited. J describes the coupling between the excited states of the monomers. Note that we disregard other terms of the coupling. Due to the coupling the monomeric states are no longer eigenstates of the Hamiltonian. From the basis of the collective states, i.e., the site basis, we can switch to the eigenbasis of the coupled system which is called exciton basis. The exciton basis with the Hamiltonian H_{exc} can be reached by diagonalization of the dimer Hamiltonian,

$$H_{\mathrm{exc}} = \boldsymbol{C}^{\top} H_{\mathrm{site}} \boldsymbol{C}. \tag{4.2}$$

Here $\boldsymbol{C}$ is the transformation matrix with the coefficients c_n^i where the index n corresponds to the molecular site and the superscript i to the new eigenstates. Solving the problem analytically results in the single-exciton states $(|2\rangle, |1\rangle)$ which can be constructed using the monomeric states $(|a\rangle |b\rangle)$ by [123]

$$|2\rangle = \cos(\theta) |a\rangle + \sin(\theta) |b\rangle , \tag{4.3}$$

and

$$|1\rangle = -\sin(\theta) |a\rangle + \cos(\theta) |b\rangle , \tag{4.4}$$

with the mixing angle θ which is defined by

$$\tan(2\theta) = \frac{2J}{\Delta\epsilon}. \tag{4.5}$$

Here $\Delta\epsilon$ is the energy difference between the two monomers. The eigenenergies of the first two excited states are

$$\epsilon_{2,1} = \frac{1}{2}(\epsilon_{\mathrm{a}} + \epsilon_{\mathrm{b}}) \pm \frac{1}{2}\sqrt{(\epsilon_{\mathrm{a}} - \epsilon_{\mathrm{b}})^2 + 4J^2}. \tag{4.6}$$

The coupling leads to an energetic splitting of the two single-excited states. This splitting is called Davydov splitting [155] and can be, for example, observed experimentally as two distinct peaks in the linear absorption spectrum [160]. The eigenenergy of the biexciton state $|\alpha\rangle$ is

$$\epsilon_{\alpha} = \epsilon_2 + \epsilon_1 \tag{4.7}$$

A schematic overview of the involved states is shown in Fig. 4.1. The transition dipole moments are also transformed into the exciton basis via the transformation matrix [123] leading to

$$\boldsymbol{\mu}_{20} = \cos(\theta)\boldsymbol{\mu}_{\mathrm{a}} + \sin(\theta)\boldsymbol{\mu}_{\mathrm{b}} \tag{4.8}$$

and

$$\boldsymbol{\mu}_{10} = -\sin(\theta)\boldsymbol{\mu}_{\mathrm{a}} + \cos(\theta)\boldsymbol{\mu}_{\mathrm{b}}. \tag{4.9}$$

The transition dipole moments from the single-exciton states to the biexciton state are

$$\boldsymbol{\mu}_{\alpha 2} = \cos(\theta)\boldsymbol{\mu}_{\mathrm{b}} + \sin(\theta)\boldsymbol{\mu}_{\mathrm{a}} \tag{4.10}$$

and

$$\boldsymbol{\mu}_{\alpha 1} = -\sin(\theta)\boldsymbol{\mu}_{\mathrm{b}} + \cos(\theta)\boldsymbol{\mu}_{\mathrm{a}}. \tag{4.11}$$
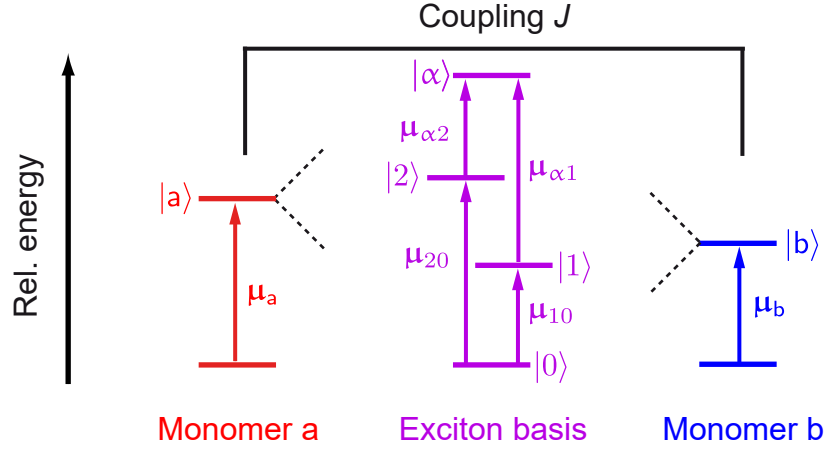
Figure 4.1.: Monomeric states with coupling J and resulting new eigenstates. Due to the coupling the monomeric states are no longer eigenstates of the system and the new eigenstates and transition dipole moments can be described in the exciton basis.

For a homodimer, i.e., a dimer made from two identical monomers the energy gap is in an idealized situation

$$\Delta\epsilon = 0. \tag{4.12}$$

Therefore the absolute value of the mixing angle is $\frac{\pi}{4}$. However, to determine the sign of the mixing angle we must take a closer look at the coupling J. For large distances between the monomers the coupling can be approximated by the dipole–dipole interaction [24, 156]. While we will restrict the discussion to this approximation and use the dipole–dipole interaction, more sophisticated methods to calculate the coupling can be found in literature [161, 162]. The sign of the coupling is dictated by the orientation of the monomers to each other.

The coupling J_{ab} (in atomic units) is

$$
\begin{aligned}
J_{\mathrm{ab}}(R_{\mathrm{ab}}, \Theta_{\mathrm{a}}, \Theta_{\mathrm{b}}, \phi_{\mathrm{ab}}) &= [\cos(\phi_{\mathrm{ab}}) - 3\cos(\Theta_{\mathrm{a}})\cos(\Theta_{\mathrm{b}})]\frac{|\boldsymbol{\mu}_{\mathrm{a}}||\boldsymbol{\mu}_{\mathrm{b}}|}{R_{\mathrm{ab}}^3} \\
&= \kappa(\Theta_{\mathrm{a}}, \Theta_{\mathrm{b}}, \phi_{\mathrm{ab}})\frac{|\boldsymbol{\mu}_{\mathrm{a}}||\boldsymbol{\mu}_{\mathrm{b}}|}{R_{\mathrm{ab}}^3}
\end{aligned}
\tag{4.13}
$$

in which R_{ab} is the distance between the center of transition charges of the two states to each other, Θ_{a} and Θ_{b} are the angles of the transition dipole moments to the axis of connection and ϕ_{ab} the angle between the two transition dipole moments to each other. The orientation can be summarized by an orientation factor κ. To see the effect of orientation we consider a dimer in which the two monomers are in one plane and oriented parallel to each other. Therefore $\phi_{\mathrm{ab}} = 0$ and $\Theta_{\mathrm{a}} = \Theta_{\mathrm{b}} = \Theta$ which reduces Eq. (4.13) to

$$
J_{\Theta}(R_{\mathrm{ab}}, \Theta) = \frac{|\boldsymbol{\mu}_{\mathrm{a}}||\boldsymbol{\mu}_{\mathrm{b}}|}{R_{\mathrm{ab}}^3}\left[1 - 3\cos^2(\Theta)\right].
\tag{4.14}
$$

Two major cases of maximal and minimal coupling can be distinguished [163]: J-type coupling [164, 165] and H-type coupling [166, 167]. For an angle of $\Theta = 0°$ the coupling is negative and can be written as

$$
J_{0°} = -2\frac{|\boldsymbol{\mu}_{\mathrm{a}}||\boldsymbol{\mu}_{\mathrm{b}}|}{R_{\mathrm{ab}}^3}.
\tag{4.15}
$$

This specific orientation is a "head-to-tail" conformation of the two dipole moments to each other resulting in a J-type coupling. For an angle of $\Theta = 90°$ (H-type coupling) which corresponds to a parallel side-by-side ("head-to-head") conformation of the transition dipole moments the coupling is positive and only half as large as for the "head-to-tail" conformation if the distance R_{ab} stays constant. The coupling for this orientation is

$$
J_{90°} = +\frac{|\boldsymbol{\mu}_{\mathrm{a}}||\boldsymbol{\mu}_{\mathrm{b}}|}{R_{\mathrm{ab}}^3}.
\tag{4.16}
$$

Interestingly there is also an angle at which no coupling appears. This angle is the zero point of κ and is $54.7°$ [156]. For a "head-to-tail" conformation of two identical monomers ($\boldsymbol{\mu}_{\mathrm{a}} = \boldsymbol{\mu}_{\mathrm{b}} = \boldsymbol{\mu}$) the mixing angle is $\theta = -\frac{\pi}{4}$. The transition dipole moments for this mixing angle are

$$
\begin{aligned}
\boldsymbol{\mu}_{20} &= 0, \\
\boldsymbol{\mu}_{10} &= \sqrt{2}\boldsymbol{\mu}, \\
\boldsymbol{\mu}_{\alpha 2} &= 0, \\
\boldsymbol{\mu}_{\alpha 1} &= \sqrt{2}\boldsymbol{\mu}.
\end{aligned}
\tag{4.17}
$$

The transition probability from the ground state to the excited state is calculated using the excitonic transition dipole moments. In the case of a J-type coupled homodimer

the transition to the higher energetic exciton state is dark while the lower exciton state is bright. A positive coupling of J (H-type) results in the case of a homodimer in a mixing angle of $+\frac{\pi}{4}$. The transition dipole moments are then

$$
\begin{aligned}
\boldsymbol{\mu}_{20} &= \sqrt{2}\boldsymbol{\mu}, \\
\boldsymbol{\mu}_{10} &= 0, \\
\boldsymbol{\mu}_{\alpha 2} &= \sqrt{2}\boldsymbol{\mu}, \\
\boldsymbol{\mu}_{\alpha 1} &= 0.
\end{aligned} \tag{4.18}
$$

In this case the energetic higher state is bright and the energetic lower state dark. The results of exciton formation for different orientations in a dimer is summarized in Fig. 4.2. The two cases of H- and J-type coupling in a homodimer result in one bright state that is either shifted to higher or lower energies compared to the monomer transition. The Davydov splitting, i.e., the energetic distance between the two single-exciton states for a homodimer is $2J$ and the coupling between two monomers with fixed distance R_{ab} is two times bigger in the case of a J-type coupled than for an H-type coupled dimer.
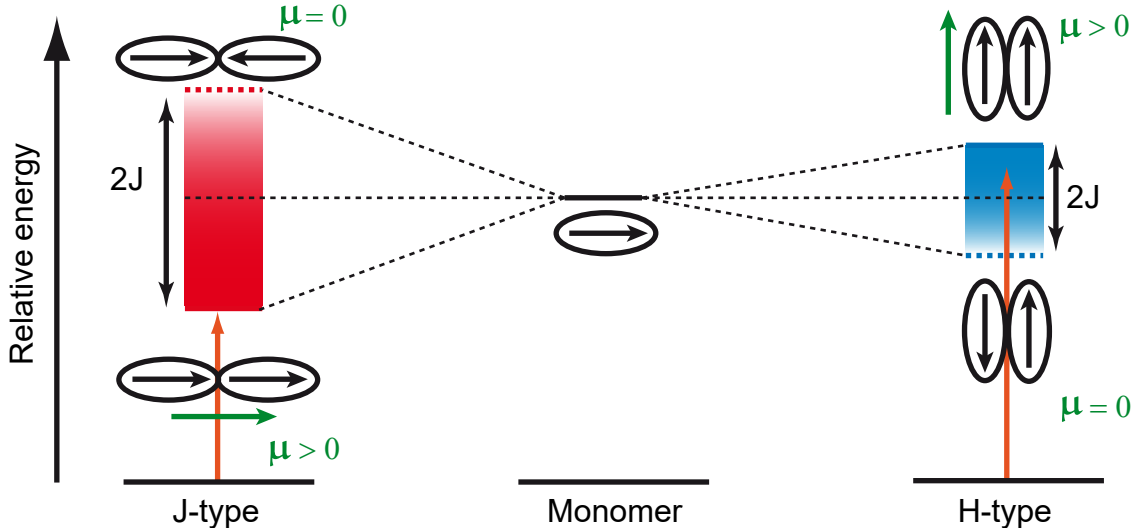
Figure 4.2.: Coupled homodimer. For a J-type coupling the lower state is bright while in the case of an H-type coupling the energetic higher state is bright. Note that for a fixed distance the Davydov splitting is two times bigger for the J-type coupling than for the H-type coupling.

4.2. Aggregate

The concept of excitons in dimers can be extended to bigger systems in which multiple molecules are coupled to each other. Typical systems for this are supramolecular aggregates [20] or polymers such as squaraine polymers [7] that were investigated throughout this thesis. In aggregates the monomers are coupled to each other weakly due to different interactions such as π–π interactions or hydrogen bonds. In polymers the units are connected by covalent bonds to each other. A detailed description of applying exciton theory to aggregates can be found in literature [24, 157, 168] as well as in Chapter 7.
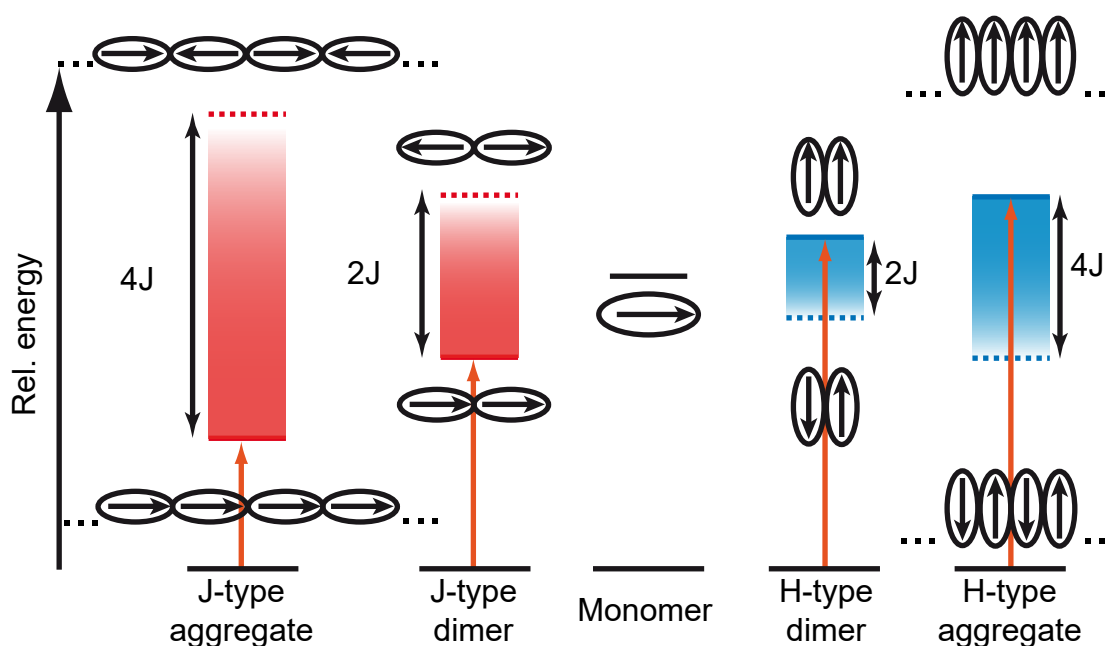
Figure 4.3.: State structure for an aggregates consisting of multiple monomers. The splitting for an aggregate is twice as large as for a dimer assuming periodic boundary conditions.

In order to describe an aggregate the same steps as for a dimer have to be carried out. First the ground state as well as the excited states must be formulated in the site basis. It is important what level of description is chosen for each monomer. For example, choosing a three-level system for a monomer allows to describe EEA within the framework of the exction basis without additional phenomenological input [7]. However, the size of the Hamiltonian increases with additional monomeric states. The Hamiltonian as well as the transition dipole moments in the site basis are transformed into the exciton basis. The single-exciton states of an aggregate made out of multiple monomers are shown in Fig. 4.3 for J-type and H-type coupling. Note that in the case of periodic boundary conditions for large aggregates, the splitting is twice as big ($4J$) as for a dimer [157]. As we have discussed above the spectral signatures for the two configurations of positive and negative coupling of J are unique. For a "head-to-tail"

conformation with negative coupling (J-type) between the monomers a bathochromic shift, i.e., a red-shift in the absorption spectrum compared to the monomer is observed [164, 165, 169–173]. In a parallel conformation of the monomers resulting in positive coupling (H-type) a hypsochromic shift, i.e., a blue-shift in the absorption spectrum is observed [174–178].

4.3. Exciton–Exciton Annihilation

The process of EEA is the relaxation from the biexciton manifold to the single-exciton manifold [179]. The two excitons interact in such away that the population of biexcitons is decreased. The process of EEA in the site basis as well as in the exciton basis is discussed in this section. For simplicity we consider a heterodimer with both first excited states of the two monomers at different energies. However, the discussion is similar for extended systems.

Let us first focus on the description of EEA in the site basis (Fig. 4.4). In contrast to the first section we now also consider a higher excited state for each monomer ($|f_a\rangle$, $|f_b\rangle$) as well. The process of annihilation starts with both of the monomers in the first excited state. Due to the coupling of the higher excited states to the state where both molecules are in the first excited states, the excited states of both sites evolve into one molecule in a higher excited state which leaves behind the other molecule in the ground state. The population in the two first exited states is effectively transferred into a population of a higher excited state. This process is also called fusion [179]. In Fig. 4.4 we exemplary consider that the fusion leads to monomer a in state $|f_a\rangle$. The higher excited state relaxes rapidly via IC to the first excited state. As a result the energy of the first excited state of one monomer is converted to heat via IC and only one monomer is left in the first excited state.
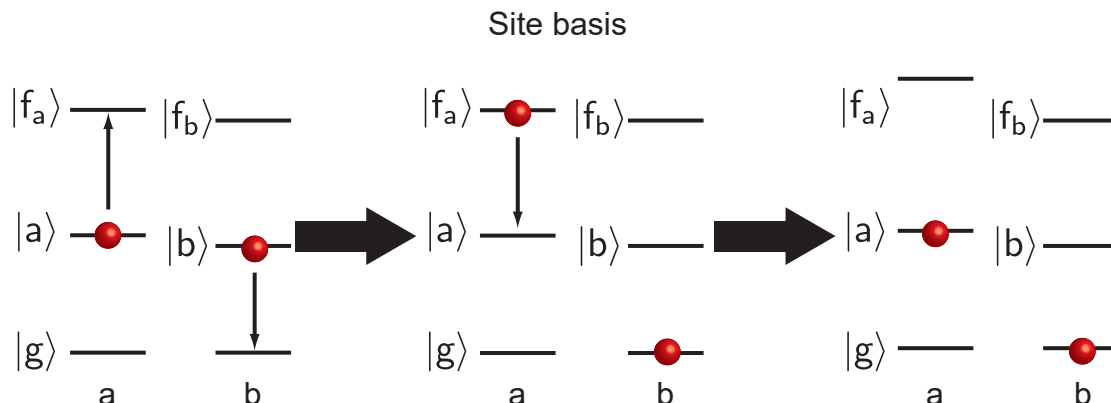
Site basis

Figure 4.4.: EEA in the picture of the individual states of the monomers, i.e, the site basis. In the initial phase of the process both molecules are excited in the first excited state ($|a\rangle$, $|b\rangle$). Due to coupling of transitions relaxation to the ground state $|g\rangle$ occurs and the other molecules is excited to a higher excited state $|f_a\rangle$. From this higher excited state rapid IC occurs. In total the energy corresponding to a single-exciton state is dissipated into heat.

The process of EEA can also be described in the exciton basis (Fig. 4.5) starting with a population in a biexciton state $|\alpha\rangle$. The biexciton manifold also includes states that are predominantly localized at one of the monomers ($|f_1\rangle$, ($|f_2\rangle$)). The biexciton population is getting transferred to one of these states ($|f_1\rangle$). From this state internal conversion to the single-exciton manifold can take place. Note that due to the coupling between the states the biexciton states and molecular higher excited states will mix. After the internal conversion a population in the single-exciton manifold is left. In summary, EEA is a relaxation processes that connects the biexciton states with the single-exciton states and converts the energy that corresponds to an excitation of a single-exciton state into heat via internal conversion.

For EEA to take place, the excitons must be spatially close to each other [180, 181]. If the excitons are spatially separated from each other a transport process along the aggregate might occur until the two excitons are in close proximity to each other. Therefore, annihilation can be used as a probe for the exciton diffusion along polymers and aggregates. However, the interplay between delocalization and exciton transport on one side and the process of annihilation on the other side is complex [4]. While the exciton transport and exciton delocalization is determined by the coupling of the first excited states of the molecules, EEA involves higher excited states as shown above. In simulations it is possible to define an annihilation radius, i.e., how close two excitons have to get to each other in order that EEA can occur. Whenever two excitons are within this radius annihilation takes place. In a recent publication we used higher-order spectroscopy to take a closer look at the interplay of exciton transport and EEA [16]. Our experiments showed that in the case of squaraine polymers the excitons may encounter on average many times before annihilation occurs. The results are further discussed in Section 8.3.5. EEA is a process that is not directly observable
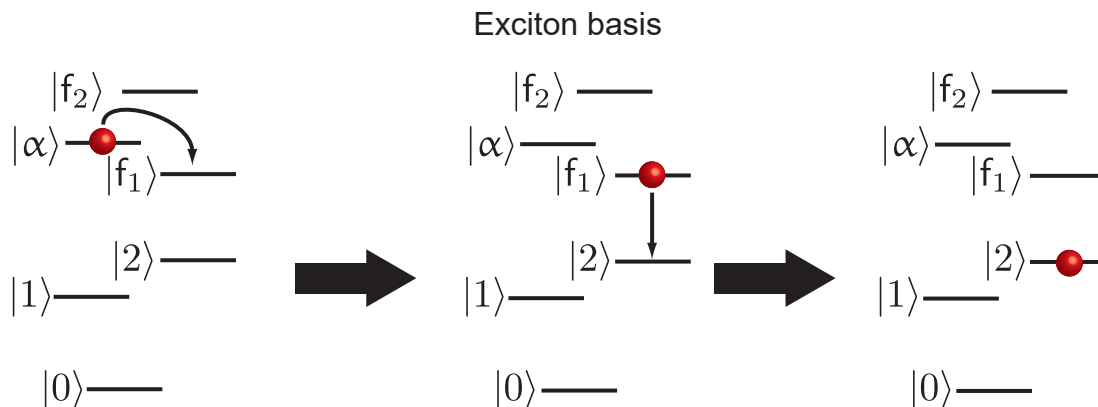
Figure 4.5.: Exciton–exciton annihilation in the picture of the coupled states, i.e., the exciton basis. As a first step the population in a biexciton state $|\alpha\rangle$ is transferred to a state $|f_1\rangle$ that is predominantly localized at one monomer. Now internal conversion to the single-exciton manifold occurs. Overall, a relaxation process from the biexciton to the single-exciton manifold occurred.

in TA or 2D experiments. It is for example possible to observe the influence of EEA in power-dependent transient absorption measurements [181, 182]. EEA occurs as a change in the dynamics of the transient absorption signal for higher excitation intensities and can be used to investigate the exciton diffusion in aggregates. Besides using EEA as a probe for exciton diffusion it can also occur as an unwanted contribution in PP and 2D measurements which is especially the case in the investigation of natural light-harvesting. Under natural conditions, i.e., when absorbing sunlight, the exciton density is too low to achieve an appreciable amount of of EEA in the photosynthetic complex. However, experiments with pulsed lasers reach such a regime easily [183]. Therefore, care has to be taken in ultrafast spectroscopy experiments using pulsed lasers to avoid that annihilation is also observed in the measured dynamics [184]. Annihilation-free conditions can be ensured by measuring that the observed TA absorption dynamics over the population time do not change with higher pump intensity [185]. However, in some systems such as chlorosomes the annihilation-free conditions are only realized under very low pump intensities which can result in a low SNR [186]. In this thesis we show a different approach to solve this dilemma by utilizing multi-quantum signals to correct for higher-order contributions. This option is further discussed in Chapter 8.

Pathway Analysis of Two-Dimensional Spectroscopy

5.1. Signatures of Coupling in Two-Dimensional Spectroscopy

We now want to combine our knowledge about excitons, 2D spectroscopy and double-sided Feynman diagrams. Let us begin our discussion with a simple system of an excitonic heterodimer which we already discussed in Chapter 4. Analyzing 2D spectra of dimers in terms of double-sided Feynman diagrams can be found in literature [120, 187]. The energy structure of a heterodimer consists of one ground state ($|0\rangle$), two single-exciton states ($|1\rangle$, $|2\rangle$), and one biexciton state ($|\alpha\rangle$) as shown in Fig. 5.1a. The transitions to the two single-exciton states can be observed as two distinct peaks in the linear absorption spectrum (Fig. 5.1b).
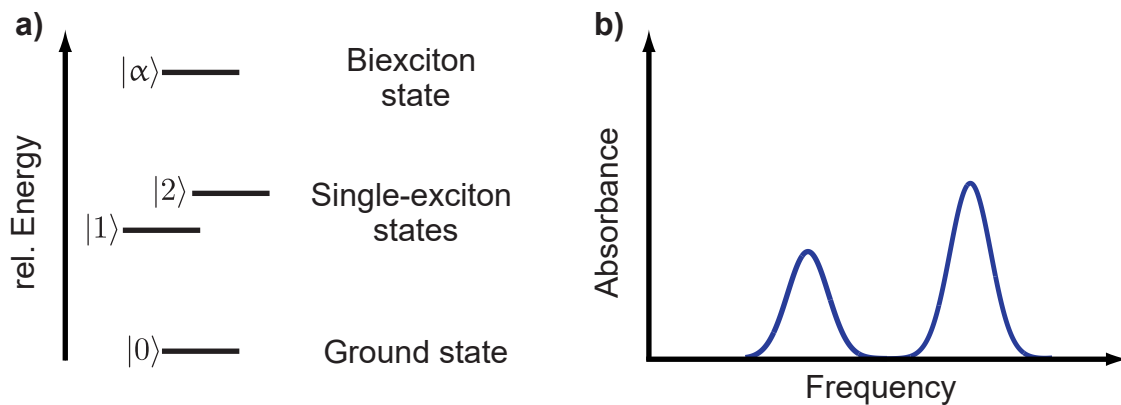
Figure 5.1.: Exemplary system of a heterodimer. (a) The system is described in the exciton basis. For a dimer, one ground state ($|0\rangle$), two single-exciton states ($|1\rangle$, $|2\rangle$), and a biexciton state ($|\alpha\rangle$) can be distinguished. (b) The two peaks in the linear absorption spectrum correspond to the transitions to the single-exciton states.

Armed with the knowledge of double-sided Feynman diagrams and excitons, we can now qualitatively predict what the 2D spectrum of a heterodimer should look like at $T = 0$. Note that our discussion is only qualitative since we do not consider

some theoretical aspects such as line shapes or any experimental parameters such as the spectra of the pump or probe pulse. A more detailed analysis of 2D spectra using double-sided Feynman diagrams can be found in literature [23, 25]. As a simple starting point, we consider the case when energy relaxation as well as transfer between different states has not occurred yet, i.e., $T = 0$. In accordance to transient absorption measurements, GSB and SE are defined as negative signals while ESA corresponds to a positive signal in the 2D spectrum. A diagonal peak in the 2D spectrum corresponds to exciting and probing of the same transition. Two diagonal peaks for the single-exciton transitions can be distinguished which we will call peak 1 and peak 2. For each of the two peaks, four diagrams, two rephasing and two non-rephasing diagrams, are contributing. The diagrams for the diagonal peak 1 and 2 are shown in Fig. 5.2.
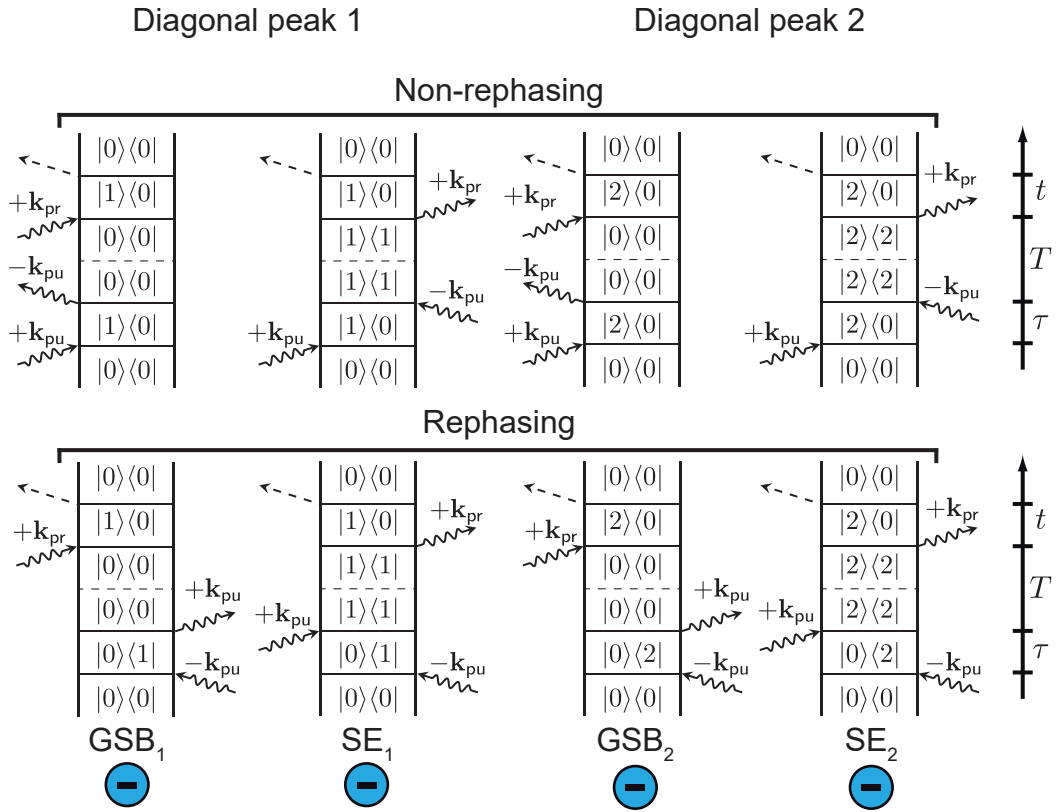
Figure 5.2.: Rephasing and non-rephasing double-sided Feynman diagrams which correspond to the diagonal peaks (peak 1 and peak 2) at the position of the single-exciton transitions.

Note that all diagrams have the same sign. The involved coherences within the diagram determine the position of the corresponding peak in the 2D spectrum. The coherence during τ fixes the position at the excitation axis while the coherence during t sets the position along the detection axis. All diagrams for one peak have the same

coherences during τ and t and therefore these diagrams contribute to the diagonal peaks. The GSB-type and SE-type pathways have per definition a negative sign while ESA-type pathways have a positive sign. Peak 1 can be described by four diagrams. A similar set of four diagrams, which involves the transition to the state $|2\rangle$, describes the diagonal peak 2. Note that we do not consider pathways with coherences during the population time T to keep the analysis simple. A detailed analysis of such pathways can be found in literature [23, 27].

Integrating over the spectral line shapes, the diagrams can be characterized by their sign, the involved transition dipole moments and the propagator during the population time. Setting $T = 0$ reduces the description of the Feynman diagrams simply to the transition dipole moments and the sign. The amplitudes of the two diagonal peaks 1 and 2 are

$$
\begin{aligned}
\mathrm{GSB}_1 + \mathrm{SE}_1 &= -4|\boldsymbol{\mu}_{10}|^4, \\
\mathrm{GSB}_2 + \mathrm{SE}_2 &= -4|\boldsymbol{\mu}_{20}|^4.
\end{aligned}
\tag{5.1}
$$

The prefactor of 4 is present because of summation of the rephasing and non-rephasing diagrams which correspond to the absorptive part of the 2D spectrum.

Furthermore, two cross peaks can be present in a 2D spectrum of a dimer. The diagrams that corresponds to the cross peaks are shown in Fig. 5.3.[1] The amplitudes of the diagrams are

$$
\begin{aligned}
\mathrm{GSB}_{\mathrm{A}} &= -2|\boldsymbol{\mu}_{20}|^2|\boldsymbol{\mu}_{10}|^2, \\
\mathrm{ESA}_{\mathrm{A}} &= 2|\boldsymbol{\mu}_{20}|^2|\boldsymbol{\mu}_{\alpha 2}|^2, \\
\mathrm{GSB}_{\mathrm{B}} &= -2|\boldsymbol{\mu}_{10}|^2|\boldsymbol{\mu}_{20}|^2, \\
\mathrm{ESA}_{\mathrm{B}} &= 2|\boldsymbol{\mu}_{10}|^2|\boldsymbol{\mu}_{\alpha 1}|^2.
\end{aligned}
\tag{5.2}
$$

The index corresponds to the peak position which is either below the diagonal (peak A) or above the diagonal (peak B). In contrast to the diagonal peak, ESA-type and GSB-type pathways with opposite sign are contributing to the cross peak. In the case of a weakly coupled dimer, the excitons are localized. In such a case, the transition dipole moments are $\boldsymbol{\mu}_{10} = \boldsymbol{\mu}_{\alpha 2}$ and $\boldsymbol{\mu}_{20} = \boldsymbol{\mu}_{\alpha 1}$. If the two monomers have similar transition dipole moments ($\boldsymbol{\mu}_{\mathrm{a}} \approx \boldsymbol{\mu}_{\mathrm{b}}$), the two diagonal peaks have similar amplitude. In the case of weak coupling, the GSB-type and ESA-type pathways that contribute to the cross peaks cancel perfectly for peak A and peak B. As a result, no cross peak can be observed in the case of a weakly coupled dimer.

Let us now go one step further and consider stronger coupling. If the coupling is increased, the excitons will be partially delocalized over the monomers. For "head-to-head" orientation of the transition dipole moments, the coupling is positive and an H-type dimer is realized. The absorption spectrum of such a dimer has two peaks with a stronger peak at higher frequencies as shown in Fig. 5.1b. The amplitudes

---

[1]Again we do not consider any diagrams with coherences during the population time in order to keep the discussion simple.

of the two diagonal peaks in the 2D spectrum also change because of the coupling. Due to the coupling $|\boldsymbol{\mu}_{20}| > |\boldsymbol{\mu}_{10}|$, we can directly predict that the diagonal peak A is more intense than diagonal peak B following the spectral signature of the absorption spectrum.
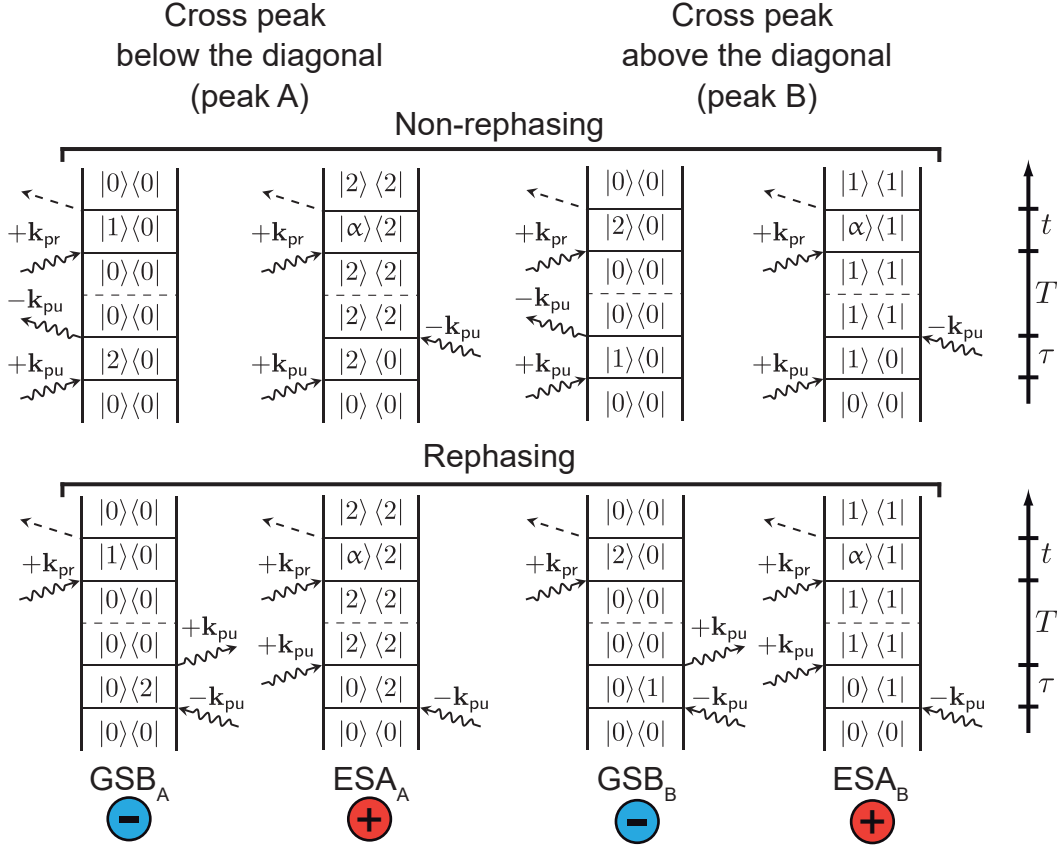
Figure 5.3.: Diagrams that correspond to the cross peaks in a 2D spectrum of a dimer for $T = 0$. The two rows correspond to rephasing and non-rephasing diagrams. The sign of the different columns of diagrams is marked below.

Due to the coupling, the two pathways that contribute to the cross peaks do not cancel anymore. While the GSB-type pathways have the same transition dipole moments involved for peak A and peak B, the ESA-type pathways for peak A, ESA$_\text{A}$, and the ESA-type pathways for peak B, ESA$_\text{B}$, contain different transition dipole moments. Using Eqs. (4.8) to (4.11) to calculate the transition dipole moments, we can compare the amplitudes of the diagrams and find

$$
\begin{aligned}
|\text{GSB}_\text{A}| &< |\text{ESA}_\text{A}|, \\
|\text{GSB}_\text{B}| &> |\text{ESA}_\text{B}|.
\end{aligned}
\tag{5.3}
$$

From that, it follows that peak A is positive and peak B is negative due to the dif-

ferent sign of GSB and ESA pathways. Note that this means that the cross peaks in the coherently detected 2D spectrum of a dimer at $T = 0$ directly reflect the degree of coupling within the dimer. The cross peaks in coherently detected 2D spectroscopy are therefore a direct spectral signature of delocalization [120]. Interestingly, in fluorescence-detected 2D spectroscopy the cross peaks can already occur for a weakly coupled dimer in the case that EEA takes place. We briefly discuss this phenomenon in Section A of the Appendix. A detailed analysis of this phenomenon can be found in literature [8, 120].

For a dimer with a head-to-tail orientation, the coupling is negative and a J-type dimer is realized. For such a situation, the sign of the cross peaks is flipped compared to the H-type dimer and the energetically lower diagonal peak (peak 1) is stronger. Depending on the mixing angle θ, the intensities of the diagonal peaks and cross peaks of a dimer change. Summarizing our discussion, we can now draw a schematic 2D spectrum of an H-type and a J-type coupled dimer (Fig. 5.4, first row) with partially delocalized states. Recently, we performed 2D measurements on dimers and the measured data match the expected 2D spectra demonstrating the power of our simple approach [8, 9].

What happens if the coupling is increased even more? In the case of strong coupling, the excitons are completely delocalized and the mixing angle in the heterodimer approaches $\pm\frac{\pi}{4}$ which corresponds to a delocalization of 50%. We refer to this situation as full delocalization. The sign is determined by the sign of the coupling which reflects the orientation of the two monomers [156]. In these strongly coupled systems, the transition dipole moments for one transition from the ground to the single-exction state and from one of the single-exciton states to the biexciton state are zero as can be seen from Eq. (4.17) and Eq. (4.18).

For the J-type coupled dimer, the amplitudes of the diagrams for the cross peaks are given by

$$
\begin{aligned}
\text{GSB}_\text{A} = \text{GSB}_\text{B} = \text{ESA}_\text{A} = 0, \\
\text{ESA}_\text{B} = 2|\boldsymbol{\mu}_{10}|^2|\boldsymbol{\mu}_{\alpha 1}|^2,
\end{aligned}
\tag{5.4}
$$

as well as for the diagonal peaks by

$$
\begin{aligned}
\text{GSB}_2 + \text{SE}_2 = 0, \\
\text{GSB}_1 + \text{SE}_1 = -4|\boldsymbol{\mu}_{10}|^4.
\end{aligned}
\tag{5.5}
$$

The corresponding 2D spectrum has only one peak on the diagonal and one cross peak as shown in Fig. 5.4 (lower row, left). The diagonal peak is negative while the cross peak is positive. Due to increased coupling, the splitting between the two single-exciton transitions is larger and the diagonal peaks are shifted more apart compared to the case of partial delocalization. For an H-type dimer, the energetically higher diagonal peak as well as a positive cross peak below the diagonal is visible.
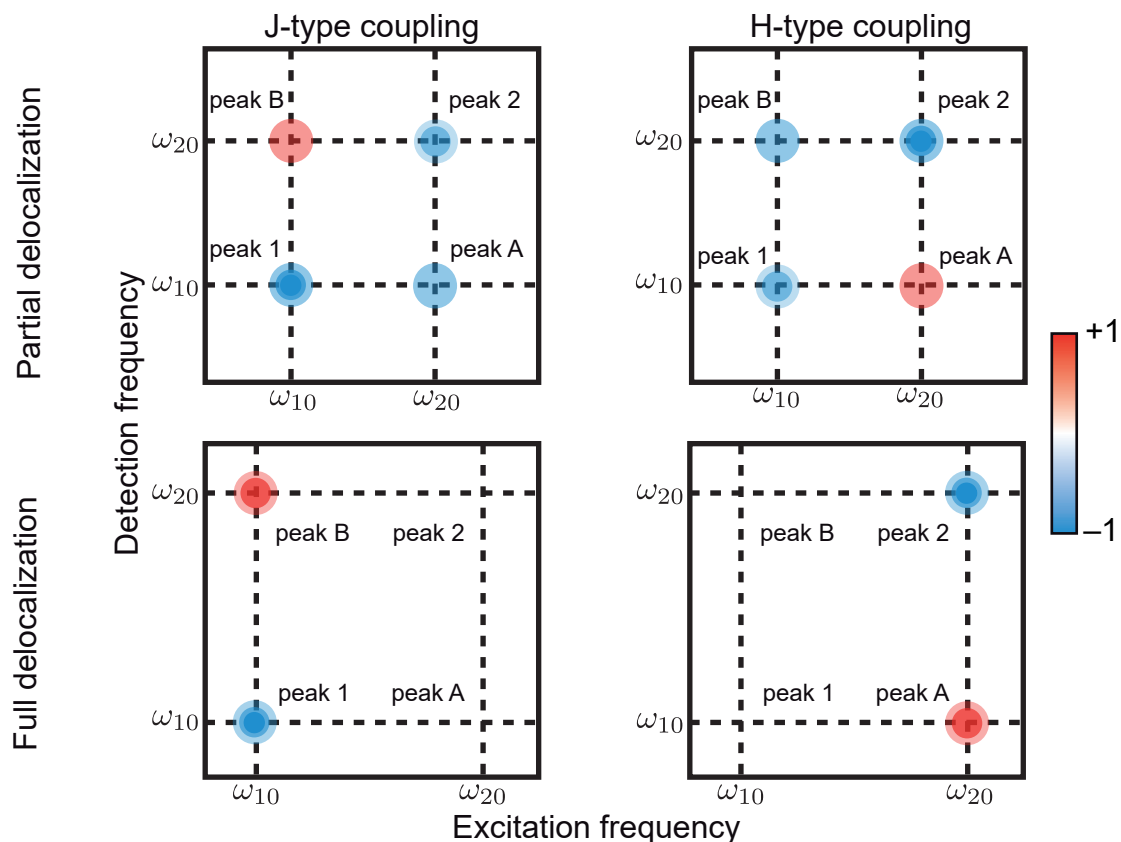
Figure 5.4.: Schematic 2D spectra of a dimer. The first row corresponds to a dimer with moderate coupling which results in partial delocalization. The cross peak amplitudes directly reflect the degree of delocalization in the dimer. The lower row corresponds to strongly coupled dimers with a delocalization of 50%. For a strongly coupled H-type (J-type) dimer, the transition to the energetically lower (higher) single-exciton state is dark and therefore not visible in the 2D spectrum.

The 2D spectra for dimers with full delocalization can also be predicted by thorough investigation of the absorption spectra. The absorption spectra for strongly coupled J- and H-type dimers consist only of one peak because the transition to one of the single-exciton state is completely dark. In the 2D spectrum, only transitions are visible that are bright, i.e., which can be excited. This results in taking a "slice" of the 2D spectrum at the excitation frequency of the allowed transition in the absorption spectrum because only this specific transition is bright. For the J-type dimer, only the red-shifted transition is allowed which corresponds to an excitation frequency of ω_{10}. Therefore, only peaks along this excitation frequency can be observed in the 2D spectrum.

5.2. **Signatures of Energy Transfer in Two-Dimensional Spectroscopy**
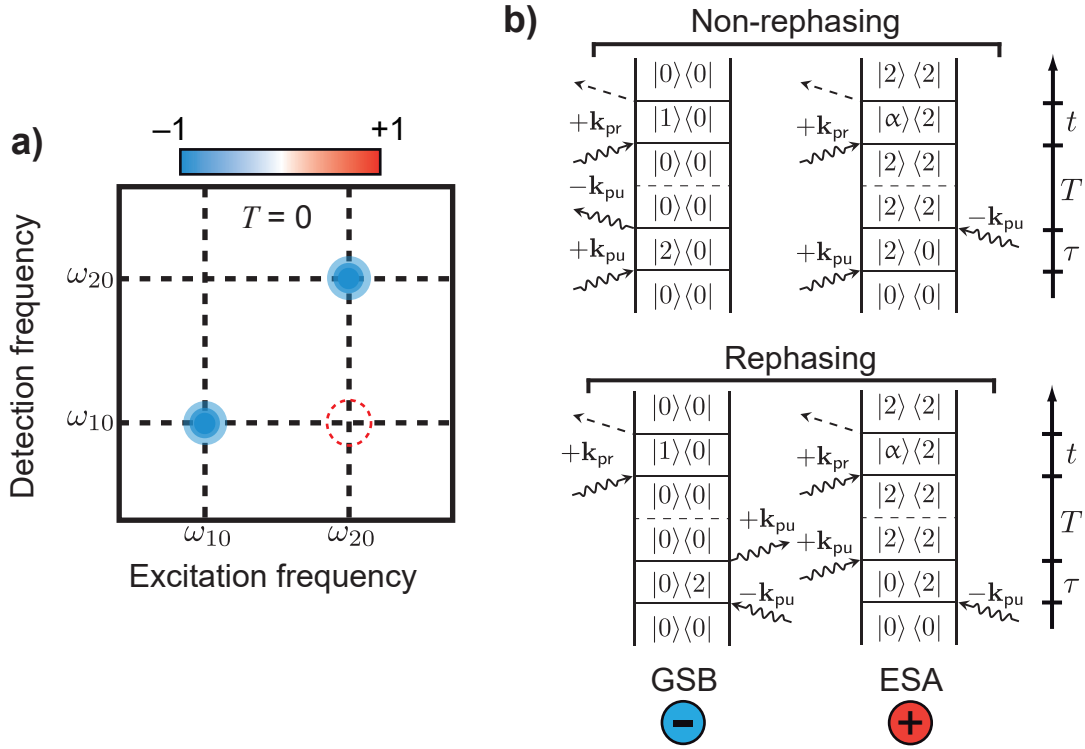
Figure 5.5.: Two-dimensional spectrum for $T = 0$ and its description with double-sided Feynman diagrams. (a) For this population time, the cross peak corresponding to the energy transfer is not visible. The missing cross peak in the 2D spectrum is indicated with a red dotted circle. (b) The corresponding Feynman diagrams for the rephasing and non-rephasing signal contributions consist out of one positive ESA-type pathway and one negative GSB-type pathway.

As a next step, we analyze dynamic processes that occur during the population time T in terms of double-sided Feynman diagrams. As an example, we chose energy transfer with its specific signatures in 2D spectroscopy. We consider the same dimer as in the previous section consisting of one ground state $|0\rangle$, two single-exciton states $|2\rangle$ and $|1\rangle$, and a biexciton state $|\alpha\rangle$. Energy transfer with the rate k_T occurs from state $|2\rangle$ to state $|1\rangle$. In order to focus on only one effect, the coupling is chosen to be weak between the states. In this case, the transition dipole moments are again $\boldsymbol{\mu}_{10} = \boldsymbol{\mu}_{\alpha 2}$ and $\boldsymbol{\mu}_{20} = \boldsymbol{\mu}_{\alpha 1}$. Energy transfer corresponds to transport from one state to another and is visible as the rise of cross peaks in the 2D spectrum over the population time [79]. Since energy transfer needs a finite time to occur, the cross peaks are not visible for $T = 0$ as shown in Fig. 5.5a. As we have seen in the previous section, four Feynman

diagrams contribute to the cross peak below the diagonal at $T = 0$: two GSB-type diagrams and two ESA-type diagrams. We focus on this specific cross peak because energy transfer typically occurs from an energetically higher state to a lower state [8]. The diagrams are shown in Fig. 5.5b. The GSB-type and ESA-type diagrams cancel each other perfectly and no cross peak is visible for $T = 0$.
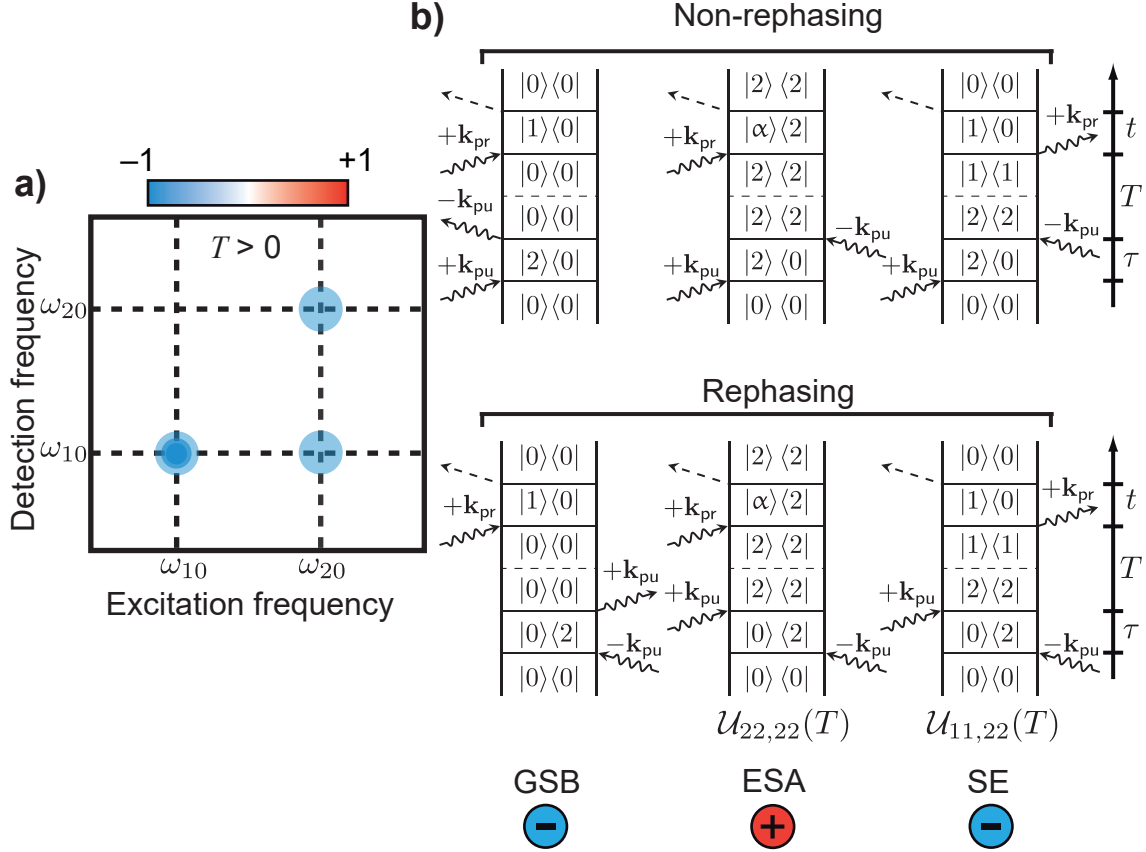
Figure 5.6.: Description of energy transfer in 2D spectroscopy with double-sided Feynman diagrams for $T > 0$. (a) For a population time larger than zero, energy transfer occurs. The energy transfer is visible as a cross peak in the 2D spectrum, which amplitude increases with the population time. With the increasing cross peak amplitude, the amplitude of the diagonal peak is getting weaker by the energy transfer. (b) The dynamics of the cross peak can be characterized by a set of double-sided Feynman diagrams. The important point is the interplay of the decaying SE-type contribution and the rising ESA-type contribution by the energy transfer.

The 2D spectrum changes when the population time increases. For population times of $T > 0$ energy transfer occurs from state $|2\rangle$ to $|1\rangle$). Due to the energy transfer, two additional SE-type diagrams contribute to the cross peak (Fig. 5.6a). The population in state $|2\rangle$ evolves to a population in state $|1\rangle$ during the population time T in these

diagrams. Therefore, during the time delay τ, a coherence between the ground state $|0\rangle$ and state $|2\rangle$ is present while during the delay t, the system is in a coherence between state $|0\rangle$ and state $|1\rangle$. The two coherences determine the spectral position at ω_{20} on the excitation axis and on ω_{10} at the detection axis, i.e., at the position of the cross peak. The dynamics during the population time can be taken into account via specific propagators [9, 24]. Since the SE-type diagrams occur via energy transfer, its amplitude scales with the propagator $\mathscr{U}_{11,22}$ which is

$$\mathscr{U}_{11,22} = 1 - e^{-k_T T}, \tag{5.6}$$

with the transfer rate k_T. For $T = 0$ the amplitude of the diagram is zero and the SE-type pathways do not contribute, i.e., the cross peak is described by the four diagrams shown in Fig. 5.5. For population times $T > 0$ the amplitude of the SE-type pathways will slowly rise (Fig. 5.6 b). On the other hand, the energy transfer will decrease the amplitude of the ESA-type pathways since it reduces the population in state $|2\rangle$. The decrease is described by another propagator

$$\mathscr{U}_{22,22} = e^{-k_T T}. \tag{5.7}$$

Therefore, the sum of the pathways will not cancel anymore with increasing population time and a negative cross peak will appear with the rate of the energy transfer. The energy transfer also decreases the amplitude of the diagonal peak. The double-sided Feynman diagrams that describe the decrease of the diagonal peak amplitude can be found in Sec, B of the Appendix. For $T \rightarrow \infty$ and efficient energy transfer, the ESA-type pathways vanish and only the SE-type and GSB-type diagrams will contribute to the cross peak. It is worth noting that it is not the absence of double-sided Feynman diagrams that leads to the absence of a cross peak at $T = 0$, but rather the complex interplay between the different diagrams lead to the correct description of the signatures of energy transfer. The example discussed here demonstrates that it is important to consider all the pathways which contribute to a physical process in order to describe the process correctly.

5.3. Potential Pitfalls

As demonstrated by the examples of coupling and energy transfer, double-sided Feynman diagrams are a powerful tool to analyze 2D spectra. Usually, a large number of diagrams are contributing to different peaks and the connected processes. The number of Feynman diagrams to be considered can be drastically reduced by time ordering of the pulses, the RWA, or experimental techniques such as phase matching and phase cycling [23]. However, care has to be taken when the concept of double-sided Feynman diagrams is applied. Here we want to discuss a few potential mistakes that can easily occur when double-sided Feynman diagrams are used for the analysis of 2D spectra.

The formalism of double-sided Feynman diagrams is a description of the signal and the connected processes that can occur due to the interaction with the electric field [188]. An accurate description of the signal and its dynamics with double-sided Feynman diagrams is only valid if **all** the relevant diagrams are considered. The nomenclature of the Feynman diagrams is misleading because the terms of GSB, SE and ESA originally used in TA spectroscopy are transferred to the formalism of double-sided Feynman diagrams. The potential pitfall that emerges from this nomenclature can be easily demonstrated with a simple system such as a two-level system. A two-level system consists of one ground state $|g\rangle$ and one excited state $|a\rangle$. In that case only two physical processes can be observed in a 2D experiment: SE and GSB. Therefore, the 2D spectrum consists only of one (negative) diagonal peak. Since there are no higher-excited states in the chosen system involved, no ESA is visible per definition. The diagonal peak decays with the rate k_L that reflects the lifetime of the system. The analysis with double-sided Feynman diagrams is only correct if all the relevant diagrams are considered. At first glance one would think that the signal can be described by two types of diagrams: GSB-type and SE-type diagrams analogously to the processes that can be measured. The rephasing and the non-rephasing double-sided Feynman diagrams are shown in Fig. 5.7b. The finite lifetime is taken into account via the rate k_L and the propagator for the SE-type pathways is

$$\mathscr{U}_{\mathrm{aa,aa}}(T) = e^{-k_L T}. \qquad (5.8)$$

The SE-type pathways decay therefore with the lifetime of the excited state. However, the GSB-type pathways will not decay with the lifetime because the diagram consists of a ground-state population during T and no further relaxation is possible. For long population times, the GSB-type pathways are still present and therefore the signal would also still be present independent of any lifetime. Clearly, the description of the GSB and SE signal only with GSB-type and SE-type diagrams is not complete and incorrect since it does not describe the lifetime decay correctly. The problem can be solved by including ESA-type pathways. The ESA-type pathways describe a decay to the ground state during the population time T with a re-excitation of the system by the probe pulse. The corresponding propagator for the ESA-type pathways is

$$\mathscr{U}_{\mathrm{gg,aa}}(T) = 1 - e^{-k_L T}. \qquad (5.9)$$

For long population times, the SE-type pathways will not contribute to the signal anymore because they decay with the lifetime described by the propagator $\mathscr{U}_{\text{aa,aa}}(T)$. The two remaining types of diagrams are the GSB-type and the ESA-type diagrams. The ESA-type diagrams have the opposite sign to the GSB-type diagrams and they will cancel each other resulting in a vanishing diagonal peak for long population times T.
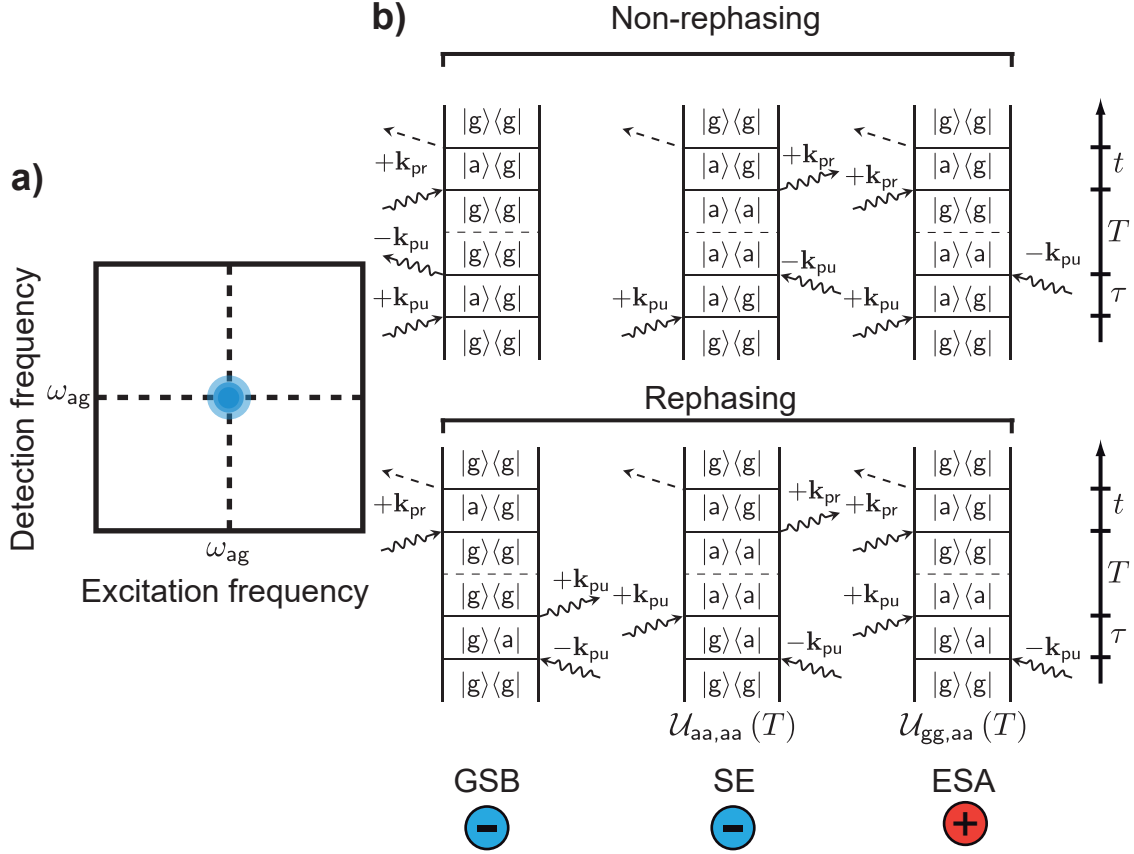
Figure 5.7.: 2D spectrum and double-sided Feynman diagrams for a two-level system. (a) In the 2D spectrum, only one diagonal peak is visible. This peak corresponds to the process of SE and GSB. (b) The decay of the peak with the rate k_L that reflects the lifetime is described by three types of double-sided Feynman diagrams.

An important concept to reduce the number of diagrams that has to be considered is time ordering. For example, time ordering between pump and probe means that first the interactions with the pump pulses take place followed by the interaction with the probe pulse. However, special care has to be taken when population times close to zero, i.e., close or in the coherent artifact, are measured. In this regime, the time ordering between the pump and the probe pulses does not hold anymore. A recent publication discussed the signatures of non-time ordered contributions in 2D spectroscopy and here we want to briefly discuss the results [124]. For positive

population times the coherence time is scanned in such a way that one pulse (labeled pump pulse 1) is moved to earlier times (Fig. 5.8a). This scanning procedure results in a fixed population time T while the coherence time τ is scanned. Therefore, both pump pulses first interact with the sample before the interaction with the probe pulse takes place. The chosen direction of scanning the coherence time has consequences for negative population times ($T < 0$). For short coherence times, the probe pulse arrives first before both pump pulses interact with the sample. For later coherence times, one pump pulse arrives first, then the probe pulse and then the other pump pulse which leads to an "incorrect" time-ordering of "pump–probe–pump" (Fig. 5.8b) [124]. Note that in this scanning procedure at $T < 0$ for each coherence time step τ the population time T is effectively changed and basically one pump pulse is scanned over the probe pulse with increasing coherence time.

This kind of different time ordering contribution can also occur if positive population times close to $T = 0$ are measured, and the pulses overlap due to their finite pulse length. Furthermore, the early time dynamics are usually not considered in the analysis because of the overlap with the coherent artifact. We want to emphasize that the term coherent artifact is misleading because it suggests that the processes that occur are unnatural. Recent studies demonstrated that the variety of phenomena such as two-photon absorption or stimulated Raman scattering that are contributing to the coherent artifact can be analyzed with the help of double-sided Feynman diagrams [189]. We will discuss the concept of time ordering more in the context of higher-order signals in Chapter 8.
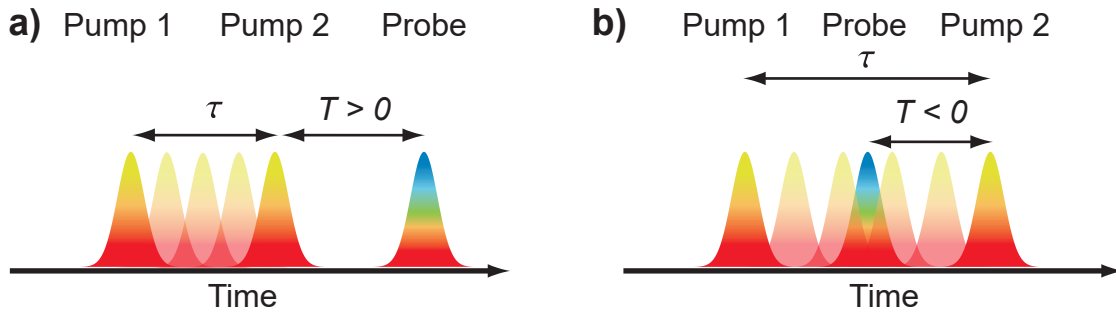
Figure 5.8.: Different time ordering of pump and probe pulses in a 2D experiment. (a) For positive population times, the two pump pulses interact first with the sample before the interaction with the probe pulse. The coherence time is scanned in such a way that pump 1 is moved to earlier times. The scanning of the coherence time is indicated by additional transparent pulses. (b) At negative population times, the same scanning of the coherence time leads to an "incorrect" time ordering in which the probe pulse is temporally located between the two pump pulses.

At the end of this chapter, we want to briefly discuss the effect of higher-order signals and their potential contamination of other signals. When 2D spectra are analyzed in terms of double-sided Feynman diagrams, a certain order of nonlinearity is assumed. In coherently detected 2D experiments, the lowest-order signal is the third-order signal while in action-detected 2D experiments, the lowest-order signal is the fourth-order signal [8]. However, higher-order contributions can be present at high excitation densities [190]. These contributions can be described in terms of double-sided Feynman diagrams as well but have to be considered in the analysis. For example, in natural light-harvesting complexes, EEA contributes to the third-order signal at high excitation densities [186, 191]. These additional processes can be described as fifth-order contributions with their respective double-sided Feynman diagrams. If the diagrams that describe the higher-order signals are not included, the analysis might be false depending on the degree of higher-order contamination. Higher-order signals carry a lot of meaningful information about higher excited states [13] or exciton diffusion which can be probed by EEA [181, 192]. In the next chapter, we discuss different techniques with which the higher-order signals can be measured and separated from the lower-order signals, and what information can be obtained by higher-order signals.

Higher-Order Multdimensional and Pump–Probe Spectroscopy

Transient absorption and coherent two-dimensional (2D) spectroscopy are widely established methods for the investigation of ultrafast dynamics in quantum systems. Conventionally, they are interpreted in the framework of perturbation theory at third order of interaction, corresponding to the excitation of single particles or quasiparticles and their kinetics. Here, we discuss the potential of higher-(than-third-)order pump–probe (PP) and multidimensional spectroscopy to provide insight into excited multi-particle states and their dynamics. We focus on recent developments from our group. In particular, we demonstrate how phase cycling can be used in fluorescence-detected two-dimensional spectroscopy to isolate higher-order spectra that provide information about highly excited states such as the correlation of multi-exciton states. Furthermore, we discuss coherently detected fifth-order two-dimensional spectroscopy and its power to track exciton diffusion. Finally, we show how to extract higher-order signals even from ordinary PP experiments, providing annihilation-free signals at high excitation densities and insight into multi-exciton interactions.

6.1. Introduction

Ultrafast spectroscopy is employed to investigate phenomena on the time scale of femtoseconds, unraveling various physical properties. The most common technique is PP spectroscopy, usually carried out in transient absorption geometry: A first pulse excites the system while a second pulse detects the frequency-resolved transient change (in absorption) after a time delay T. In terms of perturbation theory, it is the third-order polarization that is probed in a conventional PP experiment. An extension of PP is coherent 2D spectroscopy where the third-order polarization is characterized as well, but as a function of both excitation frequency and detection frequency [30, 34, 117]. 2D spectra can be acquired, for example, by replacing the single excitation pulse from PP spectroscopy with a double pulse of variable time delay τ. Fourier transformation over τ provides the excitation frequency axis while the detection frequency axis can be obtained directly by a spectrometer via measuring the spectral interference of the signal with a local oscillator (LO) pulse that may be either a separate reference pulse that does not interact with the sample or the probe pulse itself. Another option for obtaining detection frequency resolution is to vary systematically the time delay between the signal and the LO and to perform numerical Fourier transformation [73, 87, 193]. Resonant excitations of the system appear as diagonal peaks on a 2D map. Cross peaks indicate coupling or energy transfer in coherently detected 2D spectroscopy [62, 76] and energy transfer as well as EEA in "action-detected" 2D spectroscopy using incoherent observables. The evolution of the 2D spectrum as a function of delay T provides information about, for example, energy transfer [79], wavepacket dynamics [194], and coherences [83], while the analysis of the 2D line shapes can be used to determine the interaction of the system with its environment [195, 196]. Nowadays, both techniques, PP and 2D spectroscopy, are well-established and frequently used to investigate artificial [171, 197] or natural light-harvesting complexes [79, 185], supramolecular systems [83, 198], chemical reactions [48], 2D materials [199], semiconductor nanostructures [200], and many more. Recent developments include the use of incoherent observables such as fluorescence [85, 111, 113, 116, 118, 201, 202], photoelectrons [6, 109, 133, 135], photoions [37, 91, 142], or internal photocurrents [112, 119, 144, 203, 204], to measure ultrafast dynamics.

Ultrafast spectroscopy usually relies on a perturbative description of light–matter interaction. In general, all the higher-order terms of the perturbation series are present in any given experiment. The common practice to suppress unwanted higher orders is to choose the excitation laser intensities in such a way that higher-order signals do not contribute significantly, ideally are below the noise floor of the measurement, and the perturbation series has to be considered only up to a specific term. For example, in a 2D experiment, the intensity of the pulses as well as the phase-matching condition can be set in such a way that the detected 2D signal is dominated by the third-order signal and higher-order signals do not contribute significantly. For higher excitation intensities, the higher-order terms contribute more and more to the signal. This is well known for excitonic systems for which at high excitation intensities, exciton–

exciton annihilation (EEA) mixes into the 2D and PP signals [205, 206]. Especially in light-harvesting complexes, the uncontrolled mixing of EEA with the single-exciton dynamics has challenged researchers for years [186, 207]. Annihilation can only be reduced by low-power measurements that in turn may lead to low signal-to-noise ratio (SNR). Alternatively, EEA has to be included in the data analysis to avoid misinterpretation, which complicates matters and requires an a-priori model [186, 208, 209]. If a suitable model is available, however, EEA can be utilized in power-dependent PP studies to investigate exciton migration in extended systems such as light-harvesting complexes or molecular aggregates [180, 182, 183]. In such experiments, the third- and fifth-order signals (and even higher orders) are mixed together making it difficult to disentangle the data. As we outline in the present chapter, this problem can be solved using higher-order spectroscopy that allows us to obtain separated higher-order signals. We will employ the term "higher order" for such signals that are at least of fifth order in a perturbation-theory description, while the third and fourth orders are the "conventional lower-order" time-resolved methods using either coherent or incoherent detection, respectively.

Besides EEA, higher-order spectroscopy unveils system properties and dynamics that cannot be directly observed by lower-order techniques. Examples include coherences between highly excited electronic states in quantum wells [210], multistep energy transfer in light-harvesting complexes [211], and highly excited vibrational states [212]. Following the principle of 2D spectroscopy, higher-order signals can be obtained by adding additional interactions, each of them with its own associated pulse [213]. Scanning all time delays and performing Fourier transformations distributes the higher-order signal over multiple dimensions (4D or higher). Instead of using one pulse per interaction, other approaches rely on multiple interactions from the same pulse, inherently reducing the dimensionality of the obtained spectra [210, 214–217]. The dimensionality can also be reduced by setting specific time delays to zero while retaining separate laser beams. For example, multiple population-period transient spectroscopy (MUPPETS) uses two pulses from different directions that interact with the system at the same time [218, 219]. In general, the main challenge in higher-order spectroscopy is to separate the individual nonlinear orders and, at the same time, keep the experiment feasible as it is technically demanding to isolate weak higher-order signals in a multi-pulse experiment that requires scanning of multiple delays.

The chapter is structured as follows: First, we will analyze the technical approaches to isolate higher-order signals. In the following part, we demonstrate how various higher-order signals can be isolated from one single experiment in fluorescence-detected 2D spectroscopy using phase cycling. Next, we discuss coherently detected fifth-order 2D spectroscopy as a tool to investigate exciton diffusion in extended systems such as polymers. In addition, we discuss an analogous sixth-order technique using fluorescence detection. Finally, we show how higher-order signals can be isolated in a simple PP experiment by systematically varying the excitation intensity. This new technique is straightforward to implement, isolates clean nonlinear order signals, and can be extended to higher orders.

In 2D spectroscopy, the different signals contributions can be labeled by their specific coherences that occur during the various time delays. We distinguish, on the one hand, the so-called one- or multi-quantum signals, which are the signals that appear at one or several times the laser frequency, respectively, and on the other hand the nonlinear-order signals, which are the contributions arising from the various terms of the perturbative expansion of the nonlinear response. While at first glance one might think that these two definitions are equivalent, they are in fact not, and the clarification of their relation is a main topic of the present chapter.

We label the multi-quantum signals as $XQZQ$ where X and Z correspond to the quanta of coherences [one-quantum (1Q), two-quantum (2Q), etc.] with respect to the laser central frequency ω_0 that evolve as a function of the coherence times τ and t, respectively. For example, in a typical "photon-echo-type" 2D experiment, one isolates the 1Q1Q signal which correlates one-quantum coherences during τ with one-quantum coherences during t, with the possibility of tracking population dynamics during the time delay T. The coherences during τ and t determine the position of the signal on the excitation and detection axis, respectively. Additional coherences (i.e., oscillatory behavior) may occur as a function of the population time T, i.e., the delay between pump and probe, resulting in $XQYQZQ$ signals. In such signals, it is possible to isolate zero-quantum (0Q) coherences which are superpositions between states within a particular manifold ($Y = 0$) such as between two vibrational sublevels of a single-exciton state. Experimentally, one needs to ensure phase stability between the corresponding pulses [23] because a drift of the phase during measurement will result in distortion of the peaks in the 2D spectrum. Phase stabilization becomes more challenging for shorter and shorter wavelengths (because a given pathlength fluctuation leads to a larger change in relative phase between pulses) but it also becomes more challenging for an increasing number of beams.

Let us now discriminate, from such NQ signals, the nonlinear orders that correspond to the different terms of the perturbative expansion. One might naively think that, for example, the coherently detected 1Q1Q signal should correspond to a third-order signal. However, all the higher nonlinear orders in principle contribute as well. In order to reduce their influence on the 1Q1Q signal, the intensities of the pulses are usually chosen in such a way that the 1Q1Q signal is dominated by the third-order response while higher-order terms do not contribute significantly. If the intensity of the pulses is increased, the 1Q1Q signal will be substantially "contaminated" by higher-order signals. Higher-order signals can be characterized independently by isolating appropriate multi-quantum signals for which the contribution with the lowest possible order corresponds to a higher-order signal. While such a multi-quantum signal may be dominated by one particular higher-order signal, even higher-order terms also generally contribute. The fraction of those contaminating higher-order terms can then be kept low again by choosing an adequate intensity regime. For example, the population-detected 3Q1Q signal is of at least sixth order. In the correct intensity regime, it is indeed predominantly a sixth-order signal and the contribution of higher-order signals is not significant. However, for higher intensities, higher orders, i.e., eighth or higher,

will start to contribute to the 3Q1Q signal as well. This should be kept in mind and will be addressed explicitly in the final section of this chapter. To simplify the discussion until then, we will mention only the leading order for any particular multi-quantum signal, implying that the intensity regime was chosen such that the particular nonlinear order is the dominating term.

6.2. Isolation of Higher-Order Signals

Let us now focus on the experimental approaches for obtaining higher-order signals. Shown in Fig. 6.1 and Fig. 6.2 are four possibilities that can be used to distinguish higher-order from lower-order signals in multidimensional spectroscopy. We will discuss higher-order PP spectroscopy separately. As a first option, higher-order multi-quantum signals can be distinguished by their specific phase-matching direction (Fig. 6.1a) [23]. Assume that three pulses interact with the sample from three different directions with wavevectors $\mathbf{k}_i$ ($i = 1, 2, 3$). Pulses 1 and 2 excite and pulse 3 probes the system. Thus, pulses 1 and 2 are often labeled as pump pulses while pulse 3 is called probe pulse. Each particular nonlinear signal is then emitted in a specific direction given by a corresponding linear combination of the incident wavevectors. For example, the 2Q1Q signal is composed of the rephasing and non-rephasing fifth-order signals which are emitted in the directions $-2\mathbf{k}_1 + 2\mathbf{k}_2 + \mathbf{k}_3$ and $+2\mathbf{k}_1 - 2\mathbf{k}_2 + \mathbf{k}_3$, respectively, and can thus be selected with a spatial mask [220]. The individual wavevector indices indicate the time ordering of the pulses (which, however, is not necessarily the same as the time order of the light–matter interactions in the case of finite pulse duration in the region of pulse overlap) [124]. The signal is measured by heterodyne detection with a fourth pulse (LO) with wavevector $\mathbf{k}_{\mathrm{LO}}$. In the case of three beams and heterodyne detection by a separate LO as in Fig. 6.1a, the phase must be stable between pulses 1 and 2, i.e., the two pump pulses, and between pulse three and the LO, in order to resolve an $XQZQ$ signal. Once the phase is stabilized, the phase between the LO and the signal has to be determined. In the case of third-order signals, this "phasing" procedure is carried out by a separate PP experiment and by ensuring that the data from PP and 2D, integrated over the excitation frequency axis, agree according to the projection-slice theorem [23, 221]. The phase of the fifth-order signal in Fig. 6.1a can be determined analogously by comparison with a "pump–dump–probe" experiment [220]. The phasing procedure for other higher-order signals needs further theoretical investigation. The polarization of each pulse can be controlled separately in the noncollinear geometry which can be used to suppress certain signal contributions [105, 212, 222, 223].

In the PP geometry (Fig. 6.1b) the two pump pulses, i.e., pulses 1 and 2, excite the system from the same direction and the signal is emitted in the direction of the probe pulse which also acts as the LO. Therefore, no phasing procedure is needed, and the purely absorptive spectrum, i.e., the sum of the rephasing and non-rephasing parts, can be measured directly. However, a subset of fifth-order contributions, such as $-2\mathbf{k}_1 + 2\mathbf{k}_2 + \mathbf{k}_3$ and $+2\mathbf{k}_1 - 2\mathbf{k}_2 + \mathbf{k}_3$, are also emitted in the same direction as

a) Selection by **phase matching**   **b)** Selection by **excitation frequency**
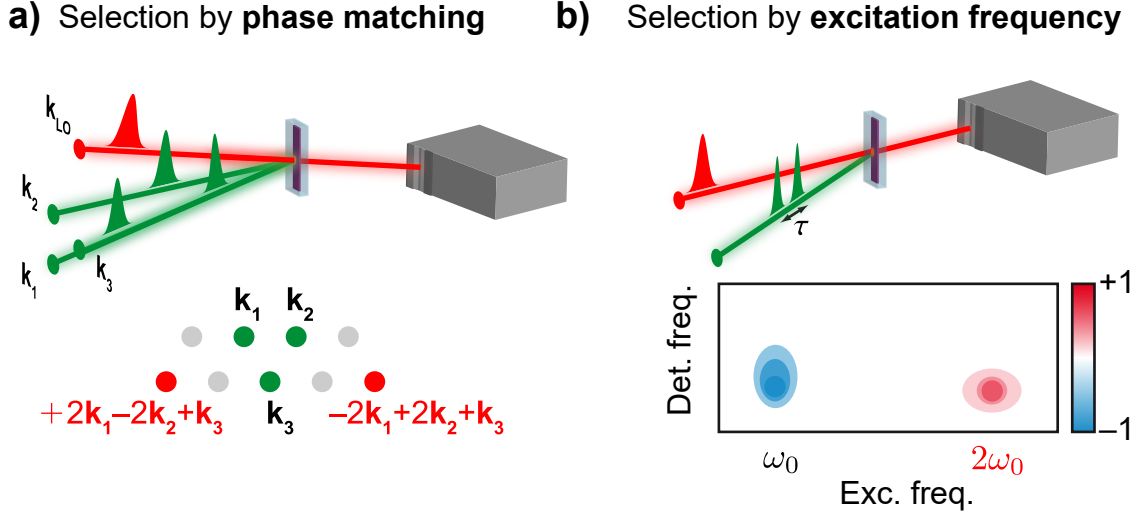
Figure 6.1.: Overview of experimental approaches to isolate high-order signals in coherently detected multidimensional spectroscopy. (a) In fully noncollinear geometry, four incident pulses illuminate the sample from four different directions, i.e., with different wavevectors $\mathbf{k}_i$ ($i = 1, 2, 3$). Various possible nonlinear signals (red: fifth-order signals with the phase-matching conditions of $\pm 2\mathbf{k}_1 \mp 2\mathbf{k}_2 + \mathbf{k}_3$, gray: lower-order signals) are separated spatially via their specific phase-matching directions. (b) In PP geometry, the first two (pump) pulses have the same wavevector. The higher-order signals are separated along the excitation axis in the 2D spectrum because they oscillate at higher frequencies during the time delay τ. For example, the fifth-order signals with the phase matching conditions of $\pm 2\mathbf{k}_1 \mp 2\mathbf{k}_2 + \mathbf{k}_3$ oscillate with a two-quantum coherence during τ and appears near $2\omega_0$ at the excitation axis, with ω_0 as the central frequency of the pump spectrum.

the third-order signals, because $\mathbf{k}_1 = \mathbf{k}_2$ in the PP geometry [20, 216]. While these signals overlap spatially, we can separate them in the frequency domain along the excitation axis in the 2D spectrum. The 2Q1Q signal appears at around twice the central frequency ($2\omega_0$) of the excitation pulses and can be spectrally separated from the 1Q1Q signal at ω_0. Again, note that if the excitation intensity is chosen so that the seventh-order contribution is small, the 2Q1Q signal will be dominated by the fifth-order signals with $-2\mathbf{k}_1 + 2\mathbf{k}_2 + \mathbf{k}_3$ and $+2\mathbf{k}_1 - 2\mathbf{k}_2 + \mathbf{k}_3$. The 2Q1Q signal oscillates with a 2Q coherence during τ. In order to avoid aliasing, the step size of the delay $\Delta\tau$ has to be chosen small enough. Otherwise, the 2Q1Q signal is folded back to a smaller frequency which can lead to spectral overlap with the 1Q1Q signal. The maximum resolvable frequency ω_N is determined by the Nyquist theorem which connects ω_N to the step size $\Delta\tau$ by [23]

$$\frac{\omega_N}{2\pi} = \frac{1}{2\Delta\tau} \tag{6.1}$$

The first two pulses, i.e., the two pump pulses, can be created via an interferometer or conveniently from one beam path by a pulse shaper or a common-path interferometer

[73, 92]. Common-path interferometers based on wedge pairs offer passive phase stabilization with inherent phase stability of the pulse pair [224]. Using pulse shapers allows one working in the rotating frame. In the rotating frame, the time-domain envelope of one pulse is shifted with respect to the other pulse upon delay variation, while the phase of the carrier oscillation of the delayed pulse with respect to the other pulse is unchanged. Measuring in the rotating frame leads to a shift of the fundamental signal frequency to lower frequencies. As a result, fewer data points have to be measured which speeds up data collection [73]. Pulse shapers need proper calibration and extra precaution is necessary to avoid artifacts [45, 125, 225]. Polarization control in the PP geometry can be achieved with vector-field pulse shaping [226, 227]. Another approach utilizes differently orientated polarizers for the probe pulse before and after the sample to suppress certain signal contributions [223]. In the PP geometry, rephasing and non-rephasing signal contributions are emitted in the same direction and can therefore not be separated spatially. However, they can be separated by phase cycling [228] which is described below in the context of action-based spectroscopy.

It is also possible to use incoherent observables to measure multidimensional spectra as shown in Fig. 6.2a and Fig. 6.2b for the example of fluorescence detection using phase cycling and phase modulation, respectively [85, 111, 113, 116, 118, 201, 202]. With these approaches, measurements using other incoherent observables such as photoelectrons [6, 109, 133, 135], ions [37, 91, 142], and internal photocurrents [112, 119, 144, 203, 204] can be carried out as well. Note that these action-based approaches measure a signal that is dependent on the excited-state population which means that a nonlinear signal of even order is measured (i.e., fourth order, sixth order, etc.). We analyzed the response functions for coherently detected and action-detected 2D spectroscopy demonstrating their similarities and differences and derived a generalized response function for both techniques [9]. Fluorescence-detected 2D spectra originate from an observable connected to an excited-state population. This excited-state population is created after the sequence of pulses and can be influenced by dynamical processes such as EEA or internal conversion. Both effects can reduce the quantum yield of certain excitation pathways resulting in their (partial) cancellation. The fundamental and practical differences of coherently and fluorescence-detected techniques were part of several recent studies [8, 120, 122]. Using fluorescence as an observable has the advantage that the solvent does not contribute to the signal because the solvent is usually not fluorescent. Solvent contributions are especially strong in the overlap region close to $T = 0$. Due to the absence of solvent artifacts, fluorescence-detected methods are well suited to track short-lived dynamics.
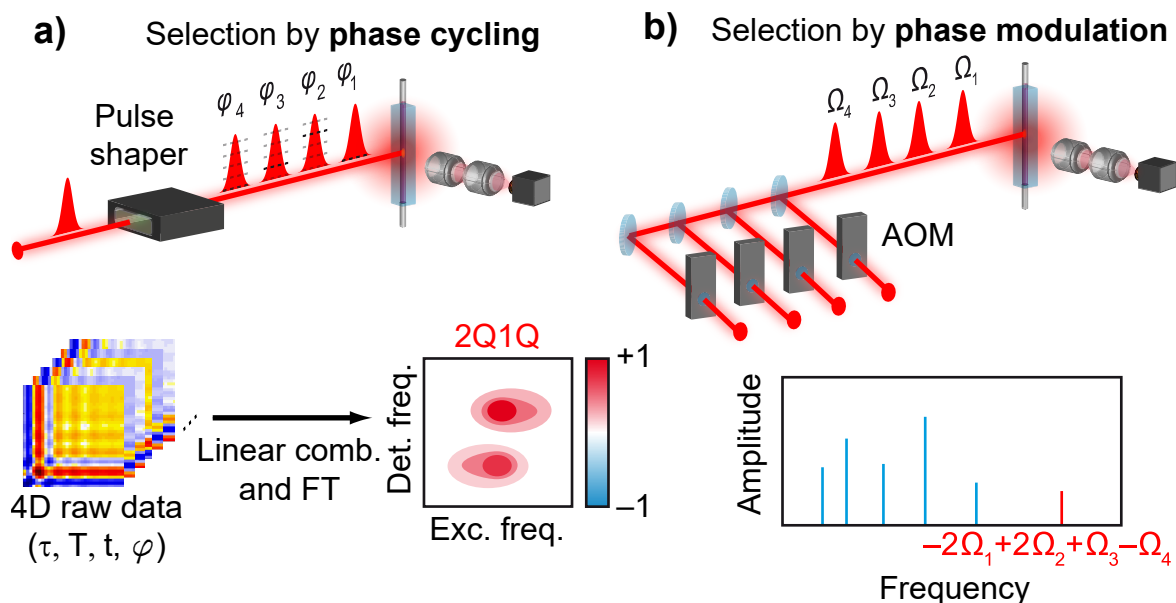
Figure 6.2.: In action-based spectroscopy (here with fluorescence detection), the signal is measured using four pulses with variable time delays. The isolation of the signals is carried out by phase cycling. For phase cycling, the relative pulse phases are systematically varied by incrementing the absolute phases φ_i $(i = 1, 2, 3, 4)$ of the second, third, and fourth pulses with respect to the first for each set of time delays. Phase cycling allows one to extract higher-order signals by constructing linear combinations of the raw data. (d) It is also possible to extract fluorescence-detected 2D spectra (or other action-based 2D spectra) by using four beams and modulating the relative phase of each of the four beams by an acousto-optic modulator (AOM). The four modulation frequencies Ω_i $(i = 1, 2, 3, 4)$ act similar to the wavevectors $\mathbf{k}_i (i = 1, 2, 3)$ in noncollinear geometry. While in noncollinear geometry, the signal is isolated by the phase-matching condition, the signal in the phase-modulation approach can be extracted by performing lock-in measurements at specific sum frequencies or difference frequencies. For example, one particular sixth-order signal has a frequency of $-2\Omega_1 + 2\Omega_2 + \Omega_3 - \Omega_4$.

In the scheme of Fig 6.2a, phase cycling is used for signal isolation. As an example, a pulse shaper creates a four-pulse sequence from one beam with variable time delays and relative phases. The advantage of a single-beam geometry is that phase stability is inherently assured. Using a pulse shaper restricts the maximum delay to a few picoseconds which makes the method preferable for fast dynamics. For each set of delays, the relative phases of the pulses are varied. The nonlinear signals therefore depend on the delays as well as on the relative phases of the pulses, analogous to the signals in noncollinear, coherently detected 2D spectroscopy that depend on the delays and on the distinct wavevectors. Various nonlinear signals in fluorescence-detected 2D spectroscopy can then be constructed by weighting the phase- and delay-dependent raw data with phase-specific factors [26]. In addition to dealing with potential artifacts introduced by the pulse shaper, one has to prevent artifacts from potential

nonlinearities of the detector either by calibration or by acquiring data in the linear regime of the detector [229]. In phase cycling, the relative phase differences between the pulses are incremented in discrete equidistant steps. For example, in order to extract the fourth-order rephasing and non-rephasing signal contributions employing a four-pulse sequence, the relative phases of the last three pulses are changed by steps of $\frac{2}{3}\pi$ [89]. Multi-quantum signals dominated by higher-order signals, i.e., higher than fourth order, can be separated by using phase-cycling schemes that employ smaller increments for the relative phases analogously to coherently detected spectroscopy where smaller delay step sizes are needed to resolve multi-quantum signals oscillating at higher frequencies [5].

Another approach to multidimensional spectroscopy that is closely related to phase cycling is phase modulation. This technique changes the relative pulse phases from shot to shot [111]. The phase-modulation approach can therefore be also seen as "dynamic phase cycling" [119]. In Fig. 6.2b we show an example of this approach based on fluorescence detection. Each of the four beams is phase-modulated at a specific frequency with an individual acousto-optic modulator (AOM). The wavevectors that distinguish the pulses in a noncollinear experiment are replaced by the modulation frequencies as shown for an exemplary higher-order signal in Fig. 6.2b [217]. In the noncollinear approach, the signal is chosen by its phase-matching condition which is the result of the interaction with different wavevectors. In the phase-modulation approach, the different pulses are now tagged by their individual modulation frequency. The pulses "imprint" their modulation frequency onto the signal, similar to how the phase-matching condition reflects the interaction with different wavevectors. The signal can be isolated by various procedures such as phase-sensitive lock-in detection [110, 111], or digital lock-in detection with Fourier analysis [118]. A measurement scheme for coherently detected signals that uses super-heterodyned detection was demonstrated as well [230]. Since shot-to-shot-varied rapid phase cycling is possible with pulse shaping as well, the main advantage of phase modulation arises for laser systems with high repetition rates, such as 76 MHz [230], for which shot-to-shot pulse shaping is not feasible. Like in phase cycling, multiple signals can be measured simultaneously by applying digital lock-in [118]. However, depending on the modulation frequencies, the acquisition of specific multi-quantum signals might be limited by the detector bandwidth [118].

6.3. Fluorescence-Detected Higher-Order Spectroscopy Using Phase Cycling

As a first application example, we now discuss how phase cycling in fluorescence-detected 2D spectroscopy can be used to separate different nonlinear signals from each other. Let us consider a three-pulse excitation sequence. The total phase of the signal, $\varphi_{\text{tot.}}$, can be decomposed into

$$\varphi_{\text{tot.}} = \alpha\varphi_1 + \beta\varphi_2 + \gamma\varphi_3 \tag{6.2}$$

of the three pulses corresponding to the zeroth-order coefficient of a Taylor expansion of spectral phase. Note that interactions with $+\varphi_i$ as well as $-\varphi_i$ are possible since these are associated with the positive and negative frequencies that are both contained in the real-valued electric field. The set of the three coefficients α, β, and γ, each of which can be positive or negative, corresponds to the interaction pattern with pulses 1 to 3. Their absolute values describe the number of excitation- and de-excitation-quanta imprinted by each pulse on the density matrix. Each coefficient can generally be described by the number of interactions with $+\varphi_i$ minus the number of interactions with $-\varphi_i$ that occur with the corresponding pulse i. An interaction with $+\varphi_i$ corresponds to an excitation of the ket side or a de-excitation of the bra side, while an interaction with $-\varphi_i$ corresponds to an excitation of the bra side or a de-excitation of the ket side of the density matrix. Since we are observing fluorescence, the final state after the interaction with the last pulse has to be a population in an excited state, i.e., a diagonal element of the density matrix. A population can only be generated by the last pulse when the condition

$$\alpha + \beta + \gamma = 0. \tag{6.3}$$

is fulfilled [26]. The highest considered nonlinearity, R, limits the absolute number of total interactions

$$|\alpha| + |\beta| + |\gamma| \leq R. \tag{6.4}$$

Note that in Eq. (6.4) the absolute values of the coefficients are taken since the coefficients can also be negative. However, for the observed nonlinearity only the number of interactions is important and not if the interaction takes place with $-\varphi_i$ or $+\varphi_i$. From Eqs. (6.3) and (6.4) it follows that the coefficients are not independent of each other. We can hence reference the phases to the phase of the first pulse resulting in $\varphi_{21} = \varphi_2 - \varphi_1$ and $\varphi_{31} = \varphi_3 - \varphi_1$.

The raw data, $p(\tau, t, \varphi_{21}, \varphi_{31})$, depends on the time delay τ between pulses 1 and 2, the delay t between pulses 2 and 3, and the relative phases of the pulses, φ_{21} and φ_{31}. After discrete 2D Fourier transformation of $p(\tau, t, \varphi_{21}, \varphi_{31})$ with respect to the relative phases φ_{21} and φ_{31}, the different nonlinear signal contributions $\tilde{p}$ can be expressed via [26]

$$\tilde{p}(\tau, t, \beta, \gamma) = \frac{1}{LM} \sum_{l=0}^{L-1} \sum_{m=0}^{M-1} p(\tau, t, l\Delta\varphi_{21}, m\Delta\varphi_{31}) e^{-i\beta l \Delta\varphi_{21}} e^{-i\gamma m \Delta\varphi_{31}} \qquad (6.5)$$

with the total number of phase-cycling steps L in φ_{21} space and M in φ_{31} space and the phase increments $\Delta\varphi_{21} = \frac{2\pi}{L}$ and $\Delta\varphi_{31} = \frac{2\pi}{M}$. Note that the nonlinear signal contributions do not depend on α because we used relative phases. We can label a phase-cycling scheme by the number of experimental steps L and M as a "$1 \times L \times M$" phase-cycling scheme where the first number reflects the fact that the relative phases are referenced to pulse 1. Each signal contribution is characterized by its interaction pattern which is reflected by the specific values of the coefficients β and γ. The different nonlinear signal contributions can thus be retrieved from one set of raw data with Eq. (6.5) by inserting signal-specific values for β and γ.

Phase-cycling schemes must have an appropriate number of steps to i) separate specific multi-quantum signals from each other and ii) separate desired nonlinear signal contributions from undesired higher-order contributions, i.e., fourth-order signals from higher-order contributions. To illustrate this, let us discuss a three-pulse sequence with the goal to separate a fourth-order multi-quantum signal from another sixth-order multi-quantum signal. In order to visualize the ability of a particular phase-cycling scheme to separate different signal contributions, we can sketch the φ_{21} and φ_{31} spaces in polar coordinates as in Fig. 6.3.[1] The number of phase-cycling steps L and M divides the unit circle into equally sized sections. We can then plot the signal-specific phase vectors of $e^{-i\beta\Delta\varphi_{21}}$ and $e^{-i\gamma\Delta\varphi_{31}}$ in φ_{21} and φ_{31} space, respectively. In Fig. 6.3 we depict the values of β and γ right next to the corresponding vectors. Exemplarily, we show the vectors for the complex conjugate of the fourth-order 1Q1Q* signal (where the asterisk denotes complex conjugation), which corresponds to the correlation of 1Q coherences during τ and t, and for the 1Q3Q signal, which corresponds to a sixth-order signal with a 1Q coherence during τ and a three-quantum (3Q) coherence during t. To distinguish the two signals via phase cycling, the vectors have to differ either in φ_{21} space or in φ_{31} space (or in both). For a $1 \times 4 \times 4$ phase-cycling scheme (Fig. 6.3, left), we can see that the vectors for $\beta = -2$ and $\beta = +2$ in φ_{21} space and for $\gamma = +1$ and $\gamma = -3$ in φ_{31} space point in the same direction. The $1 \times 4 \times 4$ phase-cycling is thus not sufficient to distinguish the 1Q1Q* signal from the 1Q3Q signal since the red vectors point in the same direction as the corresponding blue vectors. Hence, the two multi-quantum signals are mixed and we say that these signals are "aliased". In the particular example, this means that the extraction of the 1Q1Q* signal by Eq. (6.5) also yields contributions from the 1Q3Q signal, since the set of coefficients β and γ is ambiguous. For a higher phase-cycling scheme, i.e., smaller phase increment steps such as in a $1 \times 6 \times 6$ scheme, the vectors point in different directions (Fig. 6.3, right), resolving the coefficient ambiguity. Therefore, a $1 \times 6 \times 6$ phase-cycling

---

[1]A more detailed discussion on the extraction of multi-quantum signals using phase cycling can be found in Ref. [231].

scheme can distinguish between the 1Q1Q* signal and the 1Q3Q signal without aliasing [45]. Note that a $1 \times 5 \times 5$ phase-cycling scheme would be sufficient to distinguish between these two displayed exemplary contributions but would not be sufficient to discriminate between all other multi-quantum signals, for which it is mandatory to choose the higher number of phase-cycling steps. The occurrence of a multi-quantum signal that is predominantly of sixth order results in a contamination of the multi-quantum signals that are predominantly of fourth order, by sixth-order contributions. Note that eighth-, tenth- or even higher-order signals can additionally contribute, and the intensity regime needs be chosen appropriately to keep the contaminations small.

So far, our discussion was covering three-pulse experiments with two time delays, τ and t, and two inter-pulse phase coefficients, β and γ. The demonstrated concepts can be easily extended to four-pulse sequences with three time delays: τ (between pulses 1 and 2), T (between pulses 2 and 3), and t (between pulses 3 and 4), introducing the coefficient γ corresponding to the phase increment $\Delta\varphi_{41}$. The additional delay T enables one to track population dynamics or to investigate the dynamics of coherences [27, 83]. Signatures of inter-excitonic coherences can be separated from those of population dynamics in frequency space, i.e., by additional Fourier transformation over the delay T. The three Fourier transformations over τ, t, and T result in three-dimensional (3D) spectra which correlate three coherences with each other, such as in the 2Q0Q1Q 3D spectrum [5]. The power of fluorescence-detected higher-order 2D spectroscopy is that with appropriate phase-cycling schemes, many 2D spectra can be extracted from the same data set [5, 114]. Each extracted 2D spectrum shows correlations between various coherences. The phase-cycling protocol can be directly extended to specific multi-quantum signals by choosing a higher-order phase-cycling scheme. Furthermore, instead of a four-pulse sequence, multi-pulse sequences with an increasing number of pulses (and thus higher dimensions) could be applied which would allow us to systematically investigate correlations between more than three coherences.
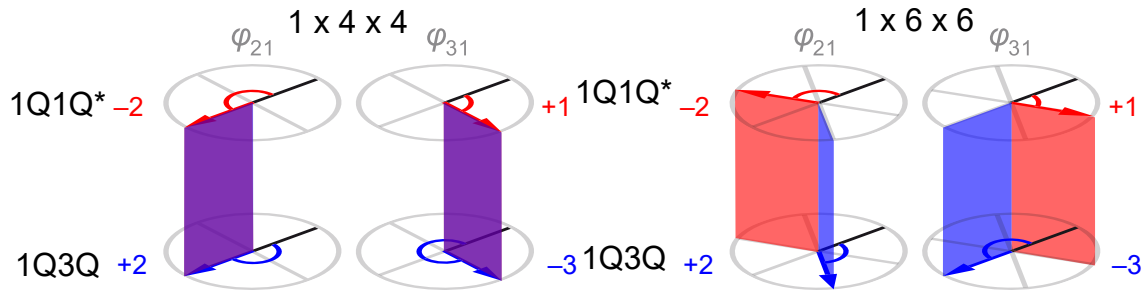
Figure 6.3.: Multidimensional spectroscopy using fluorescence detection combined with phase cycling. The isolation of two signal contributions via phase cycling is illustrated by plotting the signal-specific weighting factors as vectors in the φ_{21} space and the φ_{31} space. We show the vectors for the phase combinations of the 1Q1Q* signal and the 1Q3Q signal. For a $1 \times 4 \times 4$ phase-cycling scheme, the vectors corresponding to specific signals point in the same direction (i.e., the signals are aliased) while for a $1 \times 6 \times 6$ phase-cycling scheme, the vectors are separated.

We illustrate the capabilities of phase cycling on the example of quantum dots measured with a $1 \times 6 \times 6$ (36-fold) phase-cycling scheme in the experimental configuration of Fig. 6.2c [13]. For a 36-fold phase-cycling scheme, six predominantly sixth-order 2D spectra involving 3Q coherences, as well as two spectra containing 2Q coherences, and three spectra containing 1Q as well as 2Q coherences, which are dominated by fourth-order signals, can be isolated. In Fig. 6.4a, we show the absolute magnitude of the 1Q2Q spectrum (predominantly a fourth-order signal) of $CdSe_{1-x}S_x/ZnS$ alloyed core/shell quantum dots. The first three excitons were excited with a broadband pulse (Fig. 6.4a, top). The 1Q2Q spectrum correlates the transition from the ground state to the single-exciton manifold with the transitions from the ground state to the biexciton manifold. Due to the broadband excitation, six biexciton states were excited (Fig. 6.4a, right). Especially the biexciton states that are energetically higher than the lowest biexciton state cannot be directly probed with other methods such as time-resolved photoluminescence. With the help of simulations, the binding energies of all the six involved biexciton states as well as their transition dipole moments could be determined. The transition dipole moments are shown as vertical arrows in the energy scheme in Fig. 6.4a. While the 1Q2Q signal is dominantly of fourth order, the utilized phase-cycling scheme provided the opportunity to extract several other multi-quantum signals as higher-order contributions. One of these contributions is the 1Q3Q spectrum (Fig. 6.4b) which is dominated by sixth order. For the quantum dot sample, this spectrum provides information about the transition energy fluctuations. We find strong anticorrelation between the ground-state to single-exciton transition energy fluctuation with bandwidth $\delta_{(X, g)}$ and the single-exciton to biexciton transition energy fluctuation with bandwidth $\delta_{(BX, X)}$ as well as between the ground-state to single-exciton transition energy fluctuation and the biexciton to triexciton transi-

tion energy fluctuation with bandwidth $\delta_{(TX, BX)}$. In other words, the amplitude of the transition energy fluctuation of the single-exciton state determines whether the biexciton and triexciton states undergo stabilization, i.e., a shift to higher binding energies, or destabilization, i.e., a shift to lower binding energies.
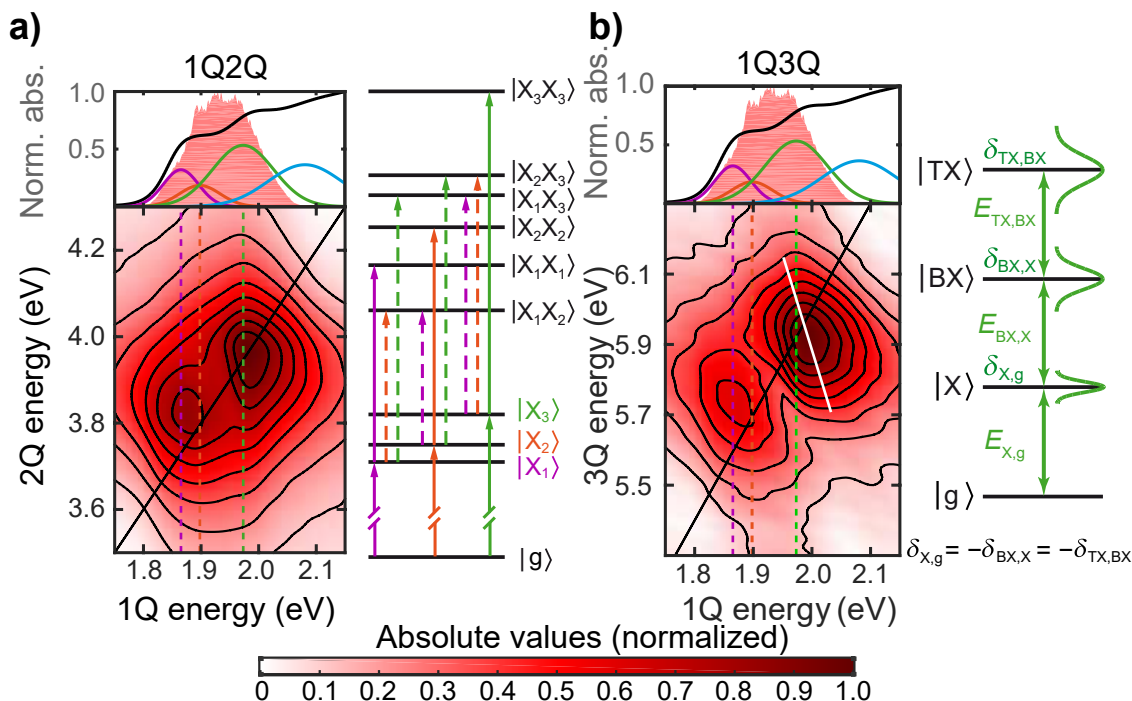
Figure 6.4.: Multidimensional spectroscopy using fluorescence detection applied to quantum dots. (a) 1Q2Q spectrum (absolute magnitude, normalized) of $CdSe_{1-x}S_x/ZnS$ quantum dots in toluene. The absorption spectrum (black line) as well as the pump spectrum (red shaded area), which predominantly excites the first three excitons, are shown on top of the 2D spectrum. The transitions of the three excitons obtained by fitting the absorption spectrum are shown as vertical dashed lines. In this experiment, six different biexciton states (shown as an energy scheme on the right side) with their specific transition dipole moments (marked as arrows) are probed. Dashed arrows correspond to transitions from single-exciton states to several biexciton states with a magnitude of 60 % of the corresponding transition from the ground state to the single-exciton state. Solid arrows connecting the single-exciton manifold with the biexction manifold correspond to transitions with the same magnitude as from the ground state to the corresponding single-exciton state. (b) 1Q3Q spectrum (absolute magnitude, normalized) of the same sample, extracted from the same experiment. The transition energy fluctuation between the ground state and the single-exciton manifold with the bandwidth $\delta_{(X, g)}$, between the single-exciton manifold and the biexciton manifold with the bandwidth $\delta_{(BX, X)}$, as well as between the biexciton manifold and the triexciton manifold with the bandwidth $\delta_{(TX, X)}$, are shown schematically on the right side. The correlation pattern between the transition energy fluctuations could be determined by analyzing the peak tilt (white line). Adapted with permission from reference [13]. Copyright © (2021) American Chemical Society.

We also used $1 \times 6 \times 6$ phase cycling in another study to investigate a laser dye
[45]. Through systematic comparison of the whole set of acquired multi-quantum 2D
spectra, we constructed a comprehensive picture of the manifold of multiple excited
states and determined properties such as the involved transition dipole moments, pure
dephasing times, and relaxation rates of the corresponding electronic states [45].

Moving from three-pulse to four-pulse sequences allows one to measure dynamics
over the additional delay T. We used a four-pulse sequence to investigate the electronic
structure of a dianion with interesting photophysical properties such as its high quan-
tum yield [5]. We combined shot-to-shot pulse shaping with a 1 kHz amplified laser
system. Shot-to-shot shaping and measurements allowed us to assign each shot from
the laser another shape, i.e., in this case another four-pulse sequence with distinct
phases and inter-pulse time delays that was different with respect to the sequence
from the previous shot. This measurement procedure allowed us to stream the full
$1 \times 5 \times 5 \times 5$ phase-cycling scheme with all time delays, i.e., a total of 421875 se-
quences, in just 8 minutes (without averaging). The employed higher phase-cycling
schemes isolated 15 different spectra, three dominantly of fourth order and twelve
dominantly of sixth order, allowing us to map the energetic landscape up to triply
excited states and decipher their energies and transition dipole moments. Such an
approach provides information that is challenging to obtain with other techniques [5].

6.4. Coherently Detected Higher-Order Spectroscopy in Pump–Probe Geometry

Coherently detected higher-order 2D spectroscopy in PP geometry (Fig. 6.1a) allows
one to isolate a 2Q1Q signal with a parametric dependence on the pump–probe delay.
We now discuss how this 2Q1Q signal can be used to study excitonic systems and
track exciton diffusion, on the example of squaraine polymers. The 2Q1Q signal is
dominated by two fifth-order signals with the phase-matching conditions of $-2\mathbf{k}_1 +
2\mathbf{k}_2 + \mathbf{k}_3$ and $+2\mathbf{k}_1 - 2\mathbf{k}_2 + \mathbf{k}_3$. In excitonic systems, the dynamics of the biexciton
population can be measured by tracking the 2Q1Q signal over the additional time
delay T between the two pump pulses and the probe pulse. What can we learn from
the biexciton dynamics? In extended systems, i.e., large excitonic systems consisting of
many coupled subunits (molecular aggregates, polymers, photosynthetic membranes
etc.), the spectral signature of excitons is not affected by propagation if their local
environment is the same everywhere on average. However, we can exploit additional
processes that occur when two excitons come close together spatially. This can lead to
the annihilation of one of the two excitons, i.e., EEA. In an extended system where the
two excitons are on average not close to each other directly after excitation, this means
that a phase of exciton transport has to occur before the annihilation takes place. The
coherently detected 2Q1Q signal in extended excitonic systems is dominated by EEA,
and thus the phase of exciton transport is reflected by a rise of the 2Q1Q signal
with time. Measuring how fast EEA occurs after excitation can therefore be used

to study the exciton migration in supramolecular systems [181]. In other words, the annihilation acts as a "probe" for exciton transport. Using EEA as a probe for exciton diffusion is well-known from intensity-dependent transient absorption studies where biexciton dynamics including EEA mixes into the single-exciton dynamics as outlined in the introduction [180, 182, 183]. However, if we obtain instead a 2Q1Q signal, we can measure the EEA dynamics directly without mixing of single- and biexciton contributions [232].
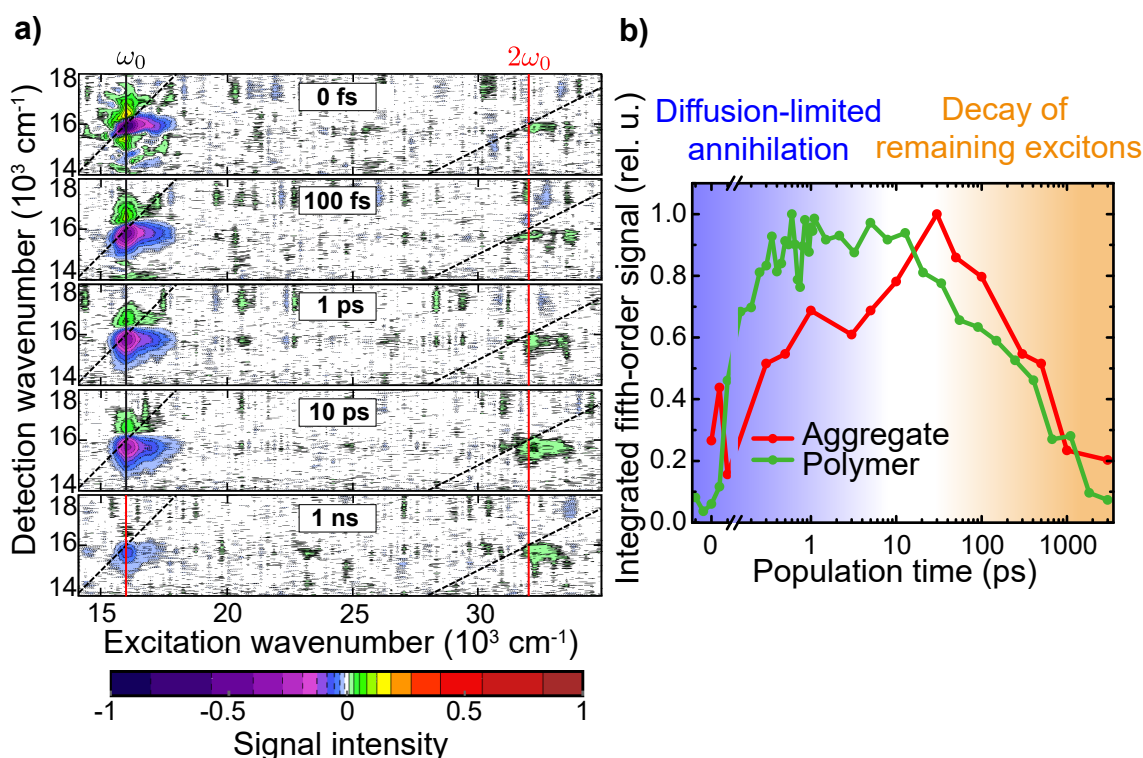
Figure 6.5.: Coherently detected 2Q1Q signals using 2D spectroscopy in PP geometry. (a) The 2D spectrum of a molecular J-aggregate of a core-substituted perylene bisimide dye (MEH-PBI) exhibits two distinct features: a predominantly negative signal at ω_0 and a positive signal at $2\omega_0$. (b) The population time evolution of the integrated 2Q1Q signal of extended systems is dominated by EEA. We show two examples of such systems: a supramolecular J-aggregate (red), obtained from the data in panel (a), and a squaraine polymer (green). The 2Q1Q signal shows a rise due to diffusion-limited annihilation (blue-shaded region) followed by a decay according to the exciton lifetime (orange-shaded region). Both transients are normalized to their individual maxima. Panel (a) and the trace of the aggregate in (b) are adapted with permission from reference [20].

As an example, we show in Fig. 6.5a the coherently detected 2D spectrum of a molecular J-aggregate, acquired in PP geometry [20]. The signal at around ω_0 on the excitation axis is dominated by a negative contribution (blue-violet) that decays

over the population time with the single-exciton lifetime. Note that in our convention, third-order ground-state bleach and stimulated emission are plotted as negative signals in accordance with the convention of transient absorption where ground-state bleach corresponds to reduced absorption. In contrast to the signal at ω_0, the 2Q1Q signal that is predominantly of fifth order at $2\omega_0$ on the excitation axis has a positive sign and rises with population time [23]. The two additional interactions of the electric field add a prefactor of $\left(\frac{i}{\hbar}\right)^2$ (from the perturbative expansion) to the fifth-order response function compared to third-order response, leading to a sign change of the signals [23].[2] The integrated 2Q1Q signal probes the biexciton dynamics which, in the case of extended systems, is dominated by EEA as shown in Fig. 6.5b (red curve). After excitation, the two excitons have to propagate and get close to each other in order to annihilate. The kinetics of the transport process is responsible for the slow rise of the 2Q1Q signal at early times (blue-shaded region). After reaching a plateau, the remaining excitons decay according to the exciton lifetime (Fig. 6.5b, orange-shaded region). In Fig. 6.5b we also show, for comparison, the integrated 2Q1Q signal of a squaraine copolymer made from 18 dimer units (green curve). This polymer, which is also an extended system made from repeating subunits, differs, however, in its electronic structure from the molecular J-aggregate because of the covalently bound subunits. While the decay of the 2Q1Q signal is similar in both systems because of their comparable exciton lifetimes, the rise of the 2Q1Q signal differs significantly reflecting the faster annihilation in the polymers compared to the J-aggregates. The diffusion coefficient as well as the exciton delocalization length can be obtained by modeling the fifth-order signal dynamics [7, 20].

Furthermore, the 2Q1Q signal can be used to study the "character" of exciton diffusion. We used the 2Q1Q signal to model exciton diffusion in a series of squaraine copolymers that differ in their average length [7]. The temporal evolution of the mean-square displacement, $\sigma^2(t)$, reflects the average exciton transport distance (squared) and can be described by

$$\sigma^2(t) = Dt^a \tag{6.6}$$

with the diffusion coefficient D. The coefficient a corresponds to the character of diffusion, i.e., for normal diffusion we have $a = 1$ and for anomalous diffusion $a \neq 1$ [233, 234]. Interestingly, we found that the often-applied assumption of normal diffusion [235, 236] does not hold in the investigated polymers and that diffusion can be better described by sub-diffusive behavior with $a = 0.4$ in the present exemplary case. The reason for such anomalous diffusion could be the energetically disordered structure of the polymers. We also used coherently detected 2Q1Q spectroscopy to investigate the exciton dynamics in double-walled tubular aggregates [4]. There, we measured the interplay between exciton transport and diffusion within each of the tubes.

Additional information about the geometrical and energetic disorder of a system can

---

[2]Compare Eq. (2.18) in Chapter 2.

be obtained by analysis of the anisotropy of the 2Q1Q signal [12]. Furthermore, analysis of the peak shape reveals information about the correlation of fluctuations between states [237] similar as already discussed in the case of fluorescence-detected higher-order spectroscopy in Fig. 6.4 [13]. While for extended systems such as polymers it was shown theoretically that the integrated 2Q1Q signal is dominated by the dynamics of the biexciton states, i.e., EEA, [7, 12] the situation is different in small systems such as dimers and trimers where the contribution of higher monomeric excited states is no longer negligible and also intra-manifold relaxation can contribute to the fifth-order signal [9, 238]. The examples provided above demonstrate that fifth-order 2D spectroscopy is well-suited to track exciton diffusion in extended systems. Compared to low-order techniques, EEA is measured directly without third-order signals contributing to the signal. The separate measurement of the biexciton dynamics including EEA simplifies the analysis. This is an advantage compared to previous studies utilizing variations of the excitation intensity where single- and biexciton dynamics are mixed together [180, 182, 183]. Higher-order spectroscopy can easily be carried out in PP geometry because the 2Q1Q signal, which is emitted in the same phase-matching direction as the 1Q1Q signal, is isolated by its position along the excitation frequency axis.

6.5. Comparison between Coherently Detected and Fluorescence-Detected Higher-Order Spectroscopy

Having provided examples for both fluorescence-detected and coherence-detected higher-order 2D spectroscopy, we now focus on their comparison. Like coherently detected 2Q1Q spectroscopy, the fluorescence-detected variant is also sensitive to EEA [9]. The analysis of nonlinear signals can be carried out by depicting the corresponding response pathways using double-sided Feynman diagrams [25]. We illustrate the correspondence of the two methods theoretically and experimentally in Fig. 6.6, comparing double-sided Feynman diagrams and measurements, respectively, for a molecular heterodimer. The heterodimer is made of a squaraine A and a squaraine B monomer that are linked by a phenyl group and can thus be described as three-level systems each that are coupled to each other (Fig. 6.6a). The dimer is closely related to the squaraine polymer that we investigated above (Fig 6.5b). In the polymer, the squaraine A and squaraine B monomers are connected directly without any additional spacer between the monomers leading to a stronger coupling between the monomers. compared to the case of a dimer with a spacer [7, 8]. The eigenstates of the dimer consist of two higher excited states ($|f_{A,B}\rangle$) that are predominantly localized either at monomer A or monomer B, one biexciton state ($|e_A e_B\rangle$), two single-exciton states ($|e_{A,B}\rangle$), and a ground state $|g\rangle$. The excited states can further be grouped into those of the singly excited manifold ($|1\rangle$) and those of the doubly excited manifold ($|2\rangle$), whereas the ground state is part of the $|0\rangle$ manifold. In general, many double-sided Feynman diagrams contribute to the 2Q1Q signal. If strict time ordering between

pump and probe pulses holds, i.e., if the interactions with the pump pulses occur before the interaction with the probe pulse, the coherently detected 2Q1Q signal can be described by 54 double-sided Feynman diagrams. If no strict order between the different interactions holds, the number of double-sided Feynman diagrams increases to 240. We used an automated Feynman-diagrams generator to calculate the number of diagrams for contributions of higher orders to various multi-quantum signals and used this knowledge to obtain clean nonlinear signals as described below [18]. However, the number of diagrams decreases drastically in the case of a molecular dimer that is considered here because some diagrams will either cancel in pairs due to their opposite sign or they involve triexciton states which are not present in a dimer. Therefore, only four double-sided Feynman diagrams contribute to the 2Q1Q signal of a molecular dimer. The four diagrams can be further separated into rephasing and non-rephasing depending on the coherences during τ and t. We show the rephasing diagrams of the coherently detected 2Q1Q signal in Fig. 6.6b. In the experiment (Fig. 6.1b), the combination of rephasing and non-rephasing signal contributions, i.e., the absorptive signal, is measured directly. Since we consider population dynamics only, for which the rephasing and the non-rephasing signal contributions only differ in the specific order of the excitation pulses, we can restrict our analysis to the double-sided Feynman diagrams of the rephasing part without loss of generality. In the double-sided Feynman diagrams, time flows from bottom to top and interactions with the density matrix are marked by solid arrows. In the diagram $+R_{11}$ we find a ground-state population and in $-R_{22}$ a biexciton population during the delay T. The dynamics during the population time can be described by propagators. For $T = 0$, both diagrams compensate each other, and the signal is zero. For time delays $T > 0$, the compensation is not perfect anymore because the biexciton population of $-R_{22}$ decreases with the annihilation rate which effectively reduces the amplitude of this pathway. For the integrated 2Q1Q signal, we thus expect, as demonstrated in Fig. 6.5b, a rise of the signal on the time scale of the annihilation time that we obtain from a fit (Fig. 6.6d). Now let us compare the behavior with a fluorescence-detected 2D experiment (Fig. 6.2c). To obtain the predominantly sixth-order multi-quantum signals, we used a four-pulse sequence with a 125-fold ($1 \times 5 \times 5 \times 5$) phase-cycling scheme with which we extracted the rephasing 2Q1Q and 1Q2Q signals. Their signal pathways are shown in Fig. 6.6c. In fluorescence-detected 2D spectroscopy, the annihilation time cannot directly be measured by integrating the 2Q1Q signal because the signal also contains single-exciton dynamics during the time delay T, indicated by pathway $+2Q_{11}^{2Q1Q}$ in Fig. 6.6c. As the phase-cycling scheme provides several nonlinear signals simultaneously, we can make use of them to isolate the annihilation dynamics nevertheless. Upon close inspection of the diagrams that correspond to the rephasing 1Q2Q signal, we can see that, under the approximations used, the dynamics during T are the same as in the rephasing 2Q1Q signal except that the diagram that contains annihilation dynamics is absent in the rephasing 1Q2Q signal. Since the rephasing 2Q1Q signal and the rephasing 1Q2Q signal are extracted from the same data set, i.e., exactly under the same experimental conditions, they can be subtracted from each other to eliminate the single-exciton dy-

namics from the rephasing 2Q1Q signal thus leaving only the annihilation dynamics [9]. The subtraction of the signals, however, is not straightforward because the rephasing 1Q2Q signal and the rephasing 2Q1Q signal feature different coherences during τ and t. In the 1Q2Q diagrams, a 1Q coherence is present during τ while the system evolves in a 2Q coherence during t. In the 2Q1Q diagrams, the roles of τ and t are interchanged, and we can find a 2Q coherence during τ and a 1Q coherence during t. In order to use the 1Q2Q signal for the subtraction, the 1Q2Q spectrum has to be transformed into a "2Q1Q-like" spectrum. This can be most easily understood by transforming the 1Q2Q pathways into the 2Q1Q pathways by flipping the direction of time in the 1Q2Q pathways including the phase signatures. In frequency domain, this operation on the diagrams corresponds to a flipping of the rephasing 1Q2Q spectrum along the diagonal and complex conjugation of the whole rephasing 1Q2Q spectrum (i.e., a Hermitian conjugation). The thus-transformed 1Q2Q spectrum can then be subtracted from the rephasing 2Q1Q spectrum to eliminate the single-exciton dynamics [9]. This subtraction works only if the propagators can be factorized between the respective time intervals, which is the case if no substantial bath reorganization takes place and the vibrational bath has no memory between the intervals. After subtraction of the processed rephasing 1Q2Q spectrum from the rephasing 2Q1Q spectrum, the so-obtained "2Q1Q" 2D spectrum is integrated along the excitation axis and along the detection axis. The absolute value of the resulting transient is shown in Fig. 6.6e. The fitted annihilation time of 24 fs agrees well with the annihilation time of 28 fs obtained with the coherently detected method (Fig. 6.6d) and thus demonstrates that both methods can be used to measure EEA. Fluorescence-detected spectroscopic methods are background-free which allows to measure without a strong coherent artifact. This is especially suitable for fast dynamics close to $T = 0$. Furthermore, the outlined concept to isolate specific effects such as EEA by using several multi-quantum signals can also be applied in other action-detected techniques.
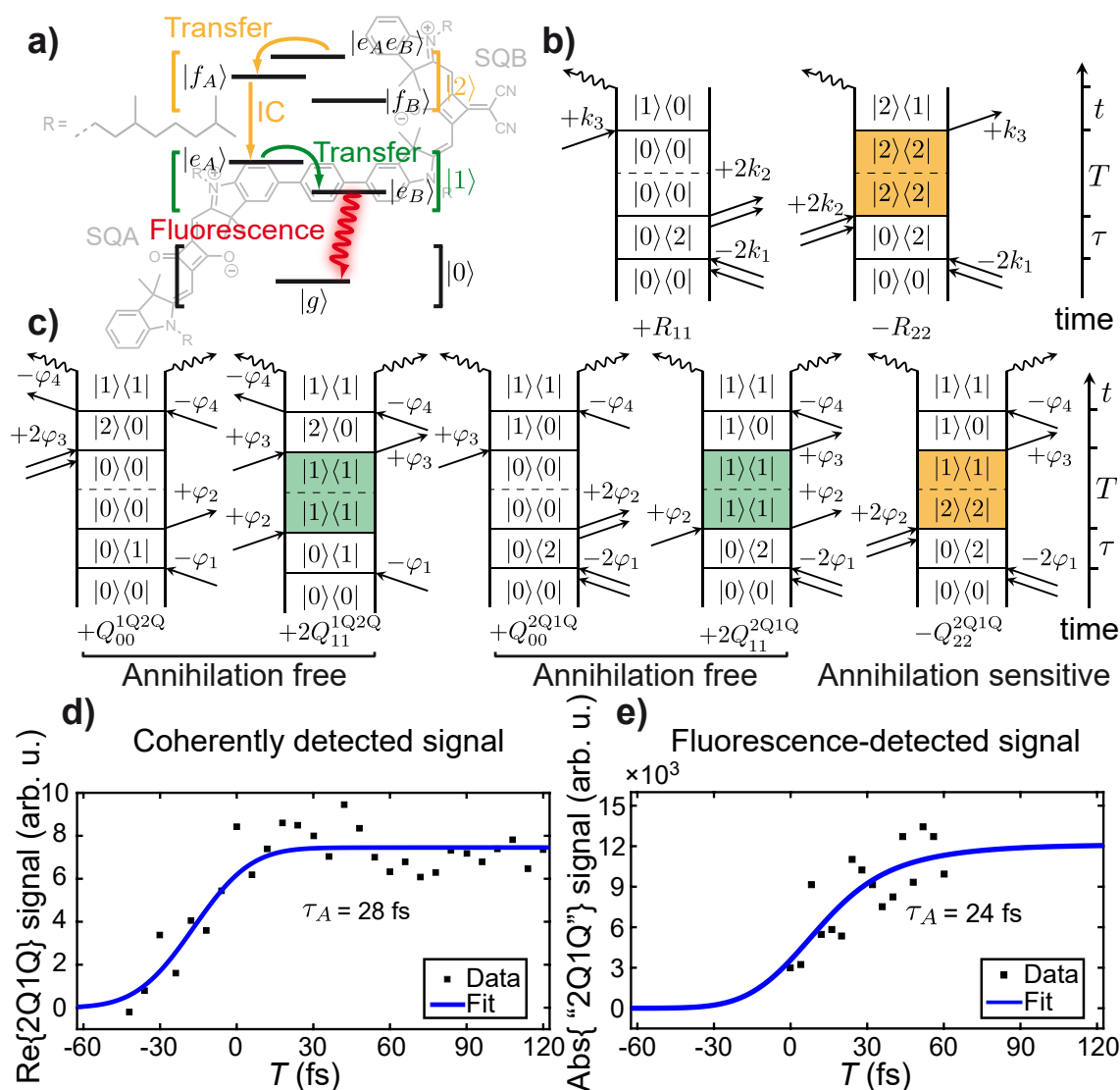
Figure 6.6.: Comparison of the annihilation in a molecular dimer measured with coherently detected and fluorescence-detected higher-order spectroscopy. (a) The excitonic structure of the dimer consists of one ground state $|g\rangle$, two single-exciton states $|e_{A,B}\rangle$, one biexciton state $|e_A e_B\rangle$, and two higher-excited states $|f_{A,B}\rangle$ that are predominantly localized at one of the monomers. Annihilation (orange) is depicted as a two-step process consisting of transfer within the doubly excited manifold $|2\rangle$ followed by internal conversion (IC) to the single-exciton manifold $|1\rangle$. Fluorescence occurs from the single-exciton state $|e_B\rangle$ to the ground state $|g\rangle$. (b) Rephasing double-sided Feynman diagrams contributing to the coherently detected 2Q1Q signal. (c) Rephasing double-sided Feynman diagrams contributing to fluorescence-detected 2Q1Q and 1Q2Q signals. The 1Q2Q signal involves ground-state and single-exciton dynamics during T (green). On the other hand, the 2Q1Q diagrams also include the process of annihilation (orange). (d) The fit of the coherently detected 2Q1Q signal (obtained by taking the real part and integrating along the excitation and detection axis) results in an annihilation time of 28 fs. (e) The fit of a "2Q1Q" signal (obtained by subtraction of the two fluorescence-detected signal contributions, integration along the detection and frequency axis, and taking the absolute of the signal) reveals an annihilation time of 24 fs. Adapted from reference [9], with the permission of AIP Publishing.

6.6. Higher-Order Pump–Probe Spectroscopy

So far, we discussed multidimensional methods to probe multi-quantum signals. The technique of PP (transient absorption) spectroscopy is closely related to multidimensional spectroscopy as outlined in the introduction. Using the close relation between the two techniques, we developed a technique to *isolate* nonlinear signals of a particular order in a PP experiment. In contrast to the previously discussed multi-quantum signals, which have been dominated by a particular nonlinear order (but are contaminated with higher orders in general), we will show in the following that we can obtain multi-quantum signals representing "clean" nonlinear orders, i.e., free of contamination by higher nonlinear orders, using the PP approach.

In coherently detected 2D experiments in PP geometry, the dynamics of EEA are measured by integrating the 2Q1Q signal at twice the excitation frequency $2\omega_0$ in the 2D spectrum. In PP geometry, the 2Q1Q signal with phase-matching condition $\pm 2\mathbf{k}_1 \mp 2\mathbf{k}_2 + \mathbf{k}_3$ is emitted in the same direction as the probe pulse itself (because $\mathbf{k}_1 = \mathbf{k}_2$) but it occurs at $2\omega_0$ along the excitation frequency axis in the 2D spectrum. In the further data processing leading to EEA kinetics of Fig. 6.5b or 6.6d, the 2Q1Q is integrated over frequency, i.e., information such as the lineshapes along the excitation and detection axes are not evaluated. The excitation axis of the 2D spectrum is only needed to separate the different multi-quantum contributions that are emitted in the same spatial direction. Integrating a 2D spectrum over all excitation frequencies corresponds to simply measuring at $\tau = 0$, i.e., a PP signal. For integration over the whole excitation frequency axis, the result would be the normal PP spectrum according to the projection-slice theorem [23, 221], with all the multi-quantum signals added up, and the unique 2Q1Q signature would be lost. It is still possible to separate the multi-quantum signals, however, even when measuring a PP spectrum with $\tau = 0$. For this purpose, we take inspiration from phase cycling. While we had introduced phase cycling for action-based detection (Fig. 6.2a) as illustrated in the fluorescence-detected 2D experiments on quantum dots (Fig. 6.4), it is also possible to implement phase-cycling protocols for coherently detected 2D spectroscopy such as in PP geometry. Viewing the single pump pulse in PP spectroscopy as two pulses with zero time delay in 2D spectroscopy, phase cycling reduces to a mere variation of intensity because the two coincident pulses interfere constructively or destructively, depending on their relative phase. To illustrate this, consider the equation for a collinear double pulse with the delay τ in phase cycling,

$$E_{\text{pump}}(t) = E_0(t)e^{i(\omega_0 t - \mathbf{k}_{\text{pump}} \cdot \mathbf{r})} \left(\underbrace{1}_{\text{pulse 1}} + \underbrace{e^{i(\omega_0 \tau + \phi_s)}}_{\text{pulse 2}} \right) + \text{c.c.} \qquad (6.7)$$

where c.c. is the complex conjugate of the previous term, $E_0(t)$ is the complex envelope of the electric field (including chirp), ω_0 denotes the central frequency, $\mathbf{k}_{\text{pump}}$ is the common wavevector of both pulses, $\mathbf{r}$ is the position (which is integrated out when considering phase matching during propagation through the sample), and ϕ_s is the

relative phase between both pulses. Evaluated at $\tau = 0$ and inserting phase-cycling steps for ϕ_s, Eq. (6.7) leads to a mere intensity variation,

$$I_s = 4I_0 \cos^2 \left(\frac{(s-1)\pi}{2N} \right), \ s = 1, ..., N, \tag{6.8}$$

with the "base" intensity I_0 and N "intensity-cycling" steps with index s. The maximum intensity of $4I_0$ in an experiment is obtained by setting $s = 1$. For other values of s, the excitation intensity is effectively reduced. For example, for $N = 3$, intensities of $4I_0$, $3I_0$, and I_0 emerge from Eq. (6.8), telling us that we should acquire PP data at these excitation intensities. Applying intensity cycling to PP spectroscopy will then allow us to obtain multi-quantum signals without requiring 2D data. Here, we focus only on intensity variation of the excitation pulses while the probe pulse is considered weak. Therefore, each multi-quantum signal will have the form nQ1Q, and for shorthand notation we will drop the 1Q and simply define multi-quantum signals as nQ signals.

We start by measuring the PP signal for the N excitation intensities given by Eq. (6.8), as shown exemplarily in Fig. 6.7 (left). The different nQ signals, $PP^{(nQ)}$, are then isolated by suitable linear combinations of the raw data, adding the measurements $PP(I_s)$ at different excitation intensities I_s with different weights (Fig. 6.7, step from the left to the middle panel),

$$PP^{(nQ)} (I_0) = \sum_{s=1}^{N} w_s^{(nQ)} PP (I_s), \tag{6.9}$$

where the weights

$$w_s^{(nQ)} = \frac{1}{2N} \frac{2 - \delta_{s,1}}{1 + \delta_{n,N}} \cos \left(\frac{n(s-1)2\pi}{2N} \right), \ s = 1, ..., N. \tag{6.10}$$

are given by the phase-cycling rules [26] now adapted to the PP case [16, 18].

For weak excitation intensities, the 1Q signal $PP^{(1Q)}$ would be dominated by the third-order nonlinear signal. For higher excitation intensities, a fifth-order signal also contributes. The fifth-order signal is present at two positions: First, as a 2Q signal and second, as a fifth-order contribution to the 1Q signal. The latter can be viewed as a "contamination" of the third-order signal. If the excitation intensity is increased even further, seventh-order contributions can no longer be neglected and they will appear at the 3Q signal and as contaminations of the 2Q and 1Q signals.

The uncontrolled mixing of nonlinear orders is a general problem in femtosecond spectroscopy, independent of the type of measured system. At low excitation intensity, one can suppress contamination from higher-order signals but has to accept a correspondingly low SNR, whereas at high excitation intensity, one can achieve improved SNR but has to deal with contamination from higher orders. We offer a solution

to this long-standing problem [239, 240] by utilizing the multi-quantum signals $\mathrm{PP}^{(n\mathrm{Q})}$ to obtain the clean nonlinear order contributions, i.e., by separating the different parts of perturbative expansion. In order to extract clean nonlinear orders from PP experiments, we have to know quantitatively how much each particular nonlinear order contributes to each $n\mathrm{Q}$ signal. We here concentrate on the odd orders seen in coherent detection such as in PP spectroscopy. The coefficients for the "contaminations" by various nonlinear orders of an $n\mathrm{Q}$ signal can be found using two ways. We can either perform an analysis of the double-sided Feynman diagrams [9] or we can use the fact that different nonlinear orders scale differently with excitation intensity [16].[3] In general, the $(2n + 1)^{\mathrm{th}}$ nonlinear PP signal scales with the power of n in terms of excitation intensity, e.g., linear in intensity for a third-order signal. This is the reason why researchers trying to avoid contaminations from higher orders often state that their experiments were carried out in the "linear regime", despite the fact that a third-order response was measured. We will now show how to remove artifacts even when outside of this linear regime. This is possible using a matrix $[(\Lambda^{-1})^r_{n\mathrm{Q}}]$ that contains suitable correction factors connecting the clean nonlinear signals $\mathrm{PP}^{(2r+1)}$ with the experimentally extracted (contaminated) multi-quantum signals $\mathrm{PP}^{(n\mathrm{Q})}$ [16, 18],

$$
\begin{pmatrix}
\mathrm{PP}^{(3)} I_0 \\
\mathrm{PP}^{(5)} I_0^2 \\
\mathrm{PP}^{(7)} I_0^3 \\
\mathrm{PP}^{(9)} I_0^4 \\
\mathrm{PP}^{(11)} I_0^5 \\
\mathrm{PP}^{(13)} I_0^6 \\
\vdots
\end{pmatrix}
=
\begin{pmatrix}
1 & -4 & 9 & -16 & 25 & -36 & \dots \\
0 & 1 & -6 & 20 & -50 & 105 & \dots \\
0 & 0 & 1 & -8 & 35 & -112 & \dots \\
0 & 0 & 0 & 1 & -10 & 54 & \dots \\
0 & 0 & 0 & 0 & 1 & -12 & \dots \\
0 & 0 & 0 & 0 & 0 & 1 & \dots \\
\vdots & \vdots & \vdots & \vdots & \vdots & \vdots & \ddots
\end{pmatrix}
\begin{pmatrix}
\mathrm{PP}^{(1\mathrm{Q})}(I_0) \\
\mathrm{PP}^{(2\mathrm{Q})}(I_0) \\
\mathrm{PP}^{(3\mathrm{Q})}(I_0) \\
\mathrm{PP}^{(4\mathrm{Q})}(I_0) \\
\mathrm{PP}^{(5\mathrm{Q})}(I_0) \\
\mathrm{PP}^{(6\mathrm{Q})}(I_0) \\
\vdots
\end{pmatrix}.
\tag{6.11}
$$

This procedure is exemplified in Fig. 6.7 (step from the middle to the right panel). We can also formally combine all steps, starting with the measurements at N excitation intensities, separation of the multi-quantum signals, and finally obtaining clean nonlinear signals, into one equation,

$$
\mathrm{PP}^{(2r+1)} I_0^r = \sum_{n=r}^{N} \left[\sum_{a=0}^{N-1} (-1)^a M^a \right]_{(r,n)} \sum_{s=1}^{N} \frac{1}{2N} \frac{2 - \delta_{s,1}}{1 + \delta_{n,N}} \cos\left(\frac{n(s-1)2\pi}{2N} \right)
$$
$$
\times \mathrm{PP}\left(\cos^2\left(\frac{s-1}{2N}\pi \right) \right),
\tag{6.12}
$$

where the inverse matrix $(\Lambda^{-1})^r_{n\mathrm{Q}}$ from Eq. (6.11) is expressed using the matrix M defined

$$
M_{(i,j)=1,\dots,N} = \begin{cases} \binom{2j}{j-i}, & j > i \\ 0, & j \leq i, \end{cases}
\tag{6.13}
$$

---

[3]Both approaches are discussed in Chapter 8.

with i as the index of the rows and j as the index of the columns. The matrix element M_{ij} quantifies the contribution of jth order response to the iQ signal, without the diagonal unity elements: $M = \Lambda - \mathbb{1}$ where $\mathbb{1}$ is the unity matrix. The full term in the square brackets in Eq. (6.12) leads to the matrix of Eq. (6.11) allowing to obtain clean nonlinear signals from the nQ signals. While Eq. (6.12) may look complicated at first sight, it is actually straightforward to implement and does not require any specialized software, nor is the data acquisition complicated, making the procedure easy to carry out in any ultrafast spectroscopy laboratory.
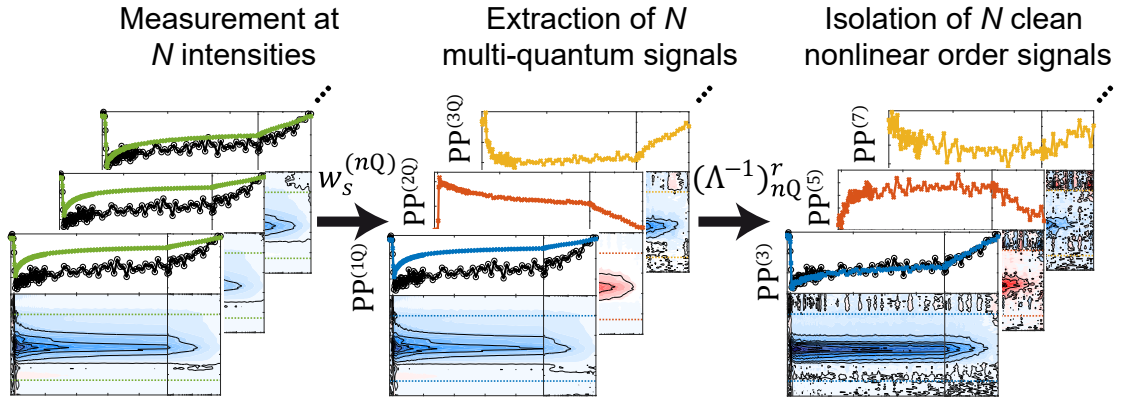
Figure 6.7.: Higher-order PP spectroscopy. A set of N PP spectra is measured in which the excitation intensity is systematically varied (left). These intensity-dependent measurements are then weighted by $w_s^{(n\text{Q})}$ to extract N multi-quantum signals (middle). Correction of the contaminations from various higher nonlinear orders using the matrix $(\Lambda^{-1})_{n\text{Q}}^r$ leads to N clean nonlinear-order signals (right). The so-obtained third-order signal (blue curve on the right panel) agrees with the low-power measurement used as a reference (black curve) demonstrating that the obtained third-order signal is free of higher-order contributions.

After the general explanation, we now demonstrate the procedure of higher-order PP spectroscopy on the example of $N = 3$. Using the three different intensities of $4I_0$, $3I_0$, and I_0, the third-, fifth-, and seventh-order signals can be isolated. We select I_0 such that no signal higher than seventh order contributes significantly (which can be checked experimentally by comparing the dynamics as well as the signal strength of the extracted third-order signal to a reference measurement at low excitation intensities). Otherwise, the intensity-cycling protocol with $N = 3$ would not be sufficient, and ninth and higher orders would contribute (which can be accounted for with more intensity-cycling steps). In a first step of evaluation, we extract the 1Q signal, following Eq. (6.9) and (6.10) and setting $n = 1$, as a linear combination from the measured PP data at the three excitations intensities,

$$\text{PP}^{(1\text{Q})} = \frac{1}{6} \left[\text{PP} \left(4I_0 \right) + \text{PP} \left(3I_0 \right) - \text{PP} \left(I_0 \right) \right]. \tag{6.14}$$

Similarly, we can obtain the 2Q and 3Q contributions by applying suitable intensity-cycling coefficients,

$$\text{PP}^{(2Q)} = \frac{1}{6} \left[\text{PP} \left(4I_0 \right) - \text{PP} \left(3I_0 \right) - \text{PP} \left(I_0 \right) \right], \tag{6.15}$$

$$\text{PP}^{(3Q)} = \frac{1}{12} \left[\text{PP} \left(4I_0 \right) - 2\text{PP} \left(3I_0 \right) + 2\text{PP} \left(I_0 \right) \right]. \tag{6.16}$$

In the case of very weak excitation, i.e., if $\text{PP}^{(1Q)}$ scaled linearly with the excitation intensity in the region from I_0 to $4I_0$, no higher-order signal would be present. In that case, only $\text{PP}^{(3)}$ would contribute to $\text{PP}^{(1Q)}$, i.e., the $\text{PP}^{(1Q)}$ signal would be contamination-free, and $\text{PP}^{(2Q)} \approx \text{PP}^{(3Q)} \approx 0$. In the case of contamination, we can correct for the higher-order contributions using Eq. (6.11). For example, fifth- and seventh-order contaminations can be corrected using the 2Q and 3Q signals by calculating

$$\text{PP}^{(3)} I_0 = \text{PP}^{(1Q)} \left(I_0 \right) - 4\text{PP}^{(2Q)} \left(I_0 \right) + 9\text{PP}^{(3Q)} \left(I_0 \right). \tag{6.17}$$

Analogously, the contamination of seventh order at the 2Q position may be corrected. Our method of higher-order PP spectroscopy thus offers a simple solution of correcting for contaminations by higher-order signals. If one is only interested in the clean third-order signal, the steps of isolation and correction for contamination can also be directly combined, i.e., essentially using Eq. (6.12), which for the present exemplary case of third order and $N = 3$ intensity-cycling steps reads

$$\text{PP}^{(3)} I_0 = \frac{1}{4} \text{PP} \left(4I_0 \right) - \frac{2}{3} \text{PP} \left(3I_0 \right) + 2\text{PP} \left(I_0 \right) \tag{6.18}$$

This provides a remarkably simple solution to the annihilation problem of ultrafast spectroscopy: Using Eq. (6.12) [or Eq. (6.18) for a useful special case], one instead employs a combination of excitation intensities to avoid the compromise, quantify the influence of higher orders, correct for them, and obtain clean third-order signals at high SNR. At the same time, one obtains "for free" the fifth- and seventh-order signals that provide additional information such as the dynamics of EEA in the system.

Contamination by higher-order signals occurs not only in PP but also in 2D spectroscopy. For example, the 1Q signal acquired in coherently detected 2D spectroscopy in PP geometry corresponds, at low excitation intensities, predominantly to a third-order signal.[4] For higher excitation intensities, the 2Q signal dominated by fifth-order contributions can be isolated at $2\omega_0$, but at the same time the 1Q signal will be contaminated with fifth-order contributions. For even higher excitation intensities, the 2Q signal will be contaminated by seventh-order contributions and the 1Q signal with

---

[4]We use again the shorthand notation for the multi-quantum signals as introduced above since we consider the probe to be weak.

fifth- and seventh-order contributions, and a 3Q signal appears at $3\omega_0$. In the same way as in PP spectroscopy, the integrated 2D signals obtained from different positions along the excitation axis, i.e., the nQ signals, can be used to correct the lower-quantum signals and isolate clean nonlinear orders [18]. This is further discussed in Chapter 8

Let us conclude our discussion with some remarks on what higher-order signals can actually tell us. In the appropriate intensity regime, it is possible to obtain multi-quantum signals beyond 3Q. Will they still provide useful, additional information? For example, we performed higher-order PP spectroscopy on a squaraine polymer with measurements at six different intensities to isolate signals up to 13$^{\text{th}}$ order in perturbation theory. In such polymers, the higher-order signals contain information about multi-exciton interaction. In our example, we were able to determine the annihilation times for each specific number of simultaneously excited excitons by fitting the transients of the increasing orders of nonlinear signals, and thus we obtained annihilation times for the biexciton, triexciton, quadexciton, etc., from which we could in turn determine the probability of annihilation when two excitons meet. We found for the squaraine polymers that the annihilation rate increases with the number of simultaneous excitations, which makes intuitive sense because there are more possibilities for interactions when there are more excitons present, and thus such interactions will occur faster. However, we can go further than that and obtain quantitative information from the higher orders. In a simplified picture, the third-order signal reports on the decay of single excitons, the fifth-order signal characterizes the diffusion of single excitons through the system, and the seventh and higher orders inform us about what happens when the propagated excitons meet. In our example, we could deduce that in squaraine polymers, the excitons only annihilate with a chance of less than 10 % if they are co-localized. The conclusion of this result is that in the one-dimensional polymer chain, each exciton can in principle interact with all the other excitons that are present in the polymer, even if other excitons are "in between" [16]. Our procedure of extracting clean nonlinear signals is general and can be extended to signals higher than 13$^{\text{th}}$ order simply by increasing the number of measured intensities beyond $N = 6$.

Note that the unique assignment of specific numbers of excited quasiparticles to particular nonlinear orders is a feature of our newly reported method. Ordinarily, the experimenter has no control over the number of excitations in a system following irradiation with a short laser pulse. Instead, illumination generally leads to a Poissonian distribution of the number of excitations (over the ensemble), and only the average number scales with excitation intensity. Thus, for example, one can create the situation, at low intensities, that it is most probable that there will only be one excitation (while not totally avoiding two or more); this is the situation for the usual "low-power" measurements desired in third-order spectroscopy. Then, for higher excitation, one might aim for two simultaneous excitations in the system, in order to study EEA, but one cannot avoid the presence of even more excitations. This leads to the problems of higher-order contamination. In our scheme, we still do not "control" the numbers of excitations precisely; the order-correction analysis allows us, however, to extract such

signals as if we did, i.e., as if we had created precisely only either two, three, or four, etc., excitations. Thus, for example, the seventh-order signal corresponds to the case as if one had exactly three excitons in the system.

6.7. Conclusion

In summary, we demonstrated how fluorescence-detected and coherently detected higher-order multidimensional spectroscopy can be used to investigate phenomena inaccessible by lower-order spectroscopy. We provided examples on exciton–exciton annihilation (EEA) and highly excited states in quantum dots, but the application potential of the method goes much further because the analysis of higher orders does not depend on any particular model, which is a main strength of the present approach. Intensity-dependent and higher-order measurements have a long tradition in ultrafast spectroscopy, with many successful examples and sophisticated analysis. The new direction treated in this chapter, however, is that nonlinear order extraction can be performed without requiring a-priori models because the method is general.

Coherently detected and fluorescence-detected techniques both have their individual advantages and features, from a technical as well as a fundamental point of view, and thus it depends on the system and the scientific question which one is better suited. In fluorescence-detected multidimensional spectroscopy, the signal is obtained by phase cycling (or phase modulation) which provides systematic access to a variety of different signals from a single data set, i.e., under the same experimental conditions. The various nonlinear signals can be used to characterize the dynamics and electronic properties of highly excited states. In coherently detected higher-order spectroscopy, we showed how to separate higher-order signals along the excitation axis in the two-dimensional (2D) spectrum by appropriate fine scanning of excitation time delays. Other implementations are possible as well, though, and one can alternatively use phase matching or phase cycling to separate multi-quantum signals. The fifth-order signal at $2\omega_0$ is specifically useful to study long-range exciton transport in extended systems such as polymers, molecular aggregates, light-harvesting systems, 2D materials, photovoltaic devices, and more. Both coherently detected as well as fluorescence-detected higher-order 2D spectroscopy can be used to study EEA as we have shown in the case of a molecular dimer.

An exciting new prospect is the extraction of higher orders directly from pump–probe (PP) signals without having to resort to 2D techniques. This can be done by exploiting the specific excitation intensity dependence in a process that we called "intensity cycling" because it is derived from phase cycling for the case of a coincident pump pulse pair. Higher-order PP spectroscopy allows one to obtain clean orders of nonlinearity in transient absorption setups by simply changing the excitation intensity without the need of scanning an additional time delay. This solves the "annihilation problem" that has been plaguing ultrafast spectroscopy for decades, and thus helps avoid errors in the assignment of time constants and the interpretations of kinetics for cases in which the excitation power cannot be chosen low enough. Intensity cycling can

be realized easily in any laboratory using a pair of rotatable polarizers or one polarizer and a half-wave plate. Since the data acquisition time of higher-order PP spectroscopy is drastically reduced compared to multidimensional spectroscopy, higher-order signals will be obtained with high SNR. This technique allows one to measure annihilation-free transient absorption spectra under high excitation intensities, i.e., with a high SNR.

Apart from this, one obtains the higher orders "for free" along with the same data set. This provides a simple method to quantify exciton diffusion as we demonstrated in the case of squaraine polymers: Measurement at multiples of one, three and four times of a base excitation intensity, followed by suitable linear combination as described above, delivers the third-order signal (cleaned for fifth-order and seventh-order contamination) that reports on single-exciton kinetics, the fifth-order signal (cleaned for seventh-order contamination) that reports on single-exciton diffusion, and the seventh-order signal that reports on the interaction probability when two excitons meet. While so far we discussed mostly excitonic systems, our methods are not limited to excitons in molecular systems and can be applied to study other quasiparticles such as polaritons [241], phonons [242], or excitons in confined systems such as quantum dots [243]. One can use higher-order PP spectroscopy to observe multi-particle processes and characterize their individual time scales, interaction energies, and the involved states. It was theoretically proposed to study a quantum system by systematically increasing the nonlinear order of excitation, i.e., by measuring increasing orders of the perturbative expansion [244]. Our developed techniques of higher-order PP and 2D spectroscopy can be viewed as the experimental realization of this theoretical concept allowing us to systematically excite higher and higher states of a quantum system.

Before we discuss additional prospects for higher-order spectroscopic experiments, we want to address the general connection between higher-order nonlinear signals and spectral dimensionality. Since we have successfully analyzed higher-order signals in one and two spectral dimensions, we may ask: Do we additionally need higher spectral dimensionality to fully interpret higher-order signals? In the standard implementation of third-order 2D spectroscopy, each laser pulse interacts once with the system (and analogously for fourth-order fluorescence-detected 2D spectroscopy with four pulses). With pulses shorter than the electronic (and vibrational) dynamics, nowadays routinely available, the nonlinear spectroscopy experiments take place in a mostly "impulsive" limit, i.e., the pulses act as "physical" delta functions and the nonlinear response of the sample is directly probed in time domain. The light–matter interactions are ordered in time and the language of response pathways, depicted by double-sided Feynman diagrams, is typically used. In four-wave-mixing 2D spectroscopy, the experimenter thus has full control over all time delays of the response function. To extend this control into higher orders of nonlinearity, one additional pulse would have to be used for each additional interaction in the perturbative description (i.e., five pulses in fifth-order coherent spectroscopy, six pulses in sixth-order action-detected spectroscopy, etc.). This approach has been realized in collinear geometry using phase cycling [213, 245] and in noncollinear geometry using phase matching for a fifth-order (six-wave mixing) signal [246, 247]. The results lead to highly multidimen-

sional (4D in case of fifth-order response) spectra, which require experimental scanning of all inter-pulse delays, making the experiment conceptually and practically challenging. While the data contain a wealth of information, the multidimensionality typically makes it necessary to resort to spectral- and time-domain cuts or spectral projections to facilitate interpretation. Because of the Fourier-transform relationship between the time and frequency domain, spectral projections can be realized directly by measuring at zero-time delay, with multiple interactions with a single pulse (projection-slice theorem). The best-known example is a PP spectrum that emerges as a projection of a third-order 2D spectrum, measured at $\tau = 0$ delay between the first two interactions, which both take place with the pump pulse [16]. One then benefits from a significant dimensionality reduction when carrying out higher-order PP spectroscopy using just one pair of pulses, rather than having to scan many individual delay times. This leads to a simplification of the experiment, reduction of measurement time, and, to an extent, a simplification of the interpretation as well [248]. Measuring at reduced dimensionality has the disadvantage that the spectral information becomes more congested. As demonstrated recently, polarization control can still be used to isolate specific contributions [223], or intensity cycling as explained in the present work allows us to isolate orders of nonlinearity despite "too low" dimensionality [16]. Despite the great advantages due to the simplicity, some information content, in case of PP the excitation lineshape, is not resolved. In the context of these opposing motivations, we see two directions for future higher-order experiments. First, the acquisition of higher-order multidimensional spectra could be combined with fully automated measurement and possibly automated data processing that precedes interpretation. This would help to find the relevant projections and correlations. Data processing and interpretation can be combined with machine learning. Early examples demonstrated the power of neural networks to predict the system response for phase-shaped femtosecond pulses [249, 250], while recent examples utilized machine learning to study energy transfer [251] as well as multidimensional spectra [252, 253]. Recent technical improvements such as high-repetition-rate setups and fast data acquisition should make it possible to measure signals of high dimensionality within a reasonable amount of time. One particular example is shot-to-shot pulse shaping using laser systems with 100 kHz repetition rates [254] that can be combined with many-step phase cycling to obtain higher-order and higher-dimensional data sets in a reasonable amount of time. As a second approach to dealing with the large amount of data in higher-order experiments, one can resort to measuring projections on relevant subspaces of the multidimensional spectral response. While we have investigated projections that correspond to overlapping pulse pairs, one might envision other scenarios employing more complex pulse shapes for exploring the nonlinear response function, a topic that was explored in the field of quantum control [255–257]. This still holds significant potential in combination with multidimensional spectroscopy, in particular in the context of separating nonlinear orders systematically.

An obvious extension of higher-order spectroscopy beyond bulk measurements is the combination with spatial resolution. Multidimensional spectroscopy has already been combined with fluorescence microscopy [126, 127]. We utilized 2D microscopy to study local differences of the coherence length on a structured molecular film [130], to quantify the exciton–phonon coupling strength in $MoSe_2$ at room temperature [128], and to observe hybridization between exciton, phonon and photon modes in a microcavity-embedded 2D material [129]. Another variant combines action-detected phase-cycling 2D spectroscopy with photoemission electron microscopy (PEEM), providing spatial resolution down to ~ 3 nm, which is why we named it "2D nanoscopy" [6, 133]. We used this, for example, to obtain local plasmon lifetime maps from a corrugated silver film that displayed Fano-like resonances [133]. We also investigated thin-film solar cells and found that Anderson localization of photon modes can lead to perfect absorption [134]. Application to metal–molecular hybrid interfaces is also possible [135], and finally 2D nanoscopy allowed us to detect a plasmon-polariton quantum wave packet [258]. In the latter example, we observed aliased 3Q coherences in an eighth-order nonlinear process that could be assigned to multiple excitations of the plasmon. This example demonstrates that higher-order signals also play an important role in plasmonic systems.

In the future, 2D fluorescence microscopy or 2D nanoscopy could be combined with higher phase-cycling schemes to isolate higher-order signals. Such experiments would allow us to obtain spatially varying local properties such as the annihilation times and properties and dynamics of highly excited states. Apart from 2D spectroscopy, higher-order PP spectroscopy using intensity cycling could be easily implemented with a microscope. Such an approach could be used to characterize the spatial variations of (multi-)exciton dynamics within a sample. Understanding local excitonic properties is important for the development of optoelectronic devices based on organic molecules. For any device, the processing into thin-film or bulk materials can result in different phases that contain varying local structures and thus modified interactions between the constituents (i.e., molecules). Such processing typically leads to a change of properties from solution to bulk material contained in an actual device [130, 259]. Spatially resolved higher-order spectroscopy could characterize the local properties and determine the influence of local structure such as in domains, at interfaces, or around local defects. For example, one might envision using fifth-order spectroscopy to resolve the local spatial variations of exciton diffusion within a thin film. This would tell us if diffusion is slower at interfaces or surfaces, for example, which is crucial information for the further improvement of optoelectronic devices such as solar cells.

Another future development for higher-order spectroscopy could be two-color experiments such as in (third-order) 2D electronic–vibrational (2DEV) [260–262] or 2D vibrational–electronic (2DVE) spectroscopy [263–265]. In current 2DEV experiments in PP geometry, the system is excited with a double pulse in the visible regime followed by a probe pulse in the mid-infrared region allowing one to follow the evolution of the excited states by their vibrational signature. Increasing the excitation intensity of the pump pulses would generate a 2Q coherence or higher coherences with the first pulse and hence grant access to highly excited states. Probing with an infrared pulse could then be used to probe the vibrations of highly excited states and to investigate the localization of the state by its specific vibrational signature. We discuss the two approaches, higher-order microscopy and higher-order two-color 2D spectroscopy, in Chapter 10.

We live in a strongly entangled universe: While we often artificially separate our object of investigation into a "system" and an "environment" part, their interaction leads to many aspects of entanglement, decoherence, and the emergence of a classical world from quantum mechanics [266]. In order to deal with the complexity of the real world, we often resort to single-particle pictures. For example, we treat multi-electron atoms by assuming a single-particle picture that leads to the establishment of (useful) atomic orbitals, or we assume a single-particle picture to arrive at the band structure of semiconductors. This concept is certainly very powerful, but it ignores an important part of physics. Correlation phenomena abound in many areas of science, from describing molecular properties to semiconductors [267–269]. This reflects the fact that the fundamental quantum wave function of a multi-particle system depends on the coordinates of all constituents and can, in general, not be written as a product of single-particle wave functions, except for special cases and approximations. Thus, in order to understand multi-particle wave functions, we need tools to investigate the interactions between their constituents. We argue that higher-order multidimensional and pump–probe spectroscopies, as outlined in this chapter, provide such tools because they offer a comprehensive approach to decipher particle and quasiparticle correlations in systematically increasing orders of interaction.

Chapter 7

Anisotropy in Fifth-Order Exciton–Exciton-Interaction Two-Dimensional Spectroscopy

Exciton–exciton-interaction two-dimensional spectroscopy is a fifth-order variant of 2D electronic spectroscopy. It can be used to probe biexciton dynamics in molecular systems and to observe exciton diffusion in extended systems such as polymers or light-harvesting complexes. The exciton transport depends strongly on the geometrical and energetic landscape and its perturbations. These can be both of local character, such as molecular orientation and energetic disorder, or long-range character, such as polymer kinks and structural domains. In the present theoretical work, we investigate the anisotropy in EEI2D spectroscopy. We introduce a general approach for how to calculate the anisotropy by the response-function formalism in an efficient way. In numerical simulations using a Frenkel exciton model with Redfield-theory dynamics, we demonstrate how the measurement of anisotropy in EEI2D spectroscopy can be used to identify various geometrical effects on exciton transport in dimers and polymers. Investigating a molecular heterodimer as an example, we demonstrate the utility of anisotropy in EEI2D for disentangling dynamic localization and annihilation. We further calculate the annihilation in extended systems such as conjugated polymers. In a polymer, a change in the anisotropy provides a unique signature for exciton transport between differently oriented sections. We analyze three types of geometry variations in polymers: a kink, varying geometric and energetic disorder, and different geometric domains. Our findings underline that employing anisotropy in EEI2D spectroscopy provides a way to distinguish between different geometries and can be used to obtain a better understanding of long-range exciton transport.

7.1. Introduction

Two-dimensional electronic spectroscopy (2DES) is a technique that allows observing exciton transport in various systems. In 2DES, two ultrashort laser pulses with a time delay τ excite a quantum system, and a third pulse probes the system after a waiting time T. Several beam geometries have been reported, featuring noncollinear [87, 151], partially collinear [73, 92], or fully collinear beam arrangements [89, 90]. In a pump–probe configuration, for example, the change of absorption with and without the excitation pulses can be recorded analogously to transient absorption measurements. In addition, Fourier transforming over the delay τ between a double-pulse pair in the pump beam provides a two-dimensional (2D) map. In the case of resonant excitation and detection at the same frequency, this leads to a signal on the diagonal. Population transfer from one state to another can be seen by evaluating the dynamics of the crosspeaks in such a 2D spectrum as a function of waiting time T. The 2DES technique is now used throughout all spectral regions [23, 36, 70, 71, 115, 270, 271] and was utilized to study many different examples such as light-harvesting complexes [39, 47], chemical reactions [48], quantum dots [35], and molecular aggregates [80].

In multichromophore systems with spectrally separable absorption features, it can be proven that the state-to-state population-transfer rate model can be recovered quantitatively and uniquely from the 2D spectrum under certain conditions [78], while a global rate-model analysis is ambiguous when based on conventional transient absorption. If the number of chromophores grows, however, the spectral features of the resulting excitonic states start to overlap more strongly and then the kinetic separation gets more and more challenging. Finally, in a supramolecular aggregate of sufficient length or a polymer system, one large excitonic band results [4]. In this case, when an exciton is transported through the system, the transient absorption spectrum does not change. Likewise, it is also difficult to observe the propagation in regular 2D spectroscopy, simply because the absorption properties are mostly independent of the spatial position at which the excitation or detection steps occur. Therefore, 2D spectroscopy cannot be used to probe exciton transport in such systems.

As an alternative, we have developed a fifth-order variant that we termed exciton–exciton-interaction two-dimensional (EEI2D) spectroscopy. It uses exciton–exciton annihilation as a signal and is well suited to probe exciton transport [20]. The dynamics of the exciton–exciton annihilation is observable in the evolution of the amplitude of the EEI2D signal over the population time. The average time between excitation and the moment that two initially separated excitons interact depends on the exciton diffusion. Apart from the initial work on perylene bisimide J-aggregates [20], the technique was also employed to identify sub-diffusive exciton transport in squaraine polymers [7], the interplay of exciton diffusion and exciton interaction in artificial light-harvesting complexes, [4] and the dynamics of exciton–exciton annihilation in small systems such as dimers and trimers of squaraines [9, 220, 238]. EEI2D spectroscopy is an example for a spectroscopic technique which uses more than two interactions with each of the two pump pulses. In EEI2D spectroscopy, a nonlinear polarization

is probed which is higher than the nonlinearity of three that is usually employed in a perturbation-theory description to describe transient absorption or 2D spectroscopy. High-order spectroscopy can be used in various ways such as investigating correlations in semiconductor nanostructures [210], visualizing multistep energy transfer in light-harvesting complexes [211], or probing the highly excited states of molecules [5, 9].

In time-resolved spectroscopy, the signal polarization dependence can be explored both for excitation and for detection. Anisotropic signal contributions and dynamics are frequently discussed in the context of fluorescence measurements. The fluorescence anisotropy is widely used to study (supramolecular) structures and interactions, especially in biochemistry [272–277]. In fluorescence anisotropy measurements, the sample is excited with linearly polarized light and the intensity of the fluorescence is measured after passing a polarizer that is either parallel or perpendicular to the polarization of the excitation field. Let us denote the fluorescence intensities $I_\parallel$ and $I_\perp$, respectively. By measuring both contributions, the polarization-isotropic signal can be constructed by [278]

$$I_{\mathrm{iso}} = I_\parallel + 2I_\perp \tag{7.1}$$

and the anisotropic signal as

$$I_{\mathrm{aniso}} = \frac{I_\parallel - I_\perp}{I_{\mathrm{iso}}}. \tag{7.2}$$

The factor of 2 for the perpendicular intensity in Eq. (7.1) comes from geometrical considerations when evaluating the ensemble-averaged response of randomly oriented molecules, as we will show later on. For a randomly oriented ensemble of molecules the anisotropy can reach values from -0.2 to 0.4. However, these limits break down either by experimental imperfections such as if scattered excitation light reaches the detector or by multiphoton excitation [278].

Similar as in fluorescence measurements, anisotropy can be measured in pump–probe spectroscopy [279–281]. In a typical measurement, signals are acquired in which the excitation and detection polarizations are both chosen to be linear. By changing the polarization of the probe pulse compared to the excitation, the parallel and perpendicular signal contributions are accessible. Then, two measurements are carried out, with mutually parallel and perpendicular polarizations. The amplitudes of the transient absorption signals replace the fluorescence intensities in Eq. (7.1) and Eq. (7.2), and the anisotropic and isotropic signal can be constructed in the same way as for measurements of fluorescence [279, 282]. One fundamental difference between the two methods is that in transient absorption different signals with opposite sign, such as excited-state absorption and stimulated emission, can overlap. Therefore, the anisotropy in pump–probe measurements can in general exceed the limits from fluorescence anisotropy measurements [279].

The concept of anisotropy measurements was extended to the field of 2DES. 2DES anisotropy measurements gave insight into hydrogen bond dynamics [283], exciton dynamics in thin films of semiconducting nanotubes [284], and exciton relaxation in LH2 [285]. Polarization in 2DES can be further utilized if the polarization of each pulse is varied independently. Such polarization sequences can be used to suppress specific

signal contributions in the 2D spectrum. Polarization-controlled 2D experiments were first introduced in the infrared region [98, 286] and further employed in the visible spectrum [99, 287]. The additional information which is obtained by using specific polarization sequences in 2D spectroscopy was used to understand the ultrafast dynamics in DNA-templated silver clusters [288] and to distinguish different coherences in natural light-harvesting systems [105]. Polarization-controlled experiments have been also discussed for high-order 2DIR spectrsocopy [212].

In this work, we extend the concept of EEI2D spectroscopy by discussing effects of anisotropy in the EEI2D signal. First, we outline the theoretical description of anisotropy in fifth-order multidimensional spectroscopy, by presenting the rotational averaging of the (rank six) tensor of the fifth-order susceptibility (Sec. 7.2.1). We explicitly arrive at the expressions for the parallel, perpendicular, and isotropic EEI2D signals (Sec. 7.2.2). This gives us the opportunity to confirm that the magic-angle condition for obtaining an isotropic signal, well-known in pump–probe spectroscopy, is still valid in the case of EEI2D spectroscopy (Sec. 7.2.3). Next, we demonstrate an efficient approach to calculate the orientationally averaged EEI2D signal amplitude, based on the response-function formalism (Sec. 7.2.4). We further use our expressions to simulate the polarization-sensitive EEI2D signals of an electronic dimer (Sec. 7.3) and a series of conjugated polymers (Sec. 7.4). We discuss and analyze the effects of a kink (Sec. 7.4.1), energetic and geometrical disorder (Sec. 7.4.2), and structural domains (Sec. 7.4.3). We demonstrate the capability of polarization-sensitive EEI2D spectroscopy to observe the interplay of dynamic localization and exciton–exciton annihilation, of short and long-range transport, and of energetic and structural disorder and then conclude (Sec. 7.5).

7.2. Theoretical Background

7.2.1. Rotational Averaging

In pump–probe spectroscopy and 2DES, a third-order polarization is responsible for the signal. In both techniques, the pump pulse (or pump-pulse pair in case of 2DES) interacts twice with the sample, while the probe pulse only interacts once. However, the situation is different for EEI2D spectroscopy because a fifth-order polarization is measured, which means that two more interactions with the pump pulse(s) take place. The nonlinear polarization, $P_A^{(A)}(t)$, is a response to the five interactions with the electric fields of the pump $E^{\text{pu}}(t)$ and the probe $E^{\text{pr}}(t)$ evaluated at various time combinations ensuring causality:

$$
\begin{aligned}
P_A^{(5)}(t) = &\sum_{B,C,D,E,F} \int_0^\infty dt_5 \int_0^\infty dt_4 \int_0^\infty dt_3 \int_0^\infty dt_2 \int_0^\infty dt_1 T_{ABCDEF}^{(6)}(t_5,t_4,t_3,t_2,t_1) \\
&\times E_B^{\text{pr}}(t-t_5) E_C^{\text{pu}}(t-t_5-t_4) E_D^{\text{pu}}(t-t_5-t_4-t_3) \\
&\times E_E^{\text{pu}*}(t-t_5-t_4-t_3-t_2) E_F^{\text{pu}*}(t-t_5-t_4-t_3-t_2-t_1),
\end{aligned}
\tag{7.3}
$$

where the star indicates the complex conjugate. The response is given by the rank-six tensor $T^{(6)}$ which is in perturbation theory the nonlinear fifth-order susceptibility $\chi_{ABCDEF}^{(5)}(t_5,t_4,t_3,t_2,t_1)$. The tensor is represented in the frame of the laboratory where the indices $A,B,C,D,E,F \in \{X,Y,Z\}$ describe Cartesian coordinates. For the sake of clarity, we will not write the time integrals explicitly in the following expressions. The generated field is proportional to the polarization under the conditions of perfect phase matching,

$$
E_A^{\text{EEI2D}}(t) = \frac{i\omega}{n\epsilon_0 c} P_A^{(5)}(t),
\tag{7.4}
$$

as can be shown by solving the Maxwell equations for the light propagation [24], where n is the refractive index, ω is the center frequency, ϵ_0 the vacuum permitivity, and c the speed of light. The field is then heterodyne-detected by spectral interference with the so-called local oscillator (LO) field $E^{\text{LO}}(\omega)$, resulting in a detected intensity

$$
I_{\text{detected}} \propto 2\text{Re}\left\{ E^{\text{LO}*}(\omega) E^{\text{EEI2D}}(\omega) \right\},
\tag{7.5}
$$

where the star means complex conjugation and the proportionality indicates that the detected intensity depends on the type of data acquisition as follows. In the case of pump–probe geometry, the LO is the probe field itself. The detected intensity can be expressed as

$$
I_{\text{detected}} \propto \sum_{A,B,C,D,E,F} T_{ABCDEF}^{(6)} E_A^{pr*} E_B^{pr} E_C^{pu} E_D^{pu} E_E^{pu*} E_F^{pu*}.
\tag{7.6}
$$

In any case, we consider the polarization of the local oscillator to be parallel to the third (probe) pulse. Our discussion then applies to a non-collinear geometry as well. Different polarization of the local oscillator and the third pulse is applied in the polarization-controlled experiments mentioned above. The macroscopic response of the sample, $T^{(6)}_{ABCDEF}$, arises from a rotationally averaged microscopic response of the individual molecules, $t^{(6)}_{abcdef}$. In contrast to the tensor $T^{(6)}_{ABCDEF}$ which is presented in the laboratory frame, the molecules are assumed to be fixed in the molecular frame with indices $a, b, c, d, e, f \in \{x, y, z\}$ indicating Cartesian molecular coordinates. For our purpose we define the measured EEI2D signal without explicit dependence on the intensity of the interacting fields as

$$\text{EEI2D} = \sum_{ABCDEF} T^{(6)}_{ABCDEF} e^{\text{pr}}_A e^{\text{pr}}_B e^{\text{pu}}_C e^{\text{pu}}_D e^{\text{pu}}_E e^{\text{pu}}_F, \tag{7.7}$$

where e are the polarization vectors of the different fields and where we also did not consider any prefactors following from signal propagation. Assuming the most common case of randomly oriented molecules (e.g., in solution), rotational averaging of the tensor of rank six therefore has to be performed to simulate the anisotropy in the EEI2D signal. Rotational averaging connects the microscopic response in the molecular frame to the macroscopic response in the laboratory frame. The concept of rotational averaging is well known for third-order polarization techniques [289–291] where it is performed by averaging the tensor of rank four. EEI2D spectroscopy, however, is a fifth-order technique in terms of perturbation theory so we have to find the rotationally averaged tensor of rank six, $\widehat{T}^{(6)}_{ABCDEF}$, with the arc indicating that the tensor $\widehat{T}^{(6)}_{ABCDEF}$ is averaged over all orientations. The rotationally averaged tensor can be calculated by

$$\widehat{T}^{(6)}_{ABCDEF} = \sum_{abcdef} I^{(6)}_{ABCDEF:abcdef} t^{(6)}_{abcdef}, \tag{7.8}$$

where the tensor $I^{(6)}_{ABCDEF:abcdef}$ is known from literature and connects the laboratory frame with the frame of the molecule [289]. More information is given in the supplementary material (Sec. 7.6.1). Considering the mathematical structure of Eq. (7.8), different tensors can be calculated by choosing different relations between the indices A, B, C, D, E, F. For example, if always two indices are chosen to be mutually equal, fifteen combinations are possible and fifteen tensors $\widehat{T}^{(6)}$ arise from Eq. (7.8). For our purposes, we need to calculate the tensor for mutually parallel as well as perpendicular linear pump and probe polarizations. Thus, we need in the one case the symmetric

combination

$$
\begin{aligned}
\widehat{T}^{(6)}_{AAAAAA} = \frac{1}{210} \sum_{abcdef} \quad & \Big(2\delta_{ab}\delta_{cd}\delta_{ef} + 2\delta_{ab}\delta_{ce}\delta_{df} + 2\delta_{ab}\delta_{cf}\delta_{de} \\
& + 2\delta_{ac}\delta_{bd}\delta_{ef} + 2\delta_{ac}\delta_{be}\delta_{df} + 2\delta_{ac}\delta_{bf}\delta_{de} \\
& + 2\delta_{ad}\delta_{bc}\delta_{ef} + 2\delta_{ad}\delta_{be}\delta_{cf} + 2\delta_{ad}\delta_{bf}\delta_{ce} \\
& + 2\delta_{ae}\delta_{bc}\delta_{df} + 2\delta_{ae}\delta_{bd}\delta_{cf} + 2\delta_{ae}\delta_{bf}\delta_{cd} \\
& + 2\delta_{af}\delta_{bc}\delta_{de} + 2\delta_{af}\delta_{bd}\delta_{ce} + 2\delta_{af}\delta_{be}\delta_{cd} \Big) \\
& \qquad t^{(6)}_{abcdef}
\end{aligned}
\tag{7.9}
$$

with δ_{ij} as the Kronecker delta. Equation (7.9) describes a situation in which the sample interacts in all cases with the electric fields of the same polarization. The second tensor component that we need is

$$
\begin{aligned}
\widehat{T}^{(6)}_{AABBBB} = \frac{1}{210} \sum_{abcdef} \quad & \Big(6\delta_{ab}\delta_{cd}\delta_{ef} + 6\delta_{ab}\delta_{ce}\delta_{df} + 6\delta_{ab}\delta_{cf}\delta_{de} \\
& - 1\delta_{ac}\delta_{bd}\delta_{ef} - 1\delta_{ac}\delta_{be}\delta_{df} - 1\delta_{ac}\delta_{bf}\delta_{de} \\
& - 1\delta_{ad}\delta_{bc}\delta_{ef} - 1\delta_{ad}\delta_{be}\delta_{cf} - 1\delta_{ad}\delta_{bf}\delta_{ce} \\
& - 1\delta_{ae}\delta_{bc}\delta_{df} - 1\delta_{ae}\delta_{bd}\delta_{cf} - 1\delta_{ae}\delta_{bf}\delta_{cd} \\
& - 1\delta_{af}\delta_{bc}\delta_{de} - 1\delta_{af}\delta_{bd}\delta_{ce} - 1\delta_{af}\delta_{be}\delta_{cd} \Big) \\
& \qquad t^{(6)}_{abcdef}, \qquad A \neq B.
\end{aligned}
\tag{7.10}
$$

$\widehat{T}^{(6)}_{AABBBB}$ with $A \neq B$ contains the information of the signal contribution for excitation with one polarization and probing with a perpendicular polarization. Concentrating on the two tensors in Eqs. (7.9) and (7.10) is similar to fluorescence or pump–probe anisotropy measurements, in which the anisotropy is constructed from the intensities of parallel and perpendicular probing. The expressions for the rotationally averaged tensors $\widehat{T}^{(6)}_{AAAAAA}$ and $\widehat{T}^{(6)}_{AABBBB}$ allow us to calculate both the anisotropy and the isotropic signal contributions in EEI2D spectroscopy.

7.2.2. Isotropic Signal Contributions

In EEI2D spectroscopy, the sample interacts with five electric fields: four times with the pump pulses and once with the probe pulse. This leads to a reduction of the rank of the susceptibility tensor, in the form of

$$
\sum_{BCDEF} \widehat{T}^{(6)}_{ABCDEF} e_B^5 e_C^4 e_D^3 e_E^2 e_F^1 = \sum_B T^{(2)}_{AB} e_B^5 = T^{(1)}_A.
\tag{7.11}
$$

in which e are the polarization vectors of the pulses [290]. Note that after four interactions (with the pump pulses) the tensor is not rotationally averaged anymore

which is depicted by the vanishing arc. Now the question arises which part of the signal is still isotropic after the interactions with the pump pulses. Considering linear pump polarization, we can, without loss of generality, take it to be in the X direction. Four times interacting with the pump pulses leads to a tensor of rank two, $T^{(2)}$. To find the condition for the isotropic signal, we perform once more rotational averaging of the tensor $T^{(2)}$. The rotational averaging provides the signal contributions which are isotropic, independently of the following two interactions with the probe pulse. Rotational averaging of a tensor of rank two is defined analogously to Eq. (7.8) by

$$\widehat{T}_{AB}^{(2)} = \sum_{CD} I_{AB:CD}^{(2)} T_{CD}^{(2)}. \tag{7.12}$$

Note that in Eq. (7.12) all indices of $I^{(2)}$ are capitalized because we perform rotational averaging on the tensor which is connected to the macroscopic polarization in the sample after the interactions with the pump. $I^{(2)}$ is known from literature [289] as

$$I_{AB:CD}^{(2)} = \frac{1}{3}\delta_{AB}\delta_{CD}. \tag{7.13}$$

Using Eqs. (7.12) and (7.13), the rotationally averaged tensor of rank two can be written as

$$\widehat{T}_{AB}^{(2)} = \delta_{AB}\frac{1}{3}\left(\widehat{T}_{XXXXXX}^{(6)} + 2\widehat{T}_{YYXXXX}^{(6)}\right) \tag{7.14}$$

where we used the symmetry of the tensor $\widehat{T}_{ZZXXXX}^{(6)} = \widehat{T}_{YYXXXX}^{(6)}$. Expressing by the microscopic response using Eqs. (7.9) and (7.10), we arrive at

$$\widehat{T}_{AB}^{(2)} = \delta_{AB}\sum_{abcdef}\frac{1}{45}\left(\delta_{ab}\delta_{cd}\delta_{ef} + \delta_{ab}\delta_{ce}\delta_{df} + \delta_{ab}\delta_{cf}\delta_{de}\right)t_{abcdef}^{(6)}. \tag{7.15}$$

The terms constituting the isotropic signal are thus: $\delta_{ab}\delta_{cd}\delta_{ef}$, $\delta_{ab}\delta_{ce}\delta_{df}$, and $\delta_{ab}\delta_{cf}\delta_{de}$.

7.2.3. Magic-Angle Condition and Parallel and Perpendicular Signal Contributions

For pump–probe spectroscopy, it is well known that for a certain angle between the (linearly chosen) polarization of pump and probe pulses the signal is purely isotropic [290]. This angle is referred to as magic angle and is given by $\tan\phi_{\mathrm{magic}} = \sqrt{2}$, which leads to a value of $\phi_{\mathrm{magic}} \approx 54.7°$. The magic angle is the specific angle at which all the anisotropic contributions vanish and only the isotropic contributions remain. In previous work, we derived generalized magic-angle conditions for arbitrary polarization states of the incident beams in third-order spectroscopy [290]. In the present work, we consider a different type of generalization and extend the analysis from third-order to fifth-order response, but assume all incident pulses to be linearly polarized. To find the condition to only measure the isotropic part of the EEI2D signal, we consider

the pump as linearly polarized in X direction and the probe as linearly polarized in an arbitrary direction in the XY plane, with an angle α between pump and probe polarization. The polarization of the probe is defined as

$$e_{\mathrm{pr}} = e_X \cos(\phi) + e_Y \sin(\phi) \tag{7.16}$$

with the unity basis vectors e_X and e_Y. In pump–probe transient absorption measurements as well as in EEI2D spectroscopy in pump–probe geometry, the probe acts also as the local oscillator. Therefore, the tensor which describes the fifth-order polarization for an isotropic sample is the rotationally averaged tensor of rank six that interacts with the six electric-field polarization vectors as follows from Eq. (7.7):

$$\mathrm{EEI2D} = \sum_{ABCDEF} \widehat{T}^{(6)}_{ABCDEF} e^{\mathrm{pr}}_A e^{\mathrm{pr}}_B e^{\mathrm{pu}}_C e^{\mathrm{pu}}_D e^{\mathrm{pu}}_E e^{\mathrm{pu}}_F. \tag{7.17}$$

Applying our definition of the polarization of the probe pulse, we can rewrite the expression as

$$\sum_{AB} \widehat{T}^{(6)}_{ABXXXX} e^{\mathrm{pr}}_A e^{\mathrm{pr}}_B e^{\mathrm{pu}}_X e^{\mathrm{pu}}_X e^{\mathrm{pu}}_X e^{\mathrm{pu}}_X = + \cos^2(\phi)\, \widehat{T}^{(6)}_{XXXXXX} + \cos(\phi)\sin(\phi)\, \widehat{T}^{(6)}_{XYXXXX}$$
$$+ \sin(\phi)\cos(\phi)\, \widehat{T}^{(6)}_{YXXXXX} + \sin^2(\phi)\, \widehat{T}^{(6)}_{YYXXXX}. \tag{7.18}$$

It follows from Eq. (7.8) that the contributions $\widehat{T}^{(6)}_{XYXXXX}$ and $\widehat{T}^{(6)}_{YXXXXX}$ vanish. The reason for this is that the tensor $I^{(6)}_{ABCDEF:abcdef}$ consists of products of Kronecker deltas in both laboratory and molecular frame [289]. By using the definitions of the rotationally averaged tensor from Eqs. (7.9) and (7.10), the EEI2D signal, dependent

on the angle ϕ between the pump and the probe polarization, can be written as

$$
\begin{aligned}
\mathrm{EEI2D}(\phi) = {} & \sum_{abcdef} \cos^2(\phi) t^{(6)}_{abcdef} \frac{1}{210} \\
& \Big(2\delta_{ab}\delta_{cd}\delta_{ef} + 2\delta_{ab}\delta_{ce}\delta_{df} + 2\delta_{ab}\delta_{cf}\delta_{de} \\
& +2\delta_{ac}\delta_{bd}\delta_{ef} + 2\delta_{ac}\delta_{be}\delta_{df} + 2\delta_{ac}\delta_{bf}\delta_{de} \\
& +2\delta_{ad}\delta_{bc}\delta_{ef} + 2\delta_{ad}\delta_{be}\delta_{cf} + 2\delta_{ad}\delta_{bf}\delta_{ce} \\
& +2\delta_{ae}\delta_{bc}\delta_{df} + 2\delta_{ae}\delta_{bd}\delta_{cf} + 2\delta_{ae}\delta_{bf}\delta_{cd} \\
& +2\delta_{af}\delta_{bc}\delta_{de} + 2\delta_{af}\delta_{bd}\delta_{ce} + 2\delta_{af}\delta_{be}\delta_{cd} \Big) \\
& + \sum_{abcdef} \sin^2(\phi) t^{(6)}_{abcdef} \frac{1}{210} \\
& \Big(6\delta_{ab}\delta_{cd}\delta_{ef} + 6\delta_{ab}\delta_{ce}\delta_{df} + 6\delta_{ab}\delta_{cf}\delta_{de} \\
& -1\delta_{ac}\delta_{bd}\delta_{ef} - 1\delta_{ac}\delta_{be}\delta_{df} - 1\delta_{ac}\delta_{bf}\delta_{de} \\
& -1\delta_{ad}\delta_{bc}\delta_{ef} - 1\delta_{ad}\delta_{be}\delta_{cf} - 1\delta_{ad}\delta_{bf}\delta_{ce} \\
& -1\delta_{ae}\delta_{bc}\delta_{df} - 1\delta_{ae}\delta_{bd}\delta_{cf} - 1\delta_{ae}\delta_{bf}\delta_{cd} \\
& -1\delta_{af}\delta_{bc}\delta_{de} - 1\delta_{af}\delta_{bd}\delta_{ce} - 1\delta_{af}\delta_{be}\delta_{cd} \Big).
\end{aligned}
\tag{7.19}
$$

The terms $\delta_{ab}\delta_{cd}\delta_{ef}$, $\delta_{ab}\delta_{ce}\delta_{df}$ and $\delta_{ab}\delta_{cf}\delta_{de}$ constitute the isotropic part of the signal when added up according to Eq. (7.15). To measure only the isotropic part, all other components in Eq. (7.19) have to vanish. All anisotropic components have in common a factor of $2\cos^2(\phi) - \sin^2(\phi)$. Demanding that this vanishes amounts to the magic-angle condition of $\tan\phi_{\mathrm{magic}} = \sqrt{2}$, which is the same as for traditional four-wave mixing spectroscopy. By using the magic angle between pump and probe polarization direction, thus, the obtained fifth-order EEI2D signal is purely isotropic:

$$
\mathrm{EEI2D_{MA}} = \sum_{abcdef} \frac{1}{45} \left(\delta_{ab}\delta_{cd}\delta_{ef} + \delta_{ab}\delta_{ce}\delta_{df} + \delta_{ab}\delta_{cf}\delta_{de} \right) t^{(6)}_{abcdef}.
\tag{7.20}
$$

Analogous to standard third-order 2DES, we can define a parallel signal,

$$
\mathrm{EEI2D}_{\parallel} = \widehat{T}^{(6)}_{XXXXXX},
\tag{7.21}
$$

obtained via Eq. (7.9), and a perpendicular signal,

$$
\mathrm{EEI2D}_{\perp} = \widehat{T}^{(6)}_{YYXXXX},
\tag{7.22}
$$

obtained via Eq. (7.10). From these, we can define the isotropic and anisotropic signals in EEI2D spectroscopy, analogous to Eqs. (7.1) and (7.2), respectively, as

$$
\mathrm{EEI2D_{iso}} = \mathrm{EEI2D}_{\parallel} + 2\mathrm{EEI2D}_{\perp},
\tag{7.23}
$$

$$
\mathrm{EEI2D_{aniso}} = \frac{\mathrm{EEI2D}_{\parallel} - \mathrm{EEI2D}_{\perp}}{\mathrm{EEI2D_{iso}}}.
\tag{7.24}
$$

7.2.4. Response-Function Liouville-Space Pathways
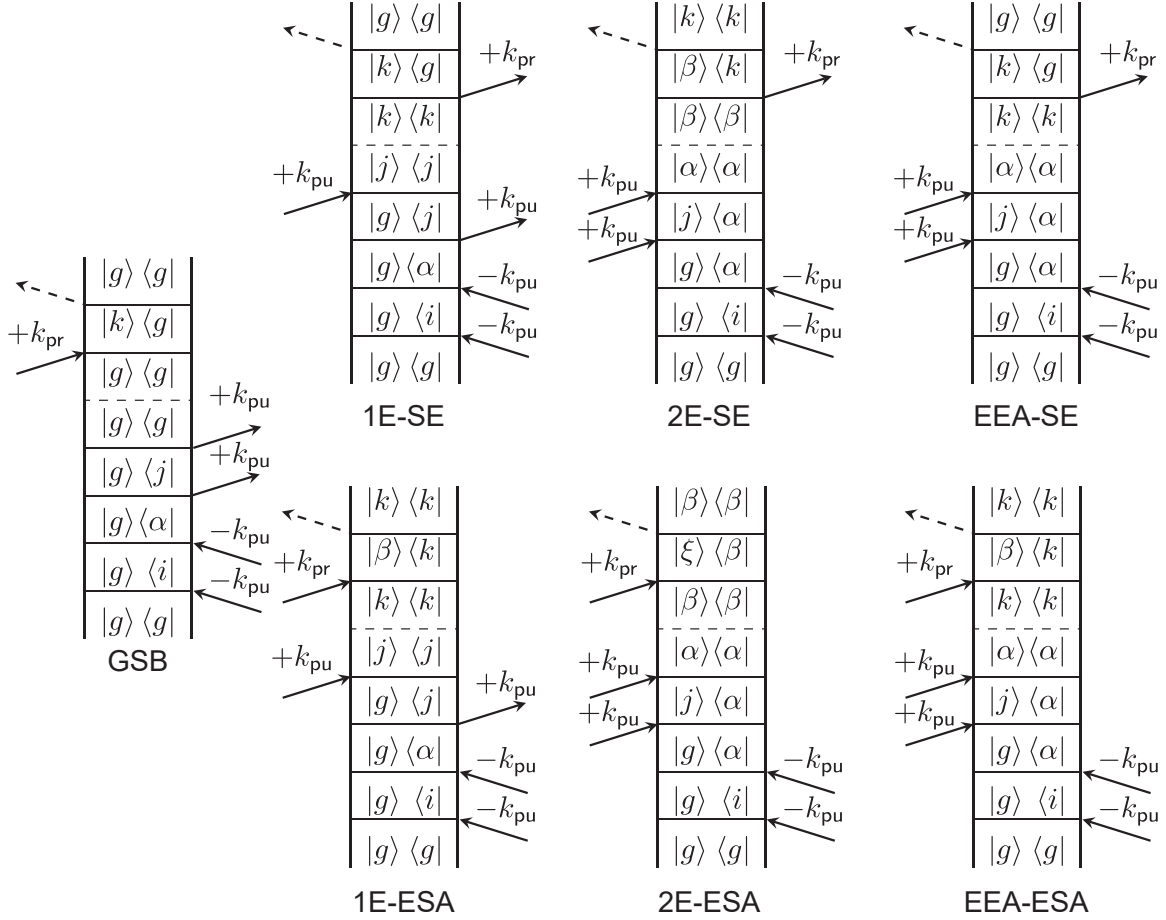
Figure 7.1.: Rephasing Liouville-space pathways contributing to the EEI2D signal. The pathways are labeled with respect to their population time dynamics (1E = one-exciton dynamics, 2E = two-exciton dynamics, and EEA = exciton–exciton annihilation) and the type of pathway (GSB = ground-state bleach, SE = stimulated emission, and ESA = excited-state absorption. The wavevectors of the pump and the probe are labeled with k_{pu} and k_{pr}, respectively. Reprinted from Ref. [12], with the permission of AIP Publishing.

The nonlinear response can be decomposed into Liouville-space pathways that are conveniently expressed by double-sided Feynman diagrams. In these diagrams time flows from bottom to top. Considering population dynamics in the waiting time, there are seven types of pathways that contribute, depicted in Fig. 7.1. The depicted pathways contain the rephasing contributions. Non-rephasing pathways are analogous by switching the time ordering of the two interactions of the first and second pump pulse [25]. When added they form the absorptive response. Each of the pathways represents a part of the total response. Considering interaction with light in the dipole approximation, the indices in the susceptibility tensor denote the (Cartesian) coordi-

nate components of the transition dipole elements of the individual transitions in the response pathways (for example, μ_{kg}^a is the a-th component of the dipole of the transition between the ground state g and the single-excited state k, where $a \in \{x, y, z\}$). In this work we will focus on the dynamics of the amplitude of the EEI2D signal in the waiting time. We will thus consider EEI2D signals integrated over their respective spectral regions around twice the excitation center frequency. Under this condition, the pathway contributions consist of the amplitude, given by the multiplication of the contributing transition dipole moments, and the propagator $\mathscr{U}(T)$ in the waiting time. The propagator indices indicate population dynamics in the population time T. The explicit expressions for the pathways in Fig. 7.1 are:

$$
\begin{aligned}
\mathrm{GSB}_{abcdef} &= \sum_{i,j,k,\alpha} \mu_{kg}^a \mu_{kg}^b \mu_{jg}^c \mu_{\alpha j}^d \mu_{\alpha i}^e \mu_{ig}^f \mathscr{U}_{gg,gg}(T), \\
\mathrm{1E\text{-}SE}_{abcdef} &= 2 \sum_{i,j,k,\alpha} \mu_{kg}^a \mu_{kg}^b \mu_{jg}^c \mu_{\alpha j}^d \mu_{\alpha i}^e \mu_{ig}^f \mathscr{U}_{kk,jj}(T), \\
\mathrm{2E\text{-}SE}_{abcdef} &= - \sum_{i,j,k,\alpha,\beta} \mu_{\beta k}^a \mu_{\beta k}^b \mu_{\alpha j}^c \mu_{jg}^d \mu_{\alpha i}^e \mu_{ig}^f \mathscr{U}_{\beta\beta,\alpha\alpha}(T), \\
\mathrm{EEA\text{-}SE}_{abcdef} &= - \sum_{i,j,k,\alpha} \mu_{kg}^a \mu_{kg}^b \mu_{\alpha j}^c \mu_{jg}^d \mu_{\alpha i}^e \mu_{ig}^f \mathscr{U}_{kk,\alpha\alpha}(T), \\
\mathrm{1E\text{-}ESA}_{abcdef} &= -2 \sum_{i,j,k,\alpha,\beta} \mu_{\beta k}^a \mu_{\beta k}^b \mu_{jg}^c \mu_{\alpha j}^d \mu_{\alpha i}^e \mu_{ig}^f \mathscr{U}_{kk,jj}(T), \\
\mathrm{2E\text{-}ESA}_{abcdef} &= \sum_{i,j,\alpha,\beta,\xi} \mu_{\xi\beta}^a \mu_{\xi\beta}^b \mu_{\alpha j}^c \mu_{jg}^d \mu_{\alpha i}^e \mu_{ig}^f \mathscr{U}_{\beta\beta,\alpha\alpha}(T), \\
\mathrm{EEA\text{-}ESA}_{abcdef} &= \sum_{i,j,k,\alpha,\beta} \mu_{\beta k}^a \mu_{\beta k}^b \mu_{\alpha j}^c \mu_{jg}^d \mu_{\alpha i}^e \mu_{ig}^f \mathscr{U}_{kk,\alpha\alpha}(T).
\end{aligned}
$$
(7.25)

They are named with reference to the dynamics in the population time (1E: one-exciton dynamics, 2E: two-exciton dynamics, and EEA: exciton–exciton annihilation) and the type of pathway (GSB: ground-state bleach, SE: stimulated emission, and ESA: excited-state absorption). The pathway sign in each term above is given by the number of interactions from the right (due to the commutator in the Liouville–von Neumann equation for the density matrix interacting with light). Note that we use the sign convention of normal transient absorption in which the third-order ground-state bleach is usually considered with a negative sign. The occasional factors of 2 in Eq. (7.25) reflect the uncertainty in time ordering of the simultaneous interactions with one of the pump pulses. To obtain the overall signal amplitude, all the components of all the pathways have to be summed up. Moreover, the expressions have to be orientationally averaged, to arrive at the macroscopic response, according to Eq. (7.19). This summation and averaging is lengthy and computationally costly. Looking closer at the structure of the pathway expressions in Eq. (7.25), it can be seen that all the pathways share a common factor of four dipole interactions with the electric field: $\mu_{jg}\mu_{\alpha j}\mu_{\alpha i}\mu_{ig}$. This factor corresponds to the four pump pulses interacting with a two-exciton state α, via the one-exciton states i, j. Making use of this fact, we can first

calculate a partially averaged tensor $T^{(2)}$, based on Eq. (7.19), where for $t^{(6)}_{abcdef}$ we take the expressions from Eq. (7.25), keeping track of the vector components. The resulting rank-two tensor is thus dependent on the angle between the pump and probe polarizations ϕ, the remaining indices α, j, and has two polarization indices:

$$T^{(2)}_{ab}(\phi; \alpha, j) = \sum_i \langle \mu_{jg} \mu_{\alpha j} \mu_{\alpha i} \mu_{ig} \rangle_\phi. \tag{7.26}$$

This tensor reflects the orientationally averaged state of the sample after the interaction with the pump pulses. All the orientationally averaged pathways can be expressed by this rank-two tensor, multiplied by the remaining two transition dipoles and the waiting time propagator $\mathscr{U}(T)$. For example, the 1E-SE pathway is calculated as

$$\text{1E-SE}(\phi) = \sum_{\alpha,j,k} \sum_{a,b} \mu^a_{kg} \mu^b_{kg} T^{(2)}_{ab}(\phi; \alpha, j) \mathscr{U}_{kk,jj}(T), \tag{7.27}$$

and the other pathways analogously. This procedure makes the orientationally averaged pathway summation much more efficient, which enables us to treat extended systems such as polymers or molecular aggregates.

7.3. Interplay of Annihilation and Localization in a Molecular Dimer

7.3.1. General Model

To gain a deeper understanding of the information contained in the anisotropy of the EEI2D signal, we investigate an excitonic dimer. We focus on the interplay of two ultrafast processes that are difficult to disentangle using conventional techniques: dynamic localization and exciton–exciton annihilation. The process of exciton localization is the change of the delocalization length with time. Delocalization itself is a result of the coupling between the ground-to-first-excited-state transitions of the individual systems. In the case of a dimer weakly interacting with the vibrational bath, the delocalization is determined by the mixing angle θ, with

$$\tan(2\theta) = \frac{2J}{\Delta E}, \tag{7.28}$$

with the coupling J and the difference of the excitation energies of the monomers ΔE. In the case of strong coupling and a small energy difference, the exciton states will be completely delocalized over both monomers [123]. In extended systems such as polymers, the delocalization length is used to describe the spatial spreading of the excitons. The delocalization length is defined by the spatial distribution over which the exciton can be found on the different parts of the system and it can be calculated by the inverse participation ratio which uses the transformation matrix that connects the exciton basis with the site basis [7, 280, 292]. The delocalization length of the excitation in a particular system can change dynamically, for example by transfer to different states. This process is called dynamic localization.

In contrast to the excitonic delocalization, exciton–exciton annihilation is a phenomenon that occurs because of coupling of the transitions from the ground state to the first excited state to transitions from the first excited state to higher excited states. In extended systems such as polymers or molecular aggregates, it is often useful to define an annihilation radius. The annihilation radius characterizes the distance dependence of exciton–exciton annihilation if two excitons approach each other. The delocalization length and the annihilation radius are both a consequence of electronic coupling, but the direct connection between the delocalization length and the annihilation radius is not trivial. Disentangling the effects of annihilation and localization gives us the chance to understand how the interplay between these two occurs, and how the annihilation radius is connected with the delocalization length of the system. Ultimately, this knowledge is vital for understanding the influence of exciton–exciton annihilation on the exciton transport in artificial light-harvesting complexes and solar cell devices.

In order to disentangle the different processes of annihilation and localization, we describe the heterodimer theoretically by two different sets of states, which we call delocalized and localized states. The delocalized and localized states are connected by a

population transfer process, which corresponds to the process of dynamic localization. The description of the whole system by two parts, i.e., by the two sets of states, might seem artificial, but it gives us the opportunity to analyze localization and annihilation independently and their influence on the isotropic and anisotropic signal contributions in EEI2D spectroscopy. The two monomers constituting the dimer are arranged at an angle Θ to each other. The first set of states corresponds to a heterodimer with an electronic coupling J. The eigenstates of this coupled system are linear superpositions of the monomeric states. Due to the electronic coupling, they are thus partially delocalized [123]. We therefore refer to this part of the system as delocalized states. The transition dipole moments of the single-excited states, i.e., exciton 1 and exciton 2, are schematically shown on the left side of Fig. 7.2. Localization is described by a rate of population transfer to the second set of states. This second set of states describes a heterodimer without any coupling between the transitions from the ground state to the first excited state of the monomers. The absence of coupling results in localized states with different orientation of the transition dipole moments, as shown in Fig. 7.2. As a result, the dynamic localization should be visible in the anisotropy of the annihilation signal.
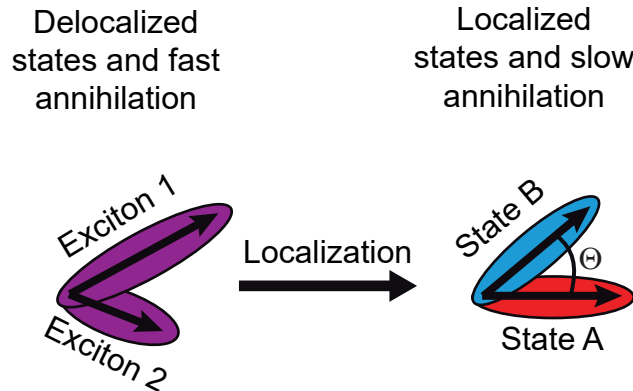
Figure 7.2.: Interplay of exciton–exciton annihilation and dynamic localization in an excitonic dimer. Left: Delocalized excitonic states with rapid annihilation. The arrows represent the transition dipole moments of the two single-exciton states, i.e., exciton 1 and exciton 2. The delocalization is indicated by the same color of the two arrows. For the parameters in our simulation the delocalization is about 15% which can be directly calculated from the mixing angle. Right: Localized states with slower annihilation. The first-excited states of the monomers are separated by an energy difference ΔE indicated by the different colors of the two monomers. The transition dipole moments of the first-excited states are arranged by an angle Θ to each other. Reprinted from Ref. [12], with the permission of AIP Publishing.

Apart from the singly excited states of the uncoupled monomer, we consider also one higher electronically excited state per monomer. The largest influence of these states is that they enable exciton–exciton annihilation. Exciton–exciton annihilation for the delocalized states is described by a transfer from a biexciton state to one of

the higher excited states of the monomers, followed by rapid internal conversion. We also included an annihilation channel in the localized set of states, because we want to understand how the annihilation after localization manifests in the isotropic and anisotropic EEI2D signal. In order to study the effects of localization and annihilation we ensure to excite only the delocalized states directly. Otherwise the signal would be influenced by the direct excitation of the localized states which will complicate the interpretation. To this end, we calculate the EEI2D signal for the full system of the two connected sets of states first with and then without any localization rate, and subtract the EEI2D signals. Finally, we add the EEI2D signal of the isolated delocalized states. The result thus corresponds to a situation in which only the delocalized set of states is directly excited while the localized states can be considered as dark during the excitation. A detailed description of our treatment of dynamic localization is given in the supplementary material (Sec. 7.6.2).

For the calculations performed in this work, we use a Frenkel exciton model of coupled molecules, represented by three-level systems. The exciton dynamics is described by secular Redfield theory, with the molecular environment described as a bath of harmonic oscillators (Brownian oscillator model). The intramolecular relaxation between the excitonic manifolds is described by an incoherent relaxation rate, within Lindblad formalism. For the localized set of states, the exciton–exciton annihilation is described explicitly by a decay rate from the biexciton state to the singly excited states. For the delocalized states, the transfer from the biexciton state to the higher excited states is described by the Redfield theory, taking the transition coupling to be proportional to the excitonic coupling J. The annihilation then proceeds *via* internal conversion. We give more background about the excitonic structure and the calculation of the system dynamics in the supplementary material (Sec. 7.6.3). From our previous studies on squaraine dimers, we fixed the internal conversion time to 30 fs [7]. The coupling for the delocalized set of states was set to 200 cm^{-1} which results in a delocalization of about 15% which can be directly obtained as $\sin^2(\theta)$ from the mixing angle [123]. The angle between the monomers was set to $\Theta = 40°$. A full set of the used parameters can be found in the supplementary material (Sec. 7.6.4).

7.3.2. Sensitivity to Dynamic Localization

To illustrate the sensitivity of the EEI2D signal kinetics with respect to the interplay of the exciton localization and annihilation, we varied two parameters: the localization rate from the delocalized set of states to the localized set of states, and the annihilation rate in the localized states. The results of the calculations can be seen in Fig. 7.3. Throughout this publication, we show the isotropic contribution of the integrated EEI2D signal on the left side and the anisotropic signal on the right side of the corresponding figures. In Fig. 7.3a and Fig. 7.3b we show the isotropic and anisotropic EEI2D signals, respectively, for our model dimer with varying localization time (different colors), while the exciton–exciton annihilation for the localized states is set to 1 ps. For the isotropic EEI2D signal we see a typical behavior: the EEI2D signal

rises first rapidly until it reaches a plateau. The time it takes the signal to reach the plateau is determined by the annihilation rate; for the coupled dimer with fast exciton–exciton annihilation this takes about 100 fs. The EEI2D signal disappears with the single-exciton lifetime, which was set to 1 ns for the delocalized as well as the localized states. In the supplementary material we demonstrate that the EEI2D signal in the system with the two sets of states is dominated by exciton–exciton annihilation (Sec. 7.6.5) which justifies our interpretation. In the system in principle two channels for exciton–exciton annihilation are realized: annihilation in the delocalized set of states and annihilation in the localized set of states. Before annihilation in the localized set of states can occur, transfer from the delocalized to the localized set of states has to take place. Depending on the rate of this transfer, annihilation either in the delocalized or localized set of states dominates the isotropic and anisotropic EEI2D signal. For increasingly smaller localization time, i.e., higher localization rate, the excitons have a chance to localize before they annihilate. The process of increasingly faster localization is visible in the isotropic signal (Fig. 7.3a). For very fast localization of 50 fs, the EEI2D signal is dominated by the annihilation dynamics in the localized dimer (Fig. 7.3a, red curve). The localization, followed by a slow annihilation, creates two phases in the rise of the isotropic EEI2D signal. These two phases are caused by the two different annihilation channels with their different timescales. For a localization time of 50 fs, the isotropic EEI2D signal reaches its maximum after 1 ps, because the annihilation channel in the localized set of states dominates. Here the limiting factor for the rise is the annihilation time in the localized states. The slower localization, i.e., higher localization time, can be seen by the faster rise within the first 100 fs of the isotropic EEI2D signal which is realized for localization times of 100 fs and 200 fs (Fig. 7.3a, yellow and green curves, respectively). For these cases the annihilation occurs in both the delocalized and localized states. For slower localization times of 500 fs, 1 ps and 10 ps (Fig. 7.3a, light blue, dark blue and purple curves, respectively) the isotropic signal is dominated by the annihilation in the delocalized states which can be seen by a rapid rise of the isotropic signal. Here, most of the annihilation occurs in the delocalized set of states. As described above the annihilation in the delocalized set of states is faster than in the localized states which explains the faster rise if the localization takes longer.
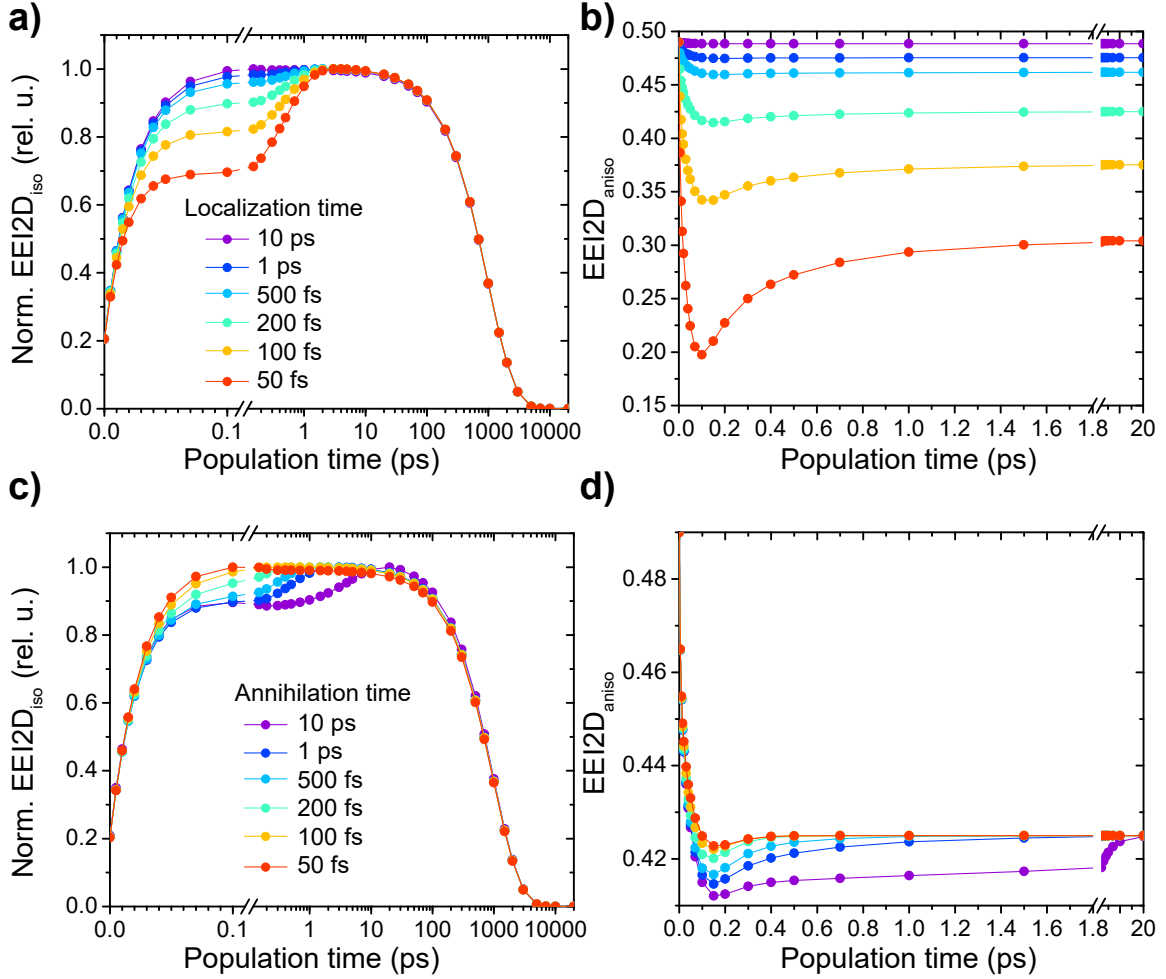
Figure 7.3.: Isotropic (left column) and anisotropic (right column) EEI2D signal for a model system of an excitonic heterodimer exhibiting dynamic exciton localization and exciton–exciton annihilation, illustrated in Fig. 7.2. (a) Isotropic EEI2D signal of a heterodimer where the localization time is varied while the annihilation time in the localized set of states is set constant to 1 ps. (b) Anisotropic EEI2D signal with varying localization time and fixed annihilation time of 1 ps in the localized set of states. (c) Isotropic EEI2D signal of a hetereodimer with fixed localization time of 200 fs and varying annihilation time in the localized set of states. (d) Anisotropic EEI2D signal for a heterodimer where the localization time was kept constant at 200 fs while the annihilation time in the localized set of states was varied. Reprinted from Ref. [12], with the permission of AIP Publishing.

In the anisotropic signal contribution, the localization is reflected by an initial decay of the anisotropy (Fig. 7.3b). This effect is strongest for a localization rate of 50 fs (Fig. 7.3b, red curve). The localization is accompanied by a change of the transient dipole moment orientation. The rise after the decay in the anisotropic signal is determined by the annihilation on the localized dimer. This will be discussed further in Sec. 7.3.3 where the annihilation rate in the localized states was varied. Note that the

initial anisotropy value is not the maximum possible. The maximum initial anisotropy is expected if a change of the direction of the transition dipole moment due to annihilation or transfer is not possible. This corresponds to a situation in which all the single-exciton dipole moments point in the same direction. This is obviously not the case in the delocalized set of states. We derive the limiting values of the anisotropy in the supplementary material (Sec. 7.6.6) and find that the maximum and minimum values of anisotropy are $4/7$ and $-2/7$, respectively. Since the direction of the transition dipole moments of the states differs for the delocalized and localized set of states, the long-term value of anisotropy is different, depending on which of the two annihilation channels is contributing more. The initial decay in the anisotropy is strongest visible for a localization time of 50 fs (Fig. 7.3b, red curve) where the anisotropy drops from an initial value of 0.48 to a minimum value of 0.2. For slower localization times such as 100 fs and 200 fs (Fig. 7.3b, yellow and green curve, respectively), the minimum anisotropy value due to the initial decay is less (0.35 and 0.42, respectively). If the localization time is increased further to 500 fs and 1 ps, the initial decay is almost not visible (Fig. 7.3b, light blue and dark blue curves, respectively). The reason for the absence of a decay is that the exciton–exciton annihilation in the delocalized set of states exceeds the slow localization time of 500 fs and 1 ps. Therefore, the dominating annihilation channel is annihilation in the delocalized set of states, while the annihilation in the localized set of states plays only a minor rule due to the slow localization. For the limiting case of a very slow localization time of 10 ps, the anisotropy does not change during the population time because the anisotropy value is purely defined by the annihilation in the delocalized states (Fig. 7.3b, purple curve).

7.3.3. Sensitivity to Exciton–Exciton Annihilation

Next, we study the influence of the annihilation time in the localized set of states. To this end, we fix the localization time to a value of 200 fs. The results for different annihilation times in the localized set of states are shown in Fig. 7.3c and Fig. 7.3d. For a slow annihilation time in the localized states of 10 ps, the isotropic EEI2D signal reaches its maximum at around 10 ps (Fig. 7.3c, purple curve). The initial rise until 200 fs reflects the annihilation in the delocalized states. For an annihilation time of 10 ps, the two annihilation channels in the localized and delocalized states are separated by their individual timescales. In the isotropic EEI2D signal, a decrease of the annihilation time to 1 ps and 500 fs is nicely visible by the shifting of the plateau to earlier waiting times (Fig. 7.3c, dark blue and light blue curves). For fast annihilation times of 200 fs, 100 fs and 50 fs, the plateau is reached before 1 ps (Fig. 7.3c green, yellow and red curves, respectively). The faster dynamics of the signals are similar to the effect of higher orders in perturbation theory, i.e., seventh-order signals contributing to the EEI2D signal [7].

Here, additional excitons in the system interact with the biexciton which results in an overall effective increase of the annihilation rate.

The anisotropic signal shows for all annihilation times a decay with a following recovery of the signal (Fig. 7.3d). For a slow annihilation time of 10 ps, the anisotropic EEI2D signal recovers on a slow timescale where the final value of anisotropy is reached after 20 ps (Fig. 7.3d, purple curve). The rise of the recovery is determined by the slow annihilation of 10 ps. For a slow annihilation time such as 10 ps, the two phases of localization and the following annihilation are separated by their different timescales. First, the anisotropic signal decays because of the depolarization via the localization. The anisotropy rises again with the annihilation rate of the localized states. If the annihilation time in the localized set of states decreases (Fig. 7.3d, dark blue and light blue curves), the recovery of anisotropy starts to vanish and the only remaining dynamics in the anisotropy is a decay. Following this argumentation, the recovery is less visible for a localization time of 200 fs and 100 fs (Fig. 7.3d, green and yellow curves). For a very fast annihilation time of 50 fs, the two phases of localization and annihilation in the localized states overlap (Fig. 7.3d, red curve). The final value of the anisotropy does not change with different annihilation times because the number of annihilation events in each set of states is determined by the localization time which is not varied. In line with our argumentation, only the time it takes to reach the final value of the anisotropy is influenced by the annihilation time in the localized set of states. Our model system demonstrates that the anisotropy of the EEI2D signal is sensitive to a change of the transition dipole-moment orientation, which can be caused by localization, and to the dynamics of exciton–exciton annihilation.

7.4. Anisotropy in Squaraine Copolymers

Armed with the understanding of EEI2D anisotropy of molecular dimers, we proceed to large, extended systems such as conjugated polymers. We take squaraine copolymers as a typical example. Squaraine polymers have excellent opto-electronic properties such as a large exciton diffusion length [7, 206] which makes them an interesting candidate for applications such as solar cells [293]. The key process is the exciton transport along the polymer chain. Long-range transport is very difficult to track by conventional techniques such as pump–probe spectroscopy, as it occurs on a mesoscopic or microscopic scale and in an energetic landscape in which the chromophores distributed along the chain have the same energy on average. Thus, it is not possible to observe any transient spectral changes as a result of transport phenomena. We have recently shown that EEI2D spectroscopy can be very well used for this task [4]. Exciton transport is influenced by the polymer disorder, which can be energetic and structural. The former results in local traps, while the latter leads to polymer segmentation, varying conjugation length, and transport bottlenecks. Advanced single-molecule studies on individual polymer strands demonstrated the connection between the local conformation and the photophysics in polymers [294, 295]. Small kinks can cause a local change in the coupling and therefore potentially influence the transport properties of the sys-

tem. Our goal is to investigate how the polarization sensitivity of the EEI2D signal can be used to disentangle the types of disorder affecting the transport. We further want to understand how local changes affect the anisotropy and how the transport is influenced by them.

7.4.1. Polymers with a Kink
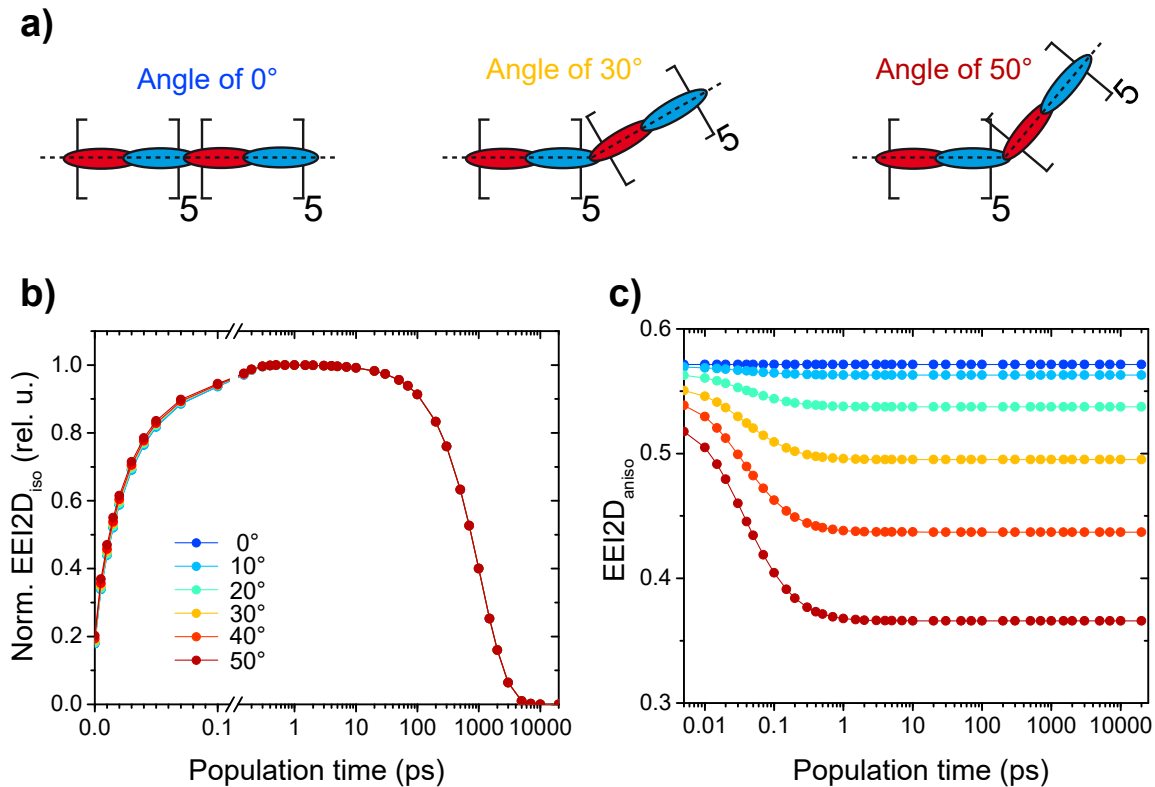
Figure 7.4.: A kink with varying angle in a polymer. (a) Our studied system is a copolymer made from twenty monomers and a central kink with an angle from 0° to 50°. (b) Dynamics of the normalized isotropic EEI2D signal over the population time. (c) Dynamics of the anisotropic EEI2D signal over population time. Reprinted from Ref. [12], with the permission of AIP Publishing.

Let us start with a simple feature of structural disorder in a polymer: a kink. For our simulations, we consider a squaraine copolymer consisting of twenty monomers (or ten dimers) with a kink with varying angle in the middle of the polymer as shown in Fig. 7.4a. The polymer chain consists of two kinds of monomers, called SQA and SQB, which build up an alternating copolymer. In Figs. 7.4b and 7.4c the isotropic and anisotropic EEI2D signal contributions, respectively, are shown. In all our simulations we use parameters derived from describing our EEI2D measurements on conjugated squaraine copolymers of varying length [7]. A full set of the parameters

can be found in the supplementary material (Sec. 7.6.7). We verified that the EEI2D signal is dominated by exciton–exciton annihilation (Sec. 7.6.8 of the supplementary material). The effect of the kink is practically not visible in the isotropic EEI2D signal (Fig. 7.4b). The isotropic signal reaches its plateau at around 300 fs, which is the average time until two excitons can meet, due to exciton diffusion, and interact with each other. To understand the dynamics in the isotropic EEI2D signal, we have to consider the excitonic structure. In the polymer, the coupling between different monomers is only broken by one kink. Since the change in the excitonic structure is only minimal, the isotropic EEI2D signal is almost not affected either. The anisotropic signal (Fig. 7.4c) shows an unambiguous sensitivity to the kink in the polymer. Note that the time for the anisotropic signal to reach its final value is the same as the time it takes the isotropic EEI2D signal to reach its plateau. The anisotropy decay increases with the angle of the kink. The reason for this behavior is the depolarization due to exciton transport from one part of the polymer to the other. If the kink is more substantial, the change in the direction of transition dipole moments due to transport of the excitons is larger, and therefore the anisotropy decay is stronger. The difference for the anisotropy for a small kink is not large which makes it difficult to observe experimentally. However, the signal-to-noise ratio can be improved by first fitting the measurements of perpendicular and parallel polarization and use the fits to construct the anisotropy [279]. Further, laser systems with high repetition rates up to 100 kHz might improve the signal-to-noise ratio of higher-order signals further [254].

Summarizing, using the isotropic signal alone one cannot attribute any spectroscopic signature to a kink. In contrast to this, the anisotropic signal is an excellent indicator for a geometry variation such as a kink in a polymer.

7.4.2. Energetic vs. Geometric Disorder in Polymers

Real polymers are significantly disordered, both energetically and structurally. Here, we demonstrate how anisotropy in EEI2D can be used to distinguish between the energetic and geometrical disorder in polymers. Again, we calculate the isotropic and anisotropic EEI2D signals for a squaraine copolymer consisting of twenty monomers. We show the isotropic EEI2D signal for large geometric and energetic disorder when the system cannot undergo any annihilation in Sec. 7.6.9 of the supplementary material. In the first calculations, we vary the energetic disorder (Figs. 7.5a and 7.5b, respectively). The transition energies of the monomers along the chain are taken from a Gaussian distribution with a width of 2σ. The values for σ are quoted in Fig. 7.5a as multiples of σ_0 that refers to the energetic disorder determined in our previous study. Since we model a copolymer, we use individual widths $(2\sigma_0)$for SQA and SQB (250 cm^{-1} for SQA and 500 cm^{-1} for SQB) [7]. We employ the values for energetic disorder of σ_0 also for all other calculations presented in this paper. For the variations of the energetic disorder both values are scaled by the same factor.

As can be seen in Fig. 7.5a, the plateau of the isotropic EEI2D signal is reached at later population times for energetic disorder larger than σ_0. This effect is already visible for a twice larger disorder (Fig. 7.5a, light blue curve). For 3 times and 4 times more energetic disorder the effect is more prominent (Fig. 7.5a, green and yellow curves, respectively; note the logarithmic population time axis). For even larger disorder such as $5\sigma_0$ a saturation of the effect is visible and the plateau is reached at around 20 ps (Fig. 7.5a, red curve). Considering all curves, we thus observe that for larger energetic disorder, the overall exciton diffusion gets slower. This can be explained by taking into account that for larger energetic disorder, the excitons are less delocalized, and they need to overcome higher energetic barriers to move trough the polymer, which results on average in a longer time for two excitons to meet and interact. In contrast to the isotropic EEI2D signal, the anisotropic EEI2D signal (Fig. 7.5b) is not affected by a varying energetic disorder, because the direction of the transition dipole moments does not change with the energetic variation. Therefore the anisotropy does not change by exciton diffusion since all parts of the polymer have the same direction of the transition dipole moment independent of the energetic disorder. The anisotropy therefore stays constant at the maximum possible value.
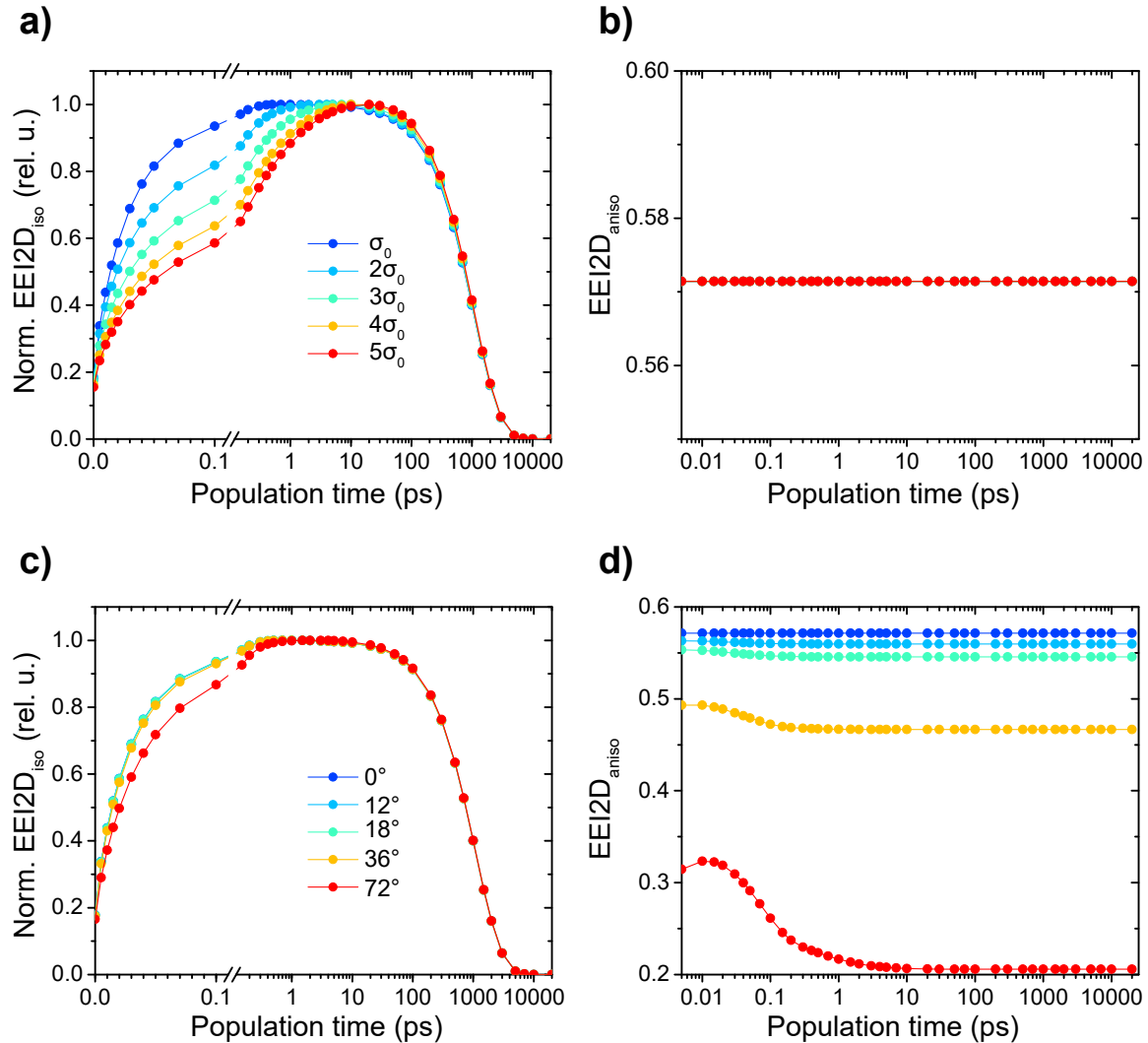
Figure 7.5.: Effect of energetic and geometric disorder in squaraine copolymers. (a) Isotropic EEI2D signal for a polymer with varying energetic disorder. (b) Anisotropic EEI2D signal for a polymer with varying energetic disorder. (c) Isotropic EEI2D signal for a polymer with varying geometric disorder. (d) Anisotropic EEI2D signal for a polymer with varying geometric disorder. Reprinted from Ref. [12], with the permission of AIP Publishing.

For geometric disorder the situation is different. To simulate a polymer with varying random geometry, we construct a polymer made of twenty monomers by adding monomers head-to-tail with an angular distribution. The angular distribution is specified in the legend of Fig. 7.5c as the width (2σ) of a Gaussian distribution. We take care that the polymer does not fold back on itself by enforcing a minimum-distance structural constraint for each randomly generated chain. In our case a constraint on the minimum distance between neighboring molecules is set to half of the molecular length, which corresponds to a back-folding angle of 60°. The isotropic and anisotropic signals are shown in Fig. 7.5c and Fig. 7.5d, respectively. The isotropic signal contri-

bution is almost unaffected by the geometric disorder. Only for the largest geometric variation (Fig. 7.5c, red curve), slightly slower annihilation dynamics are visible by the plateau which is reached at a later population time. For such a large variation of the inter-chromophore angle, the geometric disorder probably leads to some monomers with configurations for which their transition dipole moments are oriented close to an angle where the coupling is zero. In such a case, the suppressed coupling leads to overall slower dynamics in the EEI2D signal.

In contrast to the isotropic signal, the anisotropy is sensitive to the geometric disorder. In the anisotropic signal, a stronger decay is observed for larger geometric variation in the polymer chain. Due to the varying orientations of the individual monomers, the dipole moment changes its direction upon propagation of the excitons through the chain which is visible as a decay of the initial anisotropy value. In other words, the exciton transport leads to a depolarization process. For small geometric variations of a width of $12°$ and $18°$ (Fig. 7.5d, light blue and green curves, respectively), the decay is small and the final value is close to the situation without any geometric variation (Fig. 7.5d, dark blue curve). The final value of anisotropy indicates, similar to Sec. 7.4.1, how substantial the change is of the orientation of transition dipole moments by the exciton transport. Following this argumentation a decay in the anisotropy is visible for a width of $36°$ (Fig. 7.5d, yellow curve). For the largest simulated geometric variation with a width of $72°$ (Fig. 7.5d, red curve), the anisotropy first rises and then decays. Such huge random orientation results in low coupling. Lower coupling throughout the polymer leads to less delocalized excitons and slower annihilation, as already discussed. For the case of large geometric variation such as a width of $72°$, the depolarization by transfer and the exciton–exciton annihilation will be sufficiently slowed down due to the low coupling. This is similar to our model system of a dimer (Sec. 7.3.3) with slow annihilation where the recovery of the signal is significantly delayed.

Summarizing, the two examples of energetic and geometric disorder shown in Fig. 7.5 demonstrate how analyzing both the isotropic and the anisotropic EEI2D signal can distinguish between both situations. In real polymers, where energetic disorder as well as geometric disorder is present, the EEI2D anisotropy is an excellent tool to directly observe the amount of geometric disorder since a change in the anisotropy is unambiguously connected to the structural disorder of the polymer. This is in contrast to other experimental techniques such as linear absorption spectroscopy where both energetic disorder as well as geometric disorder change the spectrum (Sec. 7.6.10 of the supplementary material).

7.4.3. Polymers with Different Geometric Domains

In this section, we investigate a special behavior of squaraine copolymers. These polymers are known to form more than one type of structure within one polymer strand, depending on the solvent [296]. In a polar solvent such as acetone, these polymers form a structure in which the chain is partially oriented in a zig–zag geometry while

other parts of the polymer form a helical structure. Due to the different conformations, the electronic coupling is different in the different domains. While in the zig–zag part J-type coupling is present, the helical structure realizes H-type coupling. We simulate this situation with a polymer consisting of ten dimers out of which five are arranged in a head-to-tail configuration and the following five all parallel to each other but with angles of 65° with respect to the chromophores in the first segment (Fig. 7.6a). This situation corresponds to a part of the polymer with a J-type coupling and another part with H-type coupling similar as in squaraine copolymers in polar solvents. We vary the coupling between the different domains from no coupling to the full coupling between all the monomers of the different domains. Effectively the coupling within a domain stays constant while the coupling between the domains changes. In Fig. 7.6a the difference in the coupling is illustrated by the varying distance between the two domains. We calculate the full coupling between the domains, fractions of the full coupling, and also the case when the two domains are uncoupled. In the supplementary material (Sec. 7.6.11) we further show the situation how the signal changes if all the monomers have different orientations with respect to each other. While the coexistence of different polymer configurations seems quite specific for squaraine copolymers [296], identification of different structural domains is a much more general problem. Examples include excitation energy flow through the natural photosynthetic membrane [61] or biomimetic light harvesters such as tubular J-aggregates [171, 297]. Finally, structural domains can be found in films [130, 298–300], perovskites [301], or conjugated polymers similar to those discussed theoretically here as an example [302, 303].

In Fig. 7.6b we show the isotropic EEI2D signal for a polymer with two different domains and varying coupling between the domains. The isotropic EEI2D signal is relatively robust against different couplings between the two domains. The plateau is reached earliest for zero coupling between the domains (Fig. 7.6 b, dark blue curve). If the domains are not coupled at all, the aggregate is split effectively into two smaller fragments made out of five monomers each. Therefore, the exciton–exciton annihilation is faster compared to a longer polymer. For weak coupling such as fractions of 0.02 (Fig. 7.6b, light blue curve) or 0.1 (Fig. 7.6b, green curve) of the full coupling, the isotropic EEI2D signal reaches the plateau later as for no coupling between the domains. In the case of such weak coupling the exciton diffusion between the monomers is slowed down which results in an overall slower dynamics for the EEI2D signal. If the coupling between the domains is increased to half or full coupling (Fig. 7.6b, yellow and red curve, respectively), the plateau is reached again at earlier times but not as early as in the case without any coupling. The effect is discussed in more detail in the supplementary material where we also show the signal in the case where annihilation is forbidden (Sec. 7.6.12). In total, the isotropic signal shows some sensitivity with respect to the inter-domain coupling, but the quantitative effect is not so large, and the qualitative shape of the curves is almost unaffected. Thus, in an experiment where comparative curves for different geometries are not available, it would not be possible to deduce the configuration from the measurement. This changes when considering the anisotropic EEI2D signal that displays strong quantitative and qualitative variations

with geometry.
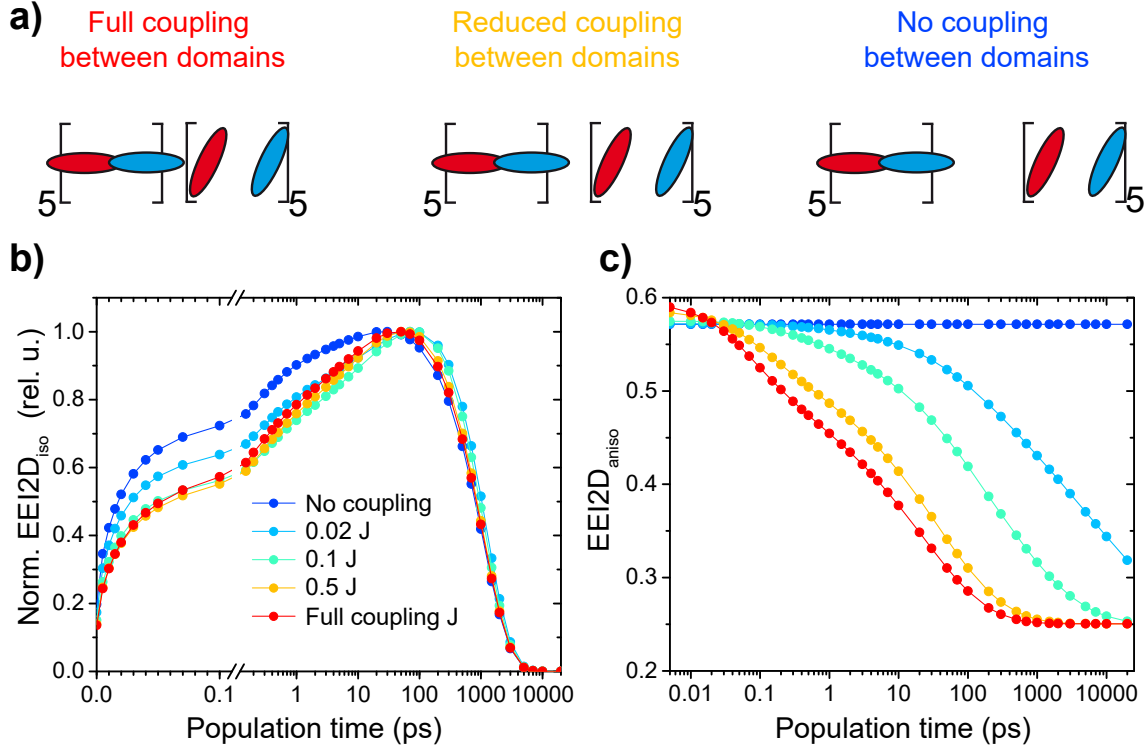
Figure 7.6.: Effect of two different geometric domains within one polymer, inspired by squaraine copolymers in polar solvents. (a) We demonstrate the effect of two different geometric domains on the anisotropic and isotropic EEI2D signal by varying the coupling between the domains but not within one domain. This is illustrated by the different distances between the domains. (b) Isotropic EEI2D signal for two domains with varying coupling between the domains. (c) Anisotropic EEI2D signal for two domains with varying coupling between the domains. Reprinted from Ref. [12], with the permission of AIP Publishing.

We show the anisotropic EEI2D signal of the polymer in Fig. 7.6c. The EEI2D anisotropy does not change with population time if the two domains are not coupled (Fig. 7.6c, dark blue curve) since the direction of the transition dipole moments cannot change within a domain. A biexciton that is partially located on one domain and partially on the other does not contribute, since this kind of biexcitons cannot undergo exciton–exciton annihilation. If the domains are coupled to each other, the anisotropy reaches its final value faster if the coupling between the two different domains is stronger. Note that if the orientation of the whole polymer is varied, the anisotropy stays constant (supplementary material, Sec. 7.6.11).

Upon varying the coupling between the domains, the initial-time value of the anisotropy changes slightly and exceeds the calculated maximum value of the anisotropy. A reason for this might be that for full coupling, the excitons may be delocalized not only

within one domain but also between the domains. In real systems, such a huge delocalization is suppressed by disorder in the system. However, our model does not describe the initial excited state correctly, since we neglect coherences during the population time; a correct description of the coherent behavior at population times around time zero is thus beyond the scope of this work. We note that within secular approximation the presence of such coherences, while present in the spectroscopic response, does not affect the population dynamics, in which we are interested [304]. The coherent dynamics will manifest as typical oscillations which lie on top of the EEI2D signal and might distort the anisotropic signal dynamics. It was recently shown that the rise of the EEI2D signal with the annihilation rate is still visible even in the presence of such coherent oscillations [220]. A possible strategy to avoid such kind of distortions especially for dynamics close to $T = 0$ might be to use fits of the measurements with parallel and perpendicular polarization. However, the spectra close to $T = 0$ are difficult to interpret anyway, due to pulse overlap effects [124].

The final anisotropy value is determined by the difference of the orientation of the two domains. If the domains are not connected by any coupling (Fig. 7.6c, dark blue curve), a change of the direction of the transition dipole moments is not possible since no transfer between the domains is realized. For the cases of full coupling, half of the full coupling and 0.1 of the full coupling between the domains, the anisotropy reaches the same final value. One might expect that for a change in the coupling between the domains, the final anisotropy value might change, similar to the case of our investigated heterodimer (Sec. 7.3), where a faster localization leads to a different final value in the anisotropy. This is not the case for the polymer. The difference between a polymer with two domains and the heterodimer in Sec. 7.3 is that in our investigated polymer both domains get excited equally, while in the heterodimer only the delocalized states are initially excited. In the polymer the orientation of transition dipole moments after the excitation changes by exciton transfer between the domains. Since we keep the relative orientation of the two domains fixed and only vary the coupling between the domains, the final value of the anisotropy does not change. Instead, the coupling changes the time it takes for the long-term value of anisotropy to be reached. If the exciton lifetime is shorter than the time needed for transfer between the domains, the excitons will decay within their lifetime before the maximum depolarization for the geometry is possible. In such cases (Fig. 7.6c, light blue curve), the anisotropy decay will be slower and the final value of anisotropy is higher than for cases with full coupling between the domains (Fig. 7.6c, red curve). The final value of anisotropy can change if the geometry of the domains changes, i.e., if the monomers of the domain are tilted by an angle different than 65° (Sec. 7.6.13 of the supplementary material).

7.5. Summary and Conclusion

We have derived the mathematical expressions for calculating the anisotropy in fifth-order exciton–exciton-interaction two-dimensional (EEI2D) spectroscopy, derived minimal and maximal anisotropy values of $-2/7$ and $4/7$, respectively, and derived that the magic angle of 54.7° between linear pump and probe polarizations, well known from anisotropy-free third-order pump–probe spectroscopy, is also valid in EEI2D spectroscopy. We have further developed an efficient response-function-based approach for calculating orientationally averaged EEI2D signals.

Using a Frenkel exciton model with open quantum system dynamics, we have demonstrated relevant properties of the anisotropic EEI2D signal in molecular systems. In a molecular heterodimer, anisotropy in EEI2D spectroscopy can be used to disentangle the interplay between localization and annihilation. While the isotropic signal provides information on the dynamics of exciton–exciton annihilation only, the anisotropy further reveals information about the change in the direction of the transition dipole moments. The process of localization is thus encoded in the dynamics of the anisotropic signal. A decay in the anisotropy is an indicator that the process of localization takes place. Further, we have analyzed the interplay of structural and energetic disorder in polymers. We have simulated four different examples of disorder in a polymer: a kink, random energetic disorder, structural disorder, and different geometric domains within one polymer chain. For a polymer with a kink, the anisotropy decay depends on how strong the polymer is bent. In contrast to the anisotropic signal, the isotropic signal is not sensitive to the kink in the polymer chain. In general, the isotropic and anisotropic signals have opposite sensitivity to the energetic and structural disorder. While the anisotropic EEI2D signal is strongly sensitive to the structural disorder, the isotropic signal changes drastically with the disorder in transition energies. Together, the signals can thus be used to determine the relative importance of the different kinds of disorder in polymers. Finally, we considered a polymer with different geometric domains. In this particular situation, the decay of the anisotropic EEI2D signal is a good indicator of the coupling between the domains. If the coupling between the domains is stronger, the excitons can transfer faster from one domain to the other. The exciton transfer changes the direction of the transition dipole moment, which is visible as a decay in the anisotropic EEI2D signal. Together, the analytical derivations and the numerically investigated examples show that measuring anisotropy is a useful extension of fifth-order multidimensional electronic spectroscopy. It enables detailed observation of exciton dynamics, from the interplay of localization and annihilation at short scales, to the long-range exciton transport in disordered systems. High-order 2D spectroscopy techniques have recently been used to investigate the structure of biexcitons and triexcitons in quantum dots [13, 216]. In such systems anisotropy in fifth-order spectroscopy gives the chance to obtain additional information about the structure of multiexcitonic states. In general, anisotropy in EEI2D spectroscopy will find use in extended isoenergetic systems such as polymers, aggregates, or natural light-harvesting complexes.

7.6. Supplementary material

7.6.1. Mathematical Description of Rotational Averaging

In this section we give a brief outline how the rotationally averaged tensors are calculated. To perform rotational averaging, we have to solve the equation

$$\widehat{T}^{(6)}_{ABCDEF} = \sum_{abcdef} I^{(6)}_{ABCDEF:abcdef} t^{(6)}_{abcdef}, \tag{7.29}$$

where $\widehat{T}^{(6)}_{ABCDEF}$ is the rotationally averaged tensor (indicated by the arc) in the frame of the laboratory with Cartesian coordinate indices $A, B, C, D, E, F \in \{X, Y, Z\}$ and $t^{(6)}_{abcdef}$ the tensor of a single molecule in the molecular-frame Cartesian coordinates $a, b, c, d, e, f \in \{x, y, z\}$ [289, 290]. I is a tensor of rank six and connects the molecular frame with the frame of the laboratory. The tensor I contains fifteen combinations of pairs of delta functions and the matrix M, [289] further defined below,

$$I^{(6)}_{ABCDEF:abcdef} = \sum_{s,R} f^{(6)}_R M_{Rs} g^{(6)}_s. \tag{7.30}$$

Here $g^{(6)}_s$ and $f^{(6)}_R$ are sets of the isotropic tensor isomers. The set of isotropic tensor isomers of rank six in the laboratory frame, i.e. $f^{(6)}_R$, is listed in Table S1.

Table 7.1.: Isotropic tensor isomers of rank six.

R	$f^{(6)}_R$	R	$f^{(6)}_R$	R	$f^{(6)}_R$
1	$\delta_{AB}\delta_{CD}\delta_{EF}$	6	$\delta_{AC}\delta_{BF}\delta_{DE}$	11	$\delta_{AE}\delta_{BD}\delta_{CF}$
2	$\delta_{AB}\delta_{CE}\delta_{DF}$	7	$\delta_{AD}\delta_{BC}\delta_{EF}$	12	$\delta_{AE}\delta_{BF}\delta_{CD}$
3	$\delta_{AB}\delta_{CF}\delta_{DE}$	8	$\delta_{AD}\delta_{BE}\delta_{CF}$	13	$\delta_{AF}\delta_{BC}\delta_{DE}$
4	$\delta_{AC}\delta_{BD}\delta_{EF}$	9	$\delta_{AD}\delta_{BF}\delta_{DE}$	14	$\delta_{AF}\delta_{BD}\delta_{CE}$
5	$\delta_{AC}\delta_{BE}\delta_{DF}$	10	$\delta_{AE}\delta_{BC}\delta_{DF}$	15	$\delta_{AF}\delta_{BE}\delta_{CD}$

While $f^{(6)}_R$ is a row vector and contains the isotropic tensor isomers in the laboratory frame, $g^{(6)}_s$ is a column vector and contains the isotropic tensor isomers in the molecular frame. It can be obtained by transposing $f^{(6)}_R$ and switching the indices to molecular frame $(A, B, C, D, E, F \to a, b, c, d, e, f)$. The two sets of isotropic tensor isomers are

connected by the matrix M, which is known from literature, [289] and is defined as

$$M = \frac{1}{210}\begin{pmatrix} 16 & -5 & -5 & -5 & 2 & 2 & -5 & 2 & 2 & 2 & 2 & -5 & 2 & 2 & -5 \\ -5 & 16 & -5 & 2 & -5 & 2 & 2 & 2 & -5 & -5 & 2 & 2 & 2 & -5 & 2 \\ -5 & -5 & 16 & 2 & 2 & -5 & 2 & -5 & 2 & 2 & -5 & 2 & -5 & 2 & 2 \\ -5 & 2 & 2 & 16 & -5 & -5 & -5 & 2 & 2 & 2 & -5 & 2 & 2 & -5 & 2 \\ 2 & -5 & 2 & -5 & 16 & -5 & 2 & -5 & 2 & -5 & 2 & 2 & 2 & 2 & -5 \\ 2 & 2 & -5 & -5 & -5 & 16 & 2 & 2 & -5 & 2 & 2 & -5 & -5 & 2 & 2 \\ -5 & 2 & 2 & -5 & 2 & 2 & 16 & -5 & -5 & -5 & 2 & 2 & -5 & 2 & 2 \\ 2 & 2 & -5 & 2 & -5 & 2 & -5 & 16 & -5 & 2 & -5 & 2 & 2 & 2 & -5 \\ 2 & -5 & 2 & 2 & 2 & -5 & -5 & -5 & 16 & 2 & 2 & -5 & 2 & -5 & 2 \\ 2 & -5 & 2 & 2 & -5 & 2 & -5 & 2 & 2 & 16 & -5 & -5 & -5 & 2 & 2 \\ 2 & 2 & -5 & -5 & 2 & 2 & 2 & -5 & 2 & -5 & 16 & -5 & 2 & -5 & 2 \\ -5 & 2 & 2 & 2 & 2 & -5 & 2 & 2 & -5 & -5 & -5 & 16 & 2 & 2 & -5 \\ 2 & 2 & -5 & 2 & 2 & -5 & -5 & 2 & 2 & -5 & 2 & 2 & 16 & -5 & -5 \\ 2 & -5 & 2 & -5 & 2 & 2 & 2 & 2 & -5 & 2 & -5 & 2 & -5 & 16 & -5 \\ -5 & 2 & 2 & 2 & -5 & 2 & 2 & -5 & 2 & 2 & 2 & -5 & -5 & -5 & 16 \end{pmatrix}. \tag{7.31}$$

Now we have the tools to perform rotational averaging for different combinations of excitation and detection polarization as discussed in the main text (Sec. 7.2). For example, if the first two and the last two interactions share the same polarization direction and the polarization of the third and fourth interactions are parallel with each other but are perpendicular to the other four, we have

$$A = B = E = F, \quad C = D, \quad A \neq C. \tag{7.32}$$

For this particular situation, all elements of the tensor $f_R^{(6)}$ are zero except for the elements 1, 12, and 15. Therefore the rotationally averaged tensor of rank six is

$$\widehat{T}_{iijjii}^{(6)} = \frac{1}{210}\sum_{abcdef}\Big(\quad 6\delta_{ab}\delta_{cd}\delta_{ef} - 1\delta_{ab}\delta_{ce}\delta_{df} - 1\delta_{ab}\delta_{cf}\delta_{de} - 1\delta_{ac}\delta_{bd}\delta_{ef} - 1\delta_{ac}\delta_{be}\delta_{df}$$

$$-1\delta_{ac}\delta_{bf}\delta_{de} - 1\delta_{ad}\delta_{bc}\delta_{ef} - 1\delta_{ad}\delta_{be}\delta_{cf} - 1\delta_{ad}\delta_{bf}\delta_{ce} - 1\delta_{ae}\delta_{bc}\delta_{df}$$

$$-1\delta_{ae}\delta_{bd}\delta_{cf} + 6\delta_{ae}\delta_{bf}\delta_{cd} - 1\delta_{af}\delta_{bc}\delta_{de} - 1\delta_{af}\delta_{bd}\delta_{ce} + 6\delta_{af}\delta_{be}\delta_{cd}\Big)$$

$$t_{abcdef}^{(6)} \qquad (i \neq j). \tag{7.33}$$

We can see that the tensor $\widehat{T}_{iijjii}^{(6)}$ can also be expressed as a linear combination of three other tensors by

$$\widehat{T}_{iijjii}^{(6)} = +\widehat{T}_{iijjkk}^{(6)} + \widehat{T}_{ijkkij}^{(6)} + \widehat{T}_{ijkkji}^{(6)}. \tag{7.34}$$

7.6.2. Dynamic Localization in a Heterodimer

The validity of our nonstandard description of the dynamic localization in Sec. 7.3 derives from the linearity of the sum of the response pathways within a given perturbative order. Let us denote the delocalized and localized sets of states with indices D and L, respectively. The total response S can be separated into the response of the individual subsystems S_{D-D} and S_{L-L} , and the response originating from both S_{D-L}:

$$S = S_{D-D} + S_{L-L} + S_{D-L}. \tag{7.35}$$

The response S_{D-L} includes the desired dynamic localization terms S_{L-D}^{loc} with transfer from $D \to L$ with the localization rate k_{loc}, but also potentially any coherence terms (and, in the collective basis, also bleach-type terms, terms with one exciton in each subsystem, etc.). It can thus be further separated as

$$S_{D-L} = S_{D-L}^{\text{loc}} + S_{D-L}^{\text{other}}. \tag{7.36}$$

Now, the key assumption is that the localization with rate k_{loc} does not affect all other parts of the response, something that has to be ensured in the microscopic model.

In the simulations, we then calculate the response of the combined system with and without the dynamic localization, and subtract the two. Finally, we add the response of the delocalized set of states S_{D-D} in the absence of the localization. The resulting response is therefore

$$S = S_{D-L}^{\text{loc}} + S_{D-L}^{\text{other}} + S_{D-D}^{\text{loc}} + S_{L-L} - \left(S_{D-L}^{\text{other}} + S_{D-D} + S_{L-L} \right) + S_{D-D}. \tag{7.37}$$

Here, S_{D-D}^{loc} is the response of the delocalized set of states in presence of localization (resulting in an exponential decay of the pathways that probe the system D), and S_{D-D} is the response of the delocalized set of states without any localization. Since our localization occurs only in one direction, there is no difference between S_{L-L} in S_{L-L}^{loc}. This calculation of the response thus results in the desired response of

$$S = S_{D-L}^{\text{loc}} + S_{D-D}^{\text{loc}} \tag{7.38}$$

which reflects the response of the delocalized set of states with dynamic localization.

7.6.3. Theoretical Model

Excitonic Structure

The calculations in this publication were performed with an excitonic model that we introduced in our previous work on squaraine co-polymers. [7] For the sake of completeness, we repeat the description of our model here. The description is based on a Frenkel exciton model known from molecular aggregates. The electronic states are described as a three level system for each molecule. As common in open-quantum system description, the molecule is taken to interact with a vibrational bath. The

Hamiltonian of a molecule at site n is:

$$H_n = |g_n\rangle \, e_g \, \langle g_n| + |e_n\rangle \, (e_n + \delta e_n + \Delta V_n(Q(t))) \, \langle e_n|$$
$$+ |f_n\rangle \left(e_n + \delta e_n + e_f + \Delta V_n^f(Q(t)) \right) \langle f_n| \, .$$

Here $|g_n\rangle$ is the ground state with the energy e_g, $|e_n\rangle$ the first excited state with energy e_n, and $|f_n\rangle$ a higher excited state with energy $e_n + e_f$. In our calculations we consider the transition energies with respect to the ground state, setting $e_g = 0$. Due to a different local environment, the transition energies can deviate from their mean values by δe_n, reflecting an energetic disorder (which we take to be normal-distributed). Fast vibrations of the bath coordinates Q cause fluctuations of the moelcular energy gap, described by the energy gap operator $\Delta V_n(Q(t))$ in the first excited state and $\Delta V_n^f(Q(t))$ in the higher excited state. The bath is described as a continuum of vibrational modes, described by their spectral density $C(\omega)$. $C(\omega)$ is related to the energy-gap correlation function by a Fourier transform:

$$C(\omega) = \int dt e^{i\omega t} \langle \Delta V(t) \Delta V(0) \rangle \, . \tag{7.39}$$

The spectral density can be expressed as

$$C(\omega) = \left(1 + \coth \frac{\hbar \omega}{2k_b T} \right) C''(\omega) \tag{7.40}$$

with

$$C''(\omega) = \frac{2\lambda \Lambda}{\omega^2 + \Lambda^2} + \frac{2\lambda_\nu \Omega^2 \omega \gamma}{(\Omega^2 - \omega^2)^2 + \omega^2 \gamma^2} \, . \tag{7.41}$$

The $C''(\omega)$ is Fourier transform of the imaginary part of the correlation function, and is typically temperature independent. Our form of $C''(\omega)$ consists of two terms, the first is an overdamped Brownian oscillator model for the continuum of modes, with reorganization energy λ (Stokes' shift is 2λ) and inverse correlation time Λ. The second term is an underdamped oscillator with frequency Ω, reorganization energy $\lambda_\nu = S\Omega$ (S is the Huang-Rhys factor), and (weak) damping γ. It represents an intramolecular vibration of the squaraine molecules themselves. In our model the spectral density is the same for each of the molecules, in all excited states (only coupled with varying strength).

The polymer consists of N molecules with electronic coupling between their transitions. It is practical to work in a collective state basis:

$$|g\rangle = |g_1\rangle \dots |g_N\rangle \, , \tag{7.42}$$

$$|e : n\rangle = |g_1\rangle \dots |e_n\rangle \dots |g_N\rangle \, , \tag{7.43}$$

$$|e : nm\rangle = |g_1\rangle \dots |e_n\rangle \dots |e_m\rangle \dots |g_N\rangle \, , \tag{7.44}$$

$$|e : nml\rangle = |g_1\rangle \dots |e_n\rangle \dots |e_m\rangle \dots |e_l\rangle \dots |g_N\rangle \, . \tag{7.45}$$
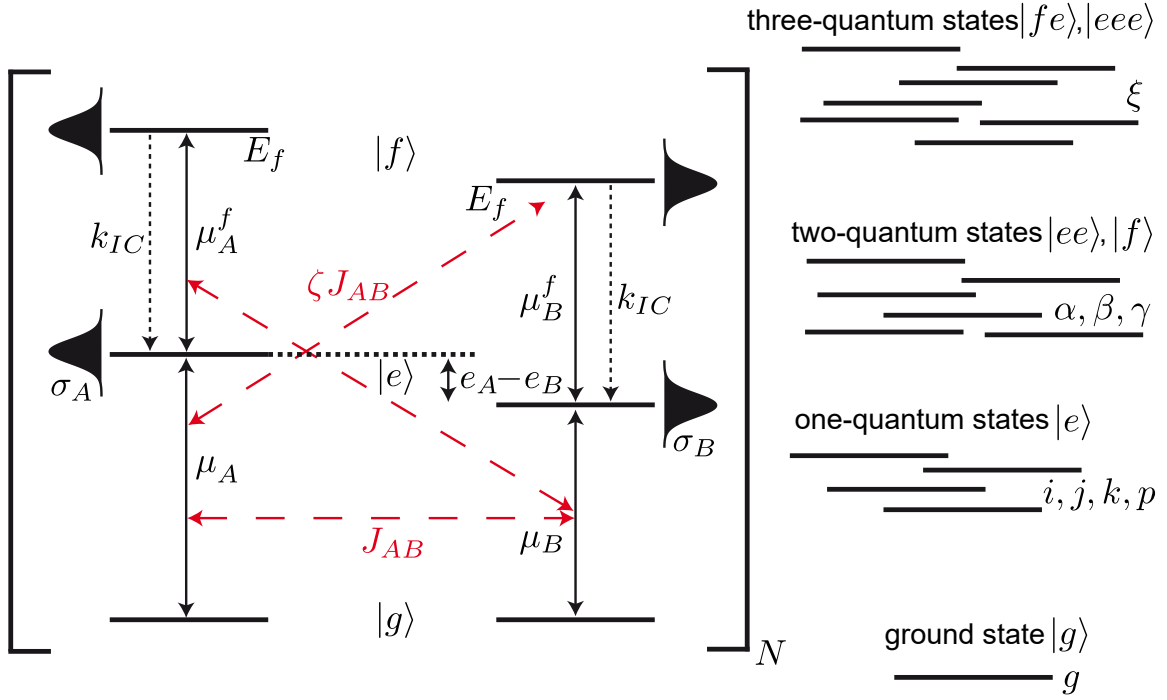
Figure 7.7.: Parameters of the SQA–SQB dimer units (left) and the structure of the electronic states (right). The coupling between the different transitions is marked in red. Reprinted from Ref. [12], with the permission of AIP Publishing.

Here $|g\rangle$ is the collective ground state and $|e{:}n\rangle$, $|e{:}nm\rangle$, and $|e{:}nml\rangle$ are electronic collective states in which one, two or three molecules, respectively, are excited to their first excited state. The states can be grouped into zero-, one-, two-, and three-quantum state manifolds, corresponding to the number of excited electronic quanta. The two-quantum states also feature the higher excited states of the molecules:

$$|f{:}n\rangle = |g_1\rangle \dots |f_n\rangle \dots |g_N\rangle \,. \tag{7.46}$$

The three-quantum states then also include a combination of a higher-excited molecule n and singly-excited molecule m:

$$|f{:}n, e{:}m\rangle = |g_1\rangle \dots |f_n\rangle \dots |e_m\rangle \dots |g_N\rangle \,, \tag{7.47}$$

The electronic states, grouped in their respective manifolds, are schematically depicted in Fig. 7.7, together with the parameters used further in the text. The Hamiltonian of

the N coupled molecules comprising the polymer is in the collective basis defined as:

$$
\begin{aligned}
H_{\text{agg}} = {} & |g\rangle\, e_g\, \langle e_g| + \sum_n |e{:}n\rangle\, (e_n + \delta e_n)\, \langle e{:}n| \\
& + \sum_{n<m} |e{:}nm\rangle\, (e_n + \delta e_n + e_m + \delta e_m)\, \langle e{:}nm| \\
& + \sum_n |f{:}n\rangle\, (e_n + e_f + \delta e_n)\, \langle f{:}n| \\
& + \sum_{n,m} |f{:}n, e{:}m\rangle\, (e_n + e_f + \delta e_n + e_m + \delta e_m)\, \langle f{:}n, e{:}m| \\
& + \sum_{n<m} |e{:}nml\rangle\, (e_n + \delta e_n + e_m + \delta e_m + e_l + \delta e_l)\, \langle e{:}nml| \\
& + \sum_{n\neq m} |e{:}n\rangle\, J_{nm}\, \langle e{:}m| + \sum_{n<m, k<l} |e{:}nm\rangle\, J_{e{:}nm;e{:}kl}\, \langle e{:}kl| \\
& + \sum_{n<m,k} \left(|e{:}nm\rangle\, J_{e{:}nm;f{:}k}\, \langle f{:}k| + |f{:}k\rangle\, J_{e{:}nm;f{:}k}\, \langle e{:}nm| \right) \\
& + \sum_{n<m<p, k<l<q} |e{:}nmp\rangle\, J_{e{:}nmp;e{:}klq}\, \langle e{:}klq| \\
& + \sum_{n\neq k, m\neq l} |f{:}n, e{:}k\rangle\, J_{f{:}n,e{:}k;f{:}m,e{:}l}\, \langle f{:}m, e{:}l| .
\end{aligned}
\tag{7.48}
$$

The first four lines comprise the diagonal elements: the energies of the zero-quantum, one-quantum, two-quantum, and three-quantum states. The last three lines describe the electronic coupling between the transitions between the states differing by one quantum (of visible light needed for the optical transition). The coupling between the one-exciton transitions in molecules n and m is J_{nm}. The coupled two-exciton states have to differ by one quantum: $J_{e{:}nm;e{:}kl} = J_{nk}\delta_{ml} + \delta_{nk}J_{ml}$ (δ_{ij} is the Kronecker delta), and an analogous expression holds pairwise for the three-exciton states. For simplicity, we take the coupling for the transitions to the higher states as $J_{e{:}nm;f{:}k} = \zeta\,(\delta_{kn} + \delta_{km})\,J_{nm}$, where ζ is just a proportionality factor. We calculate the coupling between the one-exciton transitions, J_{nm}, in the dipole–dipole approximation between all molecules according to literature [24].

The polymer transition dipole moment operator describes all possible one-quantum transitions between the molecules:

$$
\begin{aligned}
\mu = {} & \sum_n \left(|g\rangle\, \mu_n\, \langle e{:}n| + \text{h.c.} \right) + \sum_{n<m} \left(|e{:}nm\rangle\, \mu_n\, \langle e{:}m| + \text{h.c.} + |e{:}nm\rangle\, \mu_m\, \langle e{:}n| + \text{h.c.} \right) \\
& + \sum_n \left(|f{:}n\rangle\, \mu_n^f\, \langle e{:}n| + \text{h.c.} \right) + \sum_{n\neq m, k<l} \left(|f{:}n, e{:}m\rangle\, \mu_n^f (\delta_{nk}\delta_{ml} + \delta_{nl}\delta_{mk})\, \langle e{:}kl| + \text{h.c.} \right) \\
& + \sum_{n<m<l, p<q} \left(|e{:}nml\rangle\, (\delta_{mp}\delta_{lq}\mu_n + \delta_{np}\delta_{lq}\mu_m + \delta_{np}\delta_{mq}\mu_l)\, \langle e{:}pq| + \text{h.c.} \right),
\end{aligned}
\tag{7.49}
$$

wherein h.c. indicates the Hermitian conjugate of the previous term and μ_n the transition dipole moment between the the ground and first excited state of the n-th molecule. Analogously, μ_n^f is the transition dipole moment between the first excited state and a

higher excited state. In the same spirit as for the electronic couplings, we consider for simplicity $\mu_n^f \propto \mu_n$ (with a different proportionality constant compared to the case for the couplings, see Table 7.2 and Table 7.3). The (multi)excitonic states arise when the whole system Hamiltonian is diagonalized:

$$H_e = C^T H_{\text{agg}} C, \tag{7.50}$$

where C is a (orthonormal) transformation matrix from the site basis to the excitonic basis, with coefficients c_n^i (n for molecule and i for excitons) and ^{T} denotes transposition. The H_e is diagonal, with values representing the energies of the states ϵ_i, as indicated also in Fig. 7.7 (right).

The transitions between the (multi)excitonic states are described by the transformed transition dipole moment operator:

$$\mu_e = C^T \mu C. \tag{7.51}$$

System Dynamics

As we consider spectrally integrated response in this work, we will be interested only in the dynamics of the excitons in the waiting time. Moreover, we will employ a secular approximation and treat the population dynamics only. Such population dynamics can be separated into exciton transfer and EEI (exciton–exciton interaction, i.e., annihilation). We calculate the population transfer by Redfield theory [304], with rates given by state delocalization and the available bath modes. The transition rate k_{ij} from exciton $|j\rangle$ to exciton $|i\rangle$ is

$$k_{ij} = \sum_n |c_n^i|^2 |c_n^j|^2 \nu_n C(\omega_{ji}). \tag{7.52}$$

Here c_n^i are the elements of the transformation matrix C, $\hbar\omega = e_j - e_i$ is the excitonic energy gap, and ν_n is the scaling of the strength of the interaction of molecule n with the bath, described by its spectral density $C(\omega)$.

The transfer between two-exciton states (from state β to α) can be expressed by Redfield theory as well [184],

$$k_{\alpha\beta}^{ee} = \sum_{n<m,k<l} (\delta_{nk} + \delta_{nl} + \delta_{mk} + \delta_{ml}) c_{nm}^\alpha c_{nm}^\beta c_{kl}^\alpha c_{kl}^\beta C(\omega_{\beta\alpha}). \tag{7.53}$$

Here, similar to the one-exciton case, c_{nm}^α are the respective elements of the transformation matrix to the multi-exciton basis.

For simplicity, we assume the same form of interaction with the environment for all excited states and thus take the energy-gap function of the higher excited $|f_n\rangle$ states proportional to that of the $|e_n\rangle$ states, with the proportionality constant ϕ. As the bath modes are the same, we allow for a partial correlation of the energy-gap fluctuations for the $|f_n\rangle$ and $|e_n\rangle$ states (reflected by $\phi_{\text{corr}} \in [0,1]$). In this description, the $|f_n\rangle$ states contribute to the two-exciton transfer Redfield rates by the following

two terms:

$$k_{\alpha\beta}^{fee} = \phi_{\mathrm{corr}}\phi \sum_{n<m,k} (\delta_{nk} + \delta_{mk})c_{nm}^{\alpha}c_{nm}^{\beta}c_{fk}^{\alpha}c_{fk}^{\beta}C(\omega_{\beta\alpha}), \qquad (7.54)$$

$$k_{\alpha\beta}^{f} = \phi^2 \sum_{n} |c_{fn}^{\alpha}|^2 |c_{fn}^{\beta}|^2 C(\omega_{\alpha\beta}). \qquad (7.55)$$

In our calculations we set a weak correlation of $\phi_{\mathrm{corr}} = 0.1$, in agreement with the previous work, but the influence of correlation appears negligible in our parameter range anyway. The second term is the transfer of the exciton through the $|f_n\rangle$ states. It is this term that is responsible for the first step of the exciton–exciton annihilation. The overall transfer rate in the two-quantum manifold is

$$k_{\alpha\beta} = k_{\alpha\beta}^{ee} + k_{\alpha\beta}^{fee} + k_{\alpha\beta}^{f}. \qquad (7.56)$$

As we described at the beginning of this sub-section, we do not treat the coherence dynamics, as this reduces significantly the computational effort. Any oscillatory dynamics of the signal due to the excitonic coherent motion is thus not taken into account.

We already described the first stage of the exciton–exciton annhilation, in which the two-exciton state changes into one of the higher molecular excited state $|f_n\rangle$. From these states, rapid internal conversion occurs with an internal conversion rate k_{IC}. Formulated using a Lindblad formalism [24], the decay rate of the mixed two-quantum state $|\alpha\rangle$ into a (one-quantum) exciton $|k\rangle$ is

$$k_{k\alpha} = \sum_{n} |c_n^k|^2 |c_{fn}^{\alpha}|^2 k_{\mathrm{IC}}. \qquad (7.57)$$

For the long-time exciton dynamics, one has to consider the finite lifetime τ_R of the excitons due to radiative and non-radiative recombination. Since the exciton lifetime is longer than other processes such as transfer and annihilation (separation of timescales), the details of the exciton non-radiative and radiative decay are not relevant and it is sufficient to describe it with a rate constant $k_R = \tau_R^{-1}$ resulting in an exponential decay.

In this rate picture, the evolution of the system as a function of waiting time is given by the master equation for the state populations

$$\frac{d\rho(T)}{dT} = \mathcal{K}\rho(T), \qquad (7.58)$$

where $\rho(T)$ is the system density matrix at time T and $\mathcal{K}$ is a matrix containing all the population transfer rates, with the elements given by the rate expressions above. For the population dynamics, only the diagonal elements of the density matrix ρ are taken into account. The master equation is solved by using a time-evolution propagator $\mathcal{U}(T)$,

$$\rho(T) = \mathcal{U}(T)\rho(0), \qquad (7.59)$$

starting from the initial density matrix $\rho(0)$ (after interaction with the pump pulses).

The propagator is obtained by a matrix exponential of the rate matrix multiplied by the time,

$$\mathscr{U}(T) = \exp(\mathscr{K}T). \tag{7.60}$$

The elements of the propagator matrix such as $\mathscr{U}_{ii,jj}(T)$, contain conditional probabilities for the system starting at time zero in a particular state (here $|j\rangle$) to be at time T in other particular state (here $|i\rangle$). The propagator matrix elements are used directly in the response pathway formulas given in the main text.

7.6.4. Parameters for the Simulation of a Heterodimer

Table 7.2 lists the relevant parameters employed in the simulation of the heterodimer system (definitions are the same as in our previous publication) [7]. In order to demonstrate the effects of annihilation and localization more clearly, the system was defined with a few simplifications as compared to a real-world molecular system. The energetic disorder σ was set to zero and we assumed that the higher excited states of the monomers cannot be excited directly ($\mu_f = 0$).

Table 7.2.: Parameters that were used for the simulations in Sec. 7.3 (for ease of comparison all quantities were converted to wavenumbers or femtoseconds).

Quantity	Variable	Value
Transition energy of the first excited state of the monomer with the lower energy	e_B	13500 cm^{-1}
Energy gap between the first excited states of the monomers	ΔE	400 cm^{-1}
Transition energy between first and higher excited state	E_f	11800 cm^{-1}
Electronic coupling between first-excited-state transitions	J	-200 cm^{-1}
Higher-state transition coupling scale	J_{fe}/J_{eg}	2
Monomeric transition dipole moment	$\mu_A = \mu_B$	1.0
Scaling of coupling to the bath	$\nu_A = \nu_B$	1.0
Scaling of coupling to the bath to higher excited states	$\nu_{A,B}^f/\nu_{A,B}$	4.0
Bath reorganization energy	λ	180 cm^{-1}
Bath inverse correlation time	Λ	300 cm^{-1}
Exciton lifetime	τ_R	1000 ps
Internal conversion time	τ_{IC}	30 fs
Scaling factor of the fluctuation between first-excited states and higher-excited states	ϕ_{corr}	0.1
Strong vibrational mode parameters: frequency, damping, Huang–Rhys factor	$\Omega, \gamma,$ S	1280 cm^{-1}, 10 cm^{-1}, 0.18

7.6.5. Sensitivity of the EEI2D Signal to Exciton–Exciton Annihilation in a Heterodimer
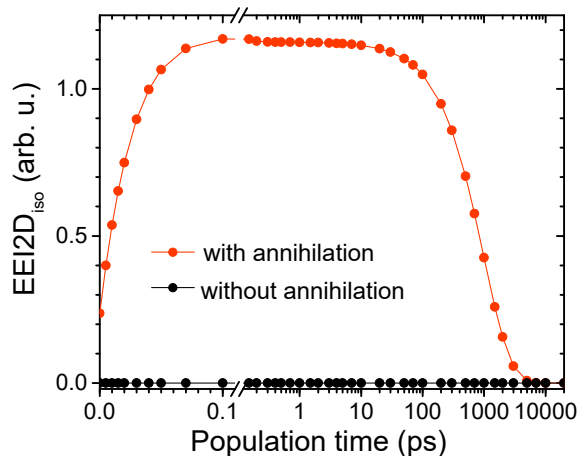
Figure 7.8.: Isotropic EEI2D signal of a heterodimer with a localization time of 200 fs. For the red curve the annihilation time in the localized set of states was set to 50 fs while for the black curve the parameters were chosen in such a way that no annihilation in the system occurs. Reprinted from Ref. [12], with the permission of AIP Publishing.

In Fig. 7.8 we demonstrate that the EEI2D signal is dominated by exciton–exciton annihilation. We prevent any annihilation in the heterodimer of Sec. 7.3. In order to achieve this, we set the higher-state transition coupling scaling (J_{fe}/J_{eg}) in the delocalized set of states to zero. This effectively decouples the higher-excited states from the biexciton states in the delocalized set of states. In addition, we set the annihilation time in the localized set of states to 10 ns, which is much longer than the lifetime of 1 ns. As can be seen the signal where no annihilation is allowed (Fig. 7.8, black curve) is much lower than the signal where annihilation is allowed. In an experiment, the signal without annihilation would probably be lower than the noise level. Note that in principle also a direct excitation of higher excited states can contribute to the EEI2D signal. For large aggregates their contribution is small as shown recently [7]. However, in all our calculations the transition dipole moments of these higher excited states were set to zero.

7.6.6. Limits of the Anisotropy Value in EEI2D Spectroscopy

Rotational averaging gives us the opportunity to calculate the maximum and minimum value of the anisotropic EEI2D signal of an isotropic sample. We obtain EEI2D anisotropy in analogy to linear fluorescence anisotropy [278] by

$$\mathrm{EEI2D}_{\mathrm{aniso}} = \frac{\mathrm{EEI2D}_\parallel - \mathrm{EEI2D}\perp}{\mathrm{EEI2D}\| + 2\mathrm{EEI2D}\perp}, \tag{7.61}$$

where $\mathrm{EEI2D}_\parallel$ is the integrated EEI2D signal measured with parallel excitation and detection polarization and $\mathrm{EEI2D}_\perp$ measured with perpendicular polarization of excitation and detection. The maximum anisotropy signal corresponds to a situation when the sample is excited by a linear polarization and no process of depolarization takes place [278]. In order to calculate the boundaries for the anisotropy in EEI2D spectroscopy, we can use the rotationally averaged tensors

$$\widehat{T}^{(6)}_{AAAAAA} = \frac{1}{210} \sum_{abcdef} \quad \Big(2\delta_{ab}\delta_{cd}\delta_{ef} + 2\delta_{ab}\delta_{ce}\delta_{df} + 2\delta_{ab}\delta_{cf}\delta_{de}$$
$$+2\delta_{ac}\delta_{bd}\delta_{ef} + 2\delta_{ac}\delta_{be}\delta_{df} + 2\delta_{ac}\delta_{bf}\delta_{de}$$
$$+2\delta_{ad}\delta_{bc}\delta_{ef} + 2\delta_{ad}\delta_{be}\delta_{cf} + 2\delta_{ad}\delta_{bf}\delta_{ce}$$
$$+2\delta_{ae}\delta_{bc}\delta_{df} + 2\delta_{ae}\delta_{bd}\delta_{cf} + 2\delta_{ae}\delta_{bf}\delta_{cd}$$
$$+2\delta_{af}\delta_{bc}\delta_{de} + 2\delta_{af}\delta_{bd}\delta_{ce} + 2\delta_{af}\delta_{be}\delta_{cd} \Big)$$
$$t^{(6)}_{abcdef} \tag{7.62}$$

and

$$\widehat{T}^{(6)}_{AABBBB} = \frac{1}{210} \sum_{abcdef} \quad \Big(6\delta_{ab}\delta_{cd}\delta_{ef} + 6\delta_{ab}\delta_{ce}\delta_{df} + 6\delta_{ab}\delta_{cf}\delta_{de}$$
$$-1\delta_{ac}\delta_{bd}\delta_{ef} - 1\delta_{ac}\delta_{be}\delta_{df} - 1\delta_{ac}\delta_{bf}\delta_{de}$$
$$-1\delta_{ad}\delta_{bc}\delta_{ef} - 1\delta_{ad}\delta_{be}\delta_{cf} - 1\delta_{ad}\delta_{bf}\delta_{ce}$$
$$-1\delta_{ae}\delta_{bc}\delta_{df} - 1\delta_{ae}\delta_{bd}\delta_{cf} - 1\delta_{ae}\delta_{bf}\delta_{cd}$$
$$-1\delta_{af}\delta_{bc}\delta_{de} - 1\delta_{af}\delta_{bd}\delta_{ce} - 1\delta_{af}\delta_{be}\delta_{cd} \Big)$$
$$t^{(6)}_{abcdef}, \qquad A \neq B. \tag{7.63}$$

Following Eqs. (7.62) and (7.63), the parallel and perpendicular signals are $\mathrm{EEI2D}_\parallel = \widehat{T}^{(6)}_{AAAAAA}$ and $\mathrm{EEI2D}_\perp = \widehat{T}^{(6)}_{AABBBB}$. A situation in which no depolarization takes place can be expressed by $a = b = c = d = e = f$. Using this condition in Eq. (7.62) and Eq. (7.63), the contributions are

$$\mathrm{EEI2D}_\parallel = \frac{30}{210} = \frac{1}{7} \tag{7.64}$$

and

$$\text{EEI2D}_\perp = \frac{6}{210} = \frac{1}{35}. \tag{7.65}$$

Therefore the maximum anisotropy is $4/7 \approx 0.5714$. The minimum value of anisotropy corresponds to $a = b \neq c = d = e = f$. The values for $\text{EEI2D}_\parallel$ and $\text{EEI2D}_\perp$ are then

$$\text{EEI2D}_\parallel = \frac{6}{210} = \frac{1}{35} \tag{7.66}$$

and

$$\text{EEI2D}_\perp = \frac{18}{210} = \frac{3}{35}. \tag{7.67}$$

From this it follows that the minimum anisotropy value is $-2/7 \approx -0.2857$. Note that these are the same boundaries as for two-photon fluorescence anisotropy measurements [278]. To illustrate the limits of anisotropy with an example, we calculated a similar
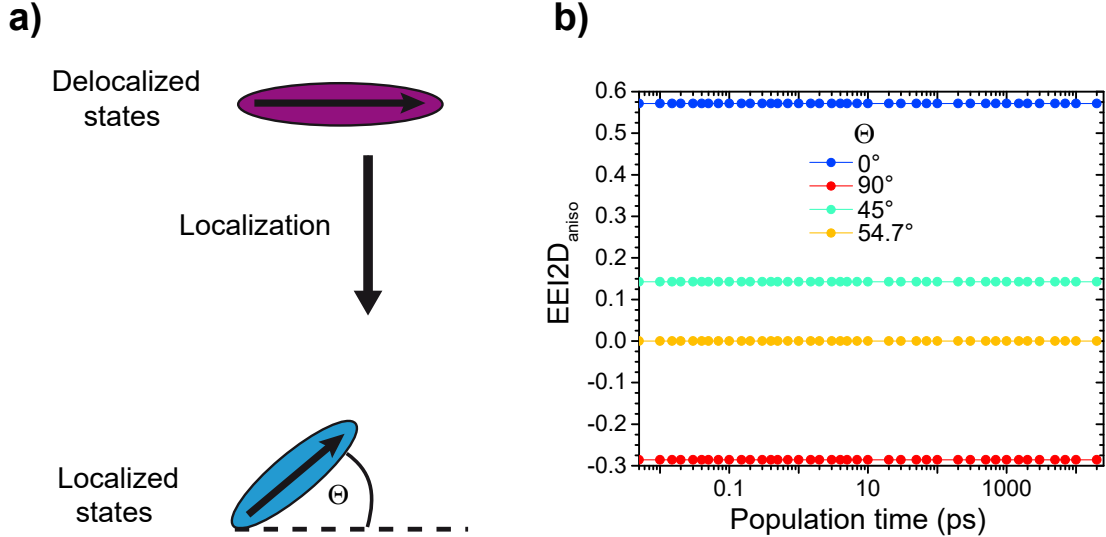
Figure 7.9.: Demonstration of the limits of EEI2D anisotropy in a system of a heterodimer. (a) In both sets of states, the dipole moments point along the same direction. For this particular situation, only one of the single-exciton states is bright. The localized states are tilted by an angle Θ compared to the delocalized states. The two transition dipole moments of the two states are directly on top of each other. (b) Anisotropy for a varying angle Θ. Reprinted from Ref. [12], with the permission of AIP Publishing.

heterodimer as in Sec. 7.3 of the manuscript, but in order to demonstrate the minimum and maximum values of anisotropy we modified the orientations of both sets of states in the following way. In the new calculation of the present section, both monomers in the delocalized sets of states point along the same direction. In addition we set the energy difference ΔE between the first-excited states of the monomers to zero which results in two exciton states. In this specific situation the delocalization is 50% and only one of the two exciton states is bright. The localized first-excited states are both

tilted by an angle Θ compared to the delocalized set of states which means both arrows in Fig. 7.9a are directly on top of each other. As a further simplification we prevent any annihilation in the delocalized set of states by decoupling the higher-excited states and the single-excited states ($J_{fe}/J_{eg} = 0$). The localization time was set to 200 fs while the annihilation time in the localized set of states was 50 fs. The situation is schematically depicted in Fig. 7.9a.

The anisotropy reaches the maximum value if the localized states are parallel to the delocalized set of states (Fig. 7.9b, dark blue curve). By contrast, if the localized states are perpendicular to the delocalized states, the anisotropy reaches the calculated minimum (Fig. 7.9b, red curve). If the states are tilted by an angle of 45°, the anisotropy is exactly in between the maximum and the minimum value (1/7) (Fig. 7.9b, green curve). For an angle of 54.7°, the anisotropy is zero (Fig. 7.9b, yellow curve). This situation is analogous to setting the probe polarization to the magic angle, but in our case the initial polarization, caused by interaction with the pump pulse(s), is rotated by the magic angle due to the process of localization, so that altogether this results in a purely isotropic signal.

7.6.7. Parameters for Simulations of Squaraine Copolymers

The parameters for our simulations in Sec. 7.4 are the same parameters as in our previous publication about squaraine copolymers [7] with two exceptions. For the sake of simplification, we chose not to allow a direct excitation of the higher excited states ($\mu_{A,B}^{f}/\mu_{A,B} = 0$). However, we showed already that their contribution in extended systems is small [7]. Compared to our earlier publication we now calculate the coupling directly in the dipole–dipole approximation.

Table 7.3.: Parameters that were used for the simulations in Sec. 7.4 (for ease of comparison all quantities were converted to wavenumbers or femtoseconds).

Quantity	Variable	Value
SQB transition energy	e_B	13500 cm^{-1}
SQA–SQB energy gap	ΔE	1200 cm^{-1}
Transition energy between first and higher excited state	E_f	12200 cm^{-1}
Energetic disorder width	$2\sigma_A,$ $2\sigma_B$	$250 \text{ cm}^{-1},$ 500 cm^{-1}
Higher-state transition coupling scale	J_{fe}/J_{eg}	2
Monomeric transition dipole moment	$\mu_A, \mu_B,$	1.2, 1.0
Transition dipole to higher states scaling	$\mu_{A,B}^{f}/\mu_{A,B}$	0.0
Scaling of coupling to the bath	ν_A, ν_B	1.0, 1.66
Scaling of coupling to the bath to higher excited states	$\nu_{A,B}^{f}/\nu_{A,B}$	4.0
Bath reorganization energy	λ	180 cm^{-1}
Bath inverse correlation time	Λ	300 cm^{-1}
Exciton lifetime	τ_R	1091 ps
Internal conversion time	τ_{IC}	30 fs
Scaling factor of the fluctuation between first-excited states and higher-excited states	ϕ_{corr}	0.1
Strong vibrational mode parameters: frequency, damping, Huang–Rhys factor	$\Omega, \gamma,$ S	$1280 \text{ cm}^{-1}, 10 \text{ cm}^{-1},$ 0.18

7.6.8. Sensitivity of the EEI2D Signal to Exciton–Exciton Annihilation in a Polymer with a Kink
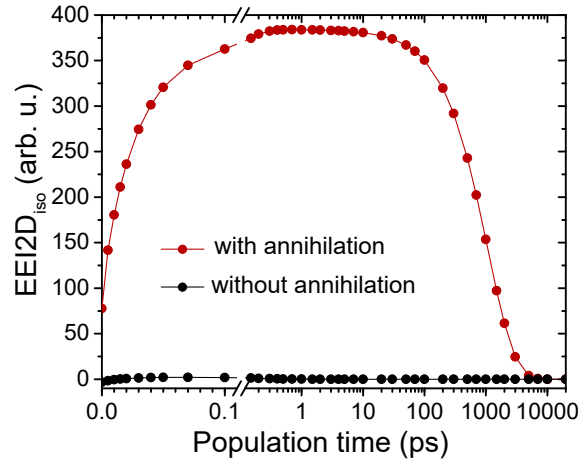
Figure 7.10.: Isotropic EEI2D signal of a polymer with a central kink of 50° with annihilation (red) and without annihilation (black). Reprinted from Ref. [12], with the permission of AIP Publishing.

In Fig. 7.10 we demonstrate that the EEI2D signal is dominated by exciton–exciton annihilation in a polymer with a central kink of 50°. To prevent any annihilation event, we set the higher-state transition coupling scaling (J_{fe}/J_{eg}) to zero (compare Fig. 7.8). Direct excitation of higher excited states does not contribute since we set the transition dipole moments of these states in all the performed calculations to zero (Sec. 7.6.7). Clearly, the signal without any annihilation (Fig. 7.10, black) is much lower than the signal in the case where annihilation is allowed (Fig. 7.10, red) and would probably not be sufficiently higher than the noise in an experiment.

7.6.9. Sensitivity of the EEI2D Signal to Exciton–Exciton Annihilation in a Polymer with Varying Geometric and Energetic Disorder
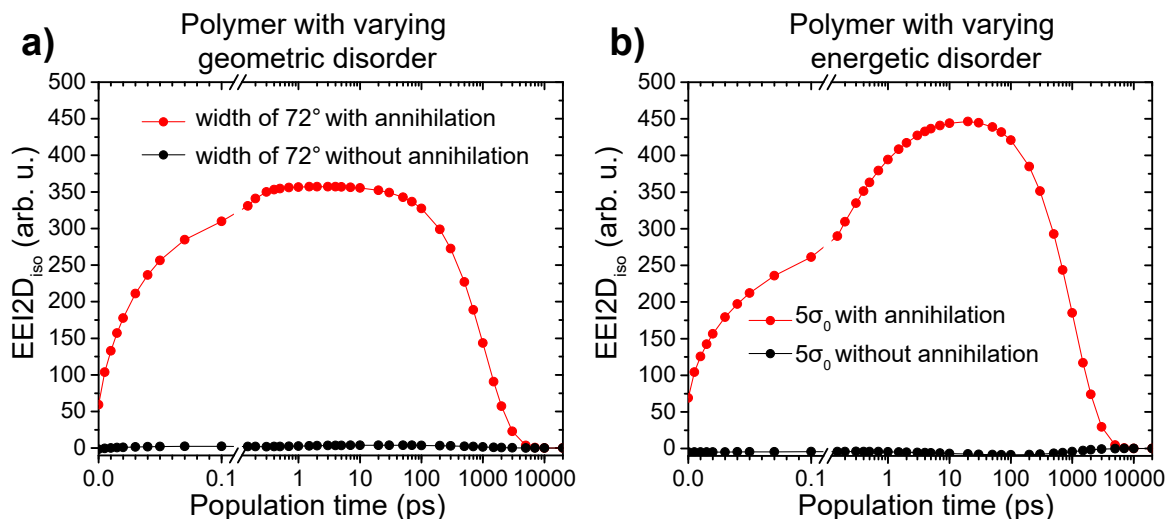
Figure 7.11.: Sensitivity of the isotropic EEI2D signal in the presence (red) or absence (black) of exciton–exciton annihilation in polymers with different types of disorder. (a) Large geometric disorder. (b) Large energetic disorder. Reprinted from Ref. [12], with the permission of AIP Publishing.

We demonstrate the sensitivity of the EEI2D signal to annihilation for a polymer with either large geometric (Fig. 7.11a) or energetic disorder (Fig. 7.11b) by setting the higher-state coupling scaling (J_{fe}/J_{eg}) to zero. In both cases of disorder the curves of the EEI2D signal where any annihilation is forbidden (Fig. 7.11a, black curve and Fig. 7.11b, black curve) have a much lower amplitude than the corresponding curves where annihilation is allowed (Fig. 7.11a, red curve and Fig. 7.11b, red curve). The EEI2D signal without annihilation might probably not be detectable in an experiment.

7.6.10. Absorption Spectra for Varying Energetic Disorder and Varying Geometric Disorder
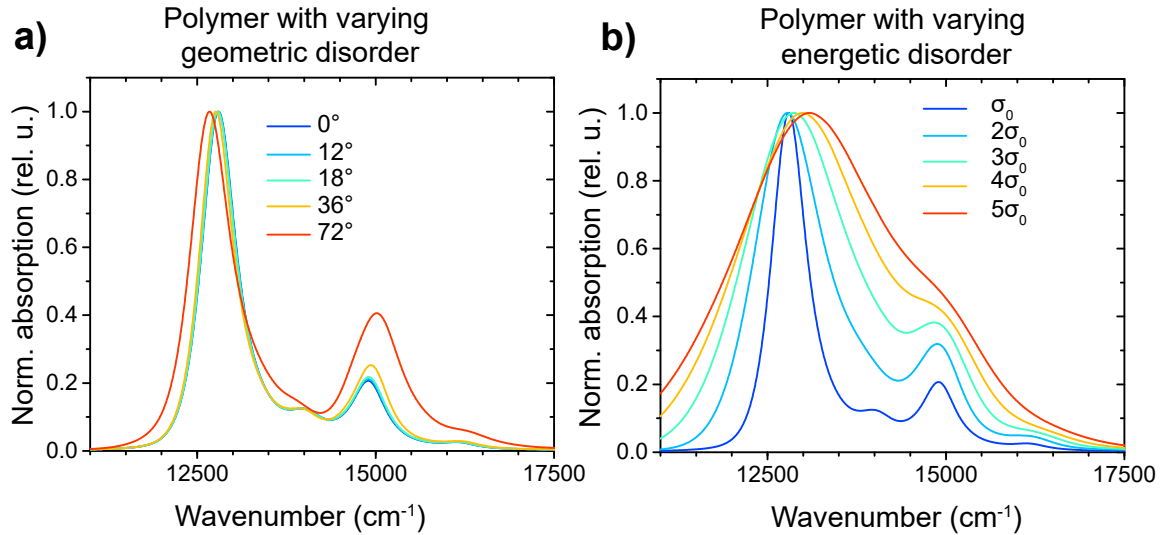
Figure 7.12.: Absorption spectra of a copolymer made out of twenty monomers. (a) Effect of varying geometric disorder. The legend refers to the width of the distribution of the angle deviation from the linear configuration. (b) Effect of varying energetic disorder. σ_0 corresponds to the width of the disorder which was used in the other calculations (250 cm^{-1} and 500 cm^{-1} for SQA and SQB, respectively). Reprinted from Ref. [12], with the permission of AIP Publishing.

In Fig. 7.12a and Fig. 7.12b we show the absorption spectra of a polymer with varying geometric disorder and varying energetic disorder, respectively. For moderate geometric disorder, the absorption spectrum does not change substantially. For large geometric disorder, such as a geometric variation with a width of 72° (Fig. 7.12a, red curve), the ratio of the peaks changes and the peaks also get broader. For increasing energetic disorder (Fig. 7.12b), the peaks in the absorption spectrum get substantially broader. For low energetic disorder of σ_0 (Fig. 7.12b, dark blue curve), several peaks in the absorption spectrum can be distinguished. For up to a double energetic disorder, the effect on the spectrum is similar as that of large structural disorder. For larger energetic disorder, the structure becomes less and less visible until, for the highest disorder of $5\sigma_0$, only a single peak with a broad lineshape and shoulder remains visible. Clearly, both kinds of disorder have an effect on the absorption spectra which makes it difficult to utilize the linear absorption spectrum alone to retrieve the amount of geometric or energetic disorder in a polymer.

7.6.11. Polymer with Varying Coupling
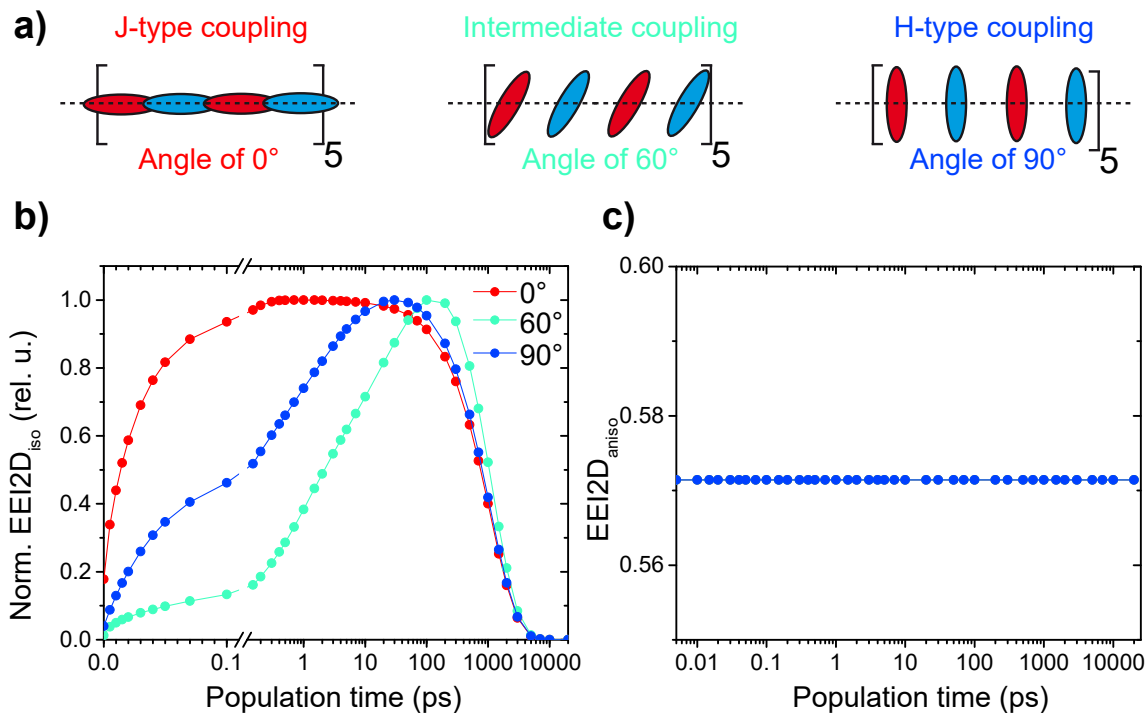
Figure 7.13.: Effect of varying coupling between the monomers of a copolymer. (a) The coupling of the monomers is varied by changing the angle of the monomers with respect to each other. (b) Isotropic EEI2D signal for varying coupling. (c) Anisotropic EEI2D signal for varying coupling. Reprinted from Ref. [12], with the permission of AIP Publishing.

In order to investigate the effect of different couplings within one polymer strand, we varied the angle between the monomers (Fig. 7.13a). The isotropic EEI2D signal rises more slowly if the coupling is smaller. For a geometry of 60°, where the coupling is close to zero, the plateau is reached at 100 ps (Fig. 7.13b, green curve). If we increase the angle further to 90° (Fig. 7.13b, dark blue curve), the coupling is larger but the absolute value is still only half as large as for an angle of zero degrees. Therefore the plateau is reached faster than in the case of 60° orientation but later than for an orientation of 0° (Fig. 7.13b, red curve). For an orientation of zero degrees the coupling is largest and the plateau is reached fastest (Fig. 7.13b, red curve). Since the polymer is homogeneous, the polarization does not change via exciton transport. This results in a constant value for the anisotropy at 4/7 (Fig. 7.13c).

7.6.12. Isotropic Signal of a Polymer with Two Domains

Figure 7.14.: Polymer with two different geometric domains and varying mutual coupling. (a) The coupling between the two geometric domains is changed as indicated by the larger distance between the domains. (b) Isotropic EEI2D signal of the polymer with geometric domains and mutual varying coupling. The EEI2D signal in the situation where no annihilation is allowed is shown in black. Reprinted from Ref. [12], with the permission of AIP Publishing.

As discussed in Sec. 7.4.3, anisotropy in EEI2D spectroscopy is sensitive to the coupling between different geometric domains. However, the isotropic signal undergoes interesting dynamics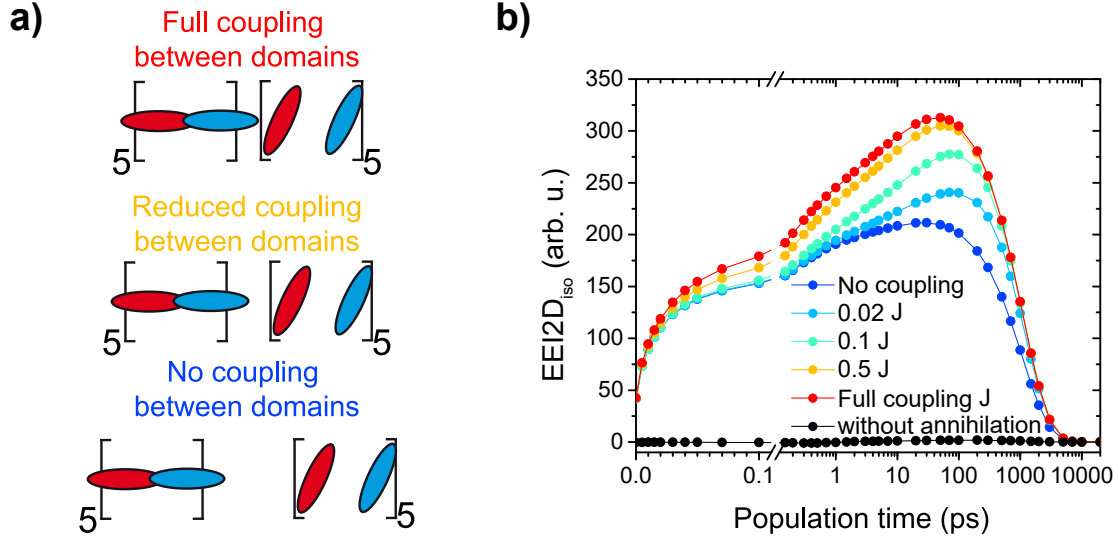 for different couplings between the domains as outlined in the main text. Here, we show a situation in which only the coupling between the domains is varied but not within the domains. Schematically, this is illustrated in Fig. 7.14a by a varying distance between the two domains. In Fig. 7.14b we show the isotropic signal for a polymer with varying coupling, but in contrast to Sec. 7.4.3 the curves are not normalized. Let us first focus on the curves in which coupling between the different domains is realized. For a coupling smaller than the full coupling, such as a fraction of 0.5 of the full coupling (Fig. 7.14b, yellow curve), the plateau is reached at later times than for full coupling between the domains (Fig. 7.14b, red curve). This trend is also visible for smaller couplings such as 0.1 and 0.02 of the full coupling (Fig. 7.14b, green and light blue curves, respectively). The coupling between the domains is the bottleneck for excitons to get transferred from one domain to the other. However, for zero coupling between the domains the plateau is reached at earlier times even compared to the case of full coupling between the domains. If the coupling between the domains is zero, the signal is set by annihilation on the two individual domains. Here the exciton–exciton annihilation is much faster because of the smaller size of the fragments. The amplitude of the EEI2D signal changes with the coupling since the

excitonic structure is broken by the change of coupling between the two domains. To demonstrate this, let us take a closer look at the extreme cases of full coupling and no coupling between the domains. For the case of full coupling, there are $\binom{20}{2}$ biexciton states and 20 higher-excited states which gives in total 210 two-quantum states. For no coupling between the domains, only the two-quantum states within one domain contribute to the EEI2D signal. For two domains with ten monomers there are $2 \cdot \binom{10}{2}$ biexciton states and 20 higher excited states, which gives 110 two-quantum states in total. The higher EEI2D signal amplitude reflects the higher number of biexciton states which contribute to the EEI2D signal by exciton–exciton annihilation.

Additionally, we show the situation where the domains are fully coupled but no annihilation in both domains is allowed (Fig. 7.14, black curve). In this case we set the higher-excited state coupling scale to zero ($J_{fe}/J_{eg} = 0$). The low amplitude of the signal in the case where no annihilation is allowed justifies that the EEI2D signal is dominated by exciton–exciton annihilation. In an experiment, the EEI2D signal without annihilation might not be large enough to be detected.

7.6.13. Polymer with Two Domains with Varying Angle
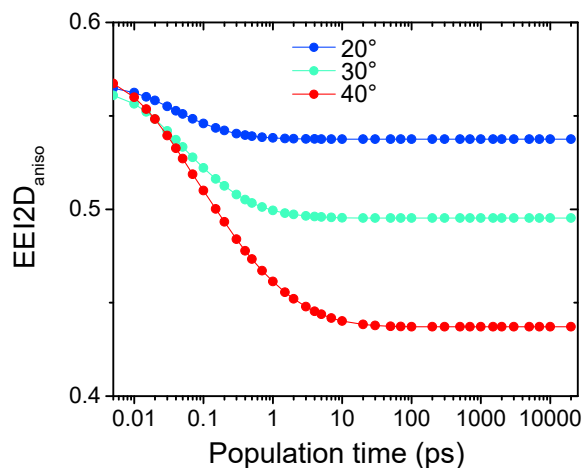
Figure 7.15.: Anisotropic signal for a polymer with two domains where the geometric orientation of the domains with respect to each other is changed. Reprinted from Ref. [12], with the permission of AIP Publishing.

In Fig. 7.15 we show the anisotropy of a polymer with two different domains. Here we changed the orientation of the domains relative to each other. In Sec. 7.4.3, the angle was fixed to 65°. Here, the anisotropy was calculated for an angle of 20° (Fig. 7.15, dark blue curve), 30° (Fig. 7.15, green curve) and 40° (Fig. 7.15, red curve). Clearly, the final value of anisotropy is smaller if the angle is larger. For a larger angle, the change in the direction of transition dipole moment which is caused by exciton transfer from one domain to the other is more substantial. Therefore the anisotropy decay is stronger for a larger angle between the two domains.

CHAPTER 8

Direct Comparison of Higher-Order Pump–Probe and Two-Dimensional Spectroscopy

Time-resolved spectroscopy is commonly used to study diverse phenomena in chemistry, biology, and physics. Pump–probe (PP) experiments and two-dimensional (2D) spectroscopy have resolved site-to-site energy transfer, visualized electronic couplings, and much more. In both techniques, one desires to acquire a nonlinear signal that is based on the polarization of third order in the electric field according to a perturbative expansion. At high excitation intensities, however, additional interactions with the excitation field can occur and lead to a contamination of the measured signal with higher-order terms, i.e., higher than third order in terms of polarization. In recent years, higher-order 2D spectroscopy was developed specifically to measure such signals, bringing new insight into highly excited states and multi-particle dynamics. In 2D spectroscopy, signals can be separated into various nonlinear orders by resolving their oscillating frequency along the excitation axis. In the present work, we provide the theoretical background for such experiments. In particular, we analyze quantitatively the emergence of higher-order signals and their contamination of lower orders, using the approach of combinatorial counting of double-sided Feynman diagrams that are generated in an automated fashion. We demonstrate how higher-order signals can be utilized to obtain clean nonlinear signals free of higher-order artifacts. Based on the analysis for 2D spectroscopy, we also discuss how the same multi-quantum separation can be realized for PP spectroscopy. Here the higher-order signals are separated by their individual power dependence. We derive the equations necessary to carry out such an analysis. Experimentally, we compare both techniques by isolating and cleaning up multi-quantum signals up to seventh order on the example of squaraine oligomers. Furthermore, we use higher-order PP spectroscopy to investigate single- and multi-exciton dynamics in squaraine polymers by extracting up to the thirteenth nonlinear order. Our approach demonstrates the full power of higher-order PP and 2D spectroscopic techniques to investigate multi-particle interactions in coupled systems.

8.1. Introduction

A common technique to investigate ultrafast phenomena is pump–probe (PP) spectroscopy. Here a first laser pulse excites a quantum system and after some time delay T ("waiting time" or "population time") another laser pulse probes the temporal evolution. The transient changes at each population time T can be constructed from the probe spectrum measured after the sample for the cases with and without a prior excitation pulse. Generally, the latter is divided by the former and taking the logarithm converts the data to an absorbance change. These transient maps, available as a function of T and of detection wavelength, can be used to investigate ultrafast dynamics [52, 60]. Two-dimensional (2D) spectroscopy can be viewed as an extension of PP spectroscopy that adds frequency resolution for the excitation step. 2D spectroscopy was used to investigate the dynamics of various different systems such as light-harvesting complexes [47, 79], reaction centers [41], quantum dots [305, 306], supramolecular aggregates [43, 197], molecular dimers [202], carbon nanotubes [284], and 2D materials [128, 199]. Exemplarily, one can extract information on relaxation processes [307], homogeneous and inhomogeneous line shapes [81], energy transfer [39], chemical reaction kinetics [48], vibrational and electronic coherences [83], and exciton delocalization [8]. It is worth pointing out that the extraction of state-to-state kinetic rate constants is uniquely determined for 2D spectroscopy under some basic conditions such as the spectral separation of excitonic states [78], unlike for PP spectroscopy where the kinetic modeling is not unique.

In 2D spectroscopy, a sequence of ultrashort laser pulses interacts with the system with varying time delays [23]. The total number of pulses for a conventional third-order 2D experiment is often either three or four depending on the beam geometry [73, 87]. Either way, this results in a 2D correlation map for each time step of the population time T in which one axis is the excitation axis and the other the detection axis. In such a 2D map, excitation and detection of the same transition results in a diagonal peak because the frequency in both steps is the same. Electronic couplings show up as cross peaks for $T = 0$, and energy transfer shows up as the time evolution of cross peaks for $T > 0$, obtained from scanning the population time T between the second pump pulse and the probe pulse [77]. Analysis of cross peaks can be used to determine properties such as exciton delocalization, energy transfer [79], or exciton–exciton annihilation [8] [120].

In the current work, we generalize the analysis to such cases in which cross peaks are separated by one or several multiples of the fundamental transition frequency and thus constitute "higher-quantum" peaks, and we also investigate their indirect influence on fundamental diagonal peaks or other, lower, multiple-quantum peaks. In conventional PP and 2D spectroscopy, one seeks to obtain the response in third order of perturbation theory. However, signals are often contaminated with higher-order contributions, and thus we must extend the analysis to higher orders. Under high laser excitation conditions, exciton–exciton interaction, in the form of exciton–exciton annihilation, will influence the single-exciton dynamics. Also, any other higher-excited states will

be excited and contribute to the signal. Such contaminations are well-known for a variety of systems and can be identified as a change in the dynamics of the third-order signal and as a deviation from the linear scaling with excitation power, e.g., a saturation [4, 20, 186, 205, 308–310]. Consider, for example, the investigation of photosynthesis with ultrafast spectroscopy [307, 311–313]. Natural light-harvesting systems utilize multiple chromophores to absorb light. These chromophores act as an "antenna" and a "funnel" directing the absorbed energy to the reaction center of the photosynthetic complex [61]. If in such a complex, single-exciton dynamics are investigated but the excitation power is too high, multiple excitons will be generated leading to distorted kinetics [186, 190, 240, 314]. In terms of interaction with the light field, such a regime can be described by additional interactions with the excitation fields, i.e., more than the usual two "pump" interactions in third-order nonlinear experiments. The onset of exciton–exciton annihilation depends on the system and on the excitation conditions. Thus, in order to reduce artifacts, the accepted approach is to measure time-dependent signals for different excitation intensities. If this leads to a change in the kinetic evolution, one has to attenuate the excitation power further until no such changes are observed [314]. The problem is that reducing the excitation power also reduces the overall signal such that the signal-to-noise ratio (SNR) decreases. In extended systems with large absorption cross sections such as molecular aggregates, polymers, or natural-light harvesting complexes, it may become impractical to achieve adequately high SNR in the annihilation-free regime, and then one has to accept compromises that may lead to erroneous interpretation of kinetic time constants. Anyway, the criterion for a sufficiently small change of kinetics upon power reduction is often subjective.

In recent years, higher-order multidimensional nonlinear spectroscopy gained popularity [4, 5, 7, 9, 13, 20, 45, 210–212, 215–217, 220, 232]. Higher-order spectroscopy can be used to measure higher-excited states of molecules [5, 45], energy transfer in light-harvesting complexes [211], high-frequency vibronic modes [215], exciton–exciton annihilation [9, 232, 238], multiexciton states in quantum dots [13, 216], coherences between multi-particle collective states [217], or exciton diffusion in aggregates and polymers via annihilation [4, 7, 20]. In coherently detected higher-order spectroscopy, a polarization higher than of third order is measured, which requires more than three interactions with the excitation fields. In action-detected spectroscopy, higher-order signals are connected to perturbation terms higher than of fourth order because of the detection of a population in an excited state [9]. In this chapter, we focus on coherently detected spectroscopy and disregard action-detected techniques.

In the PP geometry, where three pulses interact with the system (i.e., two pump pulses and one probe pulse), higher-order signals can be isolated by their position along the excitation frequency axis in the 2D spectrum. At normal excitation intensities, each pulse interacts once with the system and the signal is emitted in the phase-matched direction $\pm \mathbf{k}_{\text{pump}} \mp \mathbf{k}_{\text{pump}} + \mathbf{k}_{\text{probe}}$, where the "$\pm$" and "$\mp$" signs reflect the fact that the sum of rephasing and non-rephasing spectrum, i.e., the absorptive part of the spectrum, is directly obtained. The first pump pulse excites a single-quantum

coherence (1Q) and therefore the signal appears at around the central frequency of the pump pulse along the excitation axis. The probe pulse excites a 1Q coherence as well and therefore the signal position along the detection axis is also fixed at around the central frequency of the probe pulse. We call this the "1Q1Q signal". Note that the position of the signal is only approximately located at (in this case single) multiples of the central frequency because the exact position is influenced by the absorption and emission spectra of the system [315]. For increasing intensity of the pump pulses, multiple interactions with the excitation field take place leading to higher-order signals. One possible signal of next-highest order, with the phase-matching condition $\pm 2\mathbf{k}_{\mathrm{pump}} \mp 2\mathbf{k}_{\mathrm{pump}} + \mathbf{k}_{\mathrm{probe}}$, is emitted in the same direction, $\mathbf{k}_{\mathrm{probe}}$, as the 1Q1Q signal. However, due to one more additional interaction with the first pump pulse, the system evolves in a two-quantum (2Q) coherence after the first pump pulse, and the signal appears at around twice the central frequency of the pump spectrum. The probe pulse still only interacts once with the system, and we thus call this "2Q1Q signal". We will focus, in this chapter, on multiple interactions occurring with the pump pulses and consider the probe pulse to be always weak. Therefore, the second coherence in the signal stays always at the 1Q level, and we will drop this part of the label for the sake of simplicity. We utilized the 2Q signal previously to investigate exciton–exciton annihilation as well as exciton diffusion in supramolecular aggregates and polymers [4, 7, 20]. Other methods to isolate 2Q signals use a noncollinear setup in which the three pulses interact with the sample from three different directions, i.e., with different wavevectors [220]. The 1Q and the 2Q signals are then separated by their specific phase-matching directions. Recently, we introduced the technique of intensity cycling which allows to isolate 1Q and 2Q signals in PP spectroscopy [16]. Here, PP signals are measured at specific excitation intensities from which the 1Q and 2Q signals are extracted.

As mentioned above, the excitation intensity has to be chosen carefully in conventional PP or 2D spectroscopy experiments to reduce uncontrolled mixing in higher-order signals. In PP geometry, only odd orders of the nonlinear polarization are in general present due to the phase-matching condition. The 1Q signal contains, however, not only the usually desired third order, but all odd orders beginning with the third (and higher). The 2Q signal is a higher-order signal and likewise does not only contain fifth-order terms but includes all odd orders beginning from fifth order (and higher). Thus, if the dynamics of the 1Q signal do not change with increasing excitation intensity and the signal amplitude scales linearly with the excitation intensity, the 1Q signal is dominated by third-order response and the influence of higher-order contributions can be considered minor. The same principle holds for the 2Q signal: If the dynamics of the 2Q signal do not change as the excitation intensity increases and the signal amplitude scales quadratically, then the 2Q signal is dominated by the fifth-order response in terms of perturbation theory. However, in general all nQ signals inherently contain higher-order contributions, starting at order $2n + 1$ of perturbation theory, but their strength can be difficult to quantify experimentally. Therefore, even an isolation of different nQ signals in 2D and PP experiments, where n marks the

number of interactions with the pump pulses, does not allow for a clean separation of different orders of nonlinearity.

In this chapter, we introduce a method for isolating signals of clean nonlinear orders in 2D spectroscopy in the PP geometry. Our approach works for any nQ signals at around n times the central frequency of the pump pulse along the excitation axis. The same procedure can be used to obtain clean nonlinear signals from nQ signals isolated by PP spectroscopy via intensity cycling. As an example, we measure the 1Q, 2Q, and 3Q signal of squaraine oligomers and show how these signals can be used to eliminate the fifth- and seventh-order signal contributions at the 1Q signal and therefore obtain a clean third-order signal even at high excitation intensities. We directly compare the signals isolated with 2D and PP spectroscopy. Furthermore, we show how the concept of obtaining clean nonlinear orders can be extended to higher-order signals. As an example, we extract the clean nonlinear signals up to the thirteenth order of squaraine polymers using higher-order PP spectroscopy.

The chapter is structured as follows: In Sec. 8.2 we discuss the theoretical concepts of isolating higher-order signals focusing on double-sided Feynman diagrams. While Sec. 8.2.1 features 2D spectroscopy, Sec. 8.2.2 demonstrates the concept of isolation of higher-order signals in PP spectroscopy. Section 8.3 contains the experiment. After we discuss the experimental setup and the samples in Sec. 8.3.1, we show exemplary 1Q, 2Q, and 3Q signals, obtained on squaraine oligomers from 2D spectroscopy and PP spectroscopy, in Sec. 8.3.2 and 8.3.3, respectively. In Sec. 8.3.4 we demonstrate how the clean third-order signal can be retrieved in both techniques by weighting and adding the different nQ signals. Section 8.3.5 presents our results of higher-order PP spectroscopy on squaraine polymers. In Sec. 8.4 we summarize the main results and provide an outlook to future experiments.

8.2. Theory of Higher-Order Spectroscopy

8.2.1. Isolation of Higher-Order Signals in Two-Dimensional Spectroscopy

A common tool for visualizing and calculating the various excitation pathways of the nonlinear polarization are double-sided Feynman diagrams [25]. In these diagrams, time runs from bottom to top. The density matrix is depicted in between two vertical lines. Interactions with the electric laser fields are shown as arrows that represent either an excitation or a de-excitation of the system, depending on whether an arrow points towards or away from the density matrix, respectively. The nonlinear polarization is emitted in a phase-matching direction that is dictated by the incident wavevectors. An arrow pointing to the left contributes with a wavevector $-\mathbf{k}$, and an arrow pointing to the right with $+\mathbf{k}$, to the nonlinear polarization. In this paper we focus on 2D spectroscopy in PP geometry, wherein the two pump pulses have the same wavevector $\mathbf{k}$. In our discussion, we will call the two pump pulses "pulse a" and "pulse b" and the probe pulse "pulse c". In PP and 2D spectroscopy, the rephasing and non-rephasing

third-order signals are emitted in phase-matching directions $-\mathbf{k}_{\text{pump}} + \mathbf{k}_{\text{pump}} + \mathbf{k}_{\text{probe}}$ and $+\mathbf{k}_{\text{pump}} - \mathbf{k}_{\text{pump}} + \mathbf{k}_{\text{probe}}$, respectively. Using our notation introduced above and the fact that pulse a and pulse b have a common wavevector, we can rewrite the phase-matching directions for the rephasing contribution to $-\mathbf{k}_{\text{a}} + \mathbf{k}_{\text{b}} + \mathbf{k}_{\text{c}}$ and for the non-rephasing contribution $+\mathbf{k}_{\text{b}} - \mathbf{k}_{\text{a}} + \mathbf{k}_{\text{c}}$. In 2D spectroscopy, three different time delays can be distinguished. The coherence time τ describes the delay between the two pump pulses. The population time T is defined as the delay between the center of the second pump pulse and the probe pulse. The signal time t is defined as the delay between the probe and the emission of the signal. In a PP experiment the probe itself is the local oscillator. The signal time, t, is measured implicitly by using a spectrometer, allowing a direct measurement of the Fourier conjugate variable ω_t.

The impulsive limit is often assumed when performing calculations or developing intuition for the signals that are measured in a 2D experiment. The impulsive limit corresponds to the assumption that none of the pulses overlap in time. However, in realistic experiments, the two pump pulses always overlap when the coherence time is smaller than the pulse duration, which is of critical importance in this chapter. Thus, we will not assume time ordering between the two pump pulses. Furthermore, when the population time is smaller than the pulse duration, no time ordering exists for the interaction with the probe pulse either (with respect to the pump pulses), and we must consider all possible temporal orderings of interactions. For population times further away from zero, the probe pulse always arrives last and is well separated in time from the two pump pulses, which is a situation we will call partial time ordering.

In partial time ordering, eight double-sided Feynman diagrams describe the third-order response. The number of diagrams reduces to six if the RWA is applied [25]. Note that we switch between rephasing and non-rephasing contributions by changing the time ordering of $-\mathbf{k}_{\text{a}}$ and $+\mathbf{k}_{\text{b}}$. The six diagrams can be further divided into different types: ground-state bleach (GSB), stimulated emission (SE), and excited-state absorption (ESA). If the time ordering between pump pulses and probe pulse does not hold, ten additional diagrams contribute to the third-order signal leading to a total of 16 diagrams [28]. We show the full set of double-sided Feynman diagrams for the different cases of time ordering in the Supplementary Material (Sec. 8.5.1).

It is the purpose of the present work to find out at which frequency positions and with which amplitudes higher-order signals contribute. The fifth-order signal as the next higher-order signal appears at two different positions in a 2D spectrum: (1) at the 1Q excitation coordinate as a contamination of the third-order signal, and (2) at the 2Q excitation coordinate ($2\omega_0$) as a new signal, i.e., the 2Q signal. The presence of a fifth-order signal at the 2Q position, $\tilde{S}_{2Q}^{(5)}(\omega_\tau, T, \omega_t)$, guarantees that the 1Q signal is contaminated by fifth-order signals, such that $\tilde{S}_{1Q}^{(5)}(\omega_\tau, T, \omega_t)$ is no longer negligible. Since the 1Q phase-matching condition must still be fulfilled, such contamination occurs with two additional interactions with the same pulse, either a or b, but with oppositely signed wavevector contributions such that the emitted signal direction is not altered. In this case, the contamination leads to a contribution from multi-particle dynamics and higher-excited states and to a deviation of the linear scaling of the 1Q

signal with higher excitation powers [181, 206].

At even higher pump-pulse powers, the amplitude of the seventh-order signals will get stronger and exceed the noise threshold of the experiment, at which point it will contribute significantly to the 2D spectrum at three different locations: (1) as a contamination of the 1Q signal, (2) as a contamination of the 2Q signal, and (3) as a signal that we call the 3Q signal, and similarly for yet higher orders. In Fig. 8.1 we show the different positions of the 1Q, 2Q, and 3Q signals in the 2D spectrum with representative diagrams below. In Fig. 8.1 we consider diagrams up to the seventh-order contributions. Higher-order contributions such as the ninth-order signal would add additional diagrams to Fig. 8.1 contributing to the 1Q, 2Q, and 3Q signals as well as to the 4Q signal. Note that the Feynman diagrams do not include state labels as they customarily do, because the conclusions we draw from our analysis of time-dependent perturbation theory are valid for any system and any type of states evolving between the pulses. Furthermore, we disregard the arrow representing the signal (often shown as a dotted arrow [23]) for all diagrams presented in this chapter. Each column below the respective nQ signal in Fig. 8.1 contains the contributing nonlinear orders, each depicted by one exemplary out of many double-sided Feynman diagrams. The diagrams on the diagonal correspond to the lowest-order nonlinear signal that contributes to a specific nQ signal, and therefore no diagrams above the diagonal are present. For example, the lowest-order signal at the 2Q position is of fifth order. Let us take a closer look at the off-diagonal diagrams that represent the contamination by higher-order contributions. The contaminations must include pairs of interactions with a single pulse to maintain the phase-matching conditions associated with each type of signal. For example, the fifth-order signal contributing to 1Q (Fig. 8.1, second diagram from top in the first column) has two more interactions with pulse a, as compared to third order, and those additional interactions occur with opposite wavevectors, i.e., arrows pointing in opposite directions in the double-sided Feynman diagram.

In the weak-probe limit, the fifth-order signals $\tilde{S}_{1Q}^{(5)}(\omega_\tau, T, \omega_t)$ and $\tilde{S}_{2Q}^{(5)}(\omega_\tau, T, \omega_t)$ share many features. Both signals report on the same population dynamics, and have the same line shapes along the detection frequency axis because pulse c probes the same populations in both contributions. However, since 1Q and 2Q evolve differently during the coherence time, τ, between the two pump pulses, i.e., the colored red and blue rectangles, respectively, the line shapes differ along ω_τ. As we show in this publication, we can use the measured nQ signals for $n > r$ to eliminate higher-order contaminations in the rQ signal and obtain clean nonlinear signals. For example, the measurement of the 2Q signal allows us to eliminate the fifth-order contamination at the 1Q position resulting in a clean third-order signal. Since the fifth-order contributions at the 1Q and the 2Q position have different line shapes along ω_τ, the relationship between the two signals is not straightforward, and thus we leave any discussion of an optional correction of the ω_τ line shapes for future work. In the present contribution, we focus our attention on nQ signals that are integrated over their respective frequency regions along the ω_τ axis. Note that such finite-interval integrations (over each nQ region separately) are not equivalent to an integration over all ω_τ (that would correspond to
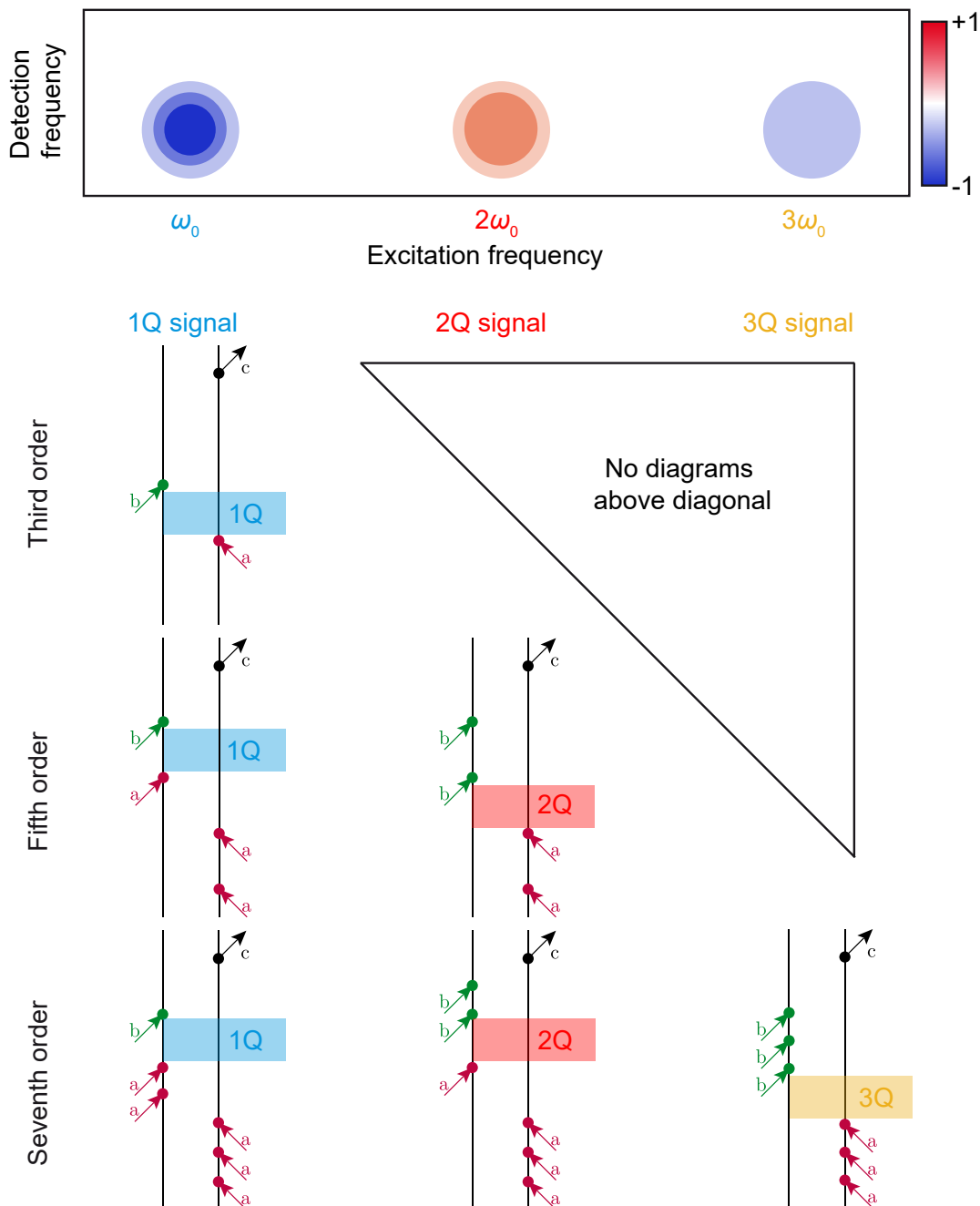
Figure 8.1.: Exemplary single- and multiple-quantum Feynman diagrams and their fre-
quency positions up to seventh order in perturbation theory. The 1Q signal appears at the
excitation frequency ω_0. The 2Q and 3Q signals appear at twice and three times ω_0, respec-
tively. Without contaminations, the nQ signals would correspond to the $(2n+1)^{\text{th}}$ nonlinear
orders represented exemplarily by the diagrams on the diagonal. Contaminations arise from
the diagrams below the diagonal. The time periods in which the 1Q, 2Q, and 3Q coherences
arise are marked by colored rectangles.

a measurement at $\tau = 0$ according to the projection-slice theorem) [23]. It is possible, however, to extract the different nQ signals in PP spectroscopy (i.e., for $\tau = 0$) by exploiting their power dependence [16] as discussed in detail in Sec. 8.2.2.

Generally speaking, the nQ signals $S_{nQ}(\tau, T, \omega_t)$ are those signals that oscillate at roughly n times the central frequency of the pump spectrum ($\sim n\omega_0$) during the coherence time τ and occur along phase-matching directions of $-n\mathbf{k}_a + n\mathbf{k}_b + \mathbf{k}_c$ [16]. In the case of two pump pulses traveling along the same direction ($\mathbf{k}_a = \mathbf{k}_b$), all nQ signals have the same wave vector $\mathbf{k}_c$, and thus all are detected as a change in probe absorption. The total signal measured, i.e., the transient change in absorption introduced by the pump pulses, may be written as

$$S(\tau, T, \omega_t) = \sum_{n=1}^{\infty} S_{nQ}(\tau, T, \omega_t), \tag{8.1}$$

where each multi-quantum signal $S_{nQ}(\tau, T, \omega_t)$ may be expanded perturbatively in powers of the pump intensity I as

$$S_{nQ}(\tau, T, \omega_t) = \sum_{r=n}^{\infty} S_{nQ}^{(2r+1)}(\tau, T, \omega_t) I^r \tag{8.2}$$

where we assume that the probe intensity is weak enough that all signals are linear in the probe intensity. The signal $S_{nQ}(\tau, T, \omega_t)$ depends also on the excitation intensity $[S_{nQ}(\tau, T, \omega_t, I)]$. However, we will discard this dependence in the following discussion to keep the notation simple. The multi-quantum signals $S_{nQ}(\tau, T, \omega_t)$ oscillate at roughly $n\omega_0$ as a function of τ with ω_0 as the carrier frequency of the pump pulses. When inspecting the 2D spectra obtained by taking the Fourier transform with respect to τ,

$$\tilde{S}_{nQ}(\omega_\tau, T, \omega_t) = \int_{-\infty}^{\infty} d\tau \, e^{i\omega_\tau \tau} S_{nQ}(\tau, T, \omega_t) \tag{8.3}$$

we expect to see peak(s) along the ω_τ axis near multiples of the pump pulse center frequency ω_0. If the pump pulse has a bandwidth Γ we expect the signal $\tilde{S}_{1Q}(\omega_\tau, T, \omega_t)$ to be mostly localized within the bounds $[\omega_0 - \Gamma/2, \omega_0 + \Gamma/2]$. More generally, we expect the signals $\tilde{S}_{nQ}(\omega_\tau, T, \omega_t)$ to be mostly localized within the bounds $[n\omega_0 - \Gamma/2, n\omega_0 + \Gamma/2]$.

We briefly note that the separation of the nQ signals along the ω_τ axis is not guaranteed. Fortunately, if the signals did not separate, it would be visually clear: instead of localized signals appearing around multiples of ω_0 (as illustrated in Fig. 8.1), the signals would blend into each other. In such a case, the technique proposed in this chapter would not be expected to work. For the purposes of this discussion, we will assume that the signals do separate along ω_τ as it was the case in our previous experiments [4, 9, 20]. Since the nQ signals separate along the ω_τ axis, we can recover,

to a good approximation, the $\tau = 0$ component of each individual nQ signal using

$$S_{n\mathrm{Q}}(\tau = 0, T, \omega_t) \approx \int\limits_{n\omega_0-\Delta}^{n\omega_0+\Delta} \mathrm{d}\omega_\tau \, \tilde{S}(\omega_\tau, T, \omega_t). \tag{8.4}$$

where $\Delta \leq \omega_0/2$. To understand why Eq. (8.4) gives the nQ signal at $\tau = 0$, it is helpful to recall that in the case where $\Delta \to \infty$, we obtain the total signal S at $\tau = 0$ by the projection-slice theorem [23, 221]. Since the nQ signals separate along the ω_τ axis, we can obtain a good approximation of $S_{n\mathrm{Q}}(\tau = 0, T, \omega_t)$. We can understand why the partial integration recovers the $\tau = 0$ components of separate nQ signals in a different way by substituting Eq. (8.3) into Eq. (8.4). This leads to

$$S_{n\mathrm{Q}}(\tau = 0, T, \omega_t) = \int\limits_{n\omega_0-\Delta}^{n\omega_0+\Delta} \mathrm{d}\omega_\tau \int\limits_{-\infty}^{\infty} \mathrm{d}\tau e^{i\omega_\tau\tau} S_{n\mathrm{Q}}(\tau, T, \omega_t) \tag{8.5}$$

and, interchanging the integrals,

$$S_{n\mathrm{Q}}(\tau = 0, T, \omega_t) = 2\Delta \int\limits_{-\infty}^{\infty} \mathrm{d}\tau \, e^{in\omega_0\tau} S_{n\mathrm{Q}}(\tau, T, \omega_t) \frac{\sin(\tau\Delta)}{\tau\Delta}. \tag{8.6}$$

With increasing Δ, the sinc function becomes increasingly localized around $\tau = 0$. In the limit of large Δ we obtain

$$\lim_{\Delta\to\infty} \Delta \frac{\sin(\tau\Delta)}{\tau\Delta} = \pi\delta(\tau). \tag{8.7}$$

This limit corresponds to integrating the complete 2D spectrum along ω_τ, and would recover the experimentally measured signal $S(\tau = 0, T, \omega_t)$. Setting an appropriate Δ thus leads to a selection of the nQ signal for each given n, while restricting the interferogram closely to $\tau \approx 0$. In the absence of noise, $\Delta = \omega_0/2$ is the optimal choice. However, in the presence of noise, smaller values of Δ may be desirable if the nQ signals are well localized near multiples of ω_0 along the ω_τ axis. In such a case, using the largest value $\Delta = \omega_0/2$ may simply add noise to the recovered signal.

We have thus far shown that we can, to good approximation, separate the contributions $S_{n\mathrm{Q}}(\tau = 0, T, \omega_t)$ via the use of a sinc filter, as shown in Eq. (8.6), even though those individual nQ signals cannot be experimentally directly measured at $\tau = 0$ in the collinear PP geometry. We now discuss how the signals $S_{n\mathrm{Q}}(\tau = 0, T, \omega_t)$ are related to each other and can be used to extract the individual perturbative orders of the total signal $S^{(2n+1)}(\tau = 0, T, \omega_t)$.
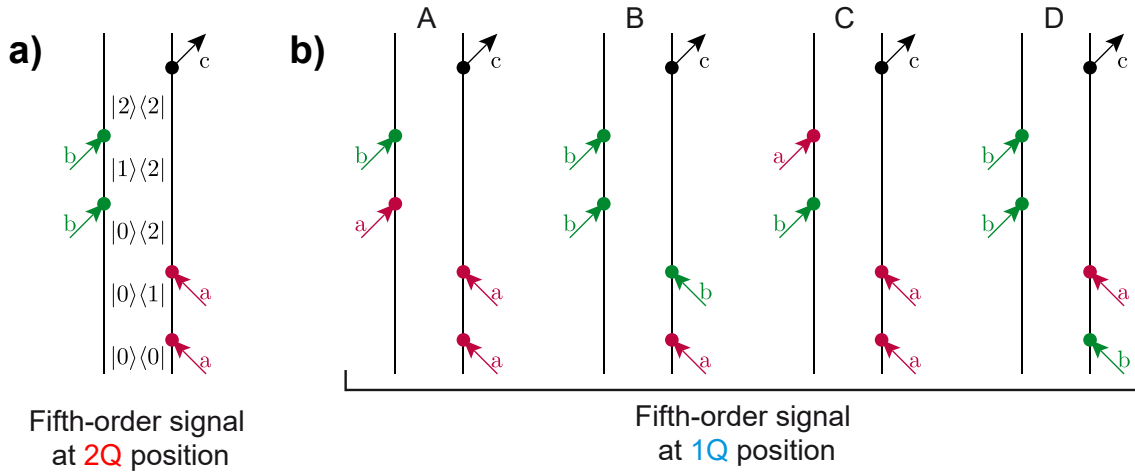
Figure 8.2.: Double-sided fifth-order Feynman diagrams. (a) For the fifth-order signal at the 2Q position each pump pulse (pulse a shown in red and pulse b shown in green) interacts twice with the system while pulse c (shown in black) only interacts once. The phase-matching direction that is connected to this diagram is $-2\mathbf{k}_a + 2\mathbf{k}_b + \mathbf{k}_c$. For better understanding we show the evolution of the density matrix explicitly with the ground state $|0\rangle$, the first excited state $|1\rangle$, and the doubly excited state $|2\rangle$. (b) Four diagrams can be constructed that correspond to a fifth-order signal at the 1Q position. For diagrams A and B, all interactions with pulse a occur before any interactions with pulse b, while for diagrams C and D, the interactions with the two pulses are intertwined. Nevertheless, all four diagrams must be considered.

Let us take a closer look at the corresponding diagrams of the two contributions $S_{2Q}^{(5)}$ and $S_{1Q}^{(5)}$. At $\tau = 0$, the interactions of the two pump pulses can occur in every possible order, and therefore all diagrams must be considered. One exemplary diagram for the fifth-order contribution at the 2Q signal and the four corresponding diagrams of the fifth-order signal at the 1Q position are shown in Fig. 8.2. For the diagram of $S_{2Q}^{(5)}$ (Fig. 8.2a), both pump pulses interact twice each with the system and with the overall phase-matching direction of $-2\mathbf{k}_a + 2\mathbf{k}_b + \mathbf{k}_c$. We show the changes in the density matrix in Fig. 8.2 explicitly with the ground state $|0\rangle$, the first excited state $|1\rangle$, and the doubly excited state $|2\rangle$. After the interaction with pulse a, the system evolves in a 2Q coherence while during the population time a population in a doubly excited state is reached. Other types of diagrams with a ground-state population or a single-exciton population after the interaction with the pump pulses can also contribute to the signal. Pulse c only interacts once with the system resulting in a de-excitation. Note that other diagrams also contribute where the interaction of pulse c results in an excitation of the ket of the density matrix [9]. For the diagram shown in Fig. 8.2a with this specific phase signature of the interactions where the first two interactions excite the bra of the density matrix and the following two interactions excite the ket of the density matrix followed by a de-excitation of the bra by pulse c, four fifth-order diagrams at the 1Q position can be constructed with exactly the same specific

interaction pattern (Fig. 8.2b). We can construct the fifth-order diagrams at the 1Q position by taking the diagram with its specific interaction pattern at the 2Q position and change one interaction from a to b or vice versa. In such a way four different diagrams can be obtained. In contrast to the diagrams at the 2Q position, now one pump pulse interacts three times and the other pump pulse only interacts once with the system. During the population time the system is in the same population state (in our example in Fig. 8.2, a doubly-excited-state population) since all four interactions (regardless if they occur with pulse a or pulse b) excite the system, i.e., point towards the density matrix. This equivalence of the interaction pattern is important because the diagrams shown in Fig. 8.2a and Fig. 8.2b report on the same system dynamics and only differ to which specific multi-quantum signal they contribute. All four diagrams in Fig. 8.2b contribute to the 1Q signal. For the two diagrams A and B, the system is in a 1Q coherence after interaction of pulse a ($|0\rangle \langle 1|$ for diagram B and $|1\rangle \langle 2|$ for diagram A) and therefore evolves with a 1Q coherence during the coherence time τ. In diagrams A and B, all interactions with pulse a occur before any interactions with pulse b. Diagrams C and D are different because the interaction with one pulse occurs between interactions with the other pulse. However, since we are integrating the signals along the ω_τ axis we have to consider also the diagrams where the interactions from pulse a and pulse b are intermixed, i.e., at $\tau = 0$.

The procedure discussed on the example shown in Fig. 8.2 contains the key idea of this chapter: For every diagram contributing to $S_{2Q}^{(5)}$ we can construct four equivalent diagrams that contribute to $S_{1Q}^{(5)}$ at $\tau = 0$. The diagrams of the 1Q and 2Q signal are equivalent since they have the same interaction pattern and only differ with which specific pulses the interactions occur. However, for the evolution of the system it does not matter with which pulse the interaction takes place and therefore the fifth-order contributions at 1Q and 2Q position report on the same system dynamics. Note that one important assumption for the equivalence as well as the ratio between the two contributions is that the pump pulses are identical as stated above. When the two pump pulses overlap, i.e., time ordering between the pump pulses is not fulfilled, but time ordering between the pump and the probe pulses holds, $S_{2Q}^{(5)}$ is described by 54 diagrams. If time ordering between pump and probe is not fulfilled either, the number of diagrams for $S_{2Q}^{(5)}$ increases to 240. In both cases, for each diagram that contributes to $S_{2Q}^{(5)}$, there are four diagrams that give an equivalent contribution to $S_{1Q}^{(5)}$ at $\tau = 0$. Thus, the fifth-order contamination at the 1Q position, $S_{1Q}^{(5)}$, is precisely four times the fifth-order signal at the 2Q position $S_{2Q}^{(5)}$, and can be described by 216 diagrams in the case of time ordering between pump and probe pulses and 960 diagrams in the case of no time ordering between pump and probe pulses. We show the full set of double-sided Feynman diagrams for the two contributions in the case where time ordering between pump and probe pulses is fulfilled in the Supplementary Material (Sec. 8.5.2).

In general, to find the relation between a multi-quantum signal and the contribution by various higher orders, the phase signatures must be considered. For the nQ signal, the lowest order that can contribute is $2n + 1$. In addition, contributions occur from order $2(n+m)+1$ via additional interactions with phase signatures $m(+\mathbf{k}_i - \mathbf{k}_i)$, with $m = 1, 2, 3, \ldots$, and $i = \mathrm{a}, \mathrm{b}$. More generally, we show in the Supplementary Material (Sec. 8.5.3) that

$$S_{r\mathrm{Q}}^{(2n+1)}\left(\tau = 0, T, \omega_t\right) = \binom{2n}{n-r} S_{n\mathrm{Q}}^{(2n+1)}\left(\tau = 0, T, \omega_t\right) \tag{8.8}$$

and list the number of diagrams for all orders in Sec. 8.5.4.

The equality at $\tau = 0$ in Eq. (8.8) means that we can use the measured nQ signals to eliminate higher-order contributions and obtain clean nonlinear signals up to a given order. As discussed above, for each fifth-order diagram at the 2Q position, four diagrams corresponding to a fifth-order contribution at the 1Q position can be constructed. The fifth-order contribution at the 1Q position can therefore be eliminated by subtracting four times the 2Q from the 1Q signal resulting in the clean third-order signal,

$$S^{(3)}(T, \omega_t)I = S_{1\mathrm{Q}}(T, \omega_t, I) - 4S_{2\mathrm{Q}}(T, \omega_t, I) \tag{8.9}$$

where we discarded the dependence on τ for brevity because it is zero anyway and added the dependences on the excitation intensity I. Note that in previous work we already discussed contamination correction using higher-order signals in 2D spectroscopy [20]. However, in that work we had derived an incorrect factor of six instead of the correct factor of four for the relation between the fifth-order signal at 2Q and the fifth-order signal at the 1Q position because we had considered only time-ordered diagrams, whereas in the present work we take into account all diagrams including those without time ordering between the two pump pulses. The fifth-order signal at the 2Q position has an opposite sign compared to the third-order signal at the 1Q position due to two more interactions with the electric field which add an additional factor of $\left(\frac{i}{\hbar}\right)^2$, from the perturbation expansion, to the response function.

The same principle can be applied if even higher orders are present. The seventh-order signal contributes at the 1Q, 2Q, and 3Q positions (Fig. 8.1). In order to correct for the seventh-order contamination we must find the ratio between the seventh-order contribution at the 3Q and the seventh-order contribution at the 2Q position. We can use Eq. (8.8) by setting $n = 3$ and $r = 2$ resulting in a ratio of six between the two contributions. The 3Q signal can be used to correct for seventh-order contribution at the 2Q position by subtracting six times the 3Q signal from the 2Q signal. Note that the fifth-order signal scales quadratically on the excitation intensity. For obtaining a clean third-order signal, we have to eliminate both the fifth order (by subtracting four times the 2Q signal as shown above) and the seventh order (by subtracting 15 times the 3Q signal). Since the 3Q signal is also used to correct the 2Q signal, it turns up twice in the overall correction procedure: to eliminate the seventh-order contribution from

1Q and to eliminate the seventh-order contribution from 2Q. The overall correction procedure thus results in

$$
\begin{aligned}
S^{(3)}(T,\omega_t)I = \quad & [S_{1\mathrm{Q}}(T,\omega_t,I) - 15 S_{3\mathrm{Q}}(T,\omega_t,I)] \\
& - 4 \underbrace{[S_{2\mathrm{Q}}(T,\omega_t,I) - 6 S_{3Q}(T,\omega_t,I)]}_{S^{(5)}(T,\omega_t)I^2} \\
=& S_{1\mathrm{Q}}(T,\omega_t,I) - 4 S_{2\mathrm{Q}}(T,\omega_t,I) + 9 S_{3\mathrm{Q}}(T,\omega_t,I)
\end{aligned}
\tag{8.10}
$$

for a clean third-order signal.

We can proceed analogously to obtain similar ratios of double-sided Feynman diagrams for all higher orders and generalize the correction procedure accordingly. The correction factors can be written as a matrix [16] connecting the clean nonlinear signals $S^{(2n+1)}(T,\omega_t)I$ with the measured $n\mathrm{Q}$ signals $S_{n\mathrm{Q}}(T,\omega_t,I)$,

$$
\begin{pmatrix}
S^{(3)}(T,\omega_t)\,I \\
S^{(5)}(T,\omega_t)\,I^2 \\
S^{(7)}(T,\omega_t)\,I^3 \\
S^{(9)}(T,\omega_t)\,I^4 \\
S^{(11)}(T,\omega_t)\,I^5 \\
S^{(13)}(T,\omega_t)\,I^6 \\
\vdots
\end{pmatrix}
=
\begin{pmatrix}
1 & -4 & 9 & -16 & 25 & -36 & \dots \\
0 & 1 & -6 & 20 & -50 & 105 & \dots \\
0 & 0 & 1 & -8 & 35 & -112 & \dots \\
0 & 0 & 0 & 1 & -10 & 54 & \dots \\
0 & 0 & 0 & 0 & 1 & -12 & \dots \\
0 & 0 & 0 & 0 & 0 & 1 & \dots \\
\vdots & \vdots & \vdots & \vdots & \vdots & \vdots & \ddots
\end{pmatrix}
\begin{pmatrix}
S_{1\mathrm{Q}}(T,\omega_t,I) \\
S_{2\mathrm{Q}}(T,\omega_t,I) \\
S_{3\mathrm{Q}}(T,\omega_t,I) \\
S_{4\mathrm{Q}}(T,\omega_t,I) \\
S_{5\mathrm{Q}}(T,\omega_t,I) \\
S_{6\mathrm{Q}}(T,\omega_t,I) \\
\vdots
\end{pmatrix}.
\tag{8.11}
$$

For any $n\mathrm{Q}$ signal the lowest order contribution is $2n+1$ (compare Fig. 8.1) and therefore, the matrix is an upper triangular matrix. Note that the correction factors are the same whether or not time ordering between the pump and the probe pulses is fulfilled as well as if the RWA holds or not as we show in the Supplementary Material (Sec. 8.5.4). An important point is that procedure corrects up to a certain nonlinear order. For example, in Eq. (8.10) the 1Q signal is corrected for fifth- and seventh-order contributions using the 2Q and 3Q signals. However, if the 3Q signal is contaminated by ninth-order contributions the correction using only the 2Q and 3Q signal is not sufficient and the 4Q signal has to be taken into account. In summary, Eq. (8.11) allows us to obtain N clean nonlinear signals by isolating N multi-quantum signals and then evaluating a suitable linear combination.

8.2.2. Isolation of Higher-Order Signals in Pump–Probe Spectroscopy

In the present section, we show how to obtain clean nonlinear signals in PP spectroscopy without requiring 2D data sets. This was already discussed in Sec. 6.6 and here we repeat the main points for convenience. In Sec. 8.2.1, the $n\mathrm{Q}$ signals were separated by their specific frequency during τ, i.e., by their position on the excitation axis in a 2D spectrum. Those signals were then integrated over partial intervals of the

excitation axis, which we found to be analogous to measuring close to $\tau = 0$. This leads to the idea that the same information about higher-order signals, obtainable in 2D spectroscopy, can be measured in a PP experiment for which $\tau = 0$ is inherently fulfilled. However, a PP experiment corresponds to integrating the complete 2D spectrum, and not just over finite intervals around nQ signals, which means that we must separate the nQ signals in a different way. Inspired by phase cycling, we show in this section how the various nQ signals can be extracted by linear combinations of separate PP measurements at specific excitation intensities.

In 2D spectroscopy, the sample is excited by a double pulse with the delay τ and relative phase difference φ_s. We consider the case of 2D spectroscopy in PP geometry, i.e., the two pump pulses share a common wavevector. The total electric field $E_s(t)$ of the two pump pulses can be described by

$$E_s(t) = E_0(t)e^{i(\omega_0 t - \mathbf{k} \cdot \mathbf{r})} \left(\underbrace{1}_{\text{pulse 1}} + \underbrace{e^{i\omega_0 \tau + \varphi_s}}_{\text{pulse 2}} \right) + \text{c.c.}, \qquad (8.12)$$

wherein the complex-valued envelope $E_0(t)$ contains the temporal amplitude evolution, an overall absolute phase shared between all pulses, and any spectral phase beyond second order in Taylor expansion, i.e., potential chirp, $\mathbf{k}$ is the common wavevector of both pulses, ω_0 is the carrier frequency, $\mathbf{r}$ is the position (which is integrated out when taking into account the phase-matching condition from propagation through the sample), φ_s is the relative phase between the pulses, s is an index of the phase-cycling step to be explained below, and c.c. marks the complex conjugate of the previous term. In a PP experiment $\tau = 0$ and we can write the intensity as

$$I_s = 4I_0 \cos^2\left(\frac{\varphi_s}{2}\right). \qquad (8.13)$$

with I_0 as a "base" pump intensity whose meaning is discussed below. From Eq. (8.13), it is clear that phase cycling within the pump pulse pair of a 2D experiment, i.e., varying φ_s in specific steps, reduces to simply changing the intensity of the excitation pulse in a PP experiment. Using the known relation from phase cycling [26], we can write the signal $S_{n\text{Q}}(\tau = 0, T, \omega_t, \varphi_s)$ as

$$S_{n\text{Q}}(\tau = 0, T, \omega_t, \varphi_s) = \frac{1}{2N(1 + \delta_{n,N})} \sum_{s=1}^{2N} e^{in\varphi_s} S(\tau = 0, T, \omega_t, \varphi_s), \qquad (8.14)$$

where we used $S(\tau = 0, T, \omega_t, \varphi_s)$ for the PP signal to reflect the close relation between 2D and PP measurements at $\tau = 0$, $\varphi_s = \pi(s-1)/N$, is the relative phase whose role is reduced to a mere formal parameter for PP experiments in which only a single (intensity-varied) pulse results from the constructive or destructive interference of the formally two coincident pump pulses, N is the number of intensity-cycling steps, and s the intensity-cycling step index. The Kronecker delta $\delta_{n,N}$ is present because for $n = N$, the signal is counted twice by the phase-cycling scheme. The signal $S_{n\text{Q}}$

depends on the detection frequency ω_t, on the population time T as well as on the phase φ_s.

In general, phase cycling requires $2N$ separate phase-cycling steps. Following the phase-cycling procedure [26], we find that only N steps are sufficient because

$$\cos^2 \frac{\pi (2N - s)}{2N} = \cos^2 \frac{\pi s}{2N} \tag{8.15}$$

As a result the intensities I_s for $s = 1, 2, 3, \ldots, N$ are redundant with the intensities for $s = 1 + N, 2 + N, 3 + N, \ldots, 2N$. Thus we can rewrite Eq. (8.14) to

$$S_{nQ} (\tau = 0, T, \omega_t, \varphi_s) = \sum_{s=1}^{N} \underbrace{\frac{2 - \delta_{s,1}}{2N(1 + \delta_{N,n})} \cos \left(\frac{n(s - 1)2\pi}{2N} \right)}_{w_s^{(nQ)}} S (\tau = 0, T, \omega_t, \varphi_s) \tag{8.16}$$

where we defined $w_s^{(nQ)}$ as the specific weights to be multiplied with the "raw" data $S (\tau = 0, T, \omega_t, \varphi_s)$ to retrieve a particular nQ signal via linear combination. The Kronecker delta $\delta_{s,1}$ arises from the fact that N intensity-cycling steps are enough for a $2N$ phase-cycling scheme as discussed above.

Given that we can achieve a separation into nQ signals of PP data, we now want to demonstrate how to use the equations from Sec. 8.2.1 to separate these further into clean third-, fifth-, and seventh-order response contributions. In the following, we will omit τ because it is zero anyway for PP. In general, N intensity cycling steps are needed to extract N multi-quantum signals and to isolate N clean nonlinear signals. In order to isolate signals up to 3Q, we perform a six-fold phase-cycling scheme, i.e., $N = 3$. The 1Q signal can be isolated by setting $n = 1$ in Eq. (8.16), which results in

$$S_{1Q} (T, \omega_t, \varphi_s) = \frac{1}{6} \left[S (0) + 2 \cos \left(\frac{\pi}{3} \right) S \left(\frac{\pi}{3} \right) + 2 \cos \left(\frac{2\pi}{3} \right) S \left(\frac{2\pi}{3} \right) \right]. \tag{8.17}$$

Using Eq. (8.13), the phases required for the cycling of the pump pulse can be converted into intensities taking into account that for a phase of zero the maximum intensity is $4I_0$ such that we can rewrite Eq. (8.17) as

$$S_{1Q} (T, \omega_t, I_0) = \frac{1}{6} \left[S(4I_0) + S(3I_0) - S(I_0) \right]. \tag{8.18}$$

The experiment reduces to obtaining different measurements at fractions of the maximum intensity $4I_0$. Analogously, we can isolate the 2Q signal with $n = 2$ by

$$S_{2Q} (T, \omega_t, I_0) = \frac{1}{6} \left[S(4I_0) - S(3I_0) - S(I_0) \right]. \tag{8.19}$$

and the 3Q signal with $n = 3$ by

$$S_{3Q} (T, \omega_t, I_0) = \frac{1}{12} \left[S(4I_0) - 2S(3I_0) + 2S(I_0) \right]. \tag{8.20}$$

with the additional factor of 1/2 in the prefactor, as compared to 1Q and 2Q. The prefactor is necessary since $n = N$ and the signal is counted twice. As stated above N intensity cycling steps lead to N multi-quantum signals and higher multi-quantum signals can be isolated by increasing the total number of intensity-cycling steps. This results in smaller phase increment steps and, therefore, smaller steps between the different intensities.

In Sec. 8.2.1 we showed that the multi-quantum signals at $\tau = 0$ can be used to correct for higher-order contaminations. Using intensity cycling the multi-quantum signals are directly obtained at $\tau = 0$ and therefore we can use the same correction procedure summarized in Eq. (8.11) to obtain clean nonlinear signals. In other words, our analysis of double-sided Feynman diagrams at $\tau = 0$ applies to the nQ signals obtained by integrating the signals along the ω_τ axis as well as to the nQ signals obtained by intensity cycling in PP spectroscopy. In the Supplementary Material we show an alternative way to obtain the nonlinear contributions to different nQ signals (Sec. 8.5.5). The demonstrated techniques allow to extract multi-quantum signals either via their specific position along the excitation axis in 2D spectroscopy or by intensity cycling in PP spectroscopy. As a next step the multi-quantum signals can be used to extract clean nonlinear signals.

8.3. Results and Discussion

8.3.1. Experiment

We now illustrate the general concept derived in Sec. 8.2 exemplarily by describing measurements and the associated analysis on a squaraine oligomer (oSQB8) dissolved in toluene. The absorption spectrum is shown in Fig. 8.3a (green) together with the laser spectra of the pump (red shaded area) and probe pulses (black dashed). The oligomer is made from eight repeating units of the cisoid indolenine squaraine monomer SQB (Fig. 8.3b). A thorough analysis of the fluorescence and absorption spectra on a series of squaraine oligomers with varying length made out of SQB revealed that the spectroscopic properties in toluene can be explained by a structural disordered linear chain [316]. The structure in toluene results in a J-type coupling and a red-shifted absorption maximum compared to the monomer. In our measurements, we excited the blue part of the main absorption peak.

In Sec. 8.3.5 we used squaraine copolymers as a sample that were studied by us previously [7]. The polymers are made on average out of 19 dimers and were dissolved in toluene as well. Note that the length distribution is quite broad for this sample [7]. The squaraine copolymers have a similar absorption spectrum as the oligomers with an absorption maximum at around 790 nm.

Our experimental setup [8, 20] consists of a Ti:sapphire laser amplifier (Spitfire Pro, Spectra Physics, 1 kHz, 800 nm, 4 mJ) whose output was focused into a hollow-core fiber (Ultrafast Innovations) filled with neon ($\sim$ 1 bar). The resulting broadband white-light was compressed by a set of chirped mirrors and then split into a pump and a probe beam by a pair of wedges. The population time T was controlled by a mechanical delay stage (M-IMS600LM, Newport) within the probe beam. The pump beam was guided for further compression trough a GRISM compressor (Fastlite) and an acousto-optic programmable dispersive filter (AOPDF) pulse shaper (Dazzler, Fastlite). For PP measurements, the AOPDF was used to control the intensity of the pump pulse. For 2D experiments, the AOPDF was used to create a double pulse with variable delay τ. The pump and probe beams were focused into the sample via two focusing mirrors resulting in beam sizes of 59 μm full width at half maximum (FWHM) for the main axis of the probe (at an eccentricity of 0.75) and 335 μm FWHM for the pump (eccentricity of 0.83). The pulse duration of a single pump pulse was measured by pulse-shaper-assisted collinear frequency-resolved optical gating (cFROG) [153] and found to be 17 fs (FWHM of the intensity). The pump pulse characterized by cFROG was used to determine the pulse duration of the probe pulse in a second step by cross-correlation FROG [153]. The reconstructed duration of the probe pulse (42 fs FWHM) was slightly longer than the pump pulse due to some remaining dispersion because the pulse shaper acted only on the pump beam. To obtain the signal (in TA as well as in 2D), we used a double-chopping scheme in which both beams were chopped with different frequencies. In the pump beam, sequences of two consecutive pulses were blocked and then transmitted; in the probe beam, alternating pulses were blocked and transmitted. This resulted in four combinations, all measured as powers of the probe

beam: 1) both beams blocked [I_B] corresponding to the background only, 2) both beams open [$I_{Pu\text{-}Pr}$], 3) pump beam open and probe beam blocked [I_{Pu}], and 4) vice versa [I_{Pr}]. The transient absorption signal as the change of the optical density was constructed by

$$\Delta\text{OD} = -\log_{10} \frac{I_{Pu\text{-}Pr} - I_{Pu}}{I_{Pr} - I_B} \tag{8.21}$$

To avoid bleaching, the samples were continuously pumped by a micro annual gear pump through a flow cell with a 200 μm beam path.
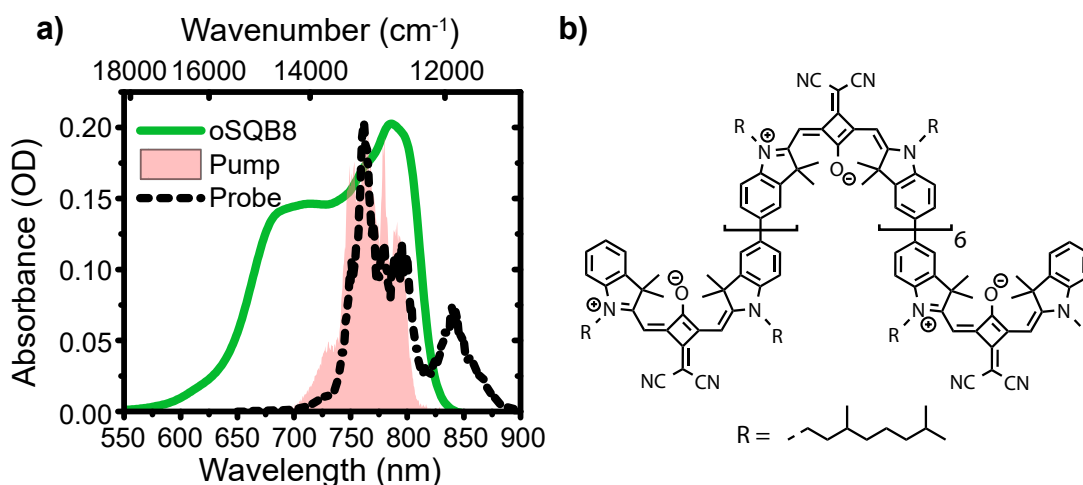

Figure 8.3.: Characteristics of the measured squaraine oligomer oSQB8. (a) The absorption spectrum (green) in toluene shows an absorption maximum at $\sim$ 780 nm which corresponds to an excitonic structure with J-type coupling. The laser pump spectrum for the 2D as well as PP measurements (red shaded) is located at the blue side of the main absorption peak while the probe spectrum (black dashed) covers $\sim$ 700 to 900 nm. (b) The squaraine oligomer consists of eight SQB monomer subunits. From the absorption spectrum, a structurally disordered linear chain structure can be deduced.

8.3.2. Two-Dimensional Spectroscopy

Before we discuss the extraction of clean third-order signals at different excitation regimes, we want to focus on the isolation of nQ signals starting with 2D spectroscopy in this section. Carrying out the procedure derived in Sec. 8.2.1 requires scanning of the coherence time in small enough steps to separate the different nQ signals along the excitation axis in the 2D spectrum. We want to demonstrate our correction procedure at different excitation intensity regimes, i.e., where different higher-order signals are contributing. Therefore, we measured 2D spectroscopy at various excitation intensities and isolated the 1Q, 2Q, and 3Q signal for each excitation intensity. In practice, we

keep all pulse parameters constant and vary the pulse energy, which is proportional to intensity, by directly using the pulse shaper. In the following we will refer to these measurements by their specific pulse energy of the excitation pulses at temporal overlap ($\tau = 0$). The probe pulse was always kept weak such that it effectively interacted only once with the system.
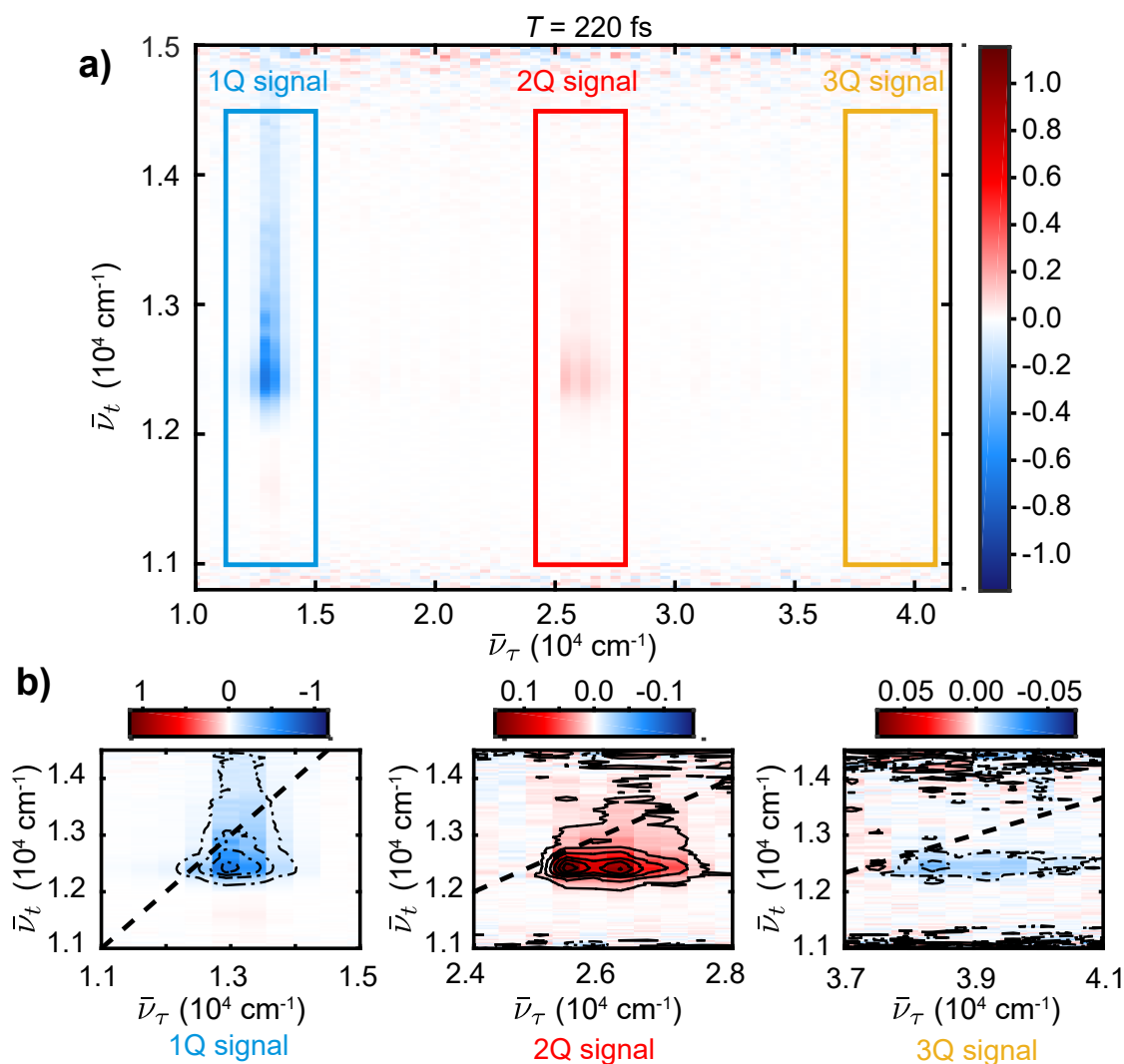
Figure 8.4.: Multi-quantum 2D spectra of squaraine oligomer oSQB8 measured at a pulse energy of 220 nJ. (a) Three signals can be distinguished at one, two, and three times the frequency of the pump pulse on the excitation frequency axis. (b) Zoomed-in data of the regions marked by colored rectangles in panel (a) containing the 1Q (left), 2Q (middle), and 3Q signals (right). The sign of the signal alternates and the line shape gets broader along the excitation axis from 1Q over 2Q to 3Q. Diagonals (dashed black) are drawn at $\bar{\nu}_\tau = \bar{\nu}_t$ for 1Q, $2\bar{\nu}_\tau = \bar{\nu}_t$, and $3\bar{\nu}_\tau = \bar{\nu}_t$ for 3Q.

The 2D spectrum at a population time of $T = 220$ fs, measured with an excitation pulse energy of 220 nJ, is shown in Fig. 8.4a. The signal near the excitation frequency of ω_0 (corresponding to ~ 13000 cm^{-1}) represents the 1Q signal (blue rectangle). It is dominated by a negative signal which is elongated along the detection axis. At around twice the excitation frequency ($2\omega_0$), a positive 2Q peak is visible (red rectangle), called "EEI2D signal" in previous publications [4][7][20]. Here, we adopt the "nQ" nomenclature to enable generalization to arbitrary orders n and non-excitonic systems.

In Fig. 8.4b we show the individual regions of the 1Q, 2Q, and 3Q regions with rescaled color bars such that we can clearly distinguish the three different nQ signals. As discussed in Sec. 8.2.1, the sign alternates between an nQ and an $(n + 1)$Q signal. Interestingly, for the higher-order signals (that we define as all nQ signals with $n > 1$) a pronounced elongation along the excitation axis can be observed. All nQ signal maxima are located slightly below their respective diagonals ($\bar{\nu}_\tau = \bar{\nu}_t$ for 1Q, $2\bar{\nu}_\tau = \bar{\nu}_t$ for 2Q, and $3\bar{\nu}_\tau = \bar{\nu}_t$ for 3Q). The reason for the peak position could be energy relaxation and stimulated emission contributions leading to a shift to smaller detection wavenumbers. The line shapes of the 2Q signal were investigated theoretically for molecular dimers and trimers [220], as well as directly compared to experimental results on the example of a squaraine trimer [220]. We leave an analysis of nQ line shapes in the present oligomer to future work and instead concentrate on the signals integrated over $\bar{\nu}_t$ for each nQ region shown in Fig. 8.4b (1Q: 11258 cm^{-1} to 15010 cm^{-1}, 2Q: 24183 cm^{-1} to 27936 cm^{-1}, and 3Q: 37109 cm^{-1} to 40862 cm^{-1}).

We show in Fig. 8.5a the integrated 2D signals of the respective regions for three different pulse energies. The $\bar{\nu}_\tau$ integration, while keeping the $\bar{\nu}_t$ coordinate, leads to effective transient absorption maps. Each of the maps is normalized to the maximum of the absolute signal of the displayed map. We adjusted small differences of the temporal overlap between pump and probe pulses ($T = 0$, $\tau = 0$) between the measurements by shifting the population time axis using the coherent artifact in the 1Q signal as described in the Supplementary Material (Sec. 8.5.6). This only affected the population time axis and not the coherence time. We show the 1Q, 2Q, and 3Q signals (from left to right) for pulse energies of 15 nJ, 120 nJ, and 220 nJ (from top to bottom). The 1Q signal at all pulse energies is dominantly negative which corresponds to ground-state bleach and stimulated emission in our sign convention of transient absorbance change. Now we focus on the higher-order signals. For the lowest pulse energy (15 nJ), only a 1Q signal is visible. At the next higher pulse energy (120 nJ), a 2Q signal can be clearly seen, and the 3Q signal just begins to emerge from the noise floor. At the highest pulse energy (220 nJ), all three signals (1Q, 2Q, and 3Q) are clearly visible.
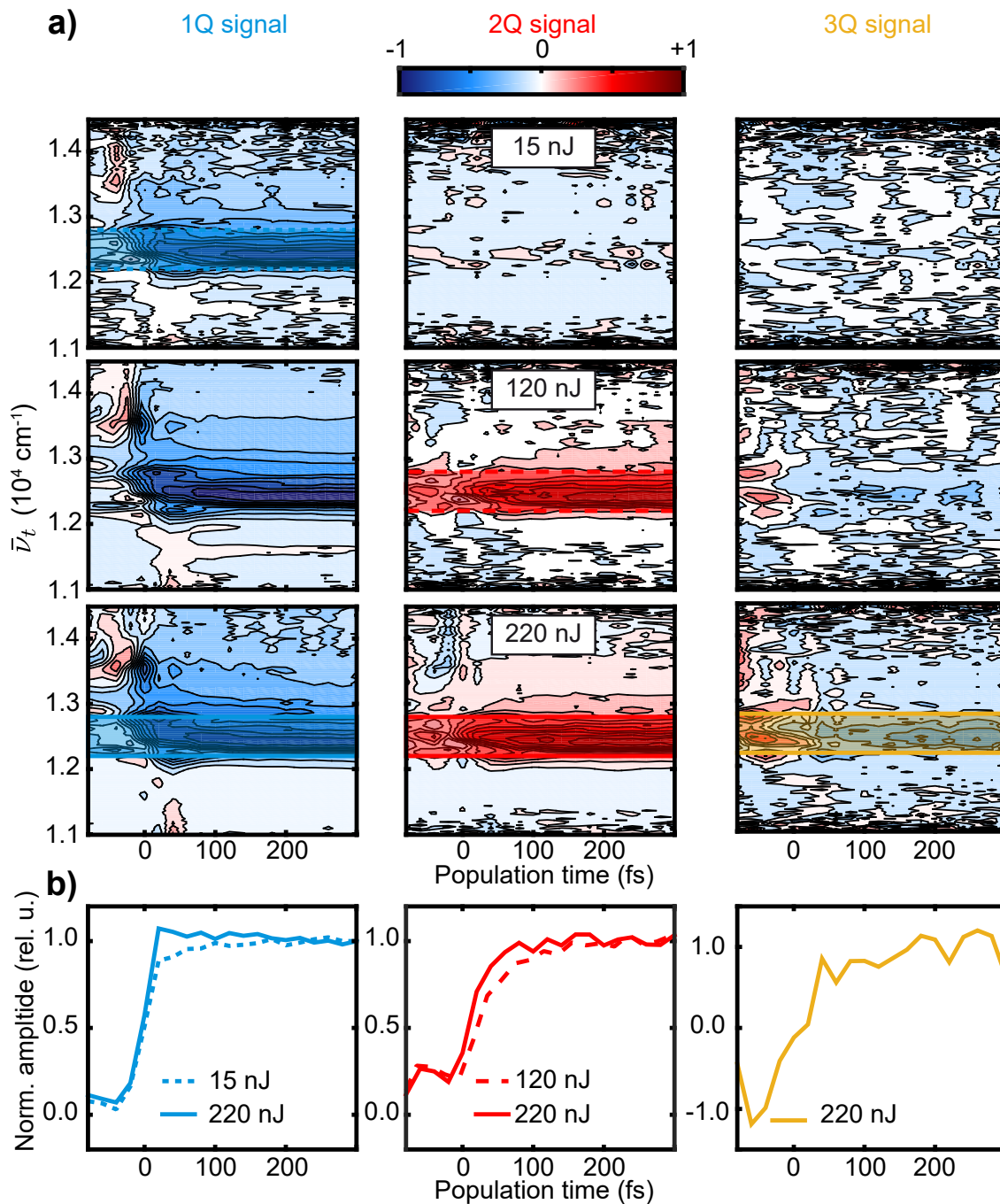
Figure 8.5.: Integrated (along $\bar{\nu}_\tau$) kinetics for the 1Q (left column), 2Q (middle column), and 3Q signals (right column). (a) Resulting effective TA maps. The pulse energy was varied from 15 nJ (top row) over 120 nJ (middle row) to 220 nJ (bottom row). Each of the maps is normalized to the maximum of the absolute signal of the displayed map. (b) Kinetics by averaging the maps from panel (a) over $\bar{\nu}_t$ (indicated by colored rectangles) and normalizing to the average between 200 and 300 fs. The 1Q signal is shown for pulse energies of 15 nJ (blue dotted) and 220 nJ (blue solid), the 2Q signal for 120 nJ (red dashed) and 220 nJ (red solid), and the 3Q signal for 220 nJ (yellow solid).

In Fig. 8.5b we show the average (along $\bar{\nu}_t$ over the marked regions in the maps) transient absorption signals for 1Q, 2Q, and 3Q. These transients are normalized to the average signal from 200 to 300 fs to facilitate direct comparison of nQ kinetics. Thus, the transients are all positive for long delay times and do no longer reflect the sign alternation from Fig. 8.5a. The 1Q signals at 220 nJ (Fig. 8.5b, blue solid) and 15 nJ (blue dotted) both rise at around $T = 0$. The differences between the two measurements are visible in the first 100 fs after $T = 0$. During the first 100 fs, the 1Q signal at 220 nJ rises to a maximum above 1.0 and then slightly decreases. The 1Q signal at 15 nJ first initially follows the signal at 220 nJ but before then rounds off without building up a maximum. The change in the dynamics between the measurements at different pulse energies is a clear indicator that at high pulse energies, higher-order contributions contaminate the 1Q signal.

With the nQ analysis described in the present work, contamination of 1Q is trivial to confirm because we can directly measure the higher-order signals, i.e., at 2Q (Fig. 8.5b, red solid) and 3Q positions (Fig. 8.5b, yellow solid) at 220 nJ. These higher-order signals correspond to excitation of higher-excited states such as biexciton states. As previously discussed, higher-order signals in extended systems such as polymers are dominated by exciton–exciton annihilation [7]. The 2Q signal at 220 nJ rises more slowly than the 1Q signal at 220 nJ during the first 100 fs, although the difference is small. The 2Q signal rises slower since it reports on the annihilation of two excitons. In order to annihilate, the excitons have to get in close proximity to each other and therefore a period of exciton diffusion takes place which is reflected by a rise of the 2Q signal. Compared to larger excitonic systems that were investigated previously such as polymers and aggregates [7, 20], the rise of the 2Q signal is faster here since the studied oligomers are smaller and therefore the excitons do not need to propagate for large distances before annihilation. At an excitation pulse energy of 120 nJ, the 2Q signal (Fig. 8.5b, red dashed) rises more slowly than for 220 nJ (red solid). The slower 2Q rise for lower pulse energies is an analogous effect as that observed for 1Q, i.e., higher-order signals contaminate the signal. In this case, at 220 nJ, the seventh-order signal appears at the 2Q position. We can observe the seventh-order signal directly at the 3Q position (Fig. 8.5b, solid yellow). The dynamics of the 3Q signal are influenced by a strong coherent artifact mostly visible as a strong signal for $T < 0$. Previous studies demonstrated that non-resonant [189] as well as non-time-ordered (between pump and probe) contributions [124] have to be considered for the early time dynamics. A comparison of the measured dynamics of the 3Q signal with the 1Q and 2Q signals is difficult because of the low SNR. While the 2Q signal is dominated by the dynamics of biexcitons, the 3Q signal will additionally contain the dynamics of triexciton dynamics, i.e., the annihilation of three excitons. A theoretical analysis of the kinetic evolution of higher-order signals in excitonic systems can be found elsewhere [16].

8.3.3. Pump–Probe Spectroscopy

As discussed in Sec. 8.2.2, nQ signals can also be extracted from PP experiments using a systematic variation of the excitation intensity. We show in Fig. 8.6a the 1Q (left), 2Q (middle), and 3Q signals (right) measured via PP. In order to obtain the 1Q, 2Q, and 3Q signal a set of three different pulse energies is needed as discussed in Sec. 8.2.2. We constructed three different sets of 1Q, 2Q, and 3Q signals using Eq. (8.16) which are labeled by the highest power in each sequence: 200 nJ (constructed from measurements at 200 nJ, 150 nJ, and 50 nJ), 50 nJ (constructed from measurements at 50 nJ, 37.5 nJ, and 12.5 nJ), and 12.5 nJ (constructed from measurements at 12.5 nJ, 9.375 nJ, and 3.125 nJ).
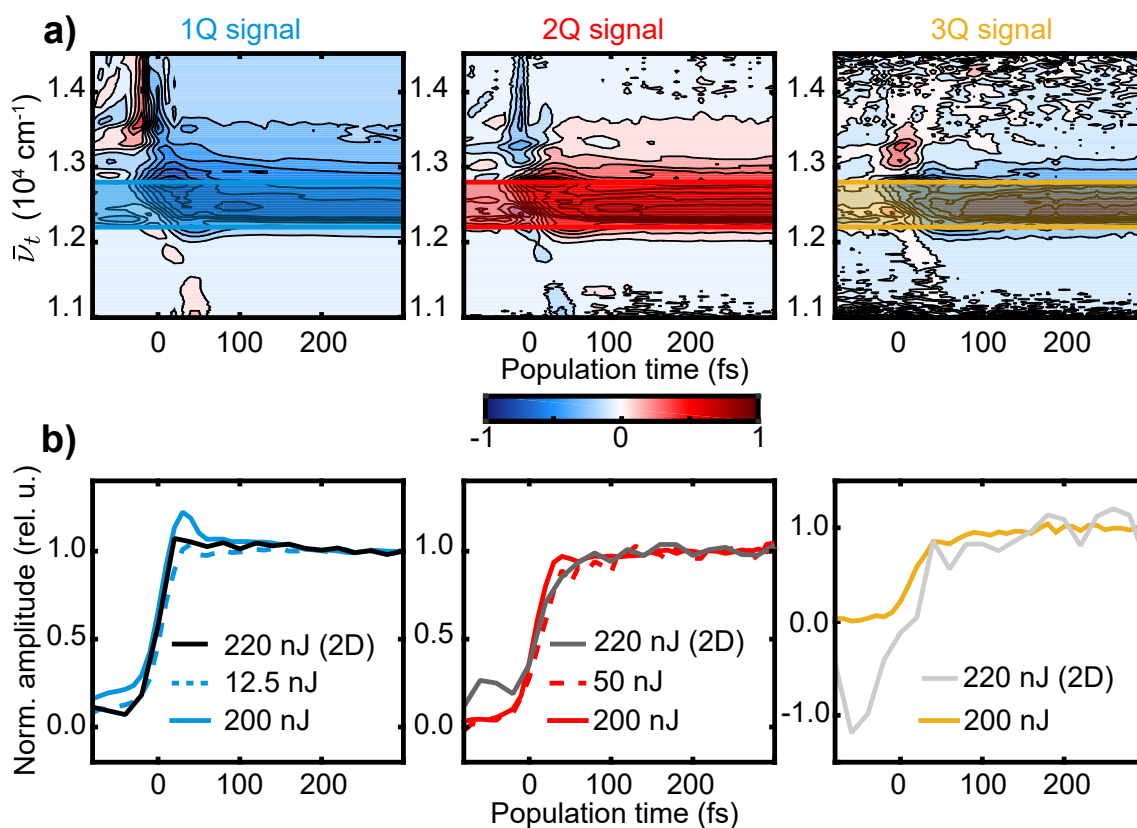
Figure 8.6.: Higher-order PP signals of a squaraine oligomer oSQB8. (a) 1Q, 2Q, and 3Q PP maps extracted from a set of three measurement with $4I_0$ corresponding to 200 nJ. In this measurement the signal is isolated by phase cycling as described above. Each map is normalized by dividing the map by the maximum of the absolute signal of the displayed map. (b) 1Q signal measured at a pulse energy of 200 nJ (blue solid line) and 12.5 nJ (blue dashed line). For comparison we show the 1Q signal of the 2D measurement at 220 nJ (black solid). (c) 2Q signal measured at a pulse energy of 200 nJ (red solid) and 50 nJ (red dashed). The corresponding signal from 2D measurements at 120 nJ (dark gray solid) is also shown. (c) 3Q signal measured at a pulse energy of 200 nJ (yellow solid line) and 3Q signal from 2D measurements at 220 nJ (light gray solid).

We show the full sets of PP data for the three different sets of $4I_0$, $3I_0$, and I_0 in the Supplementary Material (Sec. 8.5.7). Let us now focus on the transients arising after averaging over the marked regions in Fig. 8.6a and normalization to the average signal between 200 and 300 fs (Fig. 8.6b). The difference in the dynamics for the measurements at different excitation powers is again mostly visible in the population times from $T = 0$ fs to $T = 100$ fs. For the 1Q signal at 200 nJ ($4I_0$), the signal rises rapidly at around time zero, reaches a maximum above 1.0 and then decays (Fig. 5b, blue solid). The 1Q signal extracted from the set with $4I_0$ corresponding to 12.5 nJ (blue dotted) does not reach a value above 1.0 and has a more roundish shape. The differences of the dynamics between these two curves is again a clear sign that at 200 nJ the 1Q signal is contaminated by higher-order contributions. The change in the dynamics is also visible for the 2Q signal at 200 nJ (red solid) compared to 50 nJ (red dashed) which can be explained by the seventh-order contribution clearly visible as a 3Q signal (yellow solid). The 2Q signal at 200 nJ (Fig. 8.6b, red solid) rises more slowly than 1Q which is better visible by direct comparison of the traces as shown in the Supplementary Material (Sec. 8.5.8).

The difference for the measurements between low and high power in PP spectroscopy is similar to the differences between low and high excitation power in 2D spectroscopy. The 1Q signal in PP spectroscopy at low power (extracted from the data set with $4I_0$ corresponding to 12.5 nJ) has a similar roundish shape as the 1Q signal at lower powers in the 2D measurements (Fig. 8.5b, blue solid). Also, the 2Q signal for PP and 2D spectroscopy (dark grey solid) have similar dynamics. The direct comparison between the PP and the 2D 3Q signal (Fig. 8.6b, light gray) is not meaningful since the 3Q signal of the 2D measurement is strongly influenced by the coherent artifact which is absent in the case of PP spectroscopy. Interestingly, the 1Q signals of PP and 2D experiments seem to differ around time zero for the highest measured power. For the PP measurement, a small spike is visible while this is not the case for 2D spectroscopy (Fig. 8.6b, black solid). One reason could be that the 1Q signal in PP and 2D spectroscopy is contaminated to varying degrees by higher order contributions. Small variations of the experimental conditions between the PP and the 2D measurements, such as slight variations of the laser spectra, the temporal shapes of the pulses or the spatial overlap between pump and probe pulses, as well as experimental imperfections might result in a different effective excitation density and therefore in more or less contamination.

Another interesting observation is the different appearance of the coherent artifact in PP and 2D measurements. This is best visible for the negative time delays where there is almost no signal in the case of PP spectroscopy. In the region close to $T = 0$, interactions with the pulses may take place with "incorrect" time ordering such as "pump–probe–pump" for either PP or 2D spectroscopy [124]. In 2D spectroscopy, however, such "inverted" time orders can occur for larger T than in PP because the additional scan of coherence time leads to a "prolonged" incorrect order of the pulses while in PP experiments, the incorrect time-ordering contributions can only occur if the pump and the probe pulses overlap. However, a detailed analysis of the coherent artifact in both techniques is beyond the scope of this work.

In summary, the higher-order signal in 2D and PP spectroscopy reveal similar dynamics except for the population times close to $T = 0$. The contamination of higher-order signals in both methods is visible as a change in the dynamics of the 1Q signal by 2Q and 3Q contributions, and of the 2Q signal by 3Q contributions, i.e., faster rises in each signal are seen for higher excitation pulse energy.

8.3.4. Extraction of Contamination-Free Third-Order Signal

We now focus on the correction of the 1Q signal with respect to higher-order contributions, using both 2D and PP data. In Fig. 8.7 we show 1Q transients from 2D (a) and PP (b) measurements, averaged over $\bar{\nu}_t$ (from 12200 to 12800 cm^{-1}). In the case of 2D spectroscopy, the measurements of 220 nJ and 15 nJ were already shown in Fig. 8.5b. The transients extracted from a set of three PP measurements with $4I_0$ of 200 nJ were shown in Fig. 8.7b. For the high-power measurement (220 nJ for 2D, $4I_0$ of 200 nJ for PP spectroscopy) the 1Q signal is contaminated by higher-order contributions, i.e., third-, fifth-, and seventh-order signals are mixed together. As a reference for the 2D measurements we use the signal measured at 15 nJ. For PP spectroscopy we use the lowest intensity-cycling step corresponding to an excitation power of 3.125 nJ. We call these two signals reference signals. The integrated transients are scaled using two factors. First, each signal is divided by the absolute value of the transient of the reference signal (averaged from $T = 200$ fs to $T = 300$ fs). Therefore all signals are now in relative units and not in mOD anymore. However, the signals differ in their strength because they are measured with different excitation powers. For example, the 1Q signal extracted from a set of measurements with $4I_0$ of 200 nJ would be roughly four times stronger than with $4I_0$ of 50 nJ. Thus, as a second scaling factor, we divide each signal by the ratio between the pulse energy of that particular measurement and the pulse energy of the reference measurement. For 2D spectroscopy this procedure is straightforward but for our technique of PP spectroscopy care has to be taken. The reference measurement corresponds to one intensity cycling step, i.e., one PP measurement at a pump pulse energy of 3.125 nJ. Due to the normalization factor of $\frac{1}{2N}$ in Eq. (8.16) the 1Q signal extracted from a set of three measurements is normalized to I_0. Therefore the 1Q signal extracted from the set with $4I_0$ corresponding to 200 nJ, $3I_0$ corresponding to 150 nJ and I_0 corresponding to 50 nJ, is divided

by the ratio of $\frac{50}{3.125}$. Analogously the 1Q signal extracted from measurement of 50 nJ, 37.5 nJ, and 12.5 nJ is divided by $\frac{12.5}{3.125}$. If the negative 1Q signal scaled linearly with excitation intensity, i.e., if no higher-order contaminations contributed at higher pulse energies, the minimum signal of each trace would be at -1.0 with this normalization procedure because we divide the negative signal by the absolute of the averaged reference signal as well as the ratio of powers which are both positive. Saturation of the signal for higher excitation intensity leads to lower signal amplitude and, therefore, a decrease of the signal from -1.0, for example, to -0.8. In Fig. 8.7 the uncorrected transients are shown as solid lines. The spectrally resolved maps are shown in the Supplementary Material (Sec. 8.5.9). For the lowest-power measurements in the 2D experiment, no higher-order signals could be detected. Therefore, this signal should be free from contamination from higher orders (Fig. 8.7a, light blue). For higher pulse energies such as 120 nJ (Fig. 8.7a, dark blue solid) and 220 nJ (Fig. 8.7a, purple solid) the signal saturates, which leads to a signal decrease to -0.6 for the measurement at 120 nJ and to -0.4 for the measurement at 220 nJ. As stated above, the change of the signal dynamics by higher-order contributions is small in this particular sample, but changes can be dramatic in the general case of other excitonic systems [186, 205, 206]. We therefore use the signal strength as an additional indicator for whether a clean third-order signal can be recovered.
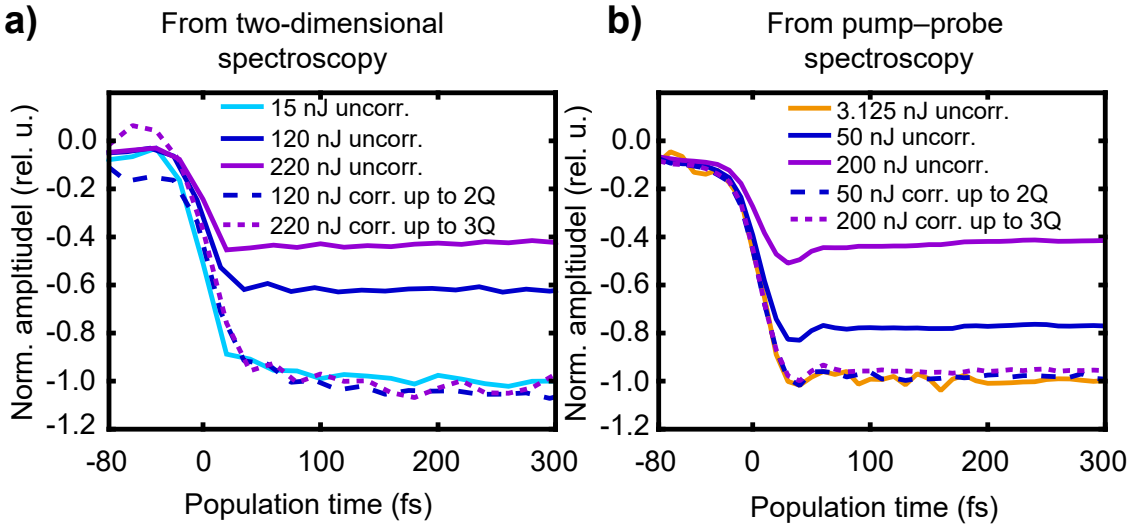
Figure 8.7.: Averaged (along $\bar{\nu}_t$) and normalized (see text) 1Q transients from (a) 2D and (b) PP measurements with the respective corrections for higher-order contaminations. The medium power (dark blue) is corrected using the 2Q signal only while the highest power (purple) is corrected using the 2Q and 3Q signals. Solid lines correspond to uncorrected signals at the powers given in the legend, blue dashed lines correspond to correction of the medium-power measurement using the 2Q signal, and purple dotted lines correspond to the highest-power measurements corrected using the 2Q and 3Q signals.

We now apply the correction procedure from Sec. 8.2 to the measurements of 120 nJ by subtracting four times the 2Q signal from the 1Q signal, resulting in a clean third-order signal which is shown in Fig. 8.7a (dark blue dashed). For the measurement at 220 nJ, we use both the 2Q and the 3Q signal for correction according to Eq. (8.10) and show the result in Fig. 8.7a (purple dotted). The corrected curves show similar dynamics as the low-power measurement, and the scaling is also correct, i.e., their minimum signals are around -1.0. At close inspection, it can be seen that the corrected curves are both slightly below the lowest-power measurements. This indicates that there is a small contribution of fifth-order contamination present even for the lowest-power measurement.

For the PP experiments (Fig. 8.7b), the situation is similar to the 2D experiments. Since the pulse energies are slightly lower in the PP measurements than in the 2D measurements, the saturation for the power of 50 nJ [Fig. 6(b), dark blue solid] is not as strong as in the 2D measurement. The change in the dynamics is also not as clear for the power of 50 nJ [Fig. 8.7b, dark blue solid] as for 2D spectroscopy. However, for the highest power of 200 nJ [Fig. 8.7b, purple solid], the signal starts to lose its roundish shape. We compare the signal to the annihilation-free PP measurement at 3.125 nJ [Fig. 8.7b, orange]. Note that this is simply the last measurement step for the experiment extracted from three measurements with $4I_0$ corresponding to 12.5 nJ shown in Fig. 8.6. We discuss the signal extracted from a set of three measurements with $4I_0$ corresponding to 12.5 nJ in the Supplementary Material (Sec. 8.5.10). The corrections of the 50 nJ data up to 2Q (dark blue dashed) and the 200 nJ data up to 3Q (purple dotted) eliminate the higher-order contaminations. We show that no seventh-order contamination is present in the 50 nJ measurement in the Supplementary Material (Sec. 8.5.11). Both of the corrected curves and the low-power measurement in Fig. 8.7b agree well and only at close inspection a slight systematic deviation can be noticed. For the highest power, the corrected curve [Fig. 8.7b, purple dotted] is slightly above the lowest-power measurement. This is a hint that at 200 nJ, the 3Q signal will be contaminated by a (small) ninth-order contribution that we did not extract with our measurement scheme but could be obtained using one more measurement step in the intensity-cycling procedure [16]. In the 2D experiment, the signal at highest pulse energy seems to be corrected reasonably well using the 2Q and 3Q signals, and not requiring any 4Q corrections. Slightly different beam sizes or a variation in the spatial overlap between pump and probe beams between the 2D and PP measurements might also be reasons for the small deviations between the two experiments.

Additionally to the transients of Fig. 8.7, we show in Fig. 8.8 cuts along $\bar{\nu}_t$ for the 1Q signal with and without correction for higher-order contamination at two population times, 40 fs and 300 fs. We directly compare the data from 2D spectroscopy (Fig. 8.8a) and from PP spectroscopy (Fig. 8.8b). The signals are scaled in a similar way as in Fig. 8.7: First the signal for each specific T step is divided by the absolute signal of the minimum of the lowest-power signal and then each signal is divided by the ratio between the pulse energy of the measurement and the lowest pulse energy.
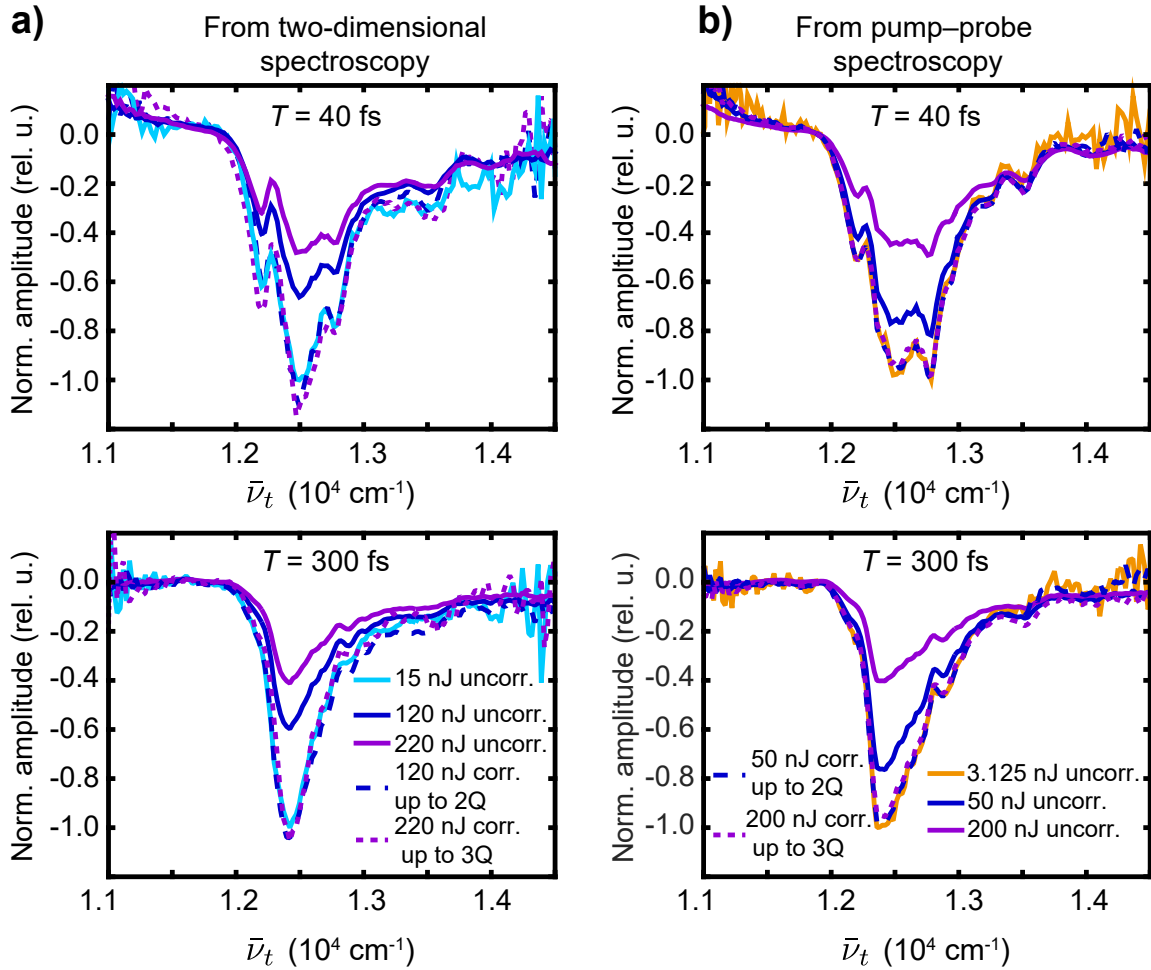
Figure 8.8.: 1Q signal as a function of $\bar{\nu}_t$ for the two population times of 40 fs (top) and 300 fs (bottom) from (a) 2D and (b) PP spectroscopy. The measurements with pulse energies of 120 nJ and 50 nJ are corrected using the 2Q signal only while the measurements with 220 nJ and 200 nJ are corrected using the 2Q and 3Q signals. The uncorrected signals with pulse energies of 120 nJ and 50 nJ are shown as dark blue solids while the corresponding corrected signals are shown as dark blue dashed lines. The uncorrected signals corresponding to 220 nJ and 200 nJ are shown as purple solids while the corrected signals are shown as purple dotted lines. As references, i.e., uncontaminated low power signals, we show measurements at 15 nJ (light blue solid) and 3.125 nJ (orange solid). For the 2D measurement at 120 nJ, we evaluated the average of the signal between 35 fs and 55 fs (top panels) as well as the average between 295 fs and 315 fs (bottom panel), since the population time axis of this measurement was shifted by 15 fs and therefore no spectral measurement for time delays exactly at 40 fs and 300 fs was taken.

Let us first focus on the 2D signals at $T = 40$ fs. The signal amplitude at 120 nJ [Fig. 8.8b, dark blue solid] and 220 nJ [Fig. 7b, purple solid] is decreased which is the result of the higher-order contaminations and the connected saturation of the signal. This means that these signals do not correspond to a clean third-order signal but are contaminated by fifth- and seventh-order contributions. For the measurement at 120 nJ, we used the 2Q signal for correction and for the measurement at 220 nJ, we used the 2Q as well as the 3Q signal. The results are shown as the dark blue dashed line for the corrected signal at 120 nJ and as the purple dotted line for the signal at 220 nJ. The minimum of both signals is now at -1.0 demonstrating that the corrected signals correspond to the clean third order. The same behavior can be observed for $T = 300$ fs. In the PP measurement, the saturation is clearly visible for measurements extracted from a set of three measurements with $4I_0$ corresponding to 50 nJ [Fig. 8.8b, dark blue solid] and $4I_0$ corresponding to 200 nJ [Fig. 8.8b), purple solid]. The corrected 1Q signals extracted from the set of measurements with $4I_0$ corresponding to 50 nJ [Fig. 8.8, dark blue dashed] and $4I_0$ corresponding to 200 nJ [Fig. 8.8b, purple dotted] agree well with the low-power measurement [Fig. 8.8b, orange solid]. At the edges of the signal, the probe spectrum is weak and the noise increases in both the 2D and the PP method. For the data from 2D spectra, the corrected curves are slightly below -1.0 which is a result of a small contribution of the fifth-order signal at 15 nJ [Fig. 8.8, light blue solid] as discussed above. At $T = 40$ fs, the spectra from the 2D and the PP measurements are slightly different which is due to the already discussed difference between the coherent artifact in both methods. For the larger population time of $T = 300$ fs, the spectra from both methods are similar. The correction to obtain a clean third-order signal for 2D as well as PP spectroscopy also works for $T = 0$ as we show in the Supplementary Material (Sec. 8.5.12). For both population times (and for both techniques), the corrections rebuild the shape of the signal of the measurement at low pulse energy. We emphasize that our procedure allows one to judge very easily the excitation regime, i.e., which higher-order contaminations are present. Besides the correction, one obtains control over the higher-order contributions allowing to obtain additional information about the interaction of multiple (quasi)particles and higher-excited states.

8.3.5. Higher-Order Pump–Probe Spectroscopy on Squaraine Polymers

As already outlined above, the technique of higher-order 2D and PP spectroscopy can be used to obtain clean nonlinear signals. In PP spectroscopy, measurements at N different excitation intensities result in N clean nonlinear signals. In principle, such an experiment allows one to systematically increase the order of excitation in the system and to investigate increasing orders in terms of perturbation theory. So far, we have only discussed cases with $N = 3$ allowing to separate the third-, fifth-, and seventh-order nonlinear signals in terms of perturbation theory.

Now we have chosen to set $N = 6$ which enables us to isolate up to the thirteenth-order signal in terms of perturbation theory. The results of this experiment are shown in Fig. 8.9. Besides the TA maps, the integrated signal over the displayed map is shown on top of each map. As a sample system, we have chosen squaraine copolymers with an average length of about 19 dimers that were already investigated by us recently [7]. Our previous experiment on this particular sample was limited to the fifth-order signal which was utilized to observe EEA. From the measured dynamics, the exciton diffusion in these systems was characterized and we found that the exciton dynamics are best described by a sub-diffusive behavior. In higher-order PP spectroscopy, we can now observe even higher-order signals.

One of the six PP measurements in which all nonlinear signal contributions are mixed together, is shown on top of Fig. 8.9. Using the six PP measurements, six different nonlinear signal contributions from third- to thirteenth-order in terms of perturbation theory can be extracted. The third-order signal consists of one strong negative feature from the SE and GSB signal contributions. The signal decays with several time constants as can be already seen from the traces on top of the TA map. Global analysis revealed that the decay consists of five different components as well as an additional component reflecting the coherent artifact. The time constants connected to the different components are in good agreement with previous TA experiments [206]. The physical nature of these components is difficult to unravel since processes such as vibrational relaxation might contribute as well as the distribution of the polymer lengths that is quite broad for this sample [7].

The first higher-order signal is the fifth-order signal. Instead of the single-exciton dynamics, the fifth-order signal probes the biexciton manifold and with that the process of EEA in the system. Compared to the third-order signal, the sign is flipped due to the prefactor of $\left(\frac{i}{\hbar}\right)^n$ with n as the order of nonlinearity in the response function. In accordance to that, the main signal corresponding to GSB and SE contributions in the fifth-order spectrum is now positive. An interesting feature of the higher-order signals is a signal with the opposite sign of the respective signal that is visible at a de-

---

This section is based on the following publication:

P. Malý, J. Lüttig, P. A. Rose, A. Turkin, C. Lambert, J. J. Krich, and T. Brixner.
Separating single- from multi-particle dynamics in nonlinear spectroscopy.
submitted (2022).

tection wavenumber of about 13000 cm^{-1}. This signal contribution that is best visible in the fifth-order signal is not present in the third-order signal and might be connected to the relaxation process between the multi-exciton manifolds via annihilation. The integrated dynamics of the fifth-order signal differ substantially from the third-order signal. The fifth-order signal rises slowly due to the diffusion-limited EEA. With our experimental approach we can now also separate other higher-order signals. Increasing the nonlinearity by two flips the overall sign of the signal resulting in a negative main feature for the seventh- and eleventh-order signals and positive signs for ninth- and thirteenth-order signals. With increasing order of nonlinearity, the number of interacting particles increases: For the fifth-order signals, biexciton states can be excited, for the seventh-order signal triexciton states and analogously for the higher-order signals.

The dynamics observed within the signals are a result of a complex interplay of the relaxation processes between the manifolds or, in other words, the seventh-order signal includes annihilation of triexcitons, annihilation of biexcitons by EEA as well as single-exciton decay. Summing up the different pathways and relaxation processes that can occur, the nonlinear signals can be fitted with analytic formulas. The fits were performed for the first four nonlinear signals ($PP^{(3)}$ to $PP^{(9)}$) and are shown as solid lines in the traces in Fig. 8.9. The single-exciton lifetimes can be approximated by effective rates from the global analysis. From the higher-order nonlinear signals, the annihilation rates for two, three, and four excitons are obtained. The scaling of the annihilation rate for increasing numbers of excitons can be used to answer a fundamental question about the interplay between exciton diffusion and EEA: Do excitons always annihilate when they are colocalized or can several encounters between the excitons occur without annihilation? In our recent study, a continuous-time random-walk model was used to investigate this question by calculating the averaged annihilation rates for two, three, and four excitons. The key parameter in the model that was varied is the local annihilation rate. For a fast local annihilation rate, the excitons will always annihilate when they are colocalized and for a slow local annihilation rate, the excitons have time to "escape" before annihilation takes place. Using our model, we could fix the local annihilation rate to 29 fs which reproduces the averaged annihilation rates of two, three, and four excitons that were obtained by fitting the fifth-, seventh-, and ninth-order signals. This local annihilation time also agrees with the annihilation time that was obtained in separate experiments on squaraine dimers [7, 9]. Such a slow local annihilation rate means that the excitons annihilate in less than 10% of the cases when they are colocalized.
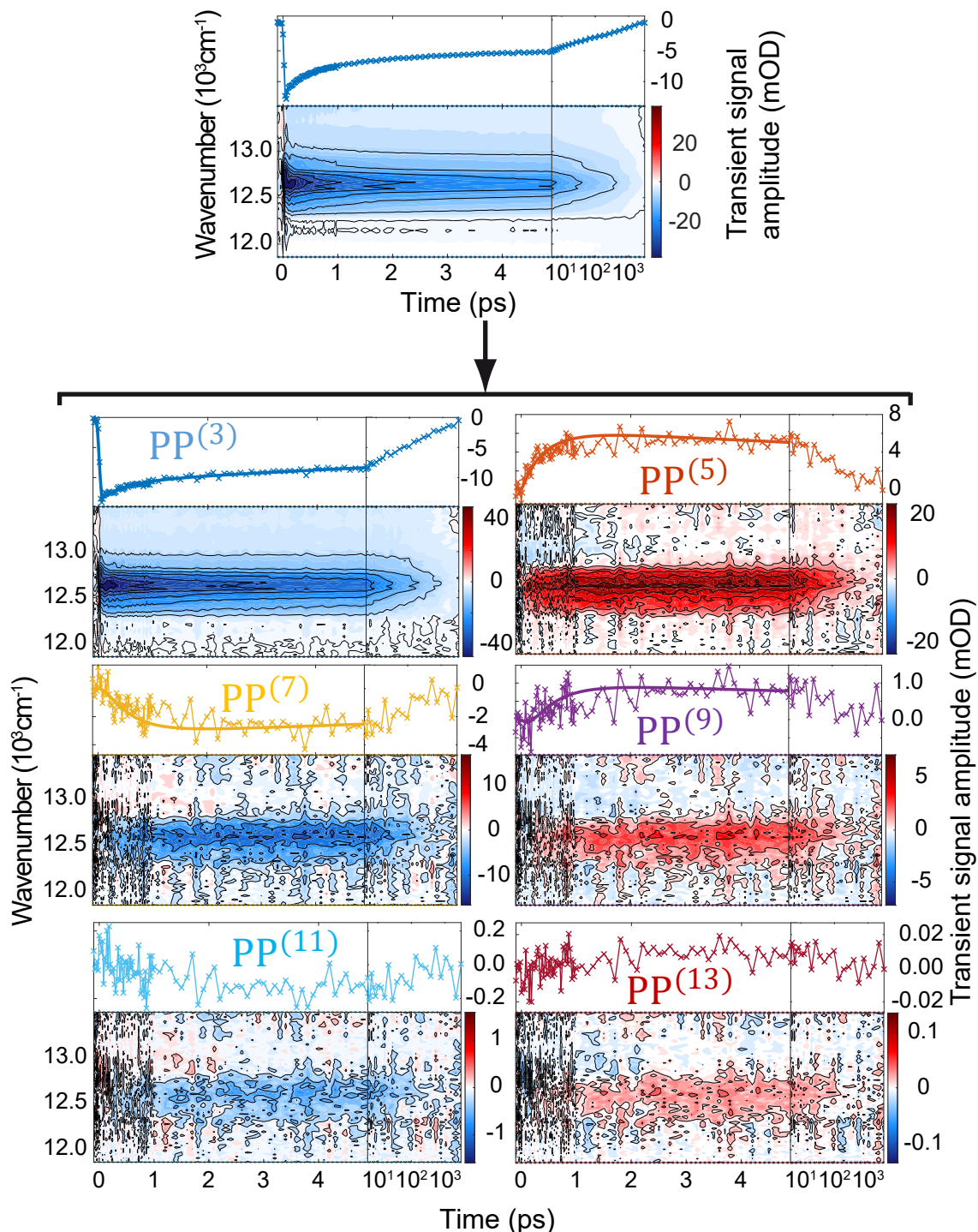
Figure 8.9.: Nonlinear signal contributions for squaraine copolymers obtained by higher-order PP spectroscopy. On the top is one of the six measured PP signals shown in which all higher-order signals are mixed together. Using our correction protocol allows us to separate six clean signal contributions up to the thirteenth-order signal. The integrated traces over the displayed map are shown on top of each map. Fits are shown as solid lines within the trace.

8.4. Conclusion

In this chapter, we demonstrated a general procedure that can be applied in two-dimensional (2D) spectroscopy as well in pump–probe (PP) spectroscopy to obtain clean nonlinear signals. The first steps in both methods is to isolate the nQ signals. In 2D spectroscopy the different signals can be isolated by their specific position along the excitation axis. In PP spectroscopy the nQ signals are isolated by an "intensity-cycling" procedure where the PP signal is measured at different excitation intensities. Linear combinations of these measurements resulted in the extraction of the various nQ signal contributions. General equations were derived that are also applicable to higher orders. As a next step we quantified how much each nonlinear signal contributes to a specific nQ signal. For 2D spectroscopy we used the well-known concept of double-sided Feynman diagrams. The crucial point to quantify the contribution of higher-order signals to a specific nQ signal using double-sided Feynman diagrams is that the diagrams at $\tau = 0$ have to be considered. The double-sided Feynman diagrams revealed the close correspondence for a higher-order signal to different nQ signals. Without distinguishing with which pulse the interactions take place the types of diagrams are the same for a higher-order contribution at different nQ signals. Taking into account with which pulse the interactions occur lead to different number of diagrams for a higher-order contribution at different nQ signals. In other words, the higher-order signals have the same dynamics at different nQ signals but differ in their amplitude. Based on the knowledge how much each higher-order signal contribute to different nQ signals we developed a correction protocol using the isolated nQ signals in PP and 2D spectroscopy. The clean nonlinear signals are extracted by adding the nQ signals together with specific correction factors. This result is remarkable because the correction procedure is independent of the explicit system properties.

We experimentally confirmed our theoretical analysis by isolating the 1Q, 2Q, and 3Q signals of squaraine oligomers in 2D spectroscopy and demonstrated that these signals can be isolated in a PP experiment as well. We showed that at high excitation pulse energies, fifth- and seventh-order contributions contaminate the 1Q signal, leading to a change in observed dynamics. In our example, these contaminations arose from multi-exciton processes such as exciton–exciton annihilation. Additionally, a saturation of the signal with higher pulse energies was observed. Following a full analysis of all contributing Feynman diagrams from all relevant higher orders, the measured 2Q and 3Q signals were utilized to correct the 1Q measurement for contaminations from higher orders resulting in a clean third-order signal. We confirmed our approach by comparing the corrected 1Q (i.e., third-order) signals with measurements at low pulse energies, i.e., in the absence of higher-order contamination, and found the dynamics to be the same. The experimental nQ results and their corrections were found to be equivalent for 2D and PP spectroscopy, apart from some small differences close to the pulse overlap that could be explained by non-time-ordered (between pump and probe) contributions that appear in a different way in 2D spectroscopy.

We furthermore used the technique of higher-order PP spectroscopy to isolate up to the thirteenth order in terms of perturbation theory on squaraine polymers. The higher-order dynamics are dominated by multi-exciton processes. The fifth-, seventh-, and ninth-order signals probes the dynamics of two, three and four excitons, respectively. The annihilation rates of two, three, and four excitons (obtained by fitting the corresponding signals) revealed that the excitons in squaraine polymers have many encounters before they finally annihilate.

The PP method is simple to implement because it does not require double-pulse scans for excitation, yet it is still possible to separate out multiple-quantum signals and correct for higher-order distortions. Our technique posses a simple solution to the long standing problem to avoid annihilation in ultrafast spectroscopic experiments. The extraction of annihilation-free signals is especially interesting for the investigation of natural light-harvesting complexes where annihilation is challenging to avoid. Furthermore, one gains simple access to higher-order signals allowing to investigate multi-particle interactions and probing their dynamics. While so far we investigated mostly excitonic systems, our method is not limited to excitons and can easily be applied to study other quasiparticles such as polaritons [241], plasmons [317] or phonons [242]. Using the extracted nQ signals to isolate clean nonlinear signals might also be possible in other spectroscopic methods such as fluorescence-detected 2D [45] and PP spectroscopy [248].

8.5. Supplementary Material

8.5.1. Double-sided Feynman Diagrams for the Third-Order 1Q Signal

In Fig. 8.10 we show the double-sided Feynman diagrams for a third-order signal at the 1Q position. We show the situations where time ordering between the pump pulses and the probe pulse is fulfilled (Fig. 8.10, black dashed box) and where no time ordering between pump pulses and the probe holds (Fig. 8.10, red dashed box). When time ordering between pump pulses and probe pulse is fulfilled, the interactions of the pump pulses (pulse a and pulse b) take place first, followed by the interaction of pulse c. For infinitesimally short pulses this is always fulfilled if $T > 0$. For finite pulse lengths, time ordering occurs if the delay T is significantly longer than the pulse duration. If the pulses overlap in time, the order of the interactions can occur in different ways, i.e., time ordering is not fulfilled anymore. Note that in both cases, time ordering is generally not fulfilled between the two pump pulses, i.e., the order of the interactions of pulse a and pulse b can be changed. If time ordering between pump and probe is fulfilled and the RWA holds, six diagrams contribute with the phase-matching directions of $-\mathbf{k}_a + \mathbf{k}_b + \mathbf{k}_c$ for the rephasing and $+\mathbf{k}_b - \mathbf{k}_a + \mathbf{k}_c$ for the non-rephasing contribution, where the indices a and b correspond to the pump pulses (considered to be identical) while the probe pulse is labeled with c. The rephasing and non-rephasing diagrams depend on the specific evolution of the density matrix

during the coherence and signal time [23]. We see that switching the time order of interactions of pulse a and pulse b results in switching from the rephasing to the non-rephasing set of diagrams. In the PP geometry we directly obtain the sum of rephasing and non-rephasing pathways. We used an algorithm to obtain all diagrams including those for which neither time ordering between pump and probe nor between the pump pulses is fulfilled [28]. While for third order, it is still relatively straightforward to take into account all diagrams manually, the automated procedure will help particularly for the many more diagrams at higher orders to be discussed below. Since we take into account all the different time ordering processes, our analysis is valid not only for infinitesimally short pulses but also for pulses with finite duration. We can further divide the diagrams by their connection to the processes of ground-state bleach (GSB), stimulated emission (SE), and excited-state absorption (ESA) as labeled in Fig. 8.10. We follow the convention of transient absorption spectroscopy where a third-order GSB signal has a negative sign. Furthermore, each interaction from the right contributes a minus sign to the diagram irrespective of whether it points towards the bra side of the density matrix or away from it.
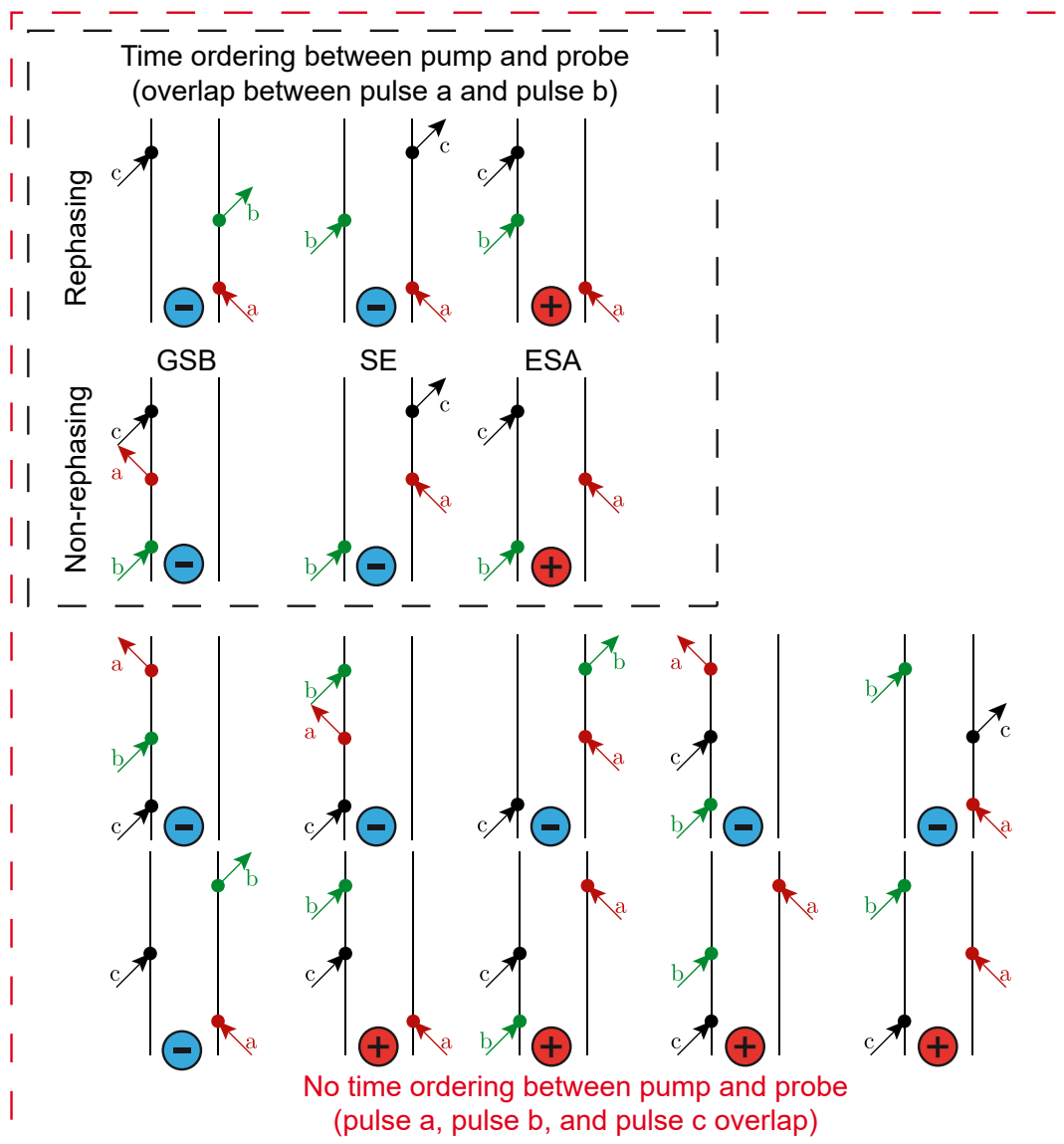
Figure 8.10.: Double-sided Feynman diagrams for a third-order signal. For the shown diagrams we assume that the RWA holds. The diagrams in the black dashed box show the six diagrams that are connected to the processes of ground-state bleach (GSB), stimulated emission (SE), and excited-state absorption (ESA) for the rephasing and non-rephasing contributions. For these six diagrams, time ordering between the pump and the probe pulses is fulfilled. The diagrams in the red dashed box show the additional pathways for which time ordering between pump and probe is not fulfilled. The sign of each pathway is shown below each diagram.

8.5.2. Double-Sided Feynman Diagrams for the Fifth-Order 1Q and 2Q Signals

In Fig. 8.11 we show the complete set of double-sided Feynman diagrams for the fifth-order signal at the 1Q as well as at the 2Q position. The diagrams for the fifth-order signal at the 2Q position correspond to the specific phase signatures of $-2\mathbf{k}_a + 2\mathbf{k}_b + \mathbf{k}_c$. Note that we take into account all diagrams including those for which time ordering between pulses a and b, i.e., between the two pump pulses, is not fulfilled. For finite pulse durations, such diagrams occur in the overlap region, i.e., when the time delay τ is shorter than the pulse duration (approximately). Note that, in Fig. 8.11, we assume time ordering between the pump pulses and the probe pulses to be fulfilled, and therefore the interaction with pulse c always occurs after the interactions with pulses a and b. For finite pulse durations, this is the case when the time delay T is longer than the duration of the pulses (approximately). It is possible, however, to conduct the analysis also without assuming any time ordering and without assuming the RWA to hold (Sec. 8.5.4), which leads to more diagrams but the same final results. As discussed in Sec. 8.2.1, the ratio of the number of fifth-order diagrams at the 2Q position to their number at the 1Q position is 1 to 4. Here we derive this ratio explicitly by showing each fifth-order diagram at the 2Q position alongside with the corresponding 4 diagrams at the 1Q position. In each case, the corresponding diagrams have the same "interaction pattern", i.e., arrows are plotted in the same order, direction, and arrangement for either 1Q or 2Q, and they differ only in the labeling of pulses. If the interactions were not connected to specific pulses a, b, or c, the pathways at the 1Q and 2Q positions would be exactly the same (but occurring four times more often at 1Q). However, due to the phase-matching directions the signals at the 1Q and 2Q positions are different because they occur in different directions: For the fifth-order signal at the 2Q position each pump pulse interacts twice while at the 1Q position one pump pulse interacts three times and the other just once. In total there are 54 diagrams for the fifth-order signal at the 2Q position (out of which 32 have a positive sign and 22 with a negative sign) and 216 diagrams for the fifth-order signal at the 1Q position. The diagrams were automatically generated by an algorithm [28]. We find exactly four 1Q diagrams for each 2Q diagram.

We want to discuss an interesting observation concerning the fifth-order signal at the 2Q position. Let us consider a simple two-level system with one ground state and one excited state that relaxes back to the ground state with a rate k_L that is the inverse of the lifetime. Let us consider the case for which the population time T is set to be much shorter than the excited-state lifetime such that the decay can be neglected. Under such conditions, most of the diagrams will not contribute because at least one doubly excited state is needed. Indeed, the only exceptions are the first 16 diagrams in Fig. 8.11, labeled 1–16. Interestingly, these diagrams all have the same sign which means that even for a two-level system, there will be some remaining 2Q signal, which may be surprising at first sight. This can be explained by close inspection of the diagrams revealing that they occur for an overlap between the first two pump pulses. The overlap between pulse a and pulse b can be seen in the diagrams since the interaction with pulse a and pulse b occur in a "mixed" order. Such a contribution will rapidly decrease when the coherence time is scanned in a 2D experiment. This will result in a weak and broad (as a function of excitation frequency) signal at the 2Q position in the 2D spectrum. Such multi-quantum signals were analyzed in a recent publication [318]. Note that for each of these diagrams, four corresponding diagrams contribute to the signal at the 1Q position.
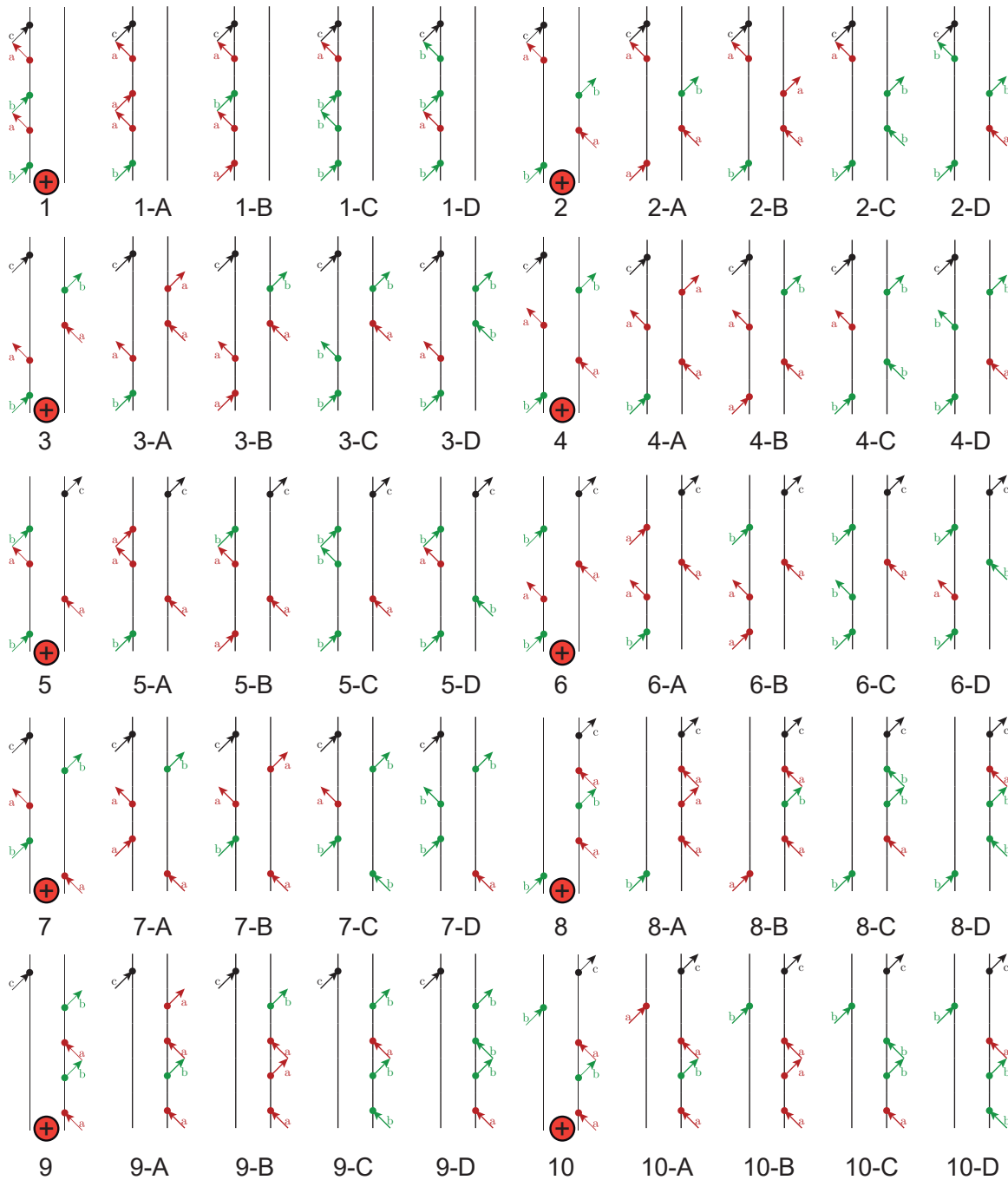
Figure 8.11.: Double-sided Feynman diagrams for the fifth-order signal at the 2Q position as well as for the fifth-order signal at the 1Q position. The 2Q signal is labeled with a number only while the 1Q signal is labeled by a number and a letter. For each diagram at the 2Q position, four corresponding diagrams at the 1Q position are present. The sign for each set of five diagrams (1 at the 2Q position and 4 at the 1Q position) is depicted below the diagram corresponding to the fifth-order signal at the 2Q position. The interactions with the different pulses are marked by color (pulse a in red, pulse b in green, and pulse c in black).
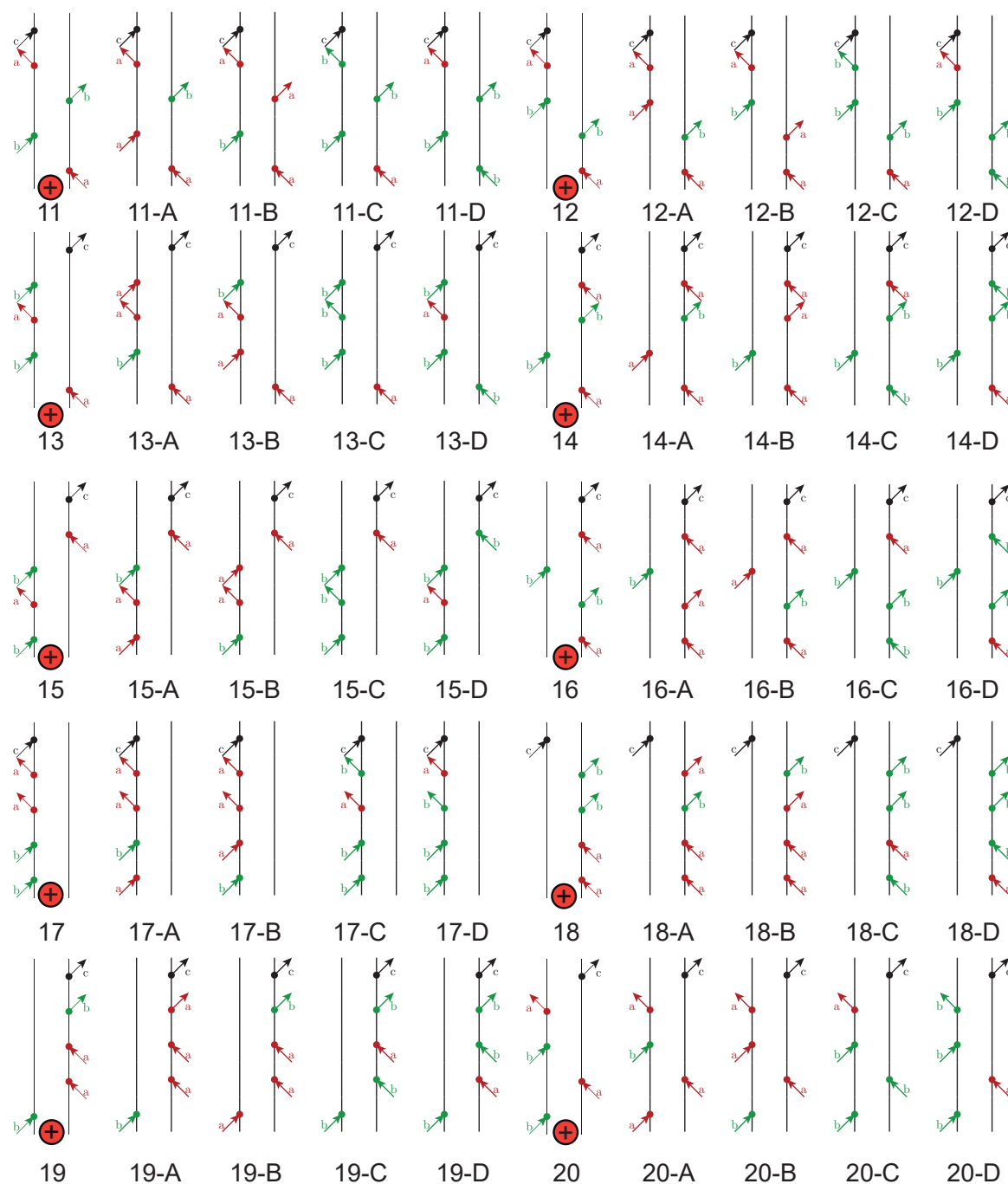
Figure 8.11.: Continued.
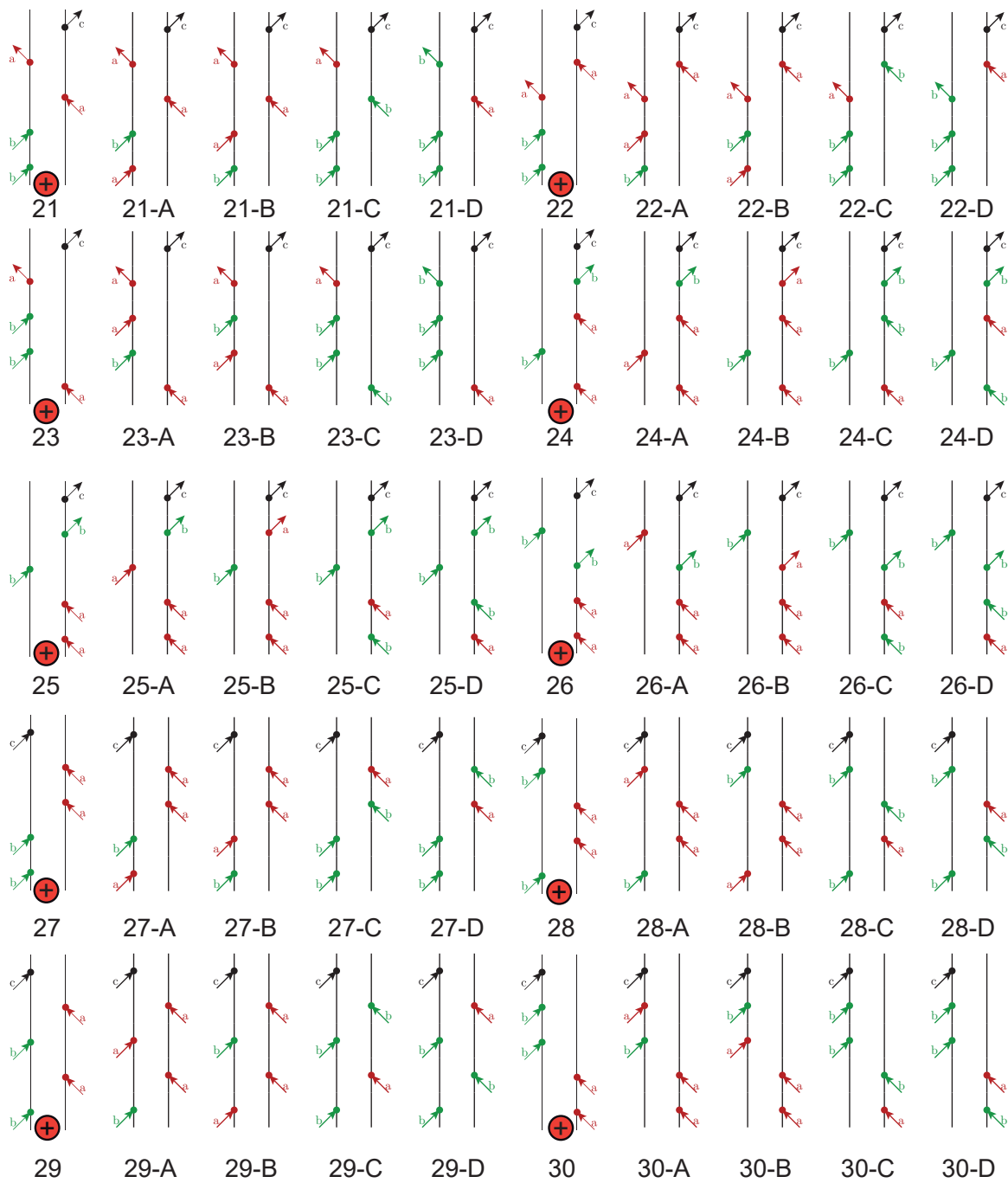
Figure 8.11.: Continued.
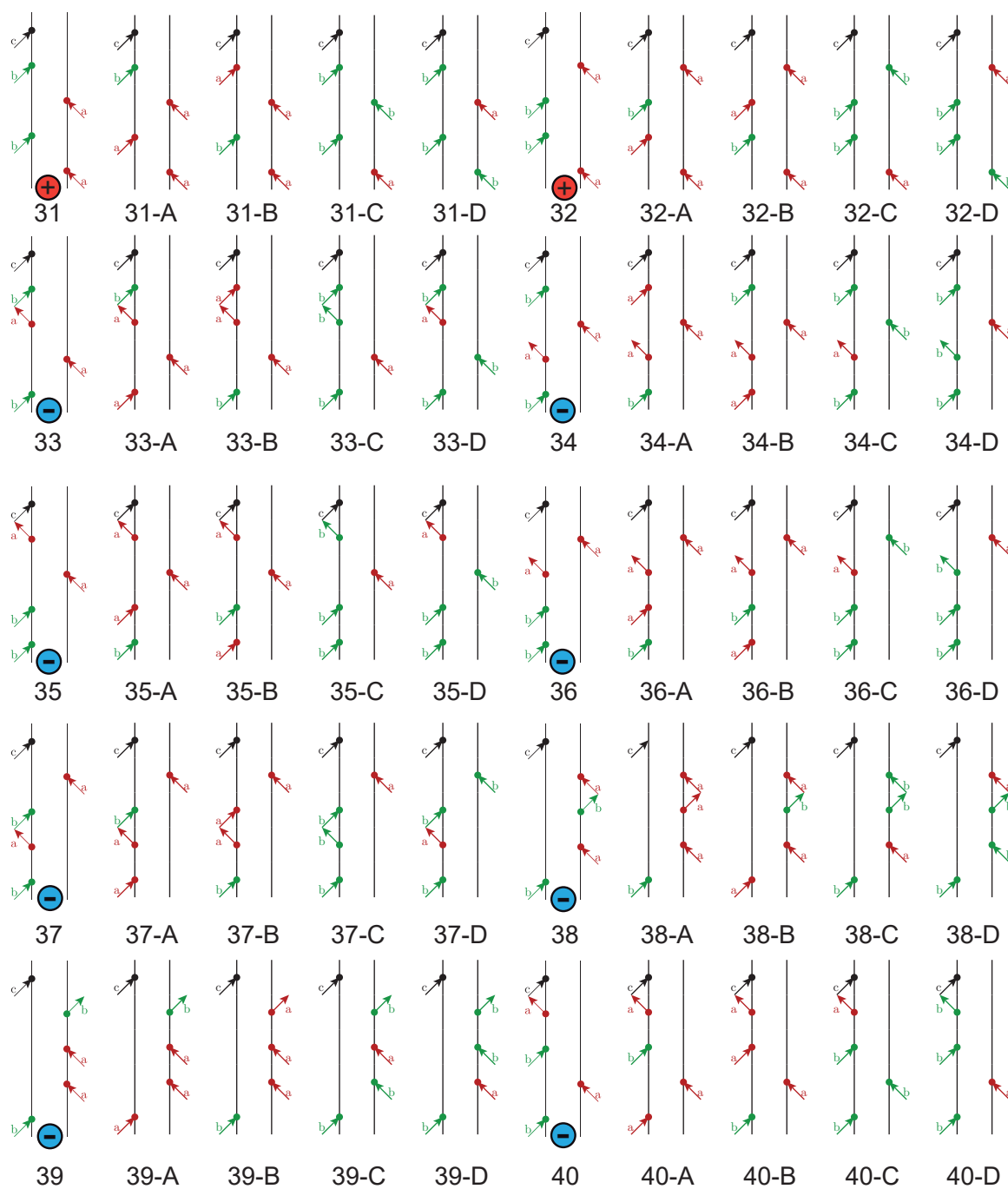
Figure 8.11.: Continued.
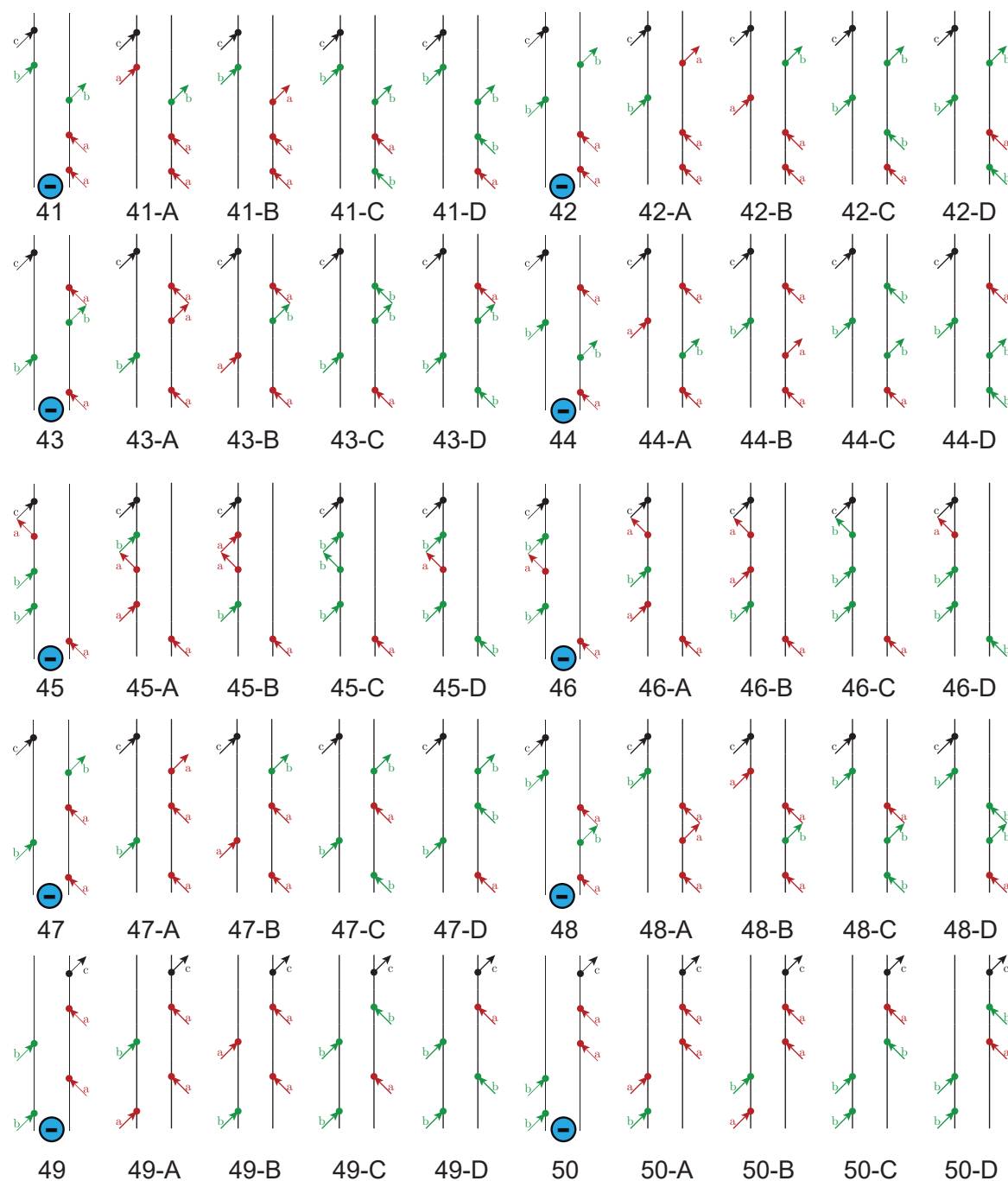
Figure 8.11.: Continued.
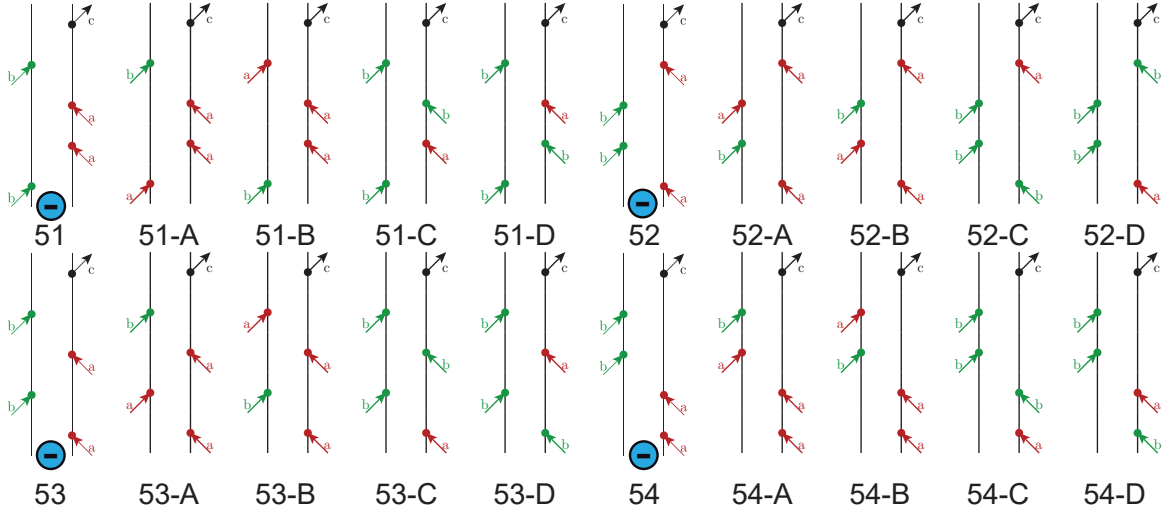
Figure 8.11.: Continued.

8.5.3. Analytic Proof of Correction Procedure

In addition to the "graphical proof" of the fifth-order correction procedure for 1Q signals shown in Sec. 8.5.2, we here derive an analytical equation that is valid for all orders. This leads to the combinatorical relationship shown in Eq. (8.8), of the main text, between the lowest-order nQ signals and the same-order contaminations that appear in other rQ signals. We begin with an open quantum system that evolves according to

$$\frac{\mathrm{d}\rho(t)}{\mathrm{d}t} = \mathscr{L}_0(t)\rho(t), \tag{8.22}$$

where $\mathscr{L}_0(t)$ is the Liouvillian describing the time evolution of the system in the absence of the pulses, and $\rho(t)$ is the system density matrix. In principle this differential equation may be integrated to give

$$\rho(t) = \mathscr{T}_0(t,t')\rho(t'), \tag{8.23}$$

where $\mathscr{T}_0(t,t')$ is the time-evolution operator. We treat the interaction with the electric field, $\mathbf{E}(t)$, in the electric-dipole approximation. In the presence of the electric fields, the system evolves according to

$$\frac{\mathrm{d}\rho(t)}{\mathrm{d}t} = \mathscr{L}_0(t)\rho(t) - \frac{i}{\hbar}\left[-\boldsymbol{\mu}\cdot\mathbf{E}(t), \rho(t)\right]. \tag{8.24}$$

with $\boldsymbol{\mu}$ as the dipole moment operator. The electric field is a sum over L pulses, which we write as

$$\mathbf{E}(t) = \sum_{j=a,b,\dots,L} \mathbf{e}_j\epsilon_j(t) + \mathbf{e}_j^*\epsilon_j(t)^* \tag{8.25}$$

where $\mathbf{e}_j$ is the polarization vector and $\epsilon_j(t)$ is the complex amplitude of pulse j,

$$\epsilon_j(t) = A_j(t - t_j)e^{-i(\omega_j(t - t_j) - \mathbf{k}_j \cdot \mathbf{r} - \phi_j)}, \tag{8.26}$$

where A_j is the complex envelope function,[2] ω_j is the central frequency, $\mathbf{k}_j$ is the wavevector, ϕ_j is the absolute phase, t_j is the pulse arrival time, and $\mathbf{r}$ is the position. We also define the quantities $f_j(t) = A_j(t - t_j)e^{-i\omega_j t}$ and $z_j = e^{i(\omega_j t_j + \mathbf{k}_j \cdot \mathbf{r} + \phi_j)}$, so that $\epsilon_j(t) = f_j(t)z_j$ where z_j is a time-independent phase factor.

The solution of Eq. (8.24) can be expanded perturbatively in powers of $-\frac{i}{\hbar}\boldsymbol{\mu} \cdot \mathbf{E}(t)$ as

$$\rho(t) = \rho^{(0)} + \rho^{(1)}(t) + \rho^{(2)}(t) + ... \tag{8.27}$$

where

$$\rho^{(n+1)}(t) = \int\limits_0^\infty \mathrm{d}t'\, \mathscr{T}_0(t') \left[-\frac{i}{\hbar}\boldsymbol{\mu} \cdot \mathbf{E}(t - t'), \rho^{(n)}(t - t') \right] \tag{8.28}$$

using quantum-mechanical commutator notation. Defining superoperators $\boldsymbol{\mu}^K \rho \equiv \boldsymbol{\mu}\rho$ (K indicates that the dipole operator acts on the ket-side of the density matrix) and $\boldsymbol{\mu}^B \rho \equiv \rho\boldsymbol{\mu}$ (B indicates that the dipole operator acts on the bra-side of the density matrix), we define the pulse propagators similar to Ref. [23],

$$\begin{aligned}
O_j &= \eta_O \frac{i}{\hbar} \int\limits_0^\infty \mathrm{d}t'\, \mathscr{T}_0(t') \left[\boldsymbol{\mu}^O \cdot \mathbf{e}_j f_j(t - t') \right], \\
O_{j^*} &= \eta_O \frac{i}{\hbar} \int\limits_0^\infty \mathrm{d}t'\, \mathscr{T}_0(t') \left[\boldsymbol{\mu}^O \cdot \mathbf{e}_j^* f_j^*(t - t') \right],
\end{aligned} \tag{8.29}$$

where $\eta_K = 1$ and $\eta_B = -1$, $O = K, B$ and the asterix denotes complex conjugation.[3] We write the solution to Eq. (8.24) as

$$\rho(t) \propto \sum_{n=0}^\infty \left[\sum_j \left(K_j z_j + K_{j^*} z_j^* + B_j z_j + B_{j^*} z_j^* \right) \right]^n \rho^{(0)}, \tag{8.30}$$

Now consider a transient-grating experiment, which involves three laser pulses, $\mathbf{E}_a$, $\mathbf{E}_b$, $\mathbf{E}_c$, in a fully noncollinear ("box-CARS") geometry, where the first tow pulses arrive at the sample simultaneously, and the delay between the first two pulses and the third pulse is scanned. The lowest leading-order signal of interest, the 1Q signal, propagates along the $-\mathbf{k}_a + \mathbf{k}_b + \mathbf{k}_c$ direction (rephasing signal) or along the $+\mathbf{k}_a - \mathbf{k}_b + \mathbf{k}_c$ direction (non-rephasing) and is measured using heterodyne detection with a fourth (" local oscillator") pulse. The language of rephasing and non-rephasing signals comes

---

[2]Note that the complex envelope function includes chirp and other spectral phase information beyond second order in a Taylor expansion.

[3]Note that the definition of O_j differs by a factor of z_j from that given in Ref. [23], where the phase factors z_j were included in O_j.

from 2D spectroscopy, wherein the time delay between the first two pulses is also scanned, and in such a case the rephasing and non-rephasing signals differ from each other. However, when the first two pulses (considered to be identical as discussed below) arrive simultaneously, the rephasing and non-rephasing signals are identical.

The time-dependent portions of $\mathbf{E}_a$ and $\mathbf{E}_b$ are assumed to be identical, so $f_a(t) = f_b(t)$, and their only difference is in the phase factor z_j, which are controlled by their propagation direction $\mathbf{k}_j$ and/or phase ϕ_j. Their pulse envelopes A_j, carrier frequencies ω_j and arrival times t_j are identical. In this case, since $f_a(t) = f_b(t)$, we have $O_a = O_b$ and $O_{a^*} = O_{b^*}$. The system polarization that couples to the far field, including all detection conditions, is calculated from Eq. (8.30) as [23]

$$P(t) = \sum_{n=0}^{\infty} \langle \boldsymbol{\mu} \left[K_j z_j + K_{j^*} z_j^* + B_j z_j + B_{j^*} z_j^* \right]^n \rho^{(0)} \rangle, \qquad (8.31)$$

where $\langle . \rangle$ indicates the expectation value. Once a phase-matching direction or phase-cycling condition is chosen, most of the terms in Eq. (8.31) do not contribute and are not calculated or considered.

The nQ signals arise from the components of the bulk polarization that couple to a far-field signal traveling along the direction $-n\mathbf{k}_a + n\mathbf{k}_b + \mathbf{k}_c$ and with phase $-n\phi_a + n\phi_b + \phi_c$. Just as with the 1Q signal, the nQ signal appear in both rephasing $(-n\mathbf{k}_a + n\mathbf{k}_b + \mathbf{k}_c)$ and non-rephasing $(+n\mathbf{k}_a - n\mathbf{k}_b + \mathbf{k}_c)$ directions. For each value of n, the rephasing and non-rephasing signals are identical, and all of the arguments presented in this section apply equally to both. We will proceed only with the rephasing diagrams for the purpose of this derivation. The polarizations contributing to the nQ signal, $P_{n\mathrm{Q}}$, are made up of all of the terms from Eq. (8.31) that have the phase factors $(z_a^* z_b)^n z_c = e^{i(-n\omega_a t_a + n\omega_b t_b + \omega_c t_c) + i(-n\mathbf{k}_a + n\mathbf{k}_b + \mathbf{k}_c) \cdot \mathbf{r} + i(-n\phi_a + n\phi_b + \phi_c)}$

We begin by calculating $P_{n\mathrm{Q}}(t)$ to lowest $(2n + 1)$ order in perturbation theory, which involves calculating the density matrix,

$$\rho_{n\mathrm{Q}}^{(2n+1)}(t) = \sum_{l=0}^{n} \sum_{m=0}^{n} \sum_{q=0}^{1} \mathscr{P} \left[(K_{a^*})^{n-l} (B_{a^*})^l (K_b)^{n-m} (B_b)^m (B_c)^q (K_c)^{1-q} \right] \rho^{(0)}, \quad (8.32)$$

where $\mathscr{P}$, the permutation operator, indicates that for each set of indices, l, m, q, we must sum over all unique permutations of the order $O_{j^{(*)}}$ operators. For example, for $l = 0$, $m = n$, $q = 0$, we have

$$\mathscr{P} \left[(K_{a^*})^n (B_b)^n K_c \right] \rho^{(0)} = (K_{a^*})^n (B_b)^n K_c \rho^{(0)}$$
$$+ (K_{a^*})^{n-1} B_b K_{a^*} (B_b)^{n-1} K_c \rho^{(0)} \qquad (8.33)$$
$$+ K_c (K_{a^*})^n (B_b)^n \rho^{(0)} + ...$$

Note that $\rho_{n\mathrm{Q}}^{(2n+1)}(t)$ is defined without the phase factors, and is related to the lowest-order polarization by

$$P_{n\mathrm{Q}}^{(2n+1)}(t) = (z_a^* z_b)^n z_c \langle \mu \rho_{n\mathrm{Q}}^{(2n+1)} \rangle, \qquad (8.34)$$

which includes phase factors. There is a unique Feynman diagram to represent each permutation of the set of values of l, m, q. We call the result of evaluating each diagram [i.e., a term in the triple sum of Eq. (8.32)] a "weight".

While Eq. (8.32) gives the lowest-order contribution to ρ_{nQ}, the full nQ signal includes higher-order contributions that all have the same phase factor $(z_{a^*}z_b)^n z_c$,

$$\rho_{nQ}(t) = \sum_{r=n}^{\infty} \rho_{nQ}^{(2r+1)}(t). \tag{8.35}$$

We assume that pulses a and b are strong, such that we must consider higher-order term in ϵ_a and ϵ_b, but that the probe pulse, c, is weak, and thus we need only consider terms that are first order in ϵ_c.

We now show how the lowest-order contributions to the nQ signal are quantitatively related to the $(2n + 1)$th order corrections to a lower-Q signal. Looking at the form of Eq. (8.32), we see that there are n terms with subscript a^*, and n terms with subscript b, which is the only way to get the phase-discrimination condition $(z_a^* z_b)^n z_c$ to lowest order. We recall now that when pulses a and b arrive at the same time ($\tau = 0$) and have the same time-dependence [$f_a(t) = f_b(t)$], that the time-propagation induced by either pulse is identical, and therefore we have that $K_a = K_b$, $K_{a^*} = K_{b^*}$, $B_a = B_b$, $B_{a^*} = B_{b^*}$, independent when pulse c arrives. Therefore, we can replace any number of a^* subscripts with b^* subscripts without changing the weight of the resulting diagram. Similarly, we can replace any number of b subscripts with a subscripts without changing the resulting weight.[4] However, changing the subscripts in this way does change the phase factors z_j, so the resulting diagram does not contribute to the nQ signal, but rather to the rQ, where $r < n$. Consider that we replace s of the b subscripts with a subscripts, and $v - s$ of the a^* subscripts with b^* subscripts. Then we change the associated phase-discrimination condition from $(z_a^* z_b)^n z_c$ to $(z_a^* z_b)^{n-v} z_c$. Such diagram is therefore associated with the signal $P_{rQ}^{(2n+1)}(t)$, where $r = n - v$.

In general, we can take any diagram from Eq. (8.32), select v of the $2n$ subscripts associated with pulses a and b and make the substitution $a \leftrightarrow b$. There are $\binom{2n}{v}$ unique ways to make this substitution. Therefore, for any diagram contributing to $\rho_{nQ}^{(2n+1)}$, there are $\binom{2n}{n-r}$ diagrams contributing to $\rho_{rQ}^{(2n+1)}$ that all have identical weights. Since this relationship is true for every diagram that contributes to $\rho_{rQ}^{(2n+1)}$, we can more generally write

$$\rho_{rQ}^{(2n+1)}(t) = \binom{2n}{n-r}\rho_{nQ}^{(2n+1)}(t), \tag{8.36}$$

in the approximation that pulse c is weak. Finally, in terms of the signals, we have

$$P_{rQ}^{(2n+1)}(t) = \binom{2n}{n-r}(z_a^* z_b)^{r-n} P_{nQ}^{(2n+1)}(t). \tag{8.37}$$

---

[4]Note that this argument holds regardless of whether or not pulse c overlaps with pulses a and b. When all of the pulses overlap, there are more diagrams [more permutations arise in Eq. (8.32)]

As an example consider $r = 1$ and $n = 2$, which corresponds to the relationship between the fifth-order 1Q and fifth-order 2Q signals. Given the particular diagram $K_\mathrm{c}K_\mathrm{b}K_\mathrm{b}B_{\mathrm{a}^*}B_{\mathrm{a}^*}\rho^{(0)}$, which contributes to the $\rho_{2\mathrm{Q}}^{(5)}$, there are four diagrams with equal weight that contribute to $\rho_{1\mathrm{Q}}^{(5)}$:

$$
\begin{aligned}
& K_\mathrm{c}\textcolor{red}{K_\mathrm{a}}K_\mathrm{b}B_{\mathrm{a}^*}B_{\mathrm{a}^*}\rho^{(0)} + K_\mathrm{c}K_\mathrm{b}\textcolor{red}{K_\mathrm{a}}B_{\mathrm{a}^*}B_{\mathrm{a}^*}\rho^{(0)} \\
& + K_\mathrm{c}K_\mathrm{b}K_\mathrm{b}\textcolor{red}{B_{\mathrm{b}^*}}B_{\mathrm{a}^*}\rho^{(0)} + K_\mathrm{c}K_\mathrm{b}K_\mathrm{b}B_{\mathrm{a}^*}\textcolor{red}{B_{\mathrm{b}^*}}\rho^{(0)}
\end{aligned}
\tag{8.38}
$$

where the red colored parts draw attention to the substitution that was made.

8.5.4. Ratio of Double-Sided Feynman Diagrams

The proof shown in Sec. 8.5.2 and 8.5.3 allows us to calculate the ratio of nonlinear contributions for different multi-quantum signals. However, in this section we want to show how the different ratios between a multi-quantum signal arise from the explicit numbers of diagrams. Note that the number of diagrams changes if conditions are applied while the ratios of nonlinear contributions for different multi-quantum signals stay constant. We used an algorithm to obtain the number of diagrams for different situations such as with and without applying the RWA or time ordering between pump and probe [28]. The number of diagrams for up to seventh order and up to the 3Q signal are summarized in Fig. 8.12. These diagrams were calculated without assuming any time ordering between the two pump pulses, i.e., the temporal order of the interactions with pulse a and pulse b was not fixed. For all four panels in Fig. 8.12, there are no contributions below the diagonal because the lowest nonlinear order that can contribute to any nQ signal is $2n + 1$. For the left column (Fig. 8.12a and c), time ordering between the pump pulses and the probe pulse is fulfilled while for the right column, such time ordering does not hold. For the top row, the RWA is assumed while for the bottom it is not assumed to hold. The relevance of the RWA as well as its limits were discussed thoroughly in the literature [189, 319].

Figure 8.12.: Number of double-sided Feynman diagrams for various nonlinear orders at specific multi-quantum signal positions. For all cases, no time ordering was assumed between the two pump pulses. The four panels show the following situation: (a) with time ordering between the pump pulses and the probe pulse and assuming the RWA, (b) without time ordering between the pump pulses and the probe pulses but applying the RWA, (c) with time ordering between the pump pulses and the probe pulse but without the RWA, and (d) without time ordering between the pump pulses and the probe pulse and without the RWA.

The number of diagrams is different for each of the corresponding entries of the four panels in Fig. 8.12. Interestingly, however, we obtain the same ratios between 1Q, 2Q, and 3Q for any given nonlinear order. For example, the ratio of the fifth-order contribution at 2Q to the fifth-order contribution at 1Q is always the same, 1 : 4, as evaluated from $54 : 216 = 240 : 960 = 192 : 768 = 960 : 3840$ in panels a–d, and similarly for the ratios at seventh and higher orders. This correspondence occurs not only for the total number of Feynman diagrams but on the individual diagrammatic level as exemplified graphically in Fig. 8.11 for the situation in Fig. 8.12a. Thus, the correction analysis is valid also when time ordering is not fulfilled between the pump pulses and the probe pulse and/or when the RWA does not hold. We list the ratios of nonlinear contributions at different multi-quantum signals up to thirteenth order in Tab. 8.1. This table can be written as a matrix whose inverse is the upper-triangular matrix of Eq. 8.11 connecting clean nonlinear signals with different nQ signals [16].

Nonlinear order / Multi-quantum signal	3	5	7	9	11	13
1Q signal	1	4	15	56	210	792
2Q signal		1	6	28	120	495
3Q signal			1	8	45	220
4Q signal				1	10	66
5Q signal					1	12
6Q signal						1

Table 8.1.: Ratios of double-sided Feynman diagrams up to 6Q and thirteenth order.

8.5.5. Analysis of Nonlinear Signal Contributions in Intensity Cycling

In this section we provide an alternative approach which is not based on double-sided Feynman diagrams to quantify the contribution of a higher-order signal to a specific nQ signal. We can understand how the higher-order signals contribute to different nQ signals by decomposing the signal $S(T, \omega_t, I)$ into a perturbation series of the excitation intensity I

$$S(T, \omega_t, I) = \sum_{n=1}^{\infty} S^{(2n+1)} I^n = S^{(3)} I + S^{(5)} I^2 + s^{(7)} I_0^3 + ... \tag{8.39}$$

where $S^{(2n+1)}$ is the $(2n + 1)$th order response of the system. Since the signals scale differently with excitation intensity for the various orders, we can use Eq. (8.39) to directly obtain the contributions of higher-order signals to the 1Q signal. As an example, we consider the case when the highest nonlinear order that contributes significantly is the seventh-order contribution, i.e., the contribution of the ninth-order signal is weak. We calculate the amplitude of the different nonlinear signal contributions for the different intensity-cycling steps of $4I_0$, $3I_0$, and I_0. For example, inserting only the fifth-order term $S^{(5)} I^2$ into Eq. (8.18) leads to

$$S_{1Q}(T, \omega_t, I_0) = \frac{1}{6} \left[16 S^{(5)} I_0^2 + 9 S^{(5)} I_0^2 - S^{(5)} I_0^2 \right] = 4 S^{(5)} I_0^2 \tag{8.40}$$

Inserting the power series up to seventh order into Eq. (8.18) results in

$$S_{1Q}(T, \omega_t, I_0) = S^{(3)} I_0 + 4 S^{(5)} I_0^2 + 15 S^{(7)} I_0^3. \tag{8.41}$$

The fifth-order as well as the seventh-order contributions to the 1Q signal are the same as already determined by counting the double-sided Feynman diagrams in 2D spectroscopy [Eq. (8.10)]. For the 2Q signal $S_{2Q}(T, \omega_t, I_0)$, the contribution of the seventh-order signal can be calculated analogously to Eq. (8.41), resulting in

$$S_{2Q}(T, \omega_t, I_0) = S^{(5)} I_0^2 + 6 S^{(7)} I_0^3. \tag{8.42}$$

Note that in Eq. (8.42) no third-order contribution is present because, in general, the $(2n+1)$th order is the highest order that can contribute to a specific signal S_{nQ}. This can be easily shown by inserting $S^{(3)} I$ into Eq. (8.19) which results in

$$S_{2Q}(T, \omega_t, I_0) = \frac{1}{6} \left(4 S^{(3)} I_0 - 3 S^{(3)} I_0 - 1 S^{(3)} I_0 \right) = 0. \tag{8.43}$$

The highest considered nonlinear order is the seventh order and S_{3Q} is therefore

$$S_{3Q}(T, \omega_t, I_0) = \frac{1}{12} \left(64 S^{(7)} I_0^3 - 54 S^{(7)} I_0^3 + 2 S^{(7)} I_0^2 \right) = S^{(7)} I_0^3, \tag{8.44}$$

where we wrote the explicit signal contributions for $4I_0$, $3I_0$, and I_0. Inserting terms higher than the seventh order allows to retrieve higher nonlinear order contributions at different nQ signals in the same way resulting in Tab. 8.1 from which the matrix in Eq. (8.11) can be constructed [16].

8.5.6. Shifting of Population Time Axis
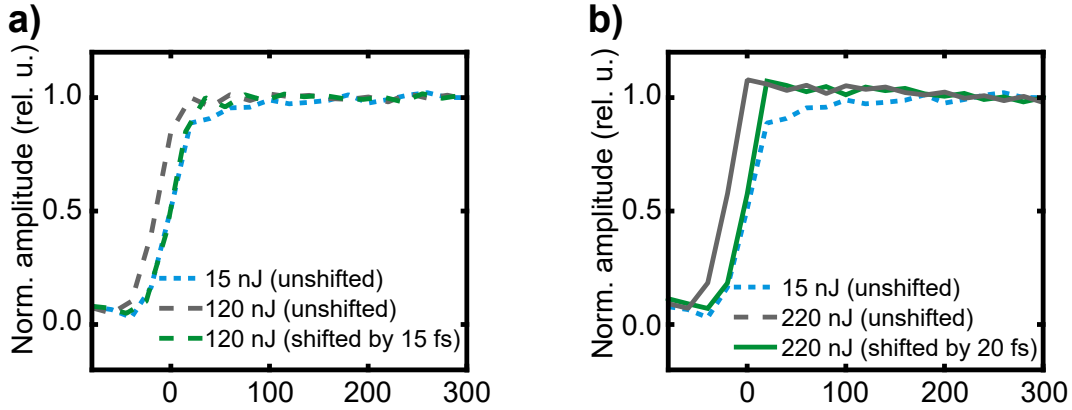
Figure 8.13.: Shifted and unshifted transients for the 1Q signal obtained by integrating the 2D spectrum (along $\bar{\nu}_\tau$) as well as averaging over $\bar{\nu}_t$. (a) Shifted (blue green dashed) and unshifted (dark grey dashed) 1Q signals measured at a pulse energy of 120 nJ and compared to the unshifted 1Q signal at 15 nJ (blue dotted). (b) Shifted (blue green solid) and unshifted (dark grey solid) 1Q signals measured at a pulse energy of 220 nJ and compared to the unshifted 1Q signal at 15 nJ (blue dotted).

The temporal overlap between the pump pulses and the probe pulse shifted slightly between the 2D measurements at different excitation powers. This was adjusted by shifting the population time axis. We show the unshifted and shifted 1Q signals obtained by integrating along $\bar{\nu}_\tau$ as well as averaging over $\bar{\nu}_t$ in Fig. 8.13. The shifted (blue dashed) and unshifted (dark gray dashed) signals for excitation powers of 120 nJ are shown in Fig. 8.13a. We compare the 1Q signals to the measurement at 15 nJ excitation energy. The transients at 120 nJ were shifted by 15 fs resulting in good agreement of the dynamics close to $T = 0$. The population time axis for the measurement at 200 nJ (Fig. 8.13b) was shifted by 20 fs.

8.5.7. Pump–Probe Signals for Different Pulse Energies
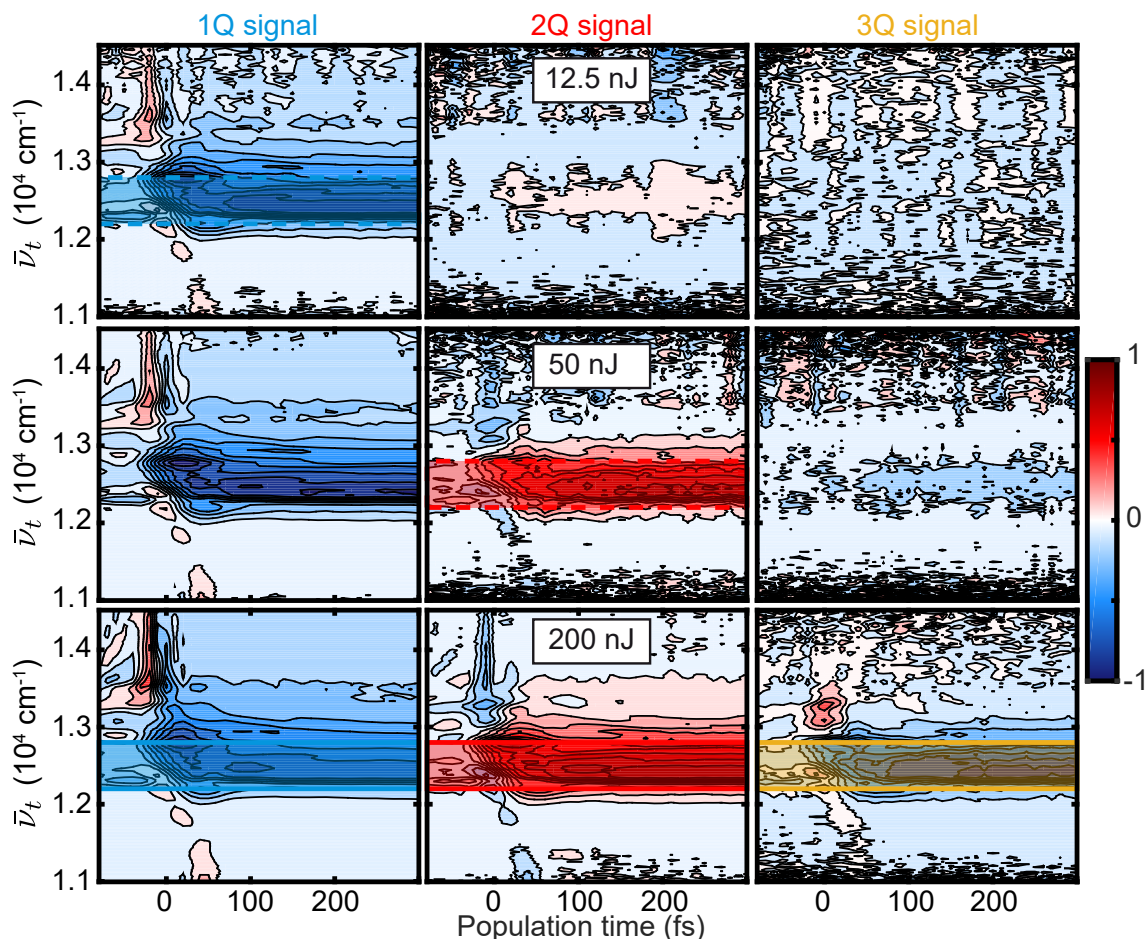
Figure 8.14.: 1Q (left) 2Q (middle), and 3Q (right) signals isolated by intensity cycling in PP spectroscopy. The three rows correspond to different sets of measurements where the label corresponds to the value of $4I_0$ (from top to bottom: 12.5 nJ, 50 nJ, and 200 nJ). Each map is normalized by dividing the map by the maximum of the absolute signal of the displayed map. Rectangles represent the regions that were used for averaging (along $\bar{\nu}_t$).

In Fig. 8.14 we show the complete set of 1Q, 2Q, and 3Q maps measured in a PP experiment for three pulse energies using three transient absorption maps at different excitation intensities for each set of nQ signals. For the nQ maps labeled with 12.5 nJ we used TA measurements at 12.5 nJ, 9.375 nJ, and 3.125 nJ. For the nQ maps labeled with 50 nJ we used TA measurements at 50 nJ, 37.5 nJ, and 12.5 nJ. For the nQ maps labeled with 200 nJ we used TA measurements at 200 nJ, 150 nJ, and 50 nJ. The given energy in the labels of Fig. 8.14 at each row correspond to $4I_0$. For the nQ signals extracted from a set with $4I_0$ corresponding to 12.5 nJ only a weak 2Q signal is visible (Fig. 8.14, first row). For 50 nJ the 2Q signal is much stronger and a

weak 3Q signal can be observed (Fig. 8.14, second row). For the maps extracted from three measurements with $4I_0$ corresponding to 200 nJ the 1Q, 2Q, and 3Q signal are strongly visible (Fig. 8.14, third row). We cannot exclude that at this measurement a weak ninth-order contribution is contaminating the signals. Note the change in the dynamics in the 1Q signal from lower to higher excitation powers. This change is directly connected to the contamination by higher-order signals.

8.5.8. Comparison of Multi-Quantum Signals
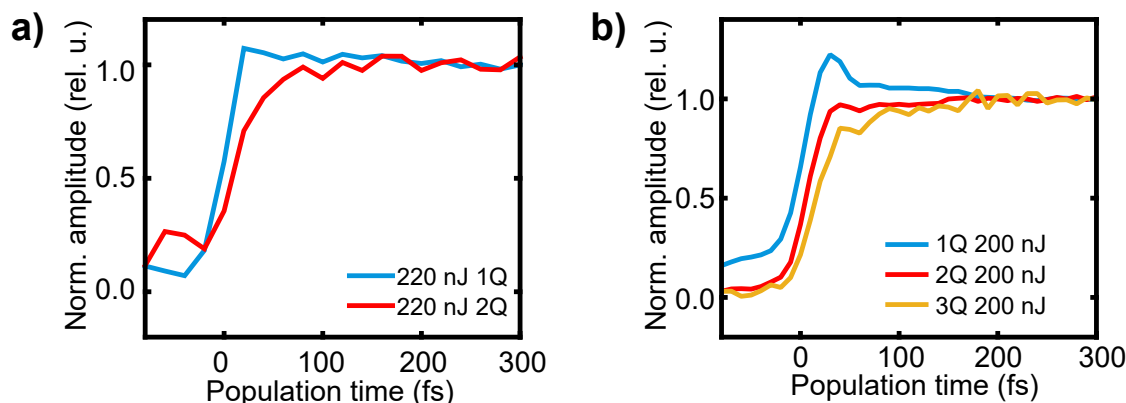
Figure 8.15.: Transients of the nQ signals obtained by averaging over $\bar{\nu}_t$ (a) 2D and (b) PP measurement. The signals are normalized to the average signal from $T = 200$ fs to $T = 300$ fs. The excitation power for the signals extracted from the 2D spectrum correspond to 200 nJ. The nQ signals from PP spectroscopy were extracted from a set of three measurements where $4I_0$ was set to 220 nJ. 1Q signals are shown as blue solids, 2Q signals as red solids, and the 3Q signal as a yellow solid line.

In Fig. 8.15a we show the averaged (over $\bar{\nu}_t$) 1Q and 2Q transients from 2D spectroscopy measured at an excitation power of 220 nJ. We disregard the 3Q signal due to its strong coherent artifact and low SNR. Clearly visible is the faster rise from the 1Q signal compared to the 2Q signal. Similar behavior is observed for the 1Q, 2Q, and 3Q transients extracted via intensity cycling from three measurements where $4I_0$ was set to 200 nJ (Fig. 8.15b). The faster rise can be explained by the mixing of higher-order signals. At high excitation intensities where a 3Q signal can be observed but higher-order signals are not contributing significantly, the 1Q signal contains third-, fifth-, and seventh-order contributions, the 2Q signal fifth- and seventh-order contributions, and the 3Q signal only seventh-order contributions. In an excitonic system such as squaraine oligomers the third-order contributions correspond to single-exciton dynamics, while higher-order signals report on multi-exciton processes such as EEA in the case of fifth-order contributions. The multi-exciton processes are reflected by a rise of the corresponding signals [16]. What is the effect of higher-order signals mixing into the 1Q signal? In the case of squaraine oligomers the 1Q signal at low excitation

intensities consists of a negative ground-state bleach decaying with the single-exciton lifetime. For higher excitation intensities the third-order single-exciton dynamics are mixing more and more with fifth-order contributions. The fifth-order signal rises with the annihilation dynamics. Furthermore, the fifth-order ground-state bleach signal has an opposite sign compared to the third-order contribution. Therefore, for higher excitation powers, i.e., increasing fifth-order contributions, a positive slow rise is added to the negative ground-state bleach contribution and both signals will (partially) cancel each other. For small population times the fifth-order signal is still rising resulting in a fast decaying component in the negative ground-state bleach signal. This behavior can be seen in Fig. 8.5 and Fig. 8.6. For longer population times third- and fifth-order ground-state bleach components decay with the exciton lifetime. However, they have opposite sign and partially cancel each other resulting in a saturation of the 1Q signal amplitude with higher excitation powers as described in Sec. 8.3.4.

8.5.9. Corrected 1Q Signal for Different Pulse Energies

In Fig. 8.16 we show the 1Q maps from 2D and PP spectroscopy which were used for the data presented in Fig. 8.7 and Fig. 8.8. The first row shows the lowest-power measurements which are only slightly contaminated by higher-order signals in the case of 2D spectroscopy and uncontaminated in the case of PP spectroscopy. The last row shows the uncorrected data set with the highest excitation pulse energy used (220 nJ for 2D and the signal extracted from a set of three measurement with $4I_0$ corresponding to 200 nJ for PP). Note that for the PP maps three different measurements (at $4I_0$, $3I_0$ and I_0) are used and the labeled power corresponds to the value of $4I_0$. Especially in the case of PP spectroscopy the influence of the high-order contamination is clearly visible. The second row from top shows the corrected (using the 2Q signal) maps for excitation pulse energies of 120 nJ for 2D and $4I_0 = 50$ nJ for PP. The third row from top contains the corrected maps (up to 3Q signal) for the highest excitation powers of 220 nJ in the case of 2D and $4I_0 = 200$ nJ in the case of PP spectroscopy. For the construction of the signal in the corrected measurement three measurements have added up which also reduces the noise by effective averaging. This is not the case for the lowest-power measurement. As already discussed in the main text the correction leads to good agreement with the dynamics of the low-power measurements.
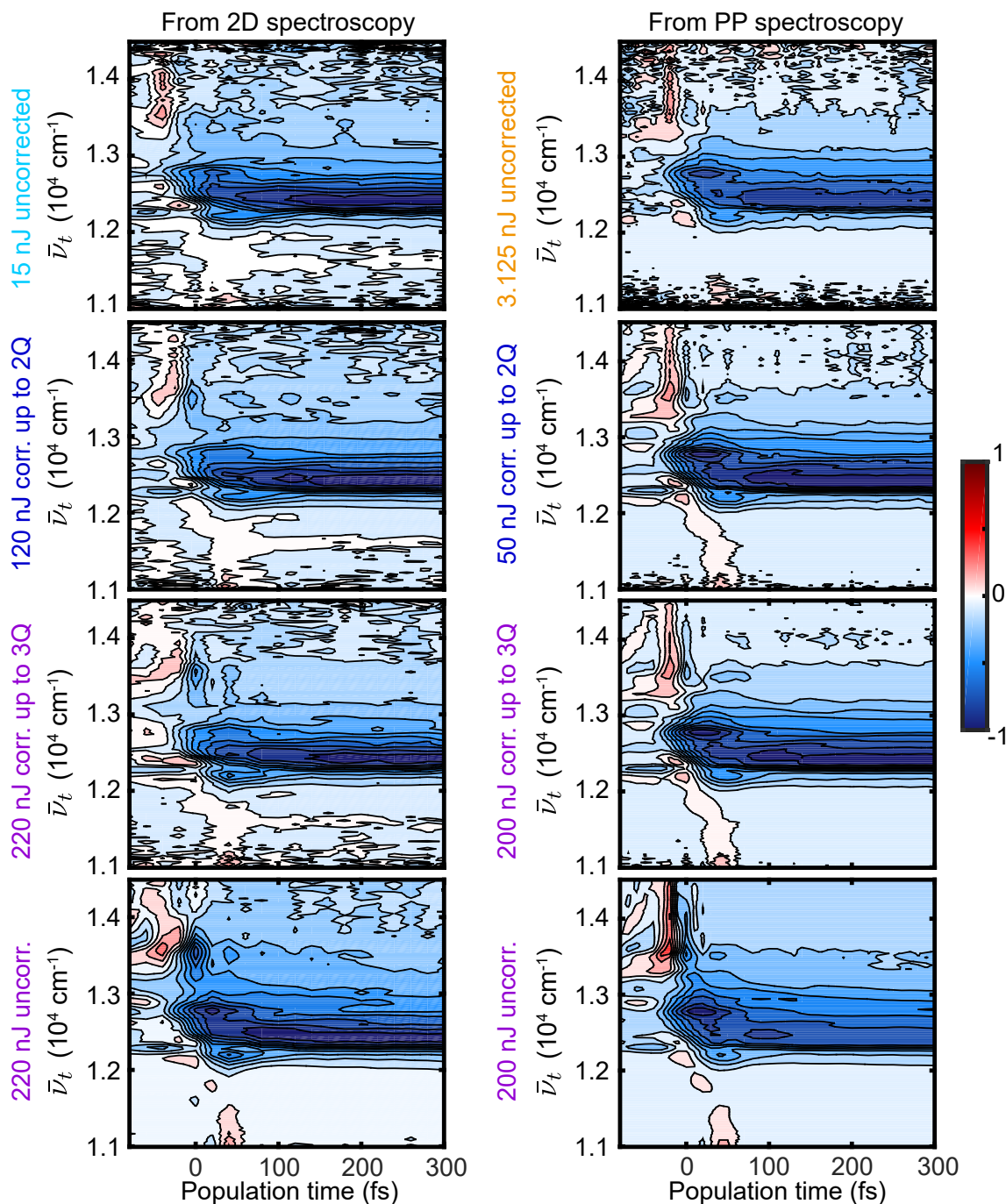
Figure 8.16.: 1Q signal obtained from 2D (left column) and PP spectroscopy (right column) for different pulse energies. The first and last rows show the uncorrected signals for low and high excitation pulse energies, respectively. The second row is measured in a power regime where the fifth-order signal is the highest contamination that has to be considered, i.e., the seventh-order signal is weak. Therefore, the signal is corrected using the 2Q signal. The third row from top is at even higher pulse energy where the seventh-order signal is contributing as well. The shown 1Q signal at this power is corrected using the 2Q and 3Q signals. Each map is normalized by dividing the map by the maximum of the absolute signal of the displayed map.

8.5.10. Corrected 1Q Signal ($4I_0$ Corresponding to 12.5 nJ)

Figure 8.17.: 1Q signal constructed out of three different measurements with $4I_0$ corresponding to 12.5 nJ. We show the uncorrected signal (light blue solid line), the corrected signal using the 2Q signal (light blue dashed line), and the corrected signal using the 2Q and 3Q signal (light blue dotted line). For comparison, we show the signal measured at a pulse energy of 3.125 nJ (orange solid line). Here we use the same style as in Fig. 8.7: solid lines correspond to uncorrected signals, dashed lines to correction up to the 2Q signal, and dotted lines to correction using the 2Q and 3Q signals.

We show the uncorrected 1Q signal (averaged from $\bar{\nu}_t = 12400$ to 12800 cm^{-1}) extracted from a set of three measurement with $4I_0$ corresponding to 12.5 nJ (Fig. 8.17, light blue solid line). The traces using the 2Q signal for correction (Fig. 8.17, light blue dashed line) and using the 2Q and 3Q signal for correction (Fig. 8.17, light blue dotted line) are shown as well. As an uncontaminated signal we show the intensity-cycling step with a pulse energy of 3.125 nJ (Fig. 8.17, solid orange line). All the signals are divided by the absolute average signal (from $T = 200$ fs to $T = 300$ fs) measured at 3.125 nJ. Note that for this measurement no additional scaling factor by the power is necessary since the 1Q signal (extracted from 12.5 nJ, 9.375 nJ, and 3.125 nJ) is already scaled to 3.125 nJ. For the uncorrected 1Q signal (light blue solid line) a slight saturation, i.e., a decrease of the signal amplitude, is visible which is corrected by the 2Q signal (light blue dashed line). Using the 3Q signal additionally for correction does not improve the signal, i.e., the correspondence to the lowest signal is the same (Fig. 8.17 light blue dotted line). Therefore, the seventh-order contamination can be considered as negligible.
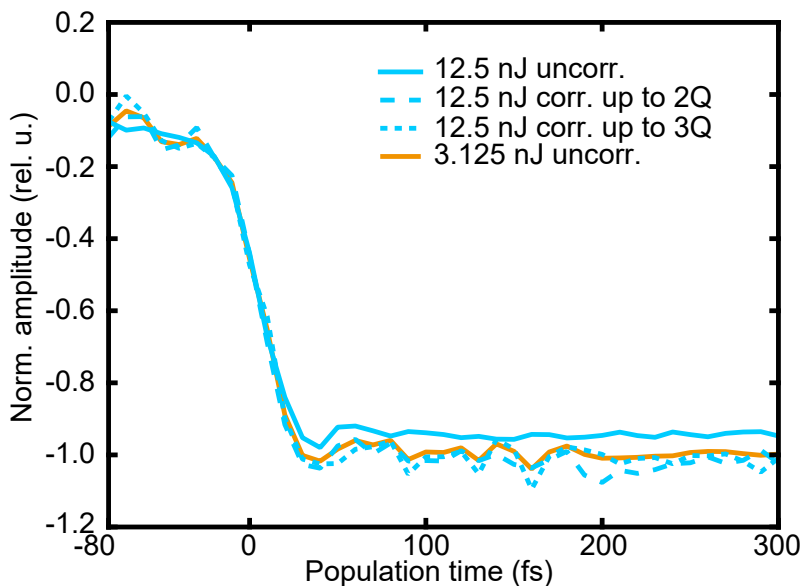
8.5.11. Corrected 1Q Signal ($4I_0$ Corresponding to 50 nJ)
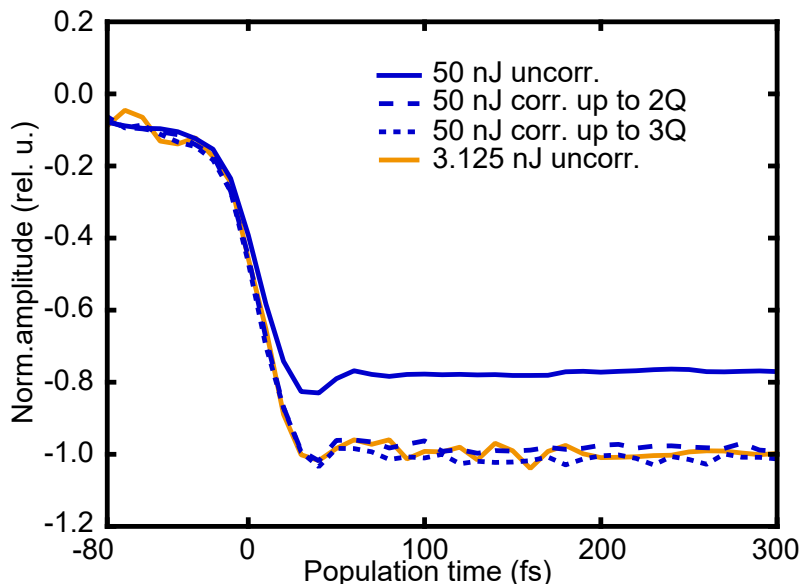
Figure 8.18.: 1Q signal constructed out of three different measurements with $4I_0$ corresponding to 50 nJ. We show the uncorrected signal (dark blue solid line), the corrected signal using the 2Q signal (dark blue dashed line), and the corrected signal using the 2Q and 3Q signal (dark blue dotted line). For comparison, we show the signal measured at a power of 3.125 nJ (orange solid line). Here we use the same style as in Fig. 8.7: solid lines correspond to uncorrected signals, dashed lines to correction up to the 2Q signal, and dotted lines to correction using the 2Q and 3Q signals.

In Fig. 8.18 we show the (averaged from $\bar{\nu}_t = 12400$ to 12800 cm^{-1}) 1Q signal for $4I_0 = 50$ nJ. The signal is scaled and normalized in the same way as described for Fig. 8.7, i.e., each signal is divided by the absolute of the average signal (from $T = 200$ fs to $T = 300$ fs) of the lowest-power measurement (Fig. 8.18, orange solid line) and then scaled by the ratio of the measured power. The uncorrected 1Q signal (Fig. 8.18, dark blue solid line) has a decreased signal amplitude which is clear sign of higher-order contaminations. The corrected curves using the 2Q signal (Fig. 8.18, dark blue dashed line) and using the 2Q and 3Q signal (Fig. 8.18, dark blue dotted line) have both very good agreement with the lowest-power measurements. At close inspection we can observe a slightly systematic deviation of the corrected signal using only the 2Q contribution (dark blue dashed) which can be improved using the 3Q signal. However, the difference between the two signals is small which agrees with the observation in the TA maps where the 3Q signal is only a minor contribution (Fig. 8.14).

8.5.12. Correction at $T = 0$ fs

In Fig. 8.19 we show the 1Q signal frequency-resolved along the $\bar{\nu}_t$ axis for different powers in 2D (left) and PP (right) spectroscopy for a population time of $T = 0$. Normalization and correction have been performed in the same way as in Fig. 8.8 but here we show the spectral cut for $T = 0$. For 2D spectroscopy as well as for PP spectroscopy the signal amplitude is decreased for higher excitation energies, i.e., the solid lines are above -1.0, indicating that higher-order effects lead to a saturation of the signal for higher pulse energies. The amplitude and spectral shape can be recovered by using the nQ signals for correction. Explicitly, we used the 2Q signal for the medium power of 120 nJ in the case of 2D spectroscopy and for the 1Q signal in PP spectroscopy extracted from a set of three measurements with $4I_0$ corresponding to 50 nJ (Fig. 8.19, dark blue dashed lines), and the 2Q and 3Q signal for the highest power of 220 nJ for 2D spectroscopy and for the 1Q signal in PP spectroscopy extracted from a set of three measurements with $4I_0$ corresponding to 200 nJ (Fig. 8.19, purple dotted lines). In 2D spectroscopy the correction does not work very well while theoretically at time zero the correction should still work. However, at time zero the signal rises rapidly and small imperfections (such as time jitters) between the measurements will have huge influence which might be the reason why the correction at this particular population time does not work in 2D spectroscopy in our case. For the PP measurements we can see that the correction works almost perfectly from 12000 cm^{-1} to 13500 cm^{-1}. At the blue edge, the correction slightly overestimates the signal. However, the signal at the edges is weak and the noise is increasing because of the low probe intensity.
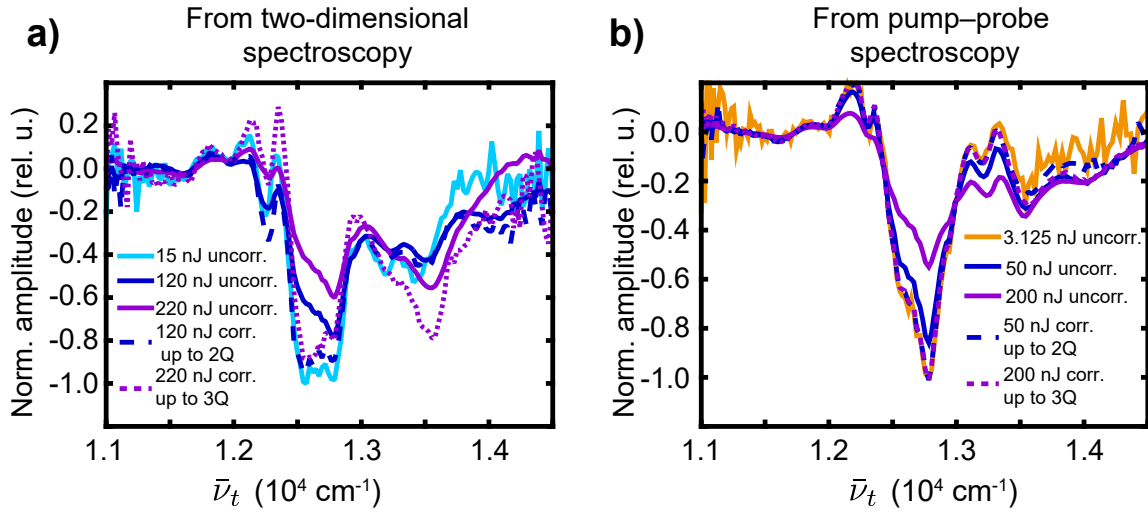
Figure 8.19.: Corrected and uncorrected 1Q signals for a population time of $T = 0$ for signals retrieved from (left) 2D spectroscopy and (right) PP spectroscopy. For comparison, we show the signal measured at a power of 15 nJ for 2D spectroscopy and 3.125 nJ (orange solid) for PP spectroscopy. Here we use the same style as in Fig. 8.8: solid lines correspond to uncorrected signals, dashed lines to correction up to the 2Q signal, and dotted lines to correction using the 2Q and 3Q signals.

CHAPTER 9

General Discussion

This thesis investigated how higher-order (higher than three in the case of coherently detected methods and higher than four in the case of action-based methods) nonlinear signals can be isolated and how these higher-order signals can be used to study multi-exciton interaction and exciton transport. While third-order techniques such as pump–probe (PP) spectroscopy and two-dimensional (2D) spectroscopy are well-established techniques, higher-order spectroscopy is now becoming more popular in the spectroscopic community. During this thesis, the technique of higher-order spectroscopy and, in particular, fifth-order exciton–exciton-interaction (EEI) 2D spectroscopy was further investigated and generalized to higher-order signals. Furthermore, inspired by EEI2D spectroscopy and phase cycling, a novel approach to isolate higher-order signals in PP spectroscopy was developed.

In Chapter 2 the basic concepts of nonlinear spectroscopy were reviewed and the concept of double-sided Feynman diagrams as a description of nonlinear spectroscopy was introduced. In Chapter 3 different lower-order, i.e., third- and fourth-order techniques were demonstrated starting with TA. The concepts of excitons was introduced in Chapter 4. In Chapter 5 2D spectroscopy was combined with exciton theory and various effects such as signatures of delocalization, energy transfer and time-ordering were analyzed in the context of 2D spectroscopy and double-sided Feynman diagrams.

After the discussion of the basics of multidimensional spectroscopy, Chapter 6 featured higher-order spectroscopy focusing on the newest developments that were part of this thesis. The key problem in higher-order spectroscopy is the isolation of the different higher-order signals from the lower-order signals. This problem was solved using two different techniques, coherently detected spectroscopy in PP geometry as well as fluorescence-detected spectroscopy using phase cycling. These two experimental approaches were discussed in more depth. Phase cycling in fluorescence-detected 2D spectroscopy allows one to separate different nonlinear signals from one measurement [26]. In phase cycling, the relative phases of the pulses are scanned in addition to the time delays which results in a raw data set depending on the delays and relative phases. Different signal contributions are obtained by linear combinations of the raw data. The step size of the relative phases determines the highest nonlinear signal contribution that can be isolated. For higher phase-cycling schemes, i.e., smaller steps of the relative phases, higher-order signals can be isolated [5].

In coherently detected EEI2D spectroscopy in the PP geometry, the fifth-order signal is emitted in the same direction as the third-order signal [20]. However, the two signal contributions are isolated by their specific spectral position along the excitation

axis due to their different coherences during τ. In the signal at around the central frequency of the excitation pulse, a single-quantum coherence is present while for the fifth-order signal a coherence between states that differ by two quanta of excitation light is present. In extended systems, the integrated fifth-order signal is dominated by EEA. The direct observation of annihilation is especially interesting in isoenergetic systems such as polymers or aggregates. In such systems, the exciton diffusion is not connected to a change in the absorption spectrum and cannot be measured with standard third-order techniques such as TA or 2D spectroscopy. Instead, the exciton diffusion can be probed by annihilation: Two excitons can only annihilate if they are in close proximity to each other, i.e., when they are colocalized. In extended systems this means that a phase of exciton diffusion takes place before annihilation. In EEI2D spectroscopy, the exciton diffusion can be observed as a rise of the integrated fifth-order signal over the population time T. Using EEA to probe diffusion is well-known from power-dependent third-order TA measurements. In such a measurement, the annihilation is mixed together with the third-order signals which complicates the interpretation and analysis of the exciton diffusion. In coherently detected EEI2D spectroscopy, the fifth-order EEI signal is well separated from the ordinary third-order signal by its specific excitation frequency. Therefore, the annihilation can be measured separately and the dynamics of the EEI signal can be used to determine the exciton delocalization and exciton diffusion properties in extended systems.

Since both techniques, coherently detected as well as fluorescence-detected 2D spectroscopy, allow one to separate higher-order 2D spectra, the question arises whether both methods provide the same information. In Chapter 6, coherently and fluorescence-based techniques were directly compared by measuring ultrafast EEA in a squaraine dimer [9]. While in coherently detected EEI2D spectroscopy the annihilation is directly measured by the fifth-order signal, in fluorescence-detected methods the annihilation cannot be directly observed. Rather, the annihilation time is obtained by subtracting two sixth-order signals from each other. In phase cycling, both of the signals are isolated from the same raw data set and therefore measured under exactly the same experimental conditions. The approach was justified by analyzing the corresponding double-sided Feynman diagrams. The example demonstrated that the extraction of several signals by phase cycling can be used to isolate different phenomena as in this case EEA. The comparison between coherently detected fifth-order EEI2D spectroscopy and sixth-order fluorescence-detected 2D spectroscopy demonstrated the technical as well as fundamental differences between the two techniques. The interpretation of fluorescence-detected 2D spectroscopy is still under ongoing discussion in the scientific community and the comparison that was shown here is an important contribution to this discussion.

In Chapter 7 the question was addressed whether additional information can be obtained with the help of anisotropy in higher-order spectroscopy. In particular, the concept of EEI2D spectroscopy was extended by the anisotropy of the fifth-order signal [12]. Anisotropy describes the dependence of the signal on the polarization of the excitation and detection pulses (Fig. 9.1a). In literature, theoretical descriptions of

polarization-dependent higher-order 2D measurements are known but do not focus on EEA. A formal description of the anisotropy in fifth-order EEI2D spectroscopy was developed and was discussed in Chapter 7. Here, the well-known concept of rotational averaging was used to derive the expressions needed to calculate the isotropic and anisotropic EEI2D signal. Furthermore, it was proven that the so-called magic angle of 54.7° known from PP spectroscopy is still valid for fifth-order EEI2D spectroscopy. The magic angle is used to measure a signal without any anisotropic contribution, i.e., only the isotropic contributions. For the simulations, the rotational averaging was incorporated into an exciton model combined with Redfield theory to simulate the isotropic and anisotropic EEI2D signal contributions. A model of a dimer was constructed to demonstrate the ability to track localization and annihilation in the isotropic and anisotropic EEI2D signals. Inspired by the third-order anisotropy measurements in polymers, the further simulations focused on the geometric variations within polymers. In previous studies third-order anisotropy was used to investigate the exciton transport in polymers. The exciton transport along the disordered chain leads to depolarization which can be observed by the anisotropy decay. In EEI2D spectroscopy, the anisotropy includes the dynamics of the depolarization by exciton transport along the polymer as well as the dynamics of EEA. Different examples of geometric variations in polymers such as kinks, geometric and energetic disorder, and geometric domains within a polymer were discussed and investigated with the theoretical model (Fig. 9.1b). Overall, anisotropy is a useful extension of EEI2D spectroscopy and can determine the geometric configuration in isoenergetic systems such as polymers and aggregates.
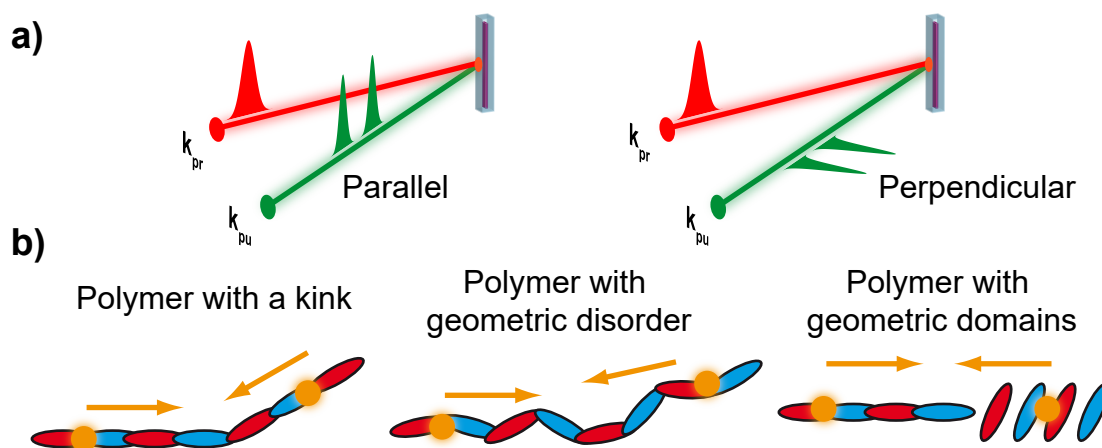

Figure 9.1.: Anisotropy in fifth-order EEI2D spectroscopy. (a) The anisotropy can be constructed from two EEI2D measurements with parallel and perpendicular polarizations of the pump pulses to the probe pulse. (b) The anisotropy of the EEI2D signal can be used to probe exciton transport in various situations in polymers such as kinks, geometric disorder, and geometric domains.

In Chapter 8, a procedure was developed to isolate clean nonlinear signals in terms of perturbation theory. The separation of 2D signals by their excitation frequency in PP geometry was extended to signals higher than the EEI2D signal. While the EEI2D signal appears at around twice the pump central frequency along the excitation axis, the next higher signal appears at the region of three times of the pump central frequency (Fig. 9.2a). Note that the different signals will not appear *exactly* at multiples of the pump central frequency because also the absorption spectrum contributes to the position along the excitation axis. Therefore, the signals will only appear at the region of multiples of the pump central frequency. The different signals vary in their coherences during the time delay τ which allows separation by the excitation frequency. The signal, which was called EEI signal before, at around twice the pump central frequency is also called two-quantum (2Q) signal because during τ, a coherence between states that differ by two quanta of light, is present. Analogously, the signal at around three times the excitation frequency is called three-quantum (3Q) signal because for this signal, a coherence between states that differ by three quanta of light is present. Note that all the nQ signals are emitted in the same direction with the phase-matching direction of $\pm n\mathbf{k}_1 \mp n\mathbf{k}_2 + \mathbf{k}_3$ with the index 1 and 2 for the two pump pulses and index 3 for the probe pulse. In order to extract the dynamics from the higher-order contributions, the 2D signals are integrated along the excitation axis (Fig. 9.2a, dashed lines). In principle, such an integration transfers the 2D spectrum to a PP spectrum. This is because integrating the complete 2D spectrum along the excitation axis corresponds to measuring at $\tau = 0$. However, measuring PP spectra would not allow to disentangle the different nQ signals because the signals are all added together. Inspired by phase cycling, a different approach was developed to separate the higher-order signals in PP spectroscopy. The signals are isolated by their specific dependence on the excitation intensity. The TA spectra at specific excitation intensities are measured separately and the different nQ signals are constructed by linear combinations of these measurements (Fig. 9.2b). For example, measurements at three different powers $4I_0$, $3I_0$ and I_0, with I_0 as an arbitrary base intensity, results in the one-quantum (1Q), 2Q, and 3Q PP signals. In contrast to 2D measurements, it is not necessary to scan an additional pulse delay τ to the population time T which reduces the measurement time drastically. Furthermore, a variation of the excitation intensity can be realized easily in an experiment by a combination of a half-wave plate and a polarizer.

a) Two-dimensional spectroscopy

b) Pump–probe spectroscopy

1Q   2Q   3Q

Detection frequency

ω_0 $2\omega_0$ $3\omega_0$

Excitation frequency

$(4I_0, 3I_0, I_0)$

$$PP^{(1Q)} = \frac{1}{6}\left[PP\left(4I_0\right) + PP\left(3I_0\right) - PP\left(I_0\right)\right]$$

$$PP^{(2Q)} = \frac{1}{6}\left[PP\left(4I_0\right) - PP\left(3I_0\right) - PP\left(I_0\right)\right]$$

$$PP^{(3Q)} = \frac{1}{12}\left[PP\left(4I_0\right) - 2PP\left(3I_0\right) + 2PP\left(I_0\right)\right]$$
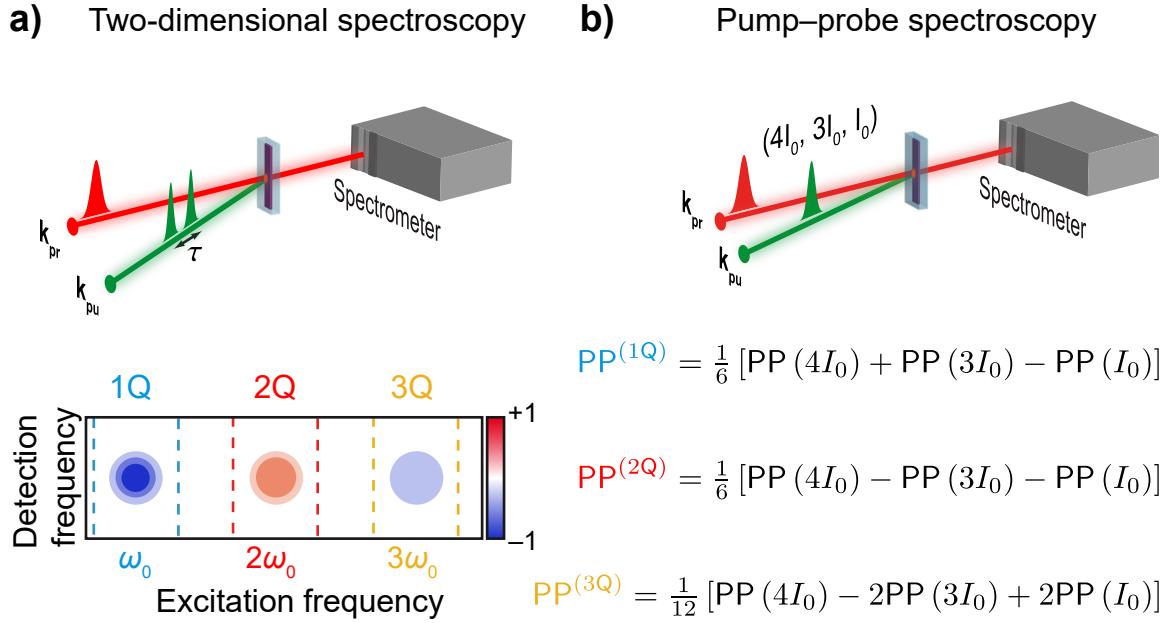
Figure 9.2.: Extraction of multi-quantum signals in 2D and and PP spectroscopy. (a) In 2D spectroscopy in the PP geometry the nQ signals are emitted in the same direction but can be disentangled by their specific position ($n\omega_0$) along the excitation axis. The separated signals are then integrated (indicated by dashed lines) along the excitation axis in order to calculate the clean nonlinear signals. (b) In PP spectroscopy the multi-quantum signals are extracted by measuring at different excitation intensities. Specific linear combinations of these measurements can be used to extract the nQ signals. Here, we show the formulas to extract the 1Q, 2Q, and 3Q signals from measurements at intensities of $4I_0$, $3I_0$, and I_0 with I_0 as an arbitrary "base" intensity.

Isolation of the nQ signals is only the first step to obtain clean nonlinear signals because the higher-order signals will be present as contaminations in the different multi-quantum signals. A procedure was developed to eliminate the contamination by using the integrated nQ signals from 2D spectroscopy. As an example, let us consider an excitation regime in which a seventh-order nonlinear signal is the highest obtained signal, i.e., the ninth-order signal is only a minor contribution that is, for example, vanishing in the noise and can therefore be neglected. Note that due to the phase-matching condition only odd orders of nonlinearity can contribute. The 3Q signal consists of a clean seventh-order signal. However, in the 2Q signal, fifth-order signals as well as seventh-order signals are present. The 1Q signal is usually measured at an intensity at which higher-order signals are not contributing significantly, and the 1Q signal is dominated by a third-order signal. Now the 1Q signal is contaminated by fifth- as well as seventh-order contributions. The third-order contribution at the 1Q position in 2D spectroscopy has the phase-matching direction of $\pm\mathbf{k}_1 \mp \mathbf{k}_2 + \mathbf{k}_3$. The fifth-order signal at the 1Q position can be described by additional interactions

with $+\mathbf{k}_i - \mathbf{k}_i$ ($i = 1, 2$) where the index shows that both interactions occur from the same pulse (either 1 or 2). Since the interactions take place with $-\mathbf{k}_i$ as well as $+\mathbf{k}_i$, the phase-matching condition is still fulfilled and the signal appears at the 1Q position in the 2D spectrum. The higher-order signals at different nQ positions are closely related since the same processes occur during the population time and the same line shape along the detection frequency axis are present. The difference in line shapes along the excitation axis for a higher-order signal at different nQ signals are not relevant because the nQ signals are integrated along the excitation axis. The only remaining question is how much each higher-order signal contributes to a specific nQ signal. To answer this question, the different signal contributions were analyzed in terms of double-sided Feynman diagrams which leads to the relation between the different signal contributions. For higher-order signals the number of double-sided Feynman diagrams increases rapidly with the order of nonlinearity. We developed a general formula that connects the higher-order signals at different nQ signals with each other. An automated Feynman diagram generator was used to calculate the explicit numbers of diagrams that contribute to the different signal contributions. By applying this knowledge, a general procedure was developed in order to eliminate the contaminations by taking advantage of the isolated nQ signals. For example, if the seventh-order signal is the highest-order signal that has to be considered, the fifth-order and seventh-order contamination in the 1Q signal can be eliminated by subtracting the integrated 2Q signal four times from the 1Q signal as well as adding nine times the integrated 3Q signal to the 1Q signal, resulting in a clean third-order signal. The procedure can be extended to higher-order signals by using the corresponding scaling factors.

The contamination by higher-order signals occurs in power-dependent higher-order PP spectroscopy as well. The relation of nonlinear order contributions for the different nQ signals can be obtained by analysis of the linear combinations in order to obtain the nQ signals. Each nQ signal is calculated by taking a specific linear combination of measurements at different excitation intensities. The nonlinear signals scale differently with the excitation intensity. For example, the third-order signal scales linearly while the fifth-order signal scales quadratically with the excitation intensity. Combining the linear combinations that are used to obtain the nQ signals with the specific intensity scaling of the nonlinear signals leads to the relation between nQ signals and nonlinear signal contributions at different nQ signal. From this relation, the scaling factors between the higher-order contributions at different nQ signals can be derived. The factors are the same as in the case of 2D spectroscopy demonstrating the close relation between the two techniques. Using the same strategy as in 2D spectroscopy, the different nQ signals can be added together upon weighing them with different factors to obtain clean nonlinear signals. PP measurements at N different excitation intensities yield N clean nonlinear signals. The developed correction procedure might also work for nQ signals that are isolated by other methods such as phase matching or phase cycling.

The isolation of higher-order signals in 2D spectroscopy as well as in PP spectroscopy was directly compared in Chapter 8. The two methods of isolating higher-order signals, once by the excitation frequency and once by their specific power dependence, were both used to measure the 1Q, 2Q, and 3Q signals of squaraine oligomers and extract a clean third-order signals at high excitation intensities. The extracted third-order signals were compared with a contamination-free low-power measurements and showed experimentally that the correction procedure results in clean nonlinear signals. For higher-order PP spectroscopy, measurements at three different excitation intensities are necessary to isolate the 3Q signal. In 2D spectroscopy, the coherence time step size has to be chosen small enough in order to avoid aliasing and to separate the nQ signals from each other. The theoretical limitations of the finite integration area in 2D spectroscopy and the consequences for the correspondence between PP and 2D spectroscopy were discussed as well. Interestingly, the signals that were obtained by the two methods differ in the dynamics close to $T = 0$. However, a detailed analysis of the early time dynamics close to $T = 0$ is challenging due to off-resonant solvent contributions and pulse overlap effects.

At the end of Chapter 8, the concept of isolation of different higher-order signals by power dependence was extended to signals higher than the seventh-order signals. In order to isolate signals of even higher order, the number of measurements at different excitation intensities was increased to six which allowed us to isolate up to the 13$^{\text{th}}$-order signal in terms of perturbation theory. As a sample, squaraine polymers were chosen with an average length of 19 dimers. The polymers correspond to an excitonic system and with increasing higher orders of nonlinearity, the dynamics and the interaction of an increasing number of excitons can be observed. While the fifth-order signal correspond to the dynamics of two excitons, three excitons can be observed with the seventh-order signal and analogously for higher-order signals. Fitting the fifth-, seventh-, and ninth-order signals with analytic expressions that were obtained from the analysis of double-sided Feynman diagrams, the specific timescale of multi-exciton annihilation for two, three, and four excitons was determined. The different annihilation times for the increasing number of excitons revealed that the excitons do not always annihilate when they are colocalized but can rather have many encounters before annihilation takes place.

While Chapter 6 addressed general aspects of higher-order spectroscopy and Chapter 7 focused on the specific extension of fifth-order EEI2D spectroscopy by the anisotropy, Chapter 8 provides a direction for the future developments of higher-order spectroscopy. Especially the technique of separating clean nonlinear signals by their power dependence in a simple PP experiment offers a platform for the investigation of various phenomena. The technique can be integrated into ordinary TA setups and allows to measure pure third-order signals even at high excitation intensities. This increases the SNR of the third-order signal drastically and simplifies the analysis because it can be ensured that no higher-order contamination is present. This procedure is in particular interesting for the investigation of natural light-harvesting complexes where annihilation is difficult to avoid due to the large absorption cross sections. The higher-order signals themselves can be further used as a tool to investigate exciton diffusion in extended systems such as polymers and aggregates. Furthermore, measuring with a higher number of different excitation intensities allows one to separate even higher-order signals such as the thirteenth-order signal as demonstrated in the case of squaraine polymers. The technique of higher-order PP spectroscopy is not limited to excitonic systems and can be applied to different systems to study multi-(quasi)particle states. The technique can determine the corresponding interactions and characterize their dynamics. In Chapter 10, we discuss three future experiments using higher-order spectroscopy.

CHAPTER 10

Outlook

As shown in this thesis, new methods of higher-order spectroscopy allow one to obtain a variety of information about the photophysical properties of molecules, aggregates, and nanocrystals. The techniques resolve phenomena that are otherwise only indirectly measurable such as EEA [20], or are otherwise completely hidden such as the biexciton binding energies of higher excited states in the case of nanocrystals [13]. However, new developed spectroscopic techniques are usually demonstrated on a model system such as laser dyes [45, 320] or systems that are already known like squaraine copolymers during the development of higher-order PP spectroscopy. As a next step, the potential of the new methods need to be demonstrated on other systems and if these applications are successful, the new techniques might become established as a standard tool for other scientists. In this chapter, different examples are discussed how the new developed methods may be further utilized to answer concrete questions in different fields.

10.1. Investigating Exciton Transport in Photosynthesis

Chapter 8 demonstrated how to measure annihilation-free signals in a PP experiment by systematically changing the excitation intensity. Annihilation-free measurements are especially challenging in the field of photosynthesis. The first step in photosynthesis is the absorption of light by antenna complexes such as the chlorosome in the case of green sulfur bacteria or a network of LH2/LH1 complexes in the case of purple bacteria [61, 321]. The antenna complexes are built from interacting pigments resulting in large absorption cross sections. From the antenna complexes, the energy is transferred by several steps to the reaction center in which the charge separation occurs. While the absorption by natural light does not lead to EEA, the situation is different when photosynthetic complexes are investigated with femtosecond lasers [322]. The intense laser pulses lead to many absorption events in a short period of time so that several excitons are present in the system simultaneously. If the measurements aim to characterize the single-exciton dynamics from the antenna complexes to the reaction center, EEA has to be avoided because it distorts the third-order signal [186, 207].
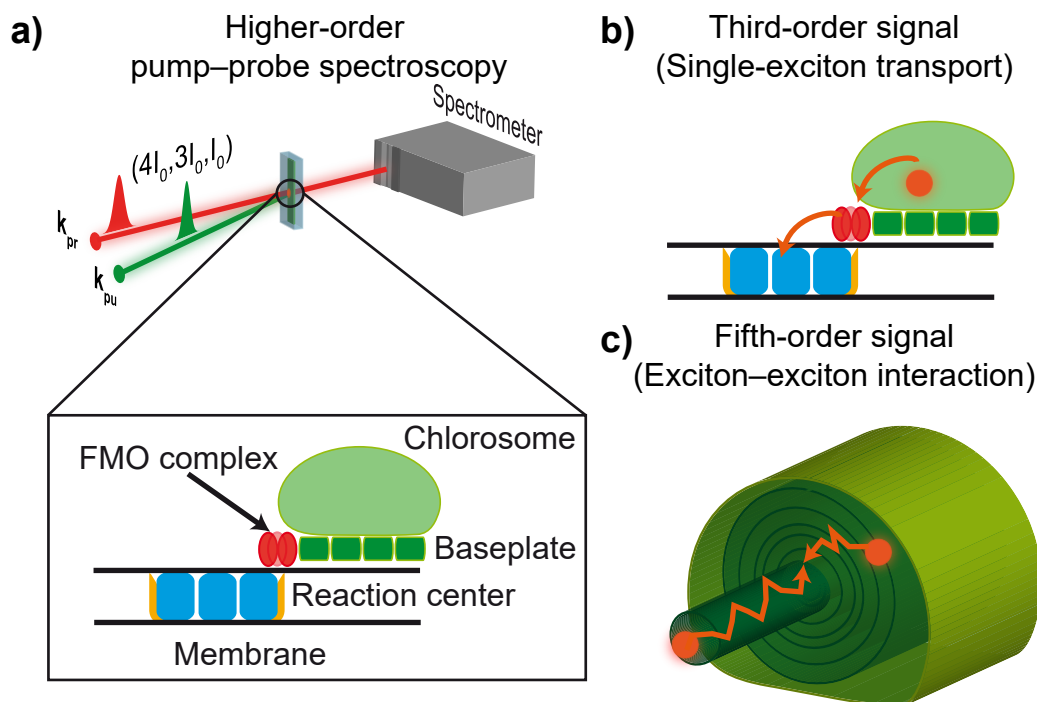
Figure 10.1.: Higher-order PP experiment on green sulfur bacteria. (a) As an outlined experiment, the PP signal with three different excitation intensities $4I_0$, $3I_0$, and I_0 on green sulfur bacteria is measured. The green sulfur bacteria is made out of different components such as the chlorosome as the main antenna complex. (b) The third-order signal tracks the exciton transport through the photosynthetic apparatus from the chlorosome to the FMO complex and further to the reaction center. (c) The fifth-order signal measures how fast two excitons meet and interact and can therefore be used to investigate the exciton diffusion within the chlorosome.

  The experimenter faces a dilemma: either measure under low laser intensities in order to avoid contributions stemming from annihilation, which, however, leads to low SNR, or measure under high excitation intensities with unavoidable and uncontrolled mixing of the higher-order contributions into the desired signal.

  The problem of uncontrolled mixing of annihilation with the single-exciton dynamics could be completely avoided using higher-order spectroscopy obtaining clean nonlinear signals. Applying this technique to photosynthetic complexes could be used in two ways. First, annihilation-free single-exciton dynamics, i.e., clean third-order signals, could be measured characterizing the transport through the photosynthetic apparatus. Second, the higher-order signals themselves could be used to get additional information about the exciton diffusion within the antenna complexes [20] similar as demonstrated in polymers [7]. We demonstrated the measurement of clean nonlinear signals using two techniques: higher-order PP spectroscopy applying power-dependent measurements and 2D spectroscopy isolating the higher-order signals by their excitation frequency. The energy transfer in light-harvesting complexes was studied for many years including

PP techniques [52, 323, 324]. In a PP experiment, the correction and isolation of clean nonlinear signals is straightforward. However, the different contributions of energy transfer can be disentangled easier using 2D spectroscopy but the correction and isolation of clean nonlinear signals in 2D spectroscopy is more difficult. The analysis of the correction and isolation of higher-order signals in this thesis has been carried out for *spectrally integrated* 2D signals. The nQ signals appear at n times the central frequency (ω_0) of the pump spectrum and the nQ signals are then integrated along the excitation axis. If we want to use 2D spectroscopy to analyze the exciton transfer, the structure of the peaks *within* nQ signals has to be resolved. In the case of light-harvesting complexes, different peaks of the nQ signals correspond to the resonances of the various parts of the photosynthetic complex such as the reaction center or the antenna complex and therefore the whole signal can not be integrated because then the information of the peak position along the excitation axis is lost. If the peaks are well separated in the 2D spectrum, a spectral region within the nQ signals could be integrated large enough that the different line shapes of the higher-order signals and the corresponding contamination do not need to be considered. However, it is an unanswered question if and how the correction works for unintegrated signals and how the line shapes of the contamination can be described. It might be possible to simply use the correction on the whole spectra, i.e., by using the complete 2D spectra without integration over the excitation axis, to obtain, e.g., a clean third-order 2D spectrum at high excitation densities.

Previous studies on photosynthetic complexes either investigated the spectrally distinguishable features such as the exciton transport from the antenna to the reaction center [79] or used power-dependent studies to determine the exciton diffusion inside the antenna complexes [192]. So far, it was not possible to measure the transport to the reaction center and the exciton diffusion within the antenna complex with *one* single experiment. With higher-order PP spectroscopy, all the information could be obtained by one single experiment and the different contributions could be clearly separated. A possible experiment to study photosynthetic complexes applying higher-order PP spectroscopy is outlined in Fig. 10.1a. As a sample complete cells of green sulfur bacteria are used. The cell consists of its primary antenna complex which is the chlorosome. Different components such as the baseplate and the FMO complex guide the energy to the reaction center. The different components act as a funnel for the exciton and at the end of transport, the exciton reaches the reaction center where charge separation takes place. The sample could be measured either at room temperature in a buffer or in a cryostat as a cryogenic glass at low temperatures. While the first option is closer to the natural conditions of these bacteria, cryogenic temperatures have the advantage of well-separated spectral features. Measurement at three different excitation intensities allows one to isolate the 1Q, 2Q, and 3Q signal contributions. In the case of green sulfur bacteria, the excitation regime should be chosen in such a way that the 3Q signal is present as a minor contribution and the 2Q signal is strong. In such a regime, photobleaching of the bacteria might be not severe and the clean fifth-order signal can be obtained. The 2Q and the 3Q signals are utilized to extract a

clean third-order signal, i.e., the single-exciton dynamics. The single-exciton dynamics could be used to characterize the timescales of exciton transport from the chlorosome to the baseplate and further to the FMO complex ending at the reaction center (Fig. 10.1b). With the correction for higher-order contamination, the SNR could be increased because higher excitation powers could be used without any contribution of annihilation. While the transport from the antenna over the baseplate to the reaction center can be characterized by a PP experiment, the transfer within the FMO complex (already known from 2D experiment [47, 62]) might be challenging to characterize with a PP experiment because of the spectrally close transitions. Applying the concept of correcting for higher-order signals to specific peaks in the 2D spectrum as outlined above might solve this issue.

Since also the clean fifth-order signal is isolated by using the 3Q signal for correction, we could study the exciton diffusion within the chlorosome (Fig. 10.1c). The chlorosome consists of layers of closely packed pigments forming complex structures such as multilayer cylinders [325, 326]. The fifth-order signal tracks the dynamics and annihilation of two excitons. In the case of aggregates such as the chlorosome, the excitons need to diffuse to each other in order to get in close proximity and ultimately annihilate. Therefore, the annihilation can be used to probe the exciton diffusion. Instead of power-dependent measurements and indirectly measuring the fifth-order signal as a contamination in the third-order signal, the proposed experiment allows one to directly measure the annihilation via the fifth-order signal. Using more excitation powers instead of only three allows to extract even higher-order signals than the fifth- and seventh-order contributions. The dynamics of the higher-order signals include the dynamics of more than two excitons. However, if the goal is to determine the exciton diffusion within the antenna complex, the fifth-order signal might already be sufficient. In conclusion, higher-order PP and 2D spectroscopy are the methods of choice to extract the transport dynamics in the complete photosynthetic apparatus of green sulfur bacteria with good SNR and within one single experiment.

10.2. Higher-Order Two-Color Two-Dimensional Spectroscopy

One direction for future higher-order experiments is two-color 2D spectroscopy [107, 327, 328]. One example of two-color 2D spectroscopy is 2DEV spectroscopy [260]. In this type of 2D experiment in the PP geometry, the system is excited with a double pulse in the visible regime followed by a probe pulse in the mid infrared region (Fig. 10.2a). This pulse sequence allows one to probe the vibrational signatures of excited states (Fig. 10.2b) [261]. In such an experiment a 1Q1Q signal is detected in which a 1Q coherence is excited from the (first) pump pulse as well as from the probe pulse. Note that these coherences correspond to a coherence between electronic states for τ and a vibrational coherence for t.
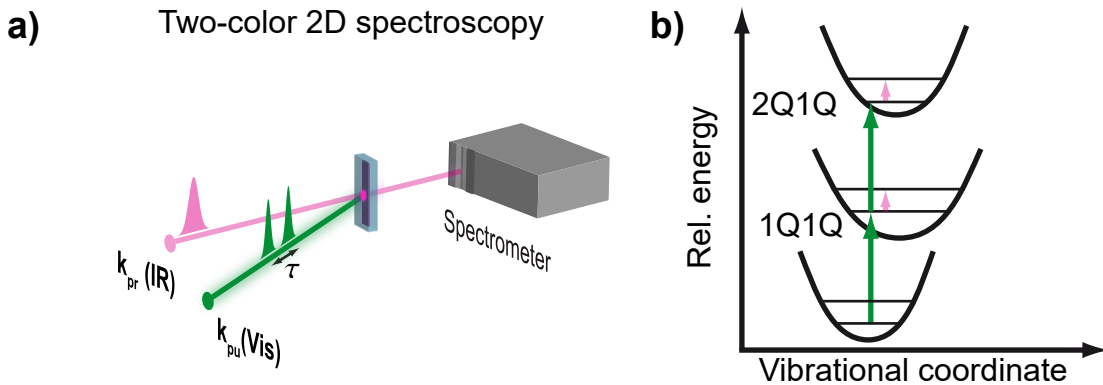
Figure 10.2.: Two-color higher-order 2D spectroscopy. (a) The setup in PP geometry consists of a pump pulse pair in the visible and a probe pulse in the IR. (b) In the 1Q1Q signal, the first electronically excited state is excited while for the 2Q1Q signal, the doubly excited state can be excited. The different vibrational states are schematically drawn as horizontal lines.

We could now combine our approach of higher-order spectroscopy which isolates different higher-order signals along the excitation axis in the 2D spectra with such a two-color experiment. Increasing the excitation intensity of the pump pulses would allow one to excite a 2Q coherence as shown in Fig. 10.2b with the first pulse in the same way as in coherently detected fifth-order spectroscopy as outlined in Section 6.4. The second pulse can convert this coherence into a population of a doubly excited state. In the example shown in Fig. 10.2b the doubly excited state is excited via resonant two-photon absorption. The contributions of the first excited state and the doubly excited state could easily be separated because of their different coherences during τ resulting in different positions along the excitation axis. If the higher excited state cannot be resonantly excited, the 2Q1Q signal will be correspondingly weaker. The concept outlined here could be extended to higher-order signals, i.e., to nQ1Q signals, that will appear accordingly at multiples of the central frequency of the pump spectrum ω_0. Probing with an IR pulse instead of another pulse in the visible regime

allows one to study the vibrational signatures of an excited state. Since the vibrational modes are sensitive to the local environment, specific vibrations can be correlated to specific parts of the system. The principle was used to study the energy flow within the light-harvesting complex II (LHC2) using specific signatures of chlorophyll *a* and *b* [261]. While the current technique is limited to the first electronically excited state the proposed higher-order two-color spectroscopy could allow one to study vibrational modes of higher-excited states like the doubly excited state in the case of the 2Q1Q signal.

10.3. Higher-Order Pump–Probe Microspectroscopy

The field of supramolecular material science utilizes the interactions between molecules to create materials with tailored photophysical properties [329–332]. Nowadays, optoelectronic devices can be built based on interactions between molecules [333–335]. Perylene bisimides (PBIs) are a promising class of pigments in the field of supramolecular chemistry because of their photostability as well as their excellent photophysical properties such as quantum yields close to unity [259, 336–338]. Changes in the chemical structure of PBI monomers lead to different aggregates with specific structures that determine the properties [259, 339, 340]. To incorporate supramolecular aggregates into a device, it is necessary to process the aggregate into a solid phase such as a film. The step from an aggregate in solution to a solid film is one of the most crucial ones. In solution, each aggregate is surrounded by a shell of solvent molecules and the properties are mostly determined by the interaction *within* an aggregate such as $\pi-\pi$-interactions or H-bonds [341]. In a film, the solvent molecules are no longer present. Therefore, the properties in a film are influenced apart from the interaction within the aggregate also by the interaction *between* the aggregates. Furthermore, additional interactions between the aggregates and the substrate can occur. As a result local effects can take place such as the building of domains or interfaces within the film. The different effects can lead to a drastic change of the photophysical properties from the solution to the film. For example, modified PBI aggregates have in solution quantum yields close to unity which drop to a few percent in the crystalline material [259]. For future developments of optoelectronic devices based on supramolecular chemistry, it is necessary to understand how and why the photophysical properties change from solution to a film.

Here we propose higher-order PP microspectroscopy to study the spatial dynamics in films and interfaces. A setup which is inspired by a TA microscope setup from literature [342] is shown in Fig. 10.3. In principle, it is a transient absorption setup with the ability to change the excitation intensity automatically, and which is incorporated into a microscope. Pump and probe beams are both collinearly guided into an objective and focused onto a sample. The transmitted light is collected by another objective. The pump light could filtered out either by frequency using an interference filter or by polarization using a polarizer (not shown in Fig. 10.3). The transmitted light is then detected with a photomultiplier tube (PMT). The PMT directly integrates

as a point detector the whole signal over the complete detection axis and therefore no spectral information can be obtained. If a narrowband detection is applied, the spectral information does not need to be resolved anyway. Instead of a PMT, also a spectrometer could be used to obtain additional spectral information [131]. The pumped and unpumped signal of the probe could be obtained by chopping the pump beam and the TA signal could be constructed from these two signal contributions. Scanning the sample position and changing the population time T by a linear translation stage results in transient absorption traces for different positions of the sample. Measuring TA at N different excitation powers allows to separate N clean nonlinear signals as shown in Chapter 6 and Chapter 8. Changing the excitation power can be easily realized with a polarizer and a half-wave plate. The polarizer is fixed, for example to the magic angle, while the half-wave plat can be adjusted with a rotation stage. However, care has to be taken in choosing the pump and probe sizes [343]. In order to avoid different high-order effects within the pump beam, it makes sense to set the pump focus sufficiently larger than the probe focus. In such a case, the excitation profile that is probed is almost uniform across the detection beam. With high-order PP spectroscopy, at each pixel, a set of clean nonlinear signals could be obtained. We will focus in our discussion on the third-order and the fifth-order signal contributions.

Similar as in TA experiments, two kinds of information could be obtained in PP microspectrosopy: dynamics over the population time T such as fast relaxation and lifetimes, and spectral information such as the ESA signals and GSB signals. In contrast to ordinary PP experiments, the information is now spatially resolved and the clean third- and fifth-order signals are measured. From the third- and fifth-order transient spectrum, information about the local structure could be obtained since the specific local structures lead to different interaction between the molecules and therefore a variation in the absorption spectrum. In supramolecular chemistry, one strategy for the fabrication of films is vapor-deposition of the monomers with consecutive treatment of the sample by thermal annealing or washing with a solvent [259, 344, 345]. These additional steps help to create a homogeneous film in which most of the molecules are aggregated to supramolecular structures. However, monomers can still be present or small zones with different structures can be formed. Measuring the transient spectrum could resolve to what extent the film can be considered homogeneous and if different domains are present which for example can be formed at structural "hotspots" of the substrate. The temporal information may be utilized to characterize the exciton dynamics within the sample. The spatially resolved fifth-order signal measures how fast two excitons are becoming colocalized and annihilate, and could be used to characterize the exciton diffusion. For each spatial position, the exciton diffusion could be determined and local differences could be investigated. For example, structural domains may have a more disordered structure compared to the film which may lead to slower exciton diffusion (Fig. 10.3b). The fifth-order signal could also be used to study the amount of EEA at a specific position by measuring the fifth-order signal amplitude for one specific T step. The T step has to be chosen in such a way that the rise of the fifth-order signal already ended and the remaining excitons decay with the exciton

lifetime. Then, the amplitude of the fifth-order signal is proportional to the amount of EEA. Such a measurement is fast because no delays have to be scanned. This experiment reveals if EEA is more pronounced at specific local positions. Additionally to the fifth-order signal, also the clean third-order signal could be measured. The third-order signal may be utilized to characterize the local lifetime and to identify local properties such as additional trap states with reduced lifetimes. Correlation between lifetimes and exciton diffusion on one side and structural information on the other side could reveal a comprehensive picture of the exciton properties of the investigated sample.
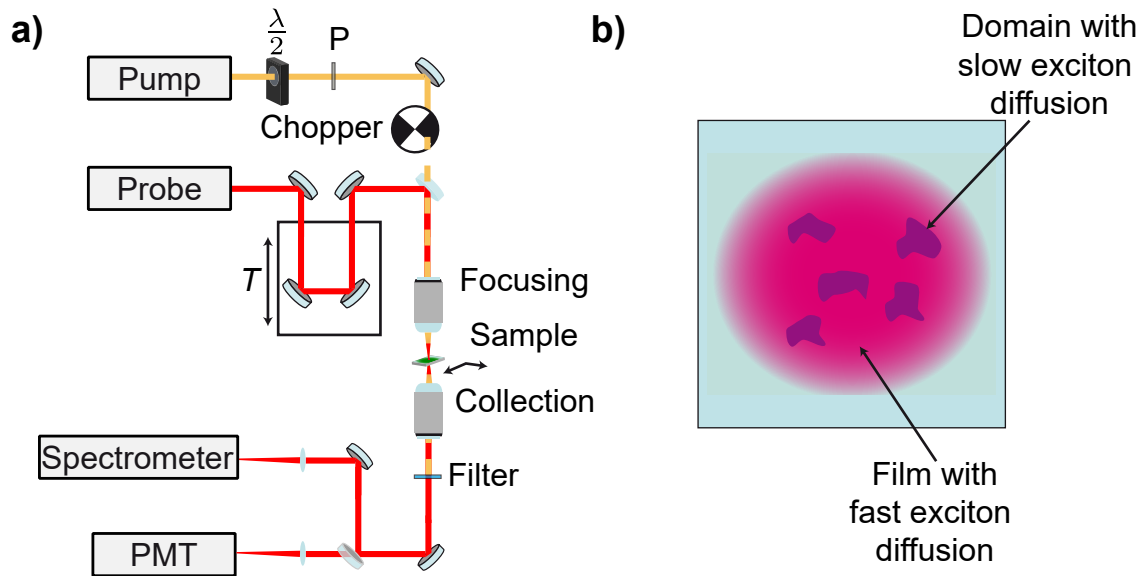
Figure 10.3.: Higher-order PP microspectroscopy on thin films. (a) The proposed setup uses two beams which are coupled into a microscope. The sample position can be systematically varied via translation stages. The pump beam could be filtered out by a bandpass filter and is then guided either to a photomultiplier tube (PMT) or to a spectrometer. The variation of excitation power that is necessary to extract the clean nonlinear signals could be realized by a combination of a polarizer and a half-wave plate. A chopper is used to measure the pumped and unpumped probe spectrum. (b) As an example for a suitable sample, a thin film with domains with varying exciton diffusion at different spatial positions is schematically shown.

Similar information such as exciton transport, structural information or EEA could be obtained by fluorescence-detected 2D microspectroscopy [9, 126]. In such an experiment, a phase-cycling scheme has to be used which can distinguish higher-order signals as recently demonstrated with a 36-fold phase-cycling scheme for a three pulse sequence [13] or 125-fold phase-cycling scheme for a four pulse sequence [5]. Combining phase cycling with a high NA objective for excitation and collection of the fluorescence allows to measure spatial resolved higher-order 2D signals. The spatial resolution can be further increased to a few tens of nanometers by measuring 2D nanoscopy with higher phase-cycling schemes. However, the problem with such measurements is that the measurement times are long due to the different time delays and phases that have to be scanned. In addition, the experimental setup involves pulse shapers which have to be thoroughly characterized to avoid artifacts [125, 225]. As an advantage, 2D spectra allow one to measure energy transfer via cross peaks and obtain additional information compared to TA measurements such as line shapes. Population-detected 2D spectroscopy has the advantage that off-resonant contributions are not present which is especially interesting for dynamics close to $T = 0$. However, higher-order PP microspectroscopy could measure EEA with shorter measurement time as 2D spectroscopy and might be a good alternative to 2D methods.

In principle, higher-order PP spectroscopy could be combined with other measurements to obtain additional information. For example, anisotropy measurements for the third- and fifth-order signal allows one to obtain extra structural information about the disorder or geometric domains within the measured sample [12]. In conclusion, the combination of higher-order spectroscopy with spatially resolved microscopy is the perfect tool to characterize the exciton properties of films and interfaces.

Summary

The goal of this thesis was the development and application of higher-order spectroscopic techniques. In contrast to ordinary pump–probe (PP) and two-dimensional (2D) spectroscopy, higher-order coherently detected spectroscopic methods measure a polarization that has an order of nonlinearity higher than three. The key idea of the techniques in this thesis is to isolate the higher-order signals from the lower-order signals either by their excitation frequency or by their excitation intensity dependence. Due to the increased number of interactions in higher-order spectroscopy, highly excited states can be probed. For excitonic systems such as aggregates and polymers, the fifth-order signal allows one to directly measure exciton–exciton annihilation (EEA). In polymers and aggregates, the exciton transport is not connected to a change of the absorption and can therefore not be investigated with conventional third-order techniques. In contrast, EEA can be used as a probe to study exciton diffusion in these isonergetic systems. As a part of this thesis, anisotropy in fifth-order 2D spectroscopy was investigated and was used to study geometric properties in polymers.

In 2D spectroscopy, the multi-quantum signals are separated from each other by their spectral position along the excitation axis. This concept can be extended systematically to higher signals. Another approach to isolate multi-quantum signals in PP spectroscopy utilizes the excitation intensity. The PP signal is measured at specific excitation intensities and linear combinations of these measurements result in different signal contributions. However, these signals do not correspond to clean nonlinear signals because the higher-order signals contaminate the lower-order multi-quantum signals. In this thesis, a correction protocol was derived that uses the isolated multi-quantum signals, both from 2D spectroscopy and from PP spectroscopy, to remove the contamination of higher-order signals resulting in clean nonlinear signals. Using the correction on the third-order signal allows one to obtain annihilation-free signals at high excitation intensities, i.e., with high signal-to-noise ratio. Isolation and correction in PP and 2D spectroscopy were directly compared by measuring the clean third-order signals of squaraine oligomers at high excitation intensities. Furthermore, higher-order PP spectroscopy was used to isolate up to the 13th nonlinear order of squaraine polymers.

The demonstrated spectroscopic techniques represent general procedures to isolate clean signals in terms of perturbation theory. The technique of higher-order PP spectroscopy needs only small modifications of ordinary PP setups which opens the field of higher-order spectroscopy to the broad scientific community. The technique to obtain clean nonlinear signals allows one to systematically increase the number of interacting (quasi)particles in a system and to characterize their interaction energies and dynamics.

Zusammenfassung

Das Ziel dieser Arbeit war die Entwicklung and Anwendung von spektroskopischen Techniken höherer Ordnung. Im Gegensatz zu herkömmlicher Anrege-Abfrage- und zweidimensionalen (2D) Spektroskopie, wird in kohärenzdetektierten spektroskopischen Methoden höherer Ordnung eine Polarisation gemessen, die höher als drei ist. Die Schlüsselidee der Techniken dieser Arbeit ist die Trennung Signale höherer Ordnung von den Signalen niedrigerer Ordnung, entweder durch ihre Anregungsfrequenz oder durch ihre Abhängigkeit zur Anregungsintensität. Durch die erhöhte Anzahl an Interaktionen in der Spektroskopie höherer Ordnung können auch hoch angeregte Zustände untersucht werden. Für exzitonische Systeme wie Aggregate und Polymere erlaubt das Signal fünfter Ordnung die direkte Messung der Exziton-Exziton-Annihilierung (EEA). In Polymeren und Aggregaten ist der Exziton-Transport nicht mit einer Änderung des Absoprtionsspektrums verbunden und kann daher nicht mit konventionellen Techniken dritter Ordnung untersucht werden. Im Gegensatz dazu kann EEA, die mit Spektroskopie fünfter Ordnung gemessen wird, als Sonde verwendet werden, um Exziton-Diffusion zu untersuchen. Als ein Teil dieser Arbeit wurde die Anisotropie in der 2D-Spektroskopie fünfter Ordnung untersucht, und es wurde gezeigt, dass diese geometrische Eigenschaften von Polymeren bestimmen kann.

In der 2D-Spektroskopie werden die sogenannten Multiquantensignale durch ihre Position entlang der Anregungsachse von anderen Signalen getrennt. Dieses Konzept kann systematisch zu höheren Signalen erweitert werden, die durch ihre spezifische Anregungsfrequenz in dem 2D-Spektrum isoliert werden. Ein anderer Ansatz, um Multiquantensignale in der Anrege-Abfrage-Spektroskopie zu isolieren, nutzt die Anregungsintensität. Das Anrege-Abfrage-Signal wird bei spezifischen Anregungsintensitäten gemessen und Linearkombinationen dieser Messungen resultieren in verschiedenen Signalbeiträgen. Allerdings entsprechen diese Signale nicht reinen nichtlinearen Signalen, weil die Signale höherer Ordnung die Multiquantensignale niedriger Ordnung kontaminieren. In dieser Arbeit wurde ein Korrekturprotokoll entwickelt, das die isolierten Multiquantensignale sowohl in der 2D- als auch in Anrege-Abfrage-Spektroskopie nutzt, um die Kontamination durch Signale höherer Ordnung zu entfernen. Die Anwendung dieser Korrektur auf das Signal dritter Ordnung erlaubt es, annihilierungsfreie Signale bei hoher Anregungsintensität, d.h. mit hohem Signal-zu-Rausch-Verhältnis zu erhalten. Isolation und Korrektur in Anrege-Abfrage- und 2D-Spektroskopie wurden direkt miteinander verglichen, indem das kontaminierungsfreie Signal dritter Ordnung von Squarain-Oligomeren bei hoher Anregungsintensität gemessen wurde. Des Weiteren wurde Anrege-Abfrage-Spektroskopie höherer Ordnung eingesetzt, um nichtlineare Signale bis zur 13ten Ordnung in Squarain-Polymeren zu isolieren.

Die gezeigten spektroskopischen Techniken stellen allgemeine Verfahren zur Isolierung verschiedener Signale im Sinne der Störungstheorie dar. Die Technik der Anrege-Abfrage-Spektroskopie höherer Ordnung erfordert nur geringfügige Änderungen an gewöhnlichen Anrege-Abfrage-Experimenten und erlaubt es, die Spektroskopie höherer Ordnung in vielen weiteren wissenschaftlichen Gebieten anzuwenden. Der Ansatz kontaminierungsfreier nichtlinearer Signale gibt die Möglichkeit, die Anzahl der wechselwirkenden Teilchen systematisch zu erhöhen und ihre Wechselwirkungsenergien und Dynamiken zu messen.

Appendix

A. Cross Peaks in Fluorescence-Detected Two-Dimensional Spectroscopy for a Weakly Coupled Dimer

The detection of fluorescence has interesting consequences for the corresponding 2D spectra. Here, we want to briefly discuss the influence of EEA on the cross peaks of a dimer. A thorough analysis can be found in literature [120]. In fluorescence-detected 2D spectroscopy a fourth-order nonlinear response is measured [8]. We discuss here the same system of a coupled dimer that was discussed in Section 4.1 consisting out of one ground state $|0\rangle$, two single-exciton states $|1\rangle$ and $|2\rangle$, and a biexciton state $|\alpha\rangle$. Since fluorescence is detected, the double-sided Feynman diagrams have in common that they end in an excited-state population. For simplicity we consider that every population in a single-excited state has the quantum yield of one. We show the rephasing diagrams for $T = 0$ that correspond to the cross peak below the diagonal (peak A) and above the diagonal (peak B) in Fig. A.1. The rephasing part of the fluorescence-detected 2D spectrum can be isolated by phase cycling [26] and has the specific phase signature $-\varphi_1 + \varphi_2 + \varphi_3 - \varphi_4$ [89].

The diagrams can be divided in two GSB-type diagram and four ESA-type diagrams. Note the difference in the sign of the diagrams compared to the diagrams of the coherently detected contributions because of the different number of interactions on the right. Two of the ESA-type diagrams end in a single-exciton state (labeled as $\mathrm{ESA_{A,B\text{-}1E}}$) while the other two end in a population of a biexciton state (labeled as $\mathrm{ESA_{A,B\text{-}2E}}$). The amplitudes of the pathways for peak A are

$$
\begin{aligned}
\mathrm{GSB_A} &= |\boldsymbol{\mu}_{20}|^2 |\boldsymbol{\mu}_{10}|^2, \\
\mathrm{ESA_{A\text{-}1E}} &= |\boldsymbol{\mu}_{20}|^2 |\boldsymbol{\mu}_{\alpha 2}|^2, \\
\mathrm{ESA_{A\text{-}2E}} &= -\Phi |\boldsymbol{\mu}_{20}|^2 |\boldsymbol{\mu}_{\alpha 2}|^2.
\end{aligned}
\tag{10.1}
$$

where we introduced the parameter Φ as the quantum yield of the biexciton state $|\alpha\rangle$. Analogously the amplitudes for the diagrams describing peak B are

$$
\begin{aligned}
\mathrm{GSB_B} &= |\boldsymbol{\mu}_{10}|^2 |\boldsymbol{\mu}_{20}|^2, \\
\mathrm{ESA_{B\text{-}1E}} &= |\boldsymbol{\mu}_{10}|^2 |\boldsymbol{\mu}_{\alpha 1}|^2, \\
\mathrm{ESA_{B\text{-}2E}} &= -\Phi |\boldsymbol{\mu}_{10}|^2 |\boldsymbol{\mu}_{\alpha 1}|^2.
\end{aligned}
\tag{10.2}
$$

Cross peak below the diagonal
(peak A)

Cross peak above the diagonal
(peak B)
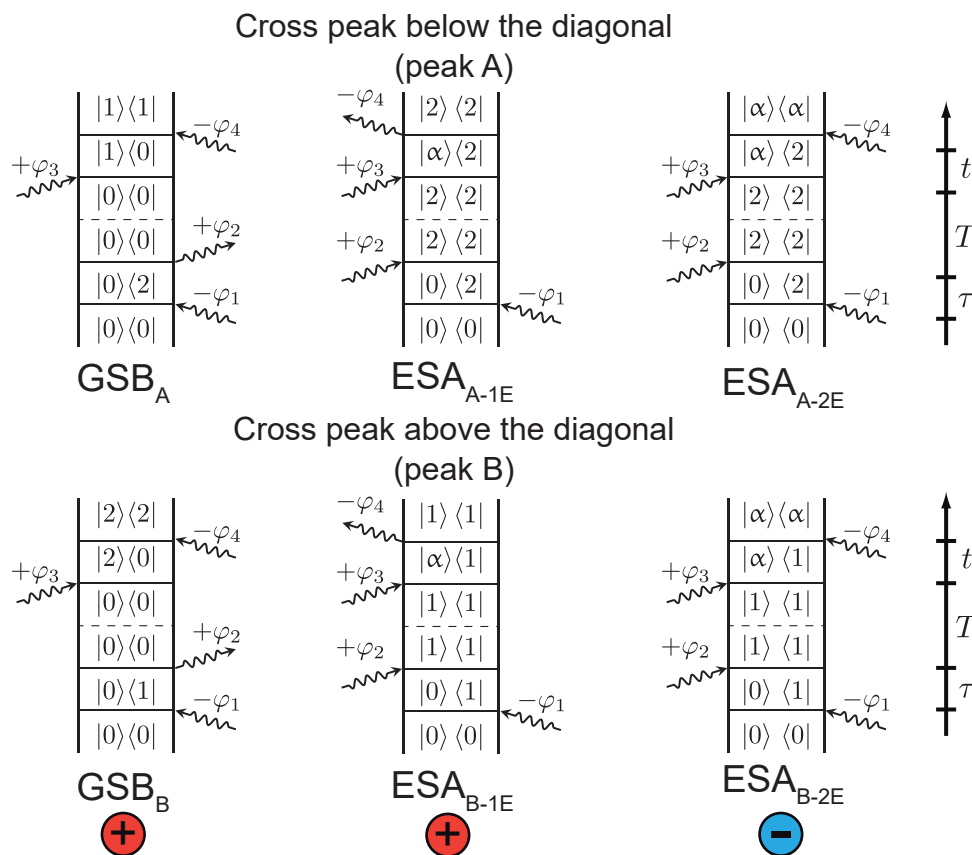
Figure A.1.: Double-sided Feynman diagrams for the cross peaks in the rephasing fluorescence-detected 2D spectrum. The signal can be isolated via phase cycling by the specific phase combination of $-\varphi_1 + \varphi_2 + \varphi_3 - \varphi_4$. While the GSB-type pathways and ESA$_{A,B\text{-1E}}$-type pathways end in a single-exciton population, the ESA$_{A,B\text{-2E}}$-type pathways end in a biexciton population.

In the case of weak coupling, the transition dipole moments are

$$\begin{aligned}
\boldsymbol{\mu}_{20} &= \boldsymbol{\mu}_{\alpha 1}, \\
\boldsymbol{\mu}_{10} &= \boldsymbol{\mu}_{\alpha 2}.
\end{aligned} \tag{10.3}$$

If no EEA occurs in the system $\Phi = 2$ because the biexciton state consists of the excitation of two molecules which do not interact and so each molecule can emit a photon. In that case the diagrams cancel and no cross peak is visible which is the same case as in coherently detected 2D spectroscopy. As a next step we consider effective EEA but without substantial delocalization. In such a case the population in the biexciton state decreases via EEA and with that the value of Φ is decreased as well. For effective EEA the biexciton population relaxes completely to one of the single-exciton states and $\Phi = 1$. In that case the ESA$_{A,B\text{-1E}}$-type pathways and

ESA$_{\text{A,B-2E}}$-type pathways have the same amplitude but opposite sign and cancel each other and the GSB-type diagrams are still contributing to peak A and peak B. Both cross peaks are visible in the 2D spectrum and have the same sign. Note that the annihilation occurs not during the population time T, since we restrict our analysis on $T = 0$, but occurs after preparation of the final state decreasing its yield.

In coherently detected 2D spectroscopy in the case of EEA without delocalization no cross peaks could be observed since EEA cannot occur during T for $T = 0$. In fluorescence-detected 2D spectroscopy such a situation results in cross peaks with the same sign in the 2D spectrum.

B. Coherently Detected Two-Dimensional Spectroscopy:
Decrease of the Diagonal Peaks by Energy transfer

As outlined in Section 5.2 energy transfer leads to the formation of cross peaks. Besides the formation of cross peaks, energy transfer also reduces the diagonal peak amplitude. Here, we consider energy transfer in a weakly coupled dimer with $\boldsymbol{\mu}_{10} = \boldsymbol{\mu}_{\alpha2}$ and $\boldsymbol{\mu}_{20} = \boldsymbol{\mu}_{\alpha1}$. In Section 5.2 we considered energy transfer from state $|2\rangle$ to state $|1\rangle$ resulting in a decrease of the diagonal peak 2. In the case of energy transfer three different types of double-sided Feynman diagrams are contributing to the diagonal peak as shown in Fig. B.2.

The influence of the energy transfer on the double-sided Feynman diagrams can be described by two propagators. The first propagator $\mathscr{U}_{22,22}$ describes the decrease of the population in state $|2\rangle$ by energy transfer. This propagator can be written as

$$\mathscr{U}_{22,22} = e^{-k_T T}, \tag{10.4}$$

with the transfer rate k_T. The second propagator $U_{11,22}$ reflects transfer from state $|2\rangle$ to state $|1\rangle$ resulting in a rise of the ESA-type pathways with the energy transfer. The propagator is

$$\mathscr{U}_{11,22} = 1 - e^{-k_T T}. \tag{10.5}$$

For $T > 0$ the emerging ESA-type pathways will cancel partially with the GSB-type and SE-type pathways. The diagonal peak amplitude decreases in comparison to the initial amplitude at $T = 0$. For effective energy transfer and $T \gg 0$ the SE-type pathways amplitude is zero and the ESA-type and GSB-type pathways cancel each other.
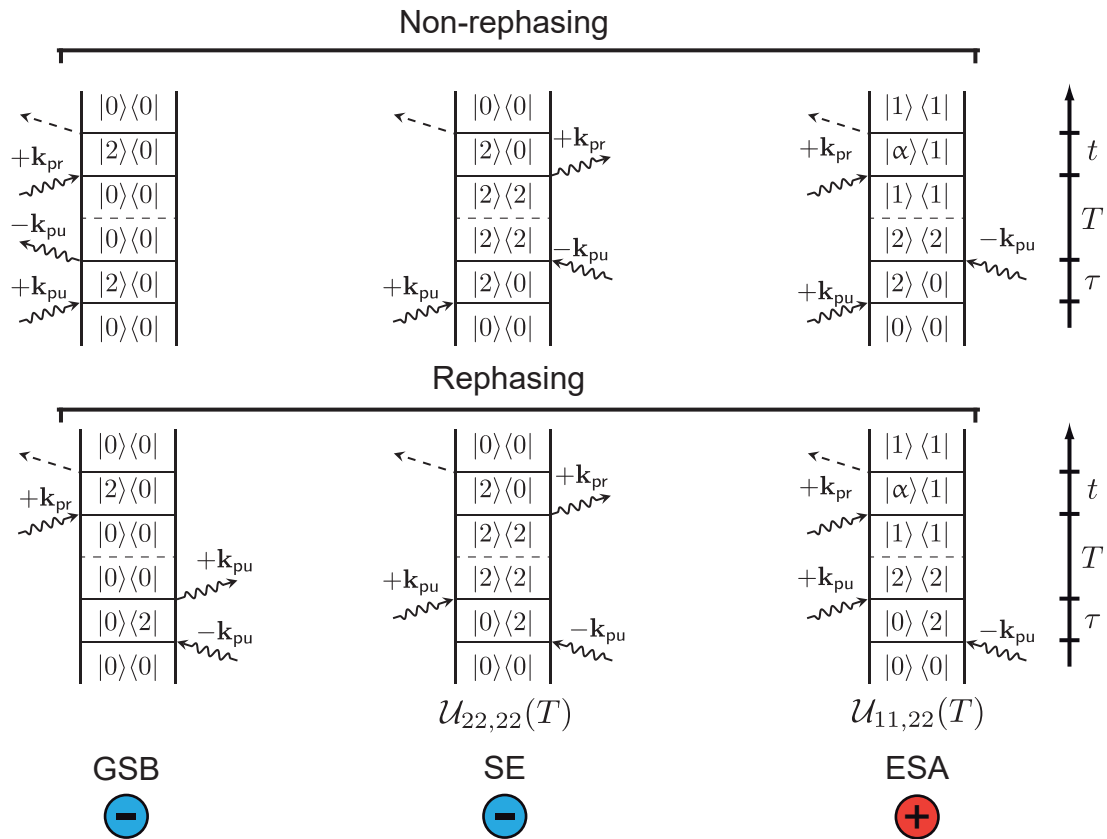
Figure B.2.: Description of a diagonal peak by double-sided Feynman diagrams and the influence of energy transfer on the diagonal peak. Three different types of diagrams are contributing. The GSB-type diagrams are not influenced by the energy transfer, while for the ESA-type and SE-type diagrams the energy transfer is reflected by specific propagators indicated below the corresponding diagrams.

List of Abbreviations

1Q	one-quantum
2D	two-dimensional
2DES	two-dimensional electronic spectroscopy
2Q	two-quantum
3Q	three-quantum
AOM	acousto-optic modulator
AOPDF	acousto-optic progammable dispersive filter
APD	avalanche photodiode
EEA	exciton–exciton annihilation
EEI	exciton–exciton interaction
ESA	excited-state absorption
EV	electronic–vibrational
FMO	Fenna–Matthews–Olson
FROG	frequency-resolved optical gating
GSB	ground-state bleach
IC	internal conversion
LHCII	light-harvesting complex II
LH2	light-harvesting 2
LO	local oscillator
PEEM	photoemission electron microscopy
PP	pump–probe
PMT	photomultiplier tube
RWA	rotating-wave approximation
SE	stimulated emission
SNR	signal-to-noise ratio
TA	transient absorption
VE	vibrational–electronic

Bibliography

[1] D. Raanan, J. Lüttig, Y. Silberberg, and D. Oron.
Vibrational spectroscopy via stimulated Raman induced Kerr lensing.
APL Photonics **3**, 092501 (2018).

[2] B. Huber, M. Hensen, S. Pres, V. Lisinetskii, J. Lüttig, E. Wittmann, E. Krauss,
D. Friedrich, B. Hecht, E. Riedle, and T. Brixner.
*Time-resolved photoemission electron microscopy of a plasmonic slit resonator
using 1 MHz, 25 fs, UV-to-NIR-tunable pulses.*
EPJ Web Conf. **205**, 08002 (2019).

[3] M. Hensen, B. Huber, D. Friedrich, E. Krauss, S. Pres, P. Grimm, D. Fersch,
J. Lüttig, V. Lisinetskii, B. Hecht, and T. Brixner.
Spatial variations in femtosecond field dynamics within a plasmonic nanoresonator mode.
Nano Lett. **19**, 4651–4658 (2019).

[4] B. Kriete, J. Lüttig, T. Kunsel, P. Malý, T. L. C. Jansen, J. Knoester, T. Brixner,
and M. S. Pshenichnikov.
*Interplay between structural hierarchy and exciton diffusion in artificial light
harvesting.*
Nat. Commun. **10**, 4615 (2019).

[5] S. Mueller, J. Lüttig, P. Malý, L. Ji, J. Han, M. Moos, T. B. Marder, U. H. F.
Bunz, A. Dreuw, C. Lambert, and T. Brixner.
*Rapid multiple-quantum three-dimensional fluorescence spectroscopy disentangles
quantum pathways.*
Nat. Commun. **10**, 4735 (2019).

[6] B. Huber, S. Pres, E. Wittmann, L. Dietrich, J. Lüttig, D. Fersch, E. Krauss,
D. Friedrich, J. Kern, V. Lisinetskii, M. Hensen, B. Hecht, R. Bratschitsch,
E. Riedle, and T. Brixner.
*Space- and time-resolved UV-to-NIR surface spectroscopy and 2D nanoscopy at
1 MHz repetition rate.*
Rev. Sci. Instrum. **90**, 113103 (2019).

[7] P. Malý, J. Lüttig, A. Turkin, J. Dostál, C. Lambert, and T. Brixner.
*From wavelike to sub-diffusive motion: Exciton dynamics and interaction in
squaraine copolymers of varying length.*
Chem. Sci. **11**, 456–466 (2020).

[8] P. Malý, J. Lüttig, S. Mueller, M. H. Schreck, C. Lambert, and T. Brixner.
Coherently and fluorescence-detected two-dimensional electronic spectroscopy: Direct comparison on squaraine dimers.
Phys. Chem. Chem. Phys. **22**, 21222–21237 (2020).

[9] P. Malý, S. Mueller, J. Lüttig, C. Lambert, and T. Brixner.
Signatures of exciton dynamics and interaction in coherently and fluorescence-detected four- and six-wave-mixing two-dimensional electronic spectroscopy.
J. Chem. Phys. **153**, 144204 (2020).

[10] J. Lüttig, P. Malý, A. Turkin, K. Mayershofer, S. Büttner, C. Lambert, and T. Brixner.
Probing exciton transport in squaraine polymers using fifth-order two-dimensional spectroscopy.
The 22nd International Conference on Ultrafast Phenomena 2020, F. Kärtner, M. Khalil, R. Li, F. Légaré, and T. Tahara, eds., OSA Technical digest (Optical Society of America, 2020), paper Th2A.3 (2020).

[11] P. Malý, S. Müller, J. Lüttig, M. Schreck, C. Lambert, and T. Brixner.
Coherently and fluorescence-detected four- and six-wave-mixing two-dimensional electronic spectroscopy: Measuring multi-exciton dynamics and delocalization.
The 22nd International Conference on Ultrafast Phenomena 2020, F. Kärtner, M. Khalil, R. Li, F. Légaré, and T. Tahara, eds., OSA Technical digest (Optical Society of America, 2020), paper Tu4A.4 (2020).

[12] J. Lüttig, T. Brixner, and P. Malý.
Anisotropy in fifth-order exciton–exciton-interaction two-dimensional spectroscopy.
J. Chem. Phys. **154**, 154202 (2021).

[13] S. Mueller, J. Lüttig, L. Brenneis, D. Oron, and T. Brixner.
Observing multiexciton correlations in colloidal semiconductor quantum dots via multiple-quantum two-dimensional fluorescence spectroscopy.
ACS Nano **15**, 4647–4657 (2021).

[14] P. Malý, J. Lüttig, P. A. Rose, A. Turkin, C. Lambert, J. J. Krich, and T. Brixner.
Highly nonlinear transient absorption spectroscopy.
The International Conference on Ultrafast Phenomena (UP) 2022, F. Légaré, T. Tahara, J. Biegert, T. Brixner, and N. Dudovich, eds., Technical Digest Series (Optica Publishing Group, 2022), paper W2A.6 (2022).

[15] P. A. Rose, J. Lüttig, P. Malý, T. Brixner, and J. J. Krich.
Isolating nonlinear orders of transient grating spectra from a single 2D spectrum.

The International Conference on Ultrafast Phenomena (UP) 2022, F. Légaré, T. Tahara, J. Biegert, T. Brixner, and N. Dudovich, eds., Technical Digest Series (Optica Publishing Group, 2022), paper Th4A.14 (2022).

[16] P. Malý, J. Lüttig, P. A. Rose, A. Turkin, C. Lambert, J. J. Krich, and T. Brixner.
Separating single- from multi-particle dynamics in nonlinear spectroscopy.
submitted (2018).

[17] J. Lüttig, P. Malý, S. Mueller, and T. Brixner.
High-order multidimensional and pump–probe spectroscopy.
in preperation (2022).

[18] J. Lüttig, P. Malý, P. A. Rose, A. Turkin, M. Bühler, C. Lambert, J. J. Krich, and T. Brixner.
High-order pump–probe and high-order two-dimensional spectroscopy on the example of squaraine oligomers.
in preperation (2022).

[19] R. Rouxel, J. Lüttig, M. R. Jones, and D. Zigmantas.
Tracking light harvesting in purple bacteria in vivo.
in preperation (2022).

[20] J. Dostál, F. Fennel, F. Koch, S. Herbst, F. Würthner, and T. Brixner.
Direct observation of exciton–exciton interactions.
Nat. Commun. **9**, 2466 (2018).

[21] T. W. Engelmann.
Neue Methode zur Untersuchung der Sauerstoffausscheidung pflanzlicher und thierischer Organismen.
Pflüger Arch. **25**, 285–292 (1881).

[22] T. W. Engelmann.
Ueber Sauerstoffausscheidung von Pflanzenzellen im Mikrospektrum.
Pflüger Arch. **27**, 485–489 (1882).

[23] P. Hamm and M. Zanni.
Concepts and methods of 2D infrared spectroscopy.
First edition. Cambridge University Press, New York (2011).

[24] L. Valkunas, D. Abramavičius, and T. Mančal.
Molecular excitation dynamics and relaxation.
First edition. Wiley-VCH, Weinheim (2013).

[25] S. Mukamel.
Principles of nonlinear optical spectroscopy.
First edition. Oxford University Press, New York (1995).

[26] H.-S. Tan.
Theory and phase-cycling scheme selection principles of collinear phase coherent multi-dimensional optical spectroscopy.
J. Chem. Phys. **129**, 124501 (2008).

[27] J. Seibt and T. Pullerits.
Beating signals in 2D spectroscopy: Electronic or nuclear coherences? Application to a quantum dot model system.
J. Phys. Chem. C **117**, 18728–18737 (2013).

[28] P. A. Rose and J. J. Krich.
Automatic Feynman diagram generation for nonlinear optical spectroscopies and application to fifth-order spectroscopy with pulse overlaps.
J. Chem. Phys. **154**, 034109 (2021).

[29] S. Mukamel.
Multidimensional femtosecond correlation spectroscopies of electronic and vibrational excitations.
Annu. Rev. Phys. Chem. **51**, 691–729 (2000).

[30] D. M. Jonas.
Two-dimensional femtosecond spectroscopy.
Annu. Rev. Phys. Chem. **54**, 425–463 (2003).

[31] R. M. Hochstrasser.
Two-dimensional spectroscopy at infrared and optical frequencies.
PNAS **104**, 14190–14196 (2007).

[32] M. Cho.
Coherent two-dimensional optical spectroscopy.
Chem. Rev. **108**, 1331–1418 (2008).

[33] M. Cho.
Two-Dimensional Optical Spectroscopy.
First edition. CRC Press, Boca Raton (2009).

[34] S. Biswas, J. Kim, X. Zhang, and G. D. Scholes.
Coherent two-dimensional and broadband electronic spectroscopies.
Chem. Rev. **122**, 4257–4321 (2022).

[35] C. Y. Wong and G. D. Scholes.
Biexcitonic fine structure of CdSe nanocrystals probed by polarization-dependent two-dimensional photon echo spectroscopy.
J. Phys. Chem. A **115**, 3797–3806 (2011).

[36] W. Kuehn, K. Reimann, M. Woerner, T. Elsaesser, and R. Hey.

Two-dimensional terahertz correlation spectra of electronic excitations in semiconductor quantum wells.
J. Phys. Chem. B **115**, 5448–5455 (2011).

[37] L. Bruder, U. Bangert, M. Binz, D. Uhl, R. Vexiau, N. Bouloufa-Maafa, O. Dulieu, and F. Stienkemeier.
Coherent multidimensional spectroscopy of dilute gas-phase nanosystems.
Nat. Commun. **9**, 4823 (2018).

[38] J. Paul, C. E. Stevens, R. P. Smith, P. Dey, V. Mapara, D. Semenov, S. A. McGill, R. A. Kaindl, D. J. Hilton, and D. Karaiskaj.
Coherent two-dimensional Fourier transform spectroscopy using a 25 Tesla resistive magnet.
Rev. Sci. Instrum. **90**, 063901 (2019).

[39] J. Dostál, F. Vácha, J. Pšenčík, and D. Zigmantas.
2D electronic spectroscopy reveals excitonic structure in the baseplate of a chlorosome.
J. Phys. Chem. Lett. **5**, 1743–1747 (2014).

[40] M. Son, S. M. Hart, and G. S. Schlau-Cohen.
Investigating carotenoid photophysics in photosynthesis with 2D electronic spectroscopy.
Trends. Chem. **3**, 733–746 (2021).

[41] Y. Song, R. Sechrist, H. H. Nguyen, W. Johnson, D. Abramavičius, K. E. Redding, and J. P. Ogilvie.
Excitonic structure and charge separation in the heliobacterial reaction center probed by multispectral multidimensional spectroscopy.
Nat. Commun. **12**, 2801 (2021).

[42] T. N. Do, H. L. Nguyen, P. Akhtar, K. Zhong, T. L. C. Jansen, J. Knoester, S. Caffarri, P. H. Lambrev, and H.-S. Tan.
Ultrafast Excitation Energy Transfer Dynamics in the LHCII–CP29–CP24 Subdomain of Plant Photosystem II.
J. Phys. Chem. Lett. **13**, 4263–4271 (2022).

[43] J. Lim, D. Paleček, F. Caycedo-Soler, C. N. Lincoln, J. Prior, H. von Berlepsch, S. F. Huelga, M. B. Plenio, D. Zigmantas, and J. Hauer.
Vibronic origin of long-lived coherence in an artificial molecular light harvester.
Nat. Commun. **6**, 7755 (2015).

[44] A. Mandal, M. Chen, E. D. Foszcz, J. D. Schultz, N. M. Kearns, R. M. Young, M. T. Zanni, and M. R. Wasielewski.
Two-dimensional electronic spectroscopy reveals excitation energy-dependent state mixing during singlet fission in a Terrylenediimide dimer.
J. Am. Chem. Soc. **140**, 17907–17914 (2018).

[45] S. Mueller and T. Brixner.
Molecular coherent three-quantum two-dimensional fluorescence spectroscopy.
J. Phys. Chem. Lett. **11**, 5139–5147 (2020).

[46] D. V. Le, J. M. de la Perrelle, T. N. Do, X. Leng, P. C. Tapping, G. D. Scholes, T. W. Kee, and H.-S. Tan.
Characterization of the ultrafast spectral diffusion and vibronic coherence of TIPS-pentacene using 2D electronic spectroscopy.
J. Chem. Phys. **155**, 014302 (2021).

[47] T. Brixner, J. Stenger, H. M. Vaswani, M. Cho, R. E. Blankenship, and G. R. Fleming.
Two-dimensional spectroscopy of electronic couplings in photosynthesis.
Nature **434**, 625–628 (2005).

[48] P. Nuernberger, S. Ruetzel, and T. Brixner.
Multidimensional electronic spectroscopy of photochemical reactions.
Angew. Chem. Int. Ed. **54**, 11368–11386 (2015).

[49] T. M. Autry, G. Nardin, C. L. Smallwood, K. Silverman, D. Bajoni, A. Lemaître, S. Bouchoule, J. Bloch, and S. Cundiff.
Excitation ladder of cavity polaritons.
Phys. Rev. Lett. **125**, 067403 (2020).

[50] M. Chachisvilis, O. Kühn, T. Pullerits, and V. Sundström.
Excitons in photosynthetic purple bacteria: wavelike motion or incoherent hopping?
J. Phys. Chem. B **101**, 7275–7283 (1997).

[51] G. Cerullo, D. Polli, G. Lanzani, S. De Silvestri, H. Hashimoto, and R. J. Cogdell.
Photosynthetic light harvesting by carotenoids: Detection of an intermediate excited state.
Science **298**, 2395–2398 (2002).

[52] R. Berera, R. van Grondelle, and J. T. M. Kennis.
Ultrafast transient absorption spectroscopy: Principles and application to photosynthetic systems.
Photosynth. Res. **101**, 105–118 (2009).

[53] G. Grancini, D. Polli, D. Fazzi, J. Cabanillas-Gonzalez, G. Cerullo, and G. Lanzani.
Transient absorption imaging of P3HT:PCBM photovoltaic blend: Evidence for interfacial charge transfer state.
J. Phys. Chem. Lett. **2**, 1099–1105 (2011).

[54] J. Cabanillas-Gonzalez, G. Grancini, and G. Lanzani.
Pump-probe spectroscopy in organic semiconductors: Monitoring fundamental processes of relevance in optoelectronics.
Adv. Mater. **23**, 5468–5485 (2011).

[55] A. L. Tong, O. C. Fiebig, M. Nairat, D. Harris, M. Giansily, A. Chenu, J. N. Sturgis, and G. S. Schlau-Cohen.
Comparison of the energy-transfer rates in structural and spectral variants of the B800–850 complex from purple bacteria.
J. Phys. Chem. B **124**, 1460–1469 (2020).

[56] H. Y. Chung, J.-H. Park, J. Cui, S.-Y. Kim, J. Oh, D. Kim, and S. Y. Park.
Influence of intramolecular charge-transfer characteristics of excitons on polaron generation at the donor/acceptor interface in polymer solar cells.
J. Phys. Chem. C **125**, 18352–18361 (2021).

[57] L. Ji, S. Riese, A. Schmiedel, M. Holzapfel, M. Fest, J. Nitsch, B. F. E. Curchod, A. Friedrich, L. Wu, H. H. A. Mamari, S. Hammer, J. Pflaum, M. A. Fox, D. J. Tozer, M. Finze, C. Lambert, and T. B. Marder.
Thermodynamic equilibrium between locally excited and charge-transfer states through thermally activated charge transfer in 1-(pyren-2′-yl)-o-carborane.
Chem. Sci. **13**, 5205–5219 (2022).

[58] D. Polli, P. Altoe, O. Weingart, K. M. Spillane, C. Manzoni, D. Brida, G. Tomasello, G. Orlandi, P. Kukura, R. A. Mathies, M. Garavelli, and G. Cerullo.
Conical intersection dynamics of the primary photoisomerization event in vision.
Nature **467**, 440–443 (2010).

[59] F. Kanal.
Femtosecond Transient Absorption Spectroscopy – Technical Improvements and Applications to Ultrafast Molecular Phenomena.
Ph.D. thesis. Universität Würzburg, Würzburg, (2015).

[60] I. H. M. van Stokkum, D. S. Larsen, and R. van Grondelle.
Global and target analysis of time-resolved spectra.
Biochim. Biophys. Acta - Bioenerg. **1657**, 82–104 (2004).

[61] R. E. Blankenship.
Molecular mechanisms of photosynthesis.
Second edition. Wiley Blackwell, Chichester (2014).

[62] E. Thyrhaug, K. Žídek, J. Dostál, D. Bína, and D. Zigmantas.
Exciton structure and energy transfer in the Fenna–Matthews–Olson complex.
J. Phys. Chem. Lett. **7**, 1653–1660 (2016).

[63] Y. Tanimura and S. Mukamel.
      Two-dimensional femtosecond vibrational spectroscopy of liquids.
      J. Chem. Phys. **99**, 9496–9511 (1993).

[64] W. P. Aue, E. Bartholdi, and R. R. Ernst.
      Two-dimensional spectroscopy. Application to nuclear magnetic resonance.
      J. Chem. Phys. **64**, 2229–2246 (1976).

[65] L. Lepetit and M. Joffre.
      Two-dimensional nonlinear optics using Fourier-transform spectral interferometry.
      Opt. Lett. **21**, 564–566 (1996).

[66] J. D. Hybl, A. W. Albrecht, S. M. Gallagher Faeder, and D. M. Jonas.
      Two-dimensional electronic spectroscopy.
      Chem. Phys. Lett. **297**, 307–313 (1998).

[67] P. Hamm, M. Lim, and R. M. Hochstrasser.
      *Structure of the amide I band of peptides measured by femtosecond nonlinear-
      infrared spectroscopy.*
      J. Phys. Chem. B **102**, 6123–6138 (1998).

[68] S. Mukamel, D. Healion, Y. Zhang, and J. D. Biggs.
      *Multidimensional attosecond resonant X-ray spectroscopy of molecules: Lessons
      from the optical regime.*
      Annu. Rev. Phys. Chem. **64**, 101–127 (2013).

[69] U. Selig, C.-F. Schleussner, M. Foerster, F. Langhojer, P. Nuernberger, and
      T. Brixner.
      Coherent two-dimensional ultraviolet spectroscopy in fully noncollinear geometry.
      Opt. Lett. **35**, 4178–4180 (2010).

[70] C. Consani, G. Auböck, F. van Mourik, and M. Chergui.
      *Ultrafast tryptophan-to-heme electron transfer in myoglobins revealed by UV 2D
      spectroscopy.*
      Science **339**, 1586–1589 (2013).

[71] T. Brixner, T. Mančal, I. V. Stiopkin, and G. R. Fleming.
      Phase-stabilized two-dimensional electronic spectroscopy.
      J. Chem. Phys. **121**, 4221–4236 (2004).

[72] M. L. Cowan, J. P. Ogilvie, and R. J. D. Miller.
      *Two-dimensional spectroscopy using diffractive optics based phased-locked photon
      echoes.*
      Chem. Phys. Lett. **386**, 184–189 (2004).

[73] S.-H. Shim and M. T. Zanni.
How to turn your pump–probe instrument into a multidimensional spectrometer:
2D IR and VIS spectroscopies via pulse shaping.
Phys. Chem. Chem. Phys. **11**, 748–761 (2009).

[74] V. Volkov, R. Schanz, and P. Hamm.
Active phase stabilization in Fourier-transform two-dimensional infrared spec-
troscopy.
Opt. Lett. **30**, 2010–2012 (2005).

[75] A. D. Bristow, D. Karaiskaj, X. Dai, T. Zhang, C. Carlsson, K. R. Hagen,
R. Jimenez, and S. T. Cundiff.
A versatile ultrastable platform for optical multidimensional Fourier-transform
spectroscopy.
Rev. Sci. Instrum. **80**, 073108 (2009).

[76] O. Bixner, V. Lukeš, T. Mančal, J. Hauer, F. Milota, M. Fischer, I. Pugliesi,
M. Bradler, W. Schmid, E. Riedle, H. F. Kauffmann, and N. Christensson.
Ultrafast photo-induced charge transfer unveiled by two-dimensional electronic
spectroscopy.
J. Chem. Phys. **136**, 204503 (2012).

[77] M. Cho, T. Brixner, I. Stiopkin, H. Vaswani, and G. R. Fleming.
Two dimensional electronic spectroscopy of molecular complexes.
J. Chin. Chem. Soc. **53**, 15–24 (2006).

[78] J. Dostál, B. Benešová, and T. Brixner.
Two-dimensional electronic spectroscopy can fully characterize the population
transfer in molecular systems.
J. Chem. Phys. **145**, 124312 (2016).

[79] J. Dostál, J. Pšenčík, and D. Zigmantas.
In situ mapping of the energy flow through the entire photosynthetic apparatus.
Nat. Chem. **8**, 705–710 (2016).

[80] N. S. Ginsberg, Y.-C. Cheng, and G. R. Fleming.
Two-dimensional electronic spectroscopy of molecular aggregates.
Acc. Chem. Res. **42**, 1352–1363 (2009).

[81] M. E. Siemens, G. Moody, H. Li, A. D. Bristow, and S. T. Cundiff.
Resonance lineshapes in two-dimensional Fourier transform spectroscopy.
Opt. Express **18**, 17699–17708 (2010).

[82] M. Ferretti, V. I. Novoderezhkin, E. Romero, R. Augulis, A. Pandit, D. Zigman-
tas, and R. van Grondelle.
The nature of coherences in the B820 bacteriochlorophyll dimer revealed by two-
dimensional electronic spectroscopy.

Phys. Chem. Chem. Phys. **16**, 9930–9939 (2014).

[83] V. Butkus, J. Alster, E. Bašinskaitė, R. Augulis, P. Neuhaus, L. Valkunas, H. L. Anderson, D. Abramavičius, and D. Zigmantas.
Discrimination of diverse coherences allows identification of electronic transitions of a molecular nanoring.
J. Phys. Chem. Lett. **8**, 2344–2349 (2017).

[84] D. B. Turner, Y. Hassan, and G. D. Scholes.
Exciton superposition states in CdSe nanocrystals measured using broadband two-dimensional electronic spectroscopy.
Nano Lett. **12**, 880–886 (2012).

[85] P. Tian, D. Keusters, Y. Suzaki, and W. S. Warren.
Femtosecond phase-coherent two-dimensional spectroscopy.
Science **300**, 1553–1555 (2003).

[86] W. Wagner, C. Li, J. Semmlow, and W. Warren.
Rapid phase-cycled two-dimensional optical spectroscopy in fluorescence and transmission mode.
Opt. Express **13**, 3697–3706 (2005).

[87] R. Augulis and D. Zigmantas.
Two-dimensional electronic spectroscopy with double modulation lock-in detection: Enhancement of sensitivity and noise resistance.
Opt. Express **19**, 13126–13133 (2011).

[88] M. Son, S. Mosquera-Vázquez, and G. S. Schlau-Cohen.
Ultrabroadband 2D electronic spectroscopy with high-speed, shot-to-shot detection.
Opt. Express **25**, 18950–18962 (2017).

[89] S. Draeger, S. Roeding, and T. Brixner.
Rapid-scan coherent 2D fluorescence spectroscopy.
Opt. Express **25**, 3259–3267 (2017).

[90] H. Seiler, S. Palato, and P. Kambhampati.
Coherent multi-dimensional spectroscopy at optical frequencies in a single beam with optical readout.
J. Chem. Phys. **147**, 094203 (2017).

[91] S. Roeding and T. Brixner.
Coherent two-dimensional electronic mass spectrometry.
Nat. Commun. **9**, 2519 (2018).

[92] L. P. DeFlores, R. A. Nicodemus, and A. Tokmakoff.
Two-dimensional Fourier transform spectroscopy in the pump-probe geometry.

Opt. Lett. **32**, 2966–2968 (2007).

[93] P. F. Tekavec, J. A. Myers, K. L. M. Lewis, and J. P. Ogilvie.
Two-dimensional electronic spectroscopy with a continuum probe.
Opt. Lett. **34**, 1390–1392 (2009).

[94] W. Zhu, R. Wang, C. Zhang, G. Wang, Y. Liu, W. Zhao, X. Dai, X. Wang,
G. Cerullo, S. Cundiff, and M. Xiao.
*Broadband two-dimensional electronic spectroscopy in an actively phase stabilized
pump-probe configuration.*
Opt. Express **25**, 21115–21126 (2017).

[95] M. Khalil, N. Demirdöven, and A. Tokmakoff.
Coherent 2D IR spectroscopy: Molecular structure and dynamics in solution.
J. Phys. Chem. A **107**, 5258–5279 (2003).

[96] F. Milota, C. N. Lincoln, and J. Hauer.
*Precise phasing of 2D-electronic spectra in a fully non-collinear phase-matching
geometry.*
Opt. Express **21**, 15904 (2013).

[97] A. Zilian and J. C. Wright.
Polarization effects in four-wave mixing of isotropic samples.
Mol. Phys. **87**, 1261–1271 (1996).

[98] R. M. Hochstrasser.
Two-dimensional IR-spectroscopy: Polarization anisotropy effects.
Chem. Phys. **266**, 273–284 (2001).

[99] S. Westenhoff, D. Paleček, P. Edlund, P. Smith, and D. Zigmantas.
Coherent picosecond exciton dynamics in a photosynthetic reaction center.
J. Am. Chem. Soc. **134**, 16484–16487 (2012).

[100] J. D. Hybl, A. Albrecht Ferro, and D. M. Jonas.
Two-dimensional Fourier transform electronic spectroscopy.
J. Chem. Phys. **115**, 6606 (2001).

[101] G. S. Engel, T. R. Calhoun, E. L. Read, T.-K. Ahn, T. Mančal, Y.-C. Cheng,
R. E. Blankenship, and G. R. Fleming.
*Evidence for wavelike energy transfer through quantum coherence in photosyn-
thetic systems.*
Nature **446**, 782–786 (2007).

[102] G. Panitchayangkoon, D. Hayes, K. A. Fransted, J. R. Caram, E. Harel, J. Wen,
R. E. Blankenship, and G. S. Engel.
*Long-lived quantum coherence in photosynthetic complexes at physiological tem-
perature.*

PNAS **107**, 12766–12770 (2010).

[103] E. Collini, C. Y. Wong, K. E. Wilk, P. M. G. Curmi, P. Brumer, and G. D. Scholes.
Coherently wired light-harvesting in photosynthetic marine algae at ambient temperature.
Nature **463**, 644–647 (2010).

[104] J. Cao, R. J. Cogdell, D. F. Coker, H.-G. Duan, J. Hauer, U. Kleinekathöfer, T. L. C. Jansen, T. Mančal, R. J. D. Miller, J. P. Ogilvie, V. I. Prokhorenko, T. Renger, H.-S. Tan, R. Tempelaar, M. Thorwart, E. Thyrhaug, S. Westenhoff, and D. Zigmantas.
Quantum biology revisited.
Sci. Adv. **6**, eaaz4888 (2020).

[105] E. Thyrhaug, R. Tempelaar, M. J. P. Alcocer, K. Žídek, D. Bína, J. Knoester, T. L. C. Jansen, and D. Zigmantas.
Identification and characterization of diverse coherences in the Fenna–Matthews–Olson complex.
Nat. Chem. **10**, 780–786 (2018).

[106] D. G. Oblinsky, E. E. Ostroumov, and G. D. Scholes.
Drop-in two-dimensional electronic spectroscopy based on dual modulation in the pump-probe geometry.
Opt. Lett. **44**, 2653 (2019).

[107] J. A. Myers, K. L. Lewis, P. F. Tekavec, and J. P. Ogilvie.
Two-color two-dimensional Fourier transform electronic spectroscopy with a pulse-shaper.
Opt. Express **16**, 17420–17428 (2008).

[108] Z. Zhang, K. L. Wells, E. W. J. Hyland, and H.-S. Tan.
Phase-cycling schemes for pump–probe beam geometry two-dimensional electronic spectroscopy.
Chem. Phys. Lett. **550**, 156–161 (2012).

[109] D. Uhl, U. Bangert, L. Bruder, and F. Stienkemeier.
Coherent optical 2D photoelectron spectroscopy.
Optica **8**, 1316–1324 (2021).

[110] P. F. Tekavec, T. R. Dyke, and A. H. Marcus.
Wave packet interferometry and quantum state reconstruction by acousto-optic phase modulation.
J. Chem. Phys. **125**, 194303 (2006).

[111] P. F. Tekavec, G. A. Lott, and A. H. Marcus.

Fluorescence-detected two-dimensional electronic coherence spectroscopy by acousto-optic phase modulation.
J. Chem. Phys. **127**, 214307 (2007).

[112] A. A. Bakulin, C. Silva, and E. Vella.
Ultrafast spectroscopy with photocurrent detection: Watching excitonic optoelectronic systems at work.
J. Phys. Chem. Lett. **7**, 250–258 (2016).

[113] A. K. De, D. Monahan, J. M. Dawlaty, and G. R. Fleming.
Two-dimensional fluorescence-detected coherent spectroscopy with absolute phasing by confocal imaging of a dynamic grating and 27-step phase-cycling.
J. Chem. Phys. **140**, 194201 (2014).

[114] S. Mueller, S. Draeger, X. Ma, M. Hensen, T. Kenneweg, W. Pfeiffer, and T. Brixner.
Fluorescence-detected two-quantum and one-quantum–two-quantum 2D electronic spectroscopy.
J. Phys. Chem. Lett. **9**, 1964–1969 (2018).

[115] K. M. Farrell, J. S. Ostrander, A. C. Jones, B. R. Yakami, S. S. Dicke, C. T. Middleton, P. Hamm, and M. T. Zanni.
Shot-to-shot 2D IR spectroscopy at 100 kHz using a Yb laser and custom-designed electronics.
Opt. Express **28**, 33584 (2020).

[116] V. Tiwari, Y. A. Matutes, A. Konar, Z. Yu, M. Ptaszek, D. F. Bocian, D. Holten, C. Kirmaier, and J. P. Ogilvie.
Strongly coupled bacteriochlorin dyad studied using phase-modulated fluorescence-detected two-dimensional electronic spectroscopy.
Opt. Express **26**, 22327–22341 (2018).

[117] V. Tiwari.
Multidimensional electronic spectroscopy in high-definition—Combining spectral, temporal, and spatial resolutions.
J. Chem. Phys. **154**, 230901 (2021).

[118] D. Agathangelou, A. Javed, F. Sessa, X. Solinas, M. Joffre, and J. P. Ogilvie.
Phase-modulated rapid-scanning fluorescence-detected two-dimensional electronic spectroscopy.
J. Chem. Phys. **155**, 094201 (2021).

[119] G. Nardin, T. M. Autry, K. L. Silverman, and S. T. Cundiff.
Multidimensional coherent photocurrent spectroscopy of a semiconductor nanostructure.
Opt. Express **21**, 28617–28627 (2013).

[120] P. Malý and T. Mančal.
Signatures of exciton delocalization and exciton–exciton annihilation in fluorescence-detected two-dimensional coherent spectroscopy.
J. Phys. Chem. Lett. **9**, 5654–5659 (2018).

[121] T. Kunsel, V. Tiwari, Y. A. Matutes, A. T. Gardiner, R. J. Cogdell, J. P. Ogilvie, and T. L. C. Jansen.
Simulating fluorescence-detected two-dimensional electronic spectroscopy of multichromophoric systems.
J. Phys. Chem. B **123**, 394–406 (2019).

[122] O. Kühn, T. Mančal, and T. Pullerits.
Interpreting fluorescence detected two-dimensional electronic spectroscopy.
J. Phys. Chem. Lett. **11**, 838–842 (2020).

[123] A. V. Pisliakov, T. Mančal, and G. R. Fleming.
Two-dimensional optical three-pulse photon echo spectroscopy. II. Signatures of coherent electronic motion and exciton population transfer in dimer two-dimensional spectra.
J. Chem. Phys. **124**, 234505 (2006).

[124] D. Paleček, P. Edlund, E. Gustavsson, S. Westenhoff, and D. Zigmantas.
Potential pitfalls of the early-time dynamics in two-dimensional electronic spectroscopy.
J. Chem. Phys. **151**, 024201 (2019).

[125] S. Pres, L. Kontschak, M. Hensen, and T. Brixner.
Coherent 2D electronic spectroscopy with complete characterization of excitation pulses during all scanning steps.
Opt. Express **29**, 4191–4209 (2021).

[126] S. Goetz, D. Li, V. Kolb, J. Pflaum, and T. Brixner.
Coherent two-dimensional fluorescence micro-spectroscopy.
Opt. Express **26**, 3915–3925 (2018).

[127] V. Tiwari, Y. A. Matutes, A. T. Gardiner, T. L. C. Jansen, R. J. Cogdell, and J. P. Ogilvie.
Spatially-resolved fluorescence-detected two-dimensional electronic spectroscopy probes varying excitonic structure in photosynthetic bacteria.
Nat. Commun. **9**, 4219 (2018).

[128] D. Li, C. Trovatello, S. Dal Conte, M. Nuß, G. Soavi, G. Wang, A. C. Ferrari, G. Cerullo, and T. Brixner.
Exciton–phonon coupling strength in single-layer MoSe₂ at room temperature.
Nat. Commun. **12**, 954 (2021).

[129] D. Li, H. Shan, C. Rupprecht, H. Knopf, K. Watanabe, T. Taniguchi, Y. Qin, S. Tongay, M. Nuß, S. Schröder, F. Eilenberger, S. Höfling, C. Schneider, and T. Brixner.
Hybridized exciton-photon-phonon states in a transition metal dichalcogenide van der waals heterostructure microcavity.
Phys. Rev. Lett. **128**, 087401 (2022).

[130] D. Li, E. Titov, M. Roedel, V. Kolb, S. Goetz, R. Mitric, J. Pflaum, and T. Brixner.
Correlating nanoscale optical coherence length and microscale topography in organic materials by coherent two-dimensional micro-spectroscopy.
Nano Lett. **20**, 6452–6458 (2020).

[131] A. C. Jones, N. M. Kearns, M. Bohlmann Kunz, J. T. Flach, and M. T. Zanni.
Multidimensional spectroscopy on the microscale: Development of a multimodal imaging system incorporating 2D white-light spectroscopy, broadband transient absorption, and atomic force microscopy.
J. Phys. Chem. A **123**, 10824–10836 (2019).

[132] A. C. Jones, N. M. Kearns, J.-J. Ho, J. T. Flach, and M. T. Zanni.
Impact of non-equilibrium molecular packings on singlet fission in microcrystals observed using 2D white-light microscopy.
Nat. Chem. **12**, 40–47 (2020).

[133] M. Aeschlimann, T. Brixner, A. Fischer, C. Kramer, P. Melchior, W. Pfeiffer, C. Schneider, C. Strüber, P. Tuchscherer, and D. V. Voronine.
Coherent two-dimensional nanoscopy.
Science **333**, 1723–1726 (2011).

[134] M. Aeschlimann, T. Brixner, D. Differt, U. Heinzmann, M. Hensen, C. Kramer, F. Lükermann, P. Melchior, W. Pfeiffer, M. Piecuch, C. Schneider, H. Stiebig, C. Strüber, and P. Thielen.
Perfect absorption in nanotextured thin films via Anderson-localized photon modes.
Nat. Photonics **9**, 663–668 (2015).

[135] M. Aeschlimann, T. Brixner, M. Cinchetti, M. Feidt, N. Haag, M. Hensen, B. Huber, T. Kenneweg, J. Kollamana, C. Kramer, W. Pfeiffer, S. Ponzoni, B. Stadtmüller, and P. Thielen.
Observation of optical coherence in a disordered metal-molecule interface by coherent optical two-dimensional photoelectron spectroscopy.
Phys. Rev. B **105**, 205415 (2022).

[136] E. Keil, P. Malevich, and J. Hauer.
Achromatic frequency doubling of supercontinuum pulses for transient absorption spectroscopy.

Opt. Express **29**, 39042–39054 (2021).

[137] L. Bruder, L. Bruder, L. Bruder, L. Wittenbecher, L. Wittenbecher, L. Wittenbecher, P. V. Kolesnichenko, P. V. Kolesnichenko, D. Zigmantas, and D. Zigmantas.
Generation and compression of 10-fs deep ultraviolet pulses at high repetition rate using standard optics.
Opt. Express **29**, 25593–25604 (2021).

[138] S. Günther, B. Kaulich, L. Gregoratti, and M. Kiskinova.
Photoelectron microscopy and applications in surface and materials science.
Prog. Surf. Sci. **70**, 187–260 (2002).

[139] N. M. Buckanie, J. Göhre, P. Zhou, D. von der Linde, M. H.-v. Hoegen, and F.-J. M. zu Heringdorf.
Space charge effects in photoemission electron microscopy using amplified femtosecond laser pulses.
J. Phys. Condens. Matter **21**, 314003 (2009).

[140] L. Wittenbecher, E. Viñas Boström, J. Vogelsang, S. Lehman, K. A. Dick, C. Verdozzi, D. Zigmantas, and A. Mikkelsen.
Unraveling the ultrafast hot electron dynamics in semiconductor nanowires.
ACS Nano **15**, 1133–1144 (2021).

[141] L. Bruder, U. Bangert, M. Binz, D. Uhl, and F. Stienkemeier.
Coherent multidimensional spectroscopy in the gas phase.
J. Phys. B: At. Mol. Opt. Phys. **52**, 183501 (2019).

[142] H.-P. Solowan, P. Malý, and T. Brixner.
Direct comparison of molecular-beam vs liquid-phase pump–probe and two-dimensional spectroscopy on the example of azulene.
J. Chem. Phys. **157**, 044201 (2022).

[143] H. Li, A. Gauthier-Houle, P. Grégoire, E. Vella, C. Silva-Acuña, and E. R. Bittner.
Probing polaron excitation spectra in organic semiconductors by photoinduced-absorption-detected two-dimensional coherent spectroscopy.
Chem. Phys. **481**, 281–286 (2016).

[144] K. J. Karki, J. R. Widom, J. Seibt, I. Moody, M. C. Lonergan, T. Pullerits, and A. H. Marcus.
Coherent two-dimensional photocurrent spectroscopy in a PbS quantum dot photocell.
Nat. Commun. **5**, 5869 (2014).

[145] J. Kim, J. Jeon, T. H. Yoon, and M. Cho.

Two-dimensional electronic spectroscopy of bacteriochlorophyll a with synchronized dual mode-locked lasers.
Nat. Commun. **11**, 6029 (2020).

[146] M. Cho.
Coherent nonlinear spectroscopy with multiple mode-locked lasers.
J. Phys. Chem. Lett. **12**, 10284–10294 (2021).

[147] B. Lomsadze and S. T. Cundiff.
Frequency combs enable rapid and high-resolution multidimensional coherent spectroscopy.
Science **357**, 1389–1391 (2017).

[148] B. Lomsadze and S. T. Cundiff.
Frequency-comb based double-quantum two-dimensional spectrum identifies collective hyperfine resonances in atomic vapor induced by dipole-dipole interactions.
Phys. Rev. Lett. **120** (2018).

[149] B. Lomsadze.
Frequency comb-based multidimensional coherent spectroscopy bridges the gap between fundamental science and cutting-edge technology.
J. Chem. Phys. **154**, 160901 (2021).

[150] B. Lomsadze, B. C. Smith, and S. T. Cundiff.
Tri-comb spectroscopy.
Nat. Photonics **12**, 676–680 (2018).

[151] X. Ma, J. Dostál, and T. Brixner.
Broadband 7-fs diffractive-optic-based 2D electronic spectroscopy using hollow-core fiber compression.
Opt. Express **24**, 20781–20791 (2016).

[152] A. A. Haddad, A. Chauvet, J. Ojeda, C. Arrell, F. van Mourik, G. Auböck, and M. Chergui.
Set-up for broadband Fourier-transform multidimensional electronic spectroscopy.
Opt. Lett. **40**, 312–315 (2015).

[153] R. Trebino.
Frequency-resolved optical gating: The measurement of ultrashort laser pulses.
First edition. Springer, New York (2002).

[154] M. Kasha.
Energy transfer mechanisms and the molecular exciton model for molecular aggregates.
Radiat. Res. **20**, 55–71 (1963).

[155] A. S. Davydov.
The theory of molecular excitons.
Sov. Phys. Usp. **7**, 145–178 (1964).

[156] M. Kasha, H. R. Rawls, and M. Ashraf El-Bayoumi.
The exciton model in molecular spectroscopy.
Pure Appl. Chem. **11**, 371–392 (1965).

[157] T. Brixner, R. Hildner, J. Köhler, C. Lambert, and F. Würthner.
Exciton transport in molecular aggregates – From natural antennas to synthetic chromophore systems.
Adv. Energy Mater. **7**, 1700236 (2017).

[158] J. Frenkel.
On the transformation of light into heat in solids. I.
Phys. Rev. **37**, 17–44 (1931).

[159] A. M. Brańczyk, D. B. Turner, and G. D. Scholes.
Crossing disciplines - A view on two-dimensional optical spectroscopy.
Ann. Phys. **526**, 31–49 (2014).

[160] M. I. S. Röhr, H. Marciniak, J. Hoche, M. H. Schreck, H. Ceymann, R. Mitric, and C. Lambert.
Exciton dynamics from strong to weak coupling limit illustrated on a series of squaraine dimers.
J. Phys. Chem. C **122**, 8082–8093 (2018).

[161] B. P. Krueger, G. D. Scholes, and G. R. Fleming.
Calculation of couplings and energy-transfer pathways between the pigments of LH2 by the ab initio transition density cube method.
J. Phys. Chem. B **102**, 5378–5386 (1998).

[162] M. E. Madjet, A. Abdurahman, and T. Renger.
Intermolecular Coulomb Couplings from Ab Initio Electrostatic Potentials: Application to Optical Transitions of Strongly Coupled Pigments in Photosynthetic Antennae and Reaction Centers.
J. Phys. Chem. B **110**, 17268–17281 (2006).

[163] N. J. Hestand and F. C. Spano.
Expanded theory of H- and J-molecular aggregates: The effects of vibronic coupling and intermolecular charge transfer.
Chem. Rev. **118**, 7069–7163 (2018).

[164] E. E. Jelley.
Spectral absorption and fluorescence of dyes in the molecular state.
Nature **138**, 1009–1010 (1936).

[165] G. Scheibe.
Reversible Polymerisation als Ursache neuartiger Absorptionsbanden von Farbstoffen.
Kolloid-Zeitschrift **82**, 1–14 (1938).

[166] W. Cooper.
Multiplet structure of aggregated states in 1,1′-diethyl-2,2′-cyanine dye.
Chem. Phys. Lett. **7**, 73–77 (1970).

[167] B. Kopainsky, J. K. Hallermeier, and W. Kaiser.
The first step of aggregation of PIC: The dimerization.
Chem. Phys. Lett. **83**, 498–502 (1981).

[168] F. C. Spano and C. Silva.
H- and J-aggregate behavior in polymeric semiconductors.
Annu. Rev. Phys. Chem. **65**, 477–500 (2014).

[169] Kawaguchi, Takeyuki and Iwata, Kaoru.
Merocyanine J aggregates: Formation and structural change on chemical and thermal treatments.
Thin Solid Films **191**, 173–191 (1990).

[170] L. Wolthaus, A. Schaper, and D. Möbius.
Brickstone arrangement in J-aggregates on an amphiphilic merocyanine dye.
Chem. Phys. Lett. **225**, 322–326 (1994).

[171] D. M. Eisele, D. H. Arias, X. Fu, E. A. Bloemsma, C. P. Steiner, R. A. Jensen, P. Rebentrost, H. Eisele, A. Tokmakoff, S. Lloyd, K. A. Nelson, D. Nicastro, J. Knoester, and M. G. Bawendi.
Robust excitons inhabit soft supramolecular nanotubes.
PNAS **111**, E3367–E3375 (2014).

[172] V. Grande, B. Soberats, S. Herbst, V. Stepanenko, and F. Würthner.
Hydrogen-bonded perylene bisimide J-aggregate aqua material.
Chem. Sci. **9**, 6904–6911 (2018).

[173] M. Hecht and F. Würthner.
Supramolecularly engineered J-aggregates based on perylene bisimide dyes.
Acc. Chem. Res. **54**, 642–653 (2021).

[174] M. J. Ahrens, L. E. Sinks, B. Rybtchinski, W. Liu, B. A. Jones, J. M. Giaimo, A. V. Gusev, A. J. Goshe, D. M. Tiede, and M. R. Wasielewski.
Self-assembly of supramolecular light-harvesting arrays from covalent multichromophore perylene-3,4:9,10-bis(dicarboximide) building blocks.
J. Am. Chem. Soc. **126**, 8284–8294 (2004).

[175] F. C. Spano.
Analysis of the UV/Vis and CD spectral line shapes of carotenoid assemblies: Spectral signatures of chiral H-aggregates.
J. Am. Chem. Soc. **131**, 4267–4278 (2009).

[176] J. M. Lim, P. Kim, M.-C. Yoon, J. Sung, V. Dehm, Z. Chen, F. Würthner, and D. Kim.
Exciton delocalization and dynamics in helical π-stacks of self-assembled perylene bisimides.
Chem. Sci. **4**, 388–397 (2012).

[177] F. Panzer, M. Sommer, H. Bässler, M. Thelakkat, and A. Köhler.
Spectroscopic signature of two distinct H-aggregate species in poly(3-hexylthiophene).
Macromolecules **48**, 1543–1553 (2015).

[178] H.-G. Duan, P. Nalbach, V. I. Prokhorenko, S. Mukamel, and M. Thorwart.
On the origin of oscillations in two-dimensional spectra of excitonically-coupled molecular systems.
New J. Phys. **17**, 072002 (2015).

[179] V. May.
Kinetic theory of exciton–exciton annihilation.
J. Chem. Phys. **140**, 054103 (2014).

[180] V. Sundström, T. Gillbro, R. A. Gadonas, and A. Piskarskas.
Annihilation of singlet excitons in J aggregates of pseudoisocyanine (PIC) studied by pico- and subpicosecond spectroscopy.
J. Chem. Phys. **89**, 2754–2762 (1988).

[181] C. Rehhagen, M. Stolte, S. Herbst, M. Hecht, S. Lochbrunner, F. Würthner, and F. Fennel.
Exciton migration in multistranded perylene bisimide j-aggregates.
J. Phys. Chem. Lett. **11**, 6612–6617 (2020).

[182] F. Fennel and S. Lochbrunner.
Exciton-exciton annihilation in a disordered molecular system by direct and multistep Förster transfer.
Phys. Rev. B **92**, 140301 (2015).

[183] L. Valkunas, E. Akesson, T. Pullerits, and V. Sundström.
Energy migration in the light-harvesting antenna of the photosynthetic bacterium Rhodospirillum rubrum studied by time-resolved excitation annihilation at 77 K.
Biophys. J. **70**, 2373–2379 (1996).

[184] V. I. Novoderezhkin, M. A. Palacios, H. van Amerongen, and R. van Grondelle.

Energy-transfer dynamics in the LHCII complex of higher plants: Modified red-field approach.
J. Phys. Chem. B **108**, 10363–10375 (2004).

[185] Y. Lee, M. Gorka, J. H. Golbeck, and J. M. Anna.
Ultrafast energy transfer involving the red chlorophylls of cyanobacterial photosystem I probed through two-dimensional electronic spectroscopy.
J. Am. Chem. Soc. **140**, 11631–11638 (2018).

[186] J. Pšenčík, Y.-Z. Ma, J. B. Arellano, J. Hála, and T. Gillbro.
Excitation energy transfer dynamics and excited-state structure in chlorosomes of Chlorobium phaeobacteroides.
Biophys. J. **84**, 1161–1179 (2003).

[187] P. Kjellberg, B. Brüggemann, and T. Pullerits.
Two-dimensional electronic spectroscopy of an excitonically coupled dimer.
Phys. Rev. B **74**, 024303 (2006).

[188] E. Bukartė, D. Paleček, P. Edlund, S. Westenhoff, and D. Zigmantas.
Dynamic band-shift signal in two-dimensional electronic spectroscopy: A case of bacterial reaction center.
J. Chem. Phys. **154**, 115102 (2021).

[189] J. Dostál.
Nonresonant coherent two-dimensional spectroscopy.
Spectrochim. Acta A **267**, 120441 (2022).

[190] L. Valkunas, G. Trinkunas, V. Liuolia, and R. van Grondelle.
Nonlinear annihilation of excitations in photosynthetic systems.
Biophys. J. **69**, 1117–1129 (1995).

[191] V. Barzda, V. Gulbinas, R. Kananavicius, V. Cervinskas, H. van Amerongen, R. van Grondelle, and L. Valkunas.
Singlet–singlet annihilation kinetics in aggregates and trimers of LHCII.
Biophys. J. **80**, 2409–2421 (2001).

[192] P. D. Dahlberg, P.-C. Ting, S. C. Massey, M. A. Allodi, E. C. Martin, C. N. Hunter, and G. S. Engel.
Mapping the ultrafast flow of harvested solar energy in living photosynthetic cells.
Nat. Commun. **8**, 988 (2017).

[193] Fuller, Wilcox, and Ogilvie.
Pulse shaping based two-dimensional electronic spectroscopy in a background free geometry.
Opt. Express **22** (2014).

[194] T. Mančal, N. Christensson, V. Lukeš, F. Milota, O. Bixner, H. F. Kauffmann,
and J. Hauer.
System-dependent signatures of electronic and vibrational coherences in electronic two-dimensional spectra.
J. Phys. Chem. Lett. **3**, 1497–1502 (2012).

[195] F. Šanda, V. Perlík, C. N. Lincoln, and J. Hauer.
Center line slope analysis in two-dimensional electronic spectroscopy.
J. Phys. Chem. A **119**, 10893–10909 (2015).

[196] T. N. Do, M. F. Khyasudeen, P. J. Nowakowski, Z. Zhang, and H.-S. Tan.
Measuring ultrafast spectral diffusion and correlation dynamics by two-dimensional electronic spectroscopy.
Chem. Asian J. **14**, 3992–4000 (2019).

[197] B. Kriete, A. S. Bondarenko, R. Alessandri, I. Patmanidis, V. V. Krasnikov,
T. L. C. Jansen, S. J. Marrink, J. Knoester, and M. S. Pshenichnikov.
Molecular versus excitonic disorder in individual artificial light-harvesting systems.
J. Am. Chem. Soc. **142**, 18073–18085 (2020).

[198] F. Milota, V. I. Prokhorenko, T. Mancal, H. von Berlepsch, O. Bixner, H. F.
Kauffmann, and J. Hauer.
Vibronic and vibrational coherences in two-dimensional electronic spectra of supramolecular J-aggregates.
J. Phys. Chem. A **117**, 6007–6014 (2013).

[199] V. R. Policht, M. Russo, F. Liu, C. Trovatello, M. Maiuri, Y. Bai, X. Zhu,
S. Dal Conte, and G. Cerullo.
Dissecting interlayer hole and electron transfer in transition metal dichalcogenide heterostructures via two-dimensional electronic spectroscopy.
Nano Lett. **21**, 4738–4743 (2021).

[200] S. T. Cundiff, T. Zhang, A. D. Bristow, D. Karaiskaj, and X. Dai.
Optical two-dimensional Fourier transform spectroscopy of semiconductor quantum wells.
Acc. Chem. Res. **42**, 1423–1432 (2009).

[201] K. J. Karki, J. Chen, A. Sakurai, Q. Shi, A. T. Gardiner, O. Kühn, R. J. Cogdell,
and T. Pullerits.
Before Förster. Initial excitation in photosynthetic light harvesting.
Chem. Sci. **10**, 7923–7928 (2019).

[202] D. Heussman, J. Kittell, P. H. von Hippel, and A. H. Marcus.
Temperature-dependent local conformations and conformational distributions of cyanine dimer labeled single-stranded–double-stranded DNA junctions by 2D fluorescence spectroscopy.

J. Chem. Phys. **156**, 045101 (2022).

[203] K. J. Karki, L. Kringle, A. H. Marcus, and T. Pullerits.
Phase-synchronous detection of coherent and incoherent nonlinear signals.
J. Opt. **18**, 015504 (2016).

[204] L. Bolzonello, F. Bernal-Texca, L. G. Gerling, J. Ockova, E. Collini, J. Martorell, and N. F. van Hulst.
Photocurrent-detected 2D electronic spectroscopy reveals ultrafast hole transfer in operating PM6/Y6 organic solar cells.
J. Phys. Chem. Lett. **12**, 3983–3988 (2021).

[205] G. Trinkunas, J. L. Herek, T. Polívka, V. Sundström, and T. Pullerits.
Exciton Delocalization Probed by Excitation Annihilation in the Light-Harvesting Antenna LH2.
Phys. Rev. Lett. **86**, 4167–4170 (2001).

[206] S. F. Völker, A. Schmiedel, M. Holzapfel, K. Renziehausen, V. Engel, and C. Lambert.
Singlet–singlet exciton annihilation in an exciton-coupled squaraine-squaraine copolymer: A model toward hetero-J-aggregates.
J. Phys. Chem. C **118**, 17467–17482 (2014).

[207] M. G. Müller, P. Lambrev, M. Reus, E. Wientjes, R. Croce, and A. R. Holzwarth.
Singlet energy dissipation in the photosystem II light-harvesting complex does not involve energy transfer to carotenoids.
ChemPhysChem **11**, 1289–1296 (2010).

[208] V. Gulbinas, L. Valkunas, D. Kuciauskas, E. Katilius, V. Liuolia, W. Zhou, and R. E. Blankenship.
Singlet-singlet annihilation and local heating in FMO complexes.
J. Phys. Chem. **100**, 17950–17956 (1996).

[209] M. G. Müller, M. Hucke, M. Reus, and A. R. Holzwarth.
Primary processes and structure of the photosystem II reaction center. 4. low-intensity femtosecond transient absorption spectra of D1-D2-cyt-b559 reaction centers,.
J. Phys. Chem. **100**, 9527–9536 (1996).

[210] D. B. Turner and K. A. Nelson.
Coherent measurements of high-order electronic correlations in quantum wells.
Nature **466**, 1089–1092 (2010).

[211] Z. Zhang, P. H. Lambrev, K. L. Wells, G. Garab, and H.-S. Tan.
Direct observation of multistep energy transfer in LHCII with fifth-order 3D electronic spectroscopy.

Nat. Commun. **6**, 7914 (2015).

[212] F. Ding, E. C. Fulmer, and M. T. Zanni.
Heterodyned fifth-order two-dimensional IR spectroscopy: Third-quantum states and polarization selectivity.
J. Chem. Phys. **123**, 094502 (2005).

[213] Z. Zhang, K. L. Wells, M. T. Seidel, and H.-S. Tan.
Fifth-order three-dimensional electronic spectroscopy using a pump–probe configuration.
J. Phys. Chem. B **117**, 15369–15385 (2013).

[214] E. C. Fulmer, F. Ding, and M. T. Zanni.
Heterodyned fifth-order 2D-IR spectroscopy of the azide ion in an ionic glass.
J. Chem. Phys. **122**, 034302 (2005).

[215] A. F. Fidler, E. Harel, and G. S. Engel.
Dissecting hidden couplings using fifth-order three-dimensional electronic spectroscopy.
J. Phys. Chem. Lett. **1**, 2876–2880 (2010).

[216] P. Brosseau, S. Palato, H. Seiler, H. Baker, and P. Kambhampati.
Fifth-order two-quantum absorptive two-dimensional electronic spectroscopy of CdSe quantum dots.
J. Chem. Phys. **153**, 234703 (2020).

[217] S. Yu, Y. Geng, D. Liang, H. Li, and X. Liu.
Double-quantum–zero-quantum 2D coherent spectroscopy reveals quantum coherence between collective states in an atomic vapor.
Opt. Lett. **47**, 997–1000 (2022).

[218] H. Wu and M. A. Berg.
Multiple population-period transient spectroscopy (MUPPETS) in excitonic systems.
J. Chem. Phys. **138**, 034201 (2013).

[219] K. Sahu, H. Wu, and M. A. Berg.
Rate dispersion in the biexciton decay of CdSe/ZnS nanoparticles from multiple population-period transient spectroscopy.
J. Am. Chem. Soc. **135**, 1002–1005 (2013).

[220] C. Heshmatpour, P. Malevich, F. Plasser, M. Menger, C. Lambert, F. Šanda, and J. Hauer.
Annihilation dynamics of molecular excitons measured at a single perturbative excitation energy.
J. Phys. Chem. Lett. **11**, 7776–7781 (2020).

[221] S. M. Gallagher Faeder and D. M. Jonas.
Two-dimensional electronic correlation and relaxation spectra: Theory and model calculations.
J. Phys. Chem. A **103**, 10489–10505 (1999).

[222] D. V. Voronine, D. Abramavičius, and S. Mukamel.
Manipulating multidimensional electronic spectra of excitons by polarization pulse shaping.
J. Chem. Phys. **126**, 044508 (2007).

[223] K. M. Farrell, N. Yang, and M. T. Zanni.
A polarization scheme that resolves cross-peaks with transient absorption and eliminates diagonal peaks in 2D spectroscopy.
PNAS **119**, e2117398119 (2022).

[224] J. Réhault, M. Maiuri, A. Oriana, and G. Cerullo.
Two-dimensional electronic spectroscopy with birefringent wedges.
Rev. Sci. Instrum. **85**, 123107 (2014).

[225] L. Wittenbecher and D. Zigmantas.
Correction of Fabry-Pérot interference effects in phase and amplitude pulse shapers based on liquid crystal spatial light modulators.
Opt. Express **27**, 22970–22982 (2019).

[226] M. Ninck, A. Galler, T. Feurer, and T. Brixner.
Programmable common-path vector field synthesizer for femtosecond pulses.
Opt. Lett. **32**, 3379–3381 (2007).

[227] C. Schwarz, O. Hüter, and T. Brixner.
Full vector-field control of ultrashort laser pulses utilizing a single dual-layer spatial light modulator in a common-path setup.
J. Opt. Soc. Am. B: Opt. Phys. **32**, 933–945 (2015).

[228] S. Yan and H.-S. Tan.
Phase cycling schemes for two-dimensional optical spectroscopy with a pump–probe beam geometry.
Chem. Phys. **360**, 110–115 (2009).

[229] L. Bruder, A. Eisfeld, U. Bangert, M. Binz, M. Jakob, D. Uhl, M. Schulz-Weiling, E. R. Grant, and F. Stienkemeier.
Delocalized excitons and interaction effects in extremely dilute thermal ensembles.
Phys. Chem. Chem. Phys. **21**, 2276–2282 (2019).

[230] T. M. Autry, G. Moody, J. Fraser, C. McDonald, R. P. Mirin, and K. Silverman.
Single-scan acquisition of multiple multidimensional spectra.
Optica **6**, 735 (2019).

[231] S. Mueller.
       Coherent Mutliple-Quantum Multidimensional Fluorescence Spectroscopy.
       Ph.D. thesis. Universität Würzburg, Würzburg, (2021).

[232] B. Brüggemann and T. Pullerits.
       *Nonperturbative modeling of fifth-order coherent multidimensional spectroscopy
       in light harvesting antennas.*
       New J. Phys. **13**, 025024 (2011).

[233] R. Metzler and J. Klafter.
       *The random walk's guide to anomalous diffusion: A fractional dynamics ap-
       proach.*
       Phys. Rep. **339**, 1–77 (2000).

[234] R. Pandya, A. M. Alvertis, Q. Gu, J. Sung, L. Legrand, D. Kréher, T. Barisien,
       A. W. Chin, C. Schnedermann, and A. Rao.
       *Exciton diffusion in highly-ordered one dimensional conjugated polymers: Effects
       of back-bone torsion, electronic symmetry, phonons and annihilation.*
       J. Phys. Chem. Lett. **12**, 3669–3678 (2021).

[235] O. V. Mikhnenko, P. W. M. Blom, and T.-Q. Nguyen.
       Exciton diffusion in organic semiconductors.
       Energy Environ. Sci. **8**, 1867–1888 (2015).

[236] X.-H. Jin, M. B. Price, J. R. Finnegan, C. E. Boott, J. M. Richter, A. Rao, S. M.
       Menke, R. H. Friend, G. R. Whittell, and I. Manners.
       *Long-range exciton transport in conjugated polymer nanofibers prepared by seeded
       growth.*
       Science **360**, 897–900 (2018).

[237] C. Heshmatpour, J. Hauer, and F. Šanda.
       *Correlated spectral fluctuations quantified by lineshape analysis of fifth order two-
       dimensional electronic spectra.*
       J. Chem. Phys. **156**, 084114 (2022).

[238] C. Heshmatpour, J. Hauer, and F. Šanda.
       *Interplay of exciton annihilation and transport in fifth order electronic spec-
       troscopy.*
       Chem. Phys. **528**, 110433 (2020).

[239] K. Leo, M. Wegener, J. Shah, D. S. Chemla, E. O. Göbel, T. C. Damen,
       S. Schmitt-Rink, and W. Schäfer.
       *Effects of coherent polarization interactions on time-resolved degenerate four-
       wave mixing.*
       Phys. Rev. Lett. **65**, 1340–1343 (1990).

[240] T. Bittner, K.-D. Irrgang, G. Renger, and M. R. Wasielewski.
Ultrafast excitation energy transfer and exciton-exciton annihilation processes in isolated light harvesting complexes of Photosystem II (LHC II) from Spinach.
J. Phys. Chem. **98**, 11821–11826 (1994).

[241] Y. Sun, Y. Yoon, M. Steger, G. Liu, L. N. Pfeiffer, K. West, D. W. Snoke, and K. A. Nelson.
Direct measurement of polariton–polariton interaction strength.
Nature Phys. **13**, 870–875 (2017).

[242] P. Giura, L. Paulatto, F. He, R. P. S. M. Lobo, A. Bosak, E. Calandrini, L. Paolasini, and D. Antonangeli.
Multiphonon anharmonicity of MgO.
Phys. Rev. B **99**, 220304 (2019).

[243] U. Woggon.
Optical Properties of Semiconductor Quantum Dots.
volume 136 of *Springer Tracts in Modern Physics.* Springer Berlin Heidelberg, Berlin, Heidelberg (1997).

[244] D. Abramavičius.
Revealing a full quantum ladder by nonlinear spectroscopy.
Lith. J. Phys. **60**, 154–166 (2020).

[245] Z. Zhang, K. L. Wells, and H.-S. Tan.
Purely absorptive fifth-order three-dimensional electronic spectroscopy.
Opt. Lett. **37**, 5058–5060 (2012).

[246] A. P. Spencer, W. O. Hutson, and E. Harel.
Quantum coherence selective 2D Raman–2D electronic spectroscopy.
Nat. Commun. **8**, 14732 (2017).

[247] A. P. Spencer, W. O. Hutson, and E. Harel.
Four-dimensional coherent spectroscopy of complex molecular systems in solution.
J. Phys. Chem. C **123**, 6303–6315 (2019).

[248] P. Malý and T. Brixner.
Fluorescence-Detected Pump–Probe Spectroscopy.
Angew. Chem. Int. Ed. **60**, 18867–18875 (2021).

[249] R. Selle, G. Vogt, T. Brixner, G. Gerber, R. Metzler, and W. Kinzel.
Modeling of light-matter interactions with neural networks.
Phys. Rev. A **76**, 023810 (2007).

[250] R. Selle, T. Brixner, T. Bayer, M. Wollenhaupt, and T. Baumert.

Modelling of ultrafast coherent strong-field dynamics in potassium with neural networks.
J. Phys. B: At. Mol. Opt. Phys. **41**, 074019 (2008).

[251] F. Häse, C. Kreisbeck, and A. Aspuru-Guzik.
Machine learning for quantum dynamics: Deep learning of excitation energy transfer properties.
Chem. Sci. **8**, 8419–8426 (2017).

[252] M. Rodríguez and T. Kramer.
Machine learning of two-dimensional spectroscopic data.
Chem. Phys. **520**, 52–60 (2019).

[253] K. A. Parker, J. D. Schultz, N. Singh, M. R. Wasielewski, and D. N. Beratan.
Mapping simulated two-dimensional spectra to molecular models using machine learning.
J. Phys. Chem. Lett. **13**, 7454–7461 (2022).

[254] N. M. Kearns, R. D. Mehlenbacher, A. C. Jones, and M. T. Zanni.
Broadband 2D electronic spectrometer using white light and pulse shaping: Noise and signal evaluation at 1 and 100 kHz.
Opt. Express **25**, 7869–7883 (2017).

[255] D. Meshulach and Y. Silberberg.
Coherent quantum control of two-photon transitions by a femtosecond laser pulse.
Nature **396**, 239–242 (1998).

[256] T. Brixner, N. H. Damrauer, P. Niklaus, and G. Gerber.
Photoselective adaptive femtosecond quantum control in the liquid phase.
Nature **414**, 57–60 (2001).

[257] T. Brixner and G. Gerber.
Quantum control of gas-phase and liquid-phase femtochemistry.
ChemPhysChem **4**, 418–438 (2003).

[258] S. Pres, B. Huber, M. Hensen, D. Fersch, E. Schatz, D. Friedrich, V. Lisinetskii, R. Pompe, B. Hecht, W. Pfeiffer, and T. Brixner.
Detection of a plasmon-polariton quantum wave packet (submitted).

[259] M. Stolte, R. Hecht, Z. Xie, L. Liu, C. Kaufmann, A. Kudzus, D. Schmidt, and F. Würthner.
Crystal engineering of 1D exciton systems composed of single- and double-stranded perylene bisimide J-aggregates.
Adv. Opt. Mater. **8**, 2000926 (2020).

[260] T. A. A. Oliver, N. H. C. Lewis, and G. R. Fleming.
Correlating the motion of electrons and nuclei with two-dimensional electronic–vibrational spectroscopy.
PNAS **111**, 10061–10066 (2014).

[261] N. H. C. Lewis, N. L. Gruenke, T. A. A. Oliver, M. Ballottari, R. Bassi, and G. R. Fleming.
Observation of electronic excitation transfer through light harvesting complex II using two-dimensional electronic–vibrational spectroscopy.
J. Phys. Chem. Lett. **7**, 4197–4206 (2016).

[262] J. D. Gaynor, T. L. Courtney, M. Balasubramanian, and M. Khalil.
Fourier transform two-dimensional electronic-vibrational spectroscopy using an octave-spanning mid-IR probe.
Opt. Lett. **41**, 2895–2898 (2016).

[263] T. L. Courtney, Z. W. Fox, K. M. Slenkamp, and M. Khalil.
Two-dimensional vibrational-electronic spectroscopy.
J. Chem. Phys. **143**, 154201 (2015).

[264] T. L. Courtney, Z. W. Fox, L. Estergreen, and M. Khalil.
Measuring coherently coupled intramolecular vibrational and charge-transfer dynamics with two-dimensional vibrational–electronic spectroscopy.
J. Phys. Chem. Lett. **6**, 1286–1292 (2015).

[265] J. D. Gaynor and M. Khalil.
Signatures of vibronic coupling in two-dimensional electronic-vibrational and vibrational-electronic spectroscopies.
J. Chem. Phys. **147**, 094202 (2017).

[266] E. Joos, H. D. Zeh, C. Kiefer, D. J. W. Giulini, J. Kupsch, and I.-O. Stamatescu.
Decoherence and the appearance of a classical world in quantum theory.
Second edition. Springer Berlin Heidelberg, Berlin, Heidelberg (2003).

[267] K. Raghavachari and J. B. Anderson.
Electron correlation effects in molecules.
J. Chem. Phys. **100**, 12960–12973 (1996).

[268] D. S. Chemla and J. Shah.
Many-body and correlation effects in semiconductors.
Nature **411**, 549–557 (2001).

[269] J. Kim, V. M. Huxter, C. Curutchet, and G. D. Scholes.
Measurement of electron-electron interactions and correlations using two-dimensional electronic double-quantum coherence spectroscopy.
J. Phys. Chem. A **113**, 12122–12133 (2009).

[270] C.-H. Tseng, S. Matsika, and T. C. Weinacht.
Two-dimensional ultrafast Fourier transform spectroscopy in the deep ultraviolet.
Opt. Express **17**, 18788–18793 (2009).

[271] S. Mukamel, D. Healion, Y. Zhang, and J. D. Biggs.
Multidimensional attosecond resonant X-ray spectroscopy of molecules: Lessons from the optical regime.
Annu. Rev. Phys. Chem. **64**, 101–127 (2013).

[272] T. Ha, J. Glass, T. Enderle, D. S. Chemla, and S. Weiss.
Hindered rotational diffusion and rotational jumps of Single molecules.
Phys. Rev. Lett. **80**, 2093–2096 (1998).

[273] A. Ruseckas, P. Wood, I. Samuel, G. Webster, W. Mitchell, P. Burn, and V. Sundström.
Ultrafast depolarization of the fluorescence in a conjugated polymer.
Phys. Rev. B **72**, 115214 (2005).

[274] D. M. Jameson and J. A. Ross.
Fluorescence polarization/anisotropy in diagnostics and imaging.
Chem. Rev. **110**, 2685–2708 (2010).

[275] F. Spreitler, M. Sommer, M. Hollfelder, M. Thelakkat, S. Gekle, and J. Köhler.
Unravelling the conformations of di-(perylene bisimide acrylate) by combining time-resolved fluorescence-anisotropy experiments and molecular modelling.
Phys. Chem. Chem. Phys. **16**, 25959–25968 (2014).

[276] A. H. Squires and W. E. Moerner.
Direct single-molecule measurements of phycocyanobilin photophysics in monomeric C-phycocyanin.
PNAS **114**, 9779–9784 (2017).

[277] R. Camacho, D. Täuber, and I. G. Scheblykin.
Fluorescence anisotropy reloaded—emerging polarization microscopy methods for assessing chromophores' organization and excitation energy transfer in single molecules, particles, films, and beyond.
Adv. Mater. **31**, 1805671 (2019).

[278] J. R. Lakowicz.
Principles of fluorescence spectroscopy.
Third edition. Springer, New York (2006).

[279] D. M. Jonas, M. J. Lang, Y. Nagasawa, T. Joo, and G. R. Fleming.
Pump-probe polarization anisotropy study of femtosecond energy transfer within the photosynthetic reaction center of rhodobacter sphaeroides R26.
J. Phys. Chem. **100**, 12660–12673 (1996).

[280] T. Pullerits, M. Chachisvilis, and V. Sundström.
Exciton delocalization length in the B850 antenna of Rhodobacter sphaeroides.
J. Phys. Chem. **100**, 10787–10792 (1996).

[281] D. A. Farrow, W. Qian, E. R. Smith, A. A. Ferro, and D. M. Jonas.
Polarized pump-probe measurements of electronic motion via a conical intersection.
J. Chem. Phys. **128**, 144510 (2008).

[282] A. Albrecht Ferro and D. M. Jonas.
Pump–probe polarization anisotropy study of doubly degenerate electronic reorientation in silicon naphthalocyanine.
J. Chem. Phys. **115**, 6281–6284 (2001).

[283] M. Ji, M. Odelius, and K. J. Gaffney.
Large angular jump mechanism observed for hydrogen bond exchange in aqueous perchlorate solution.
Science **328**, 1003–1005 (2010).

[284] R. D. Mehlenbacher, J. Wang, N. M. Kearns, M. J. Shea, J. T. Flach, T. J. McDonough, M.-Y. Wu, M. S. Arnold, and M. T. Zanni.
Ultrafast exciton hopping observed in bare semiconducting carbon nanotube thin films with two-dimensional white-light spectroscopy.
J. Phys. Chem. Lett. **7**, 2024–2031 (2016).

[285] S. C. Massey, P.-C. Ting, S.-H. Yeh, P. D. Dahlberg, S. H. Sohail, M. A. Allodi, E. C. Martin, S. Kais, C. N. Hunter, and G. S. Engel.
Orientational dynamics of transition dipoles and exciton relaxation in LH2 from ultrafast two-dimensional anisotropy.
J. Phys. Chem. Lett. **10**, 270–277 (2019).

[286] M. T. Zanni, N.-H. Ge, Y. S. Kim, and R. M. Hochstrasser.
Two-dimensional IR spectroscopy can be designed to eliminate the diagonal peaks and expose only the crosspeaks needed for structure determination.
PNAS **98**, 11265–11270 (2001).

[287] G. S. Schlau-Cohen, A. Ishizaki, T. R. Calhoun, N. S. Ginsberg, M. Ballottari, R. Bassi, and G. R. Fleming.
Elucidation of the timescales and origins of quantum electronic coherence in LHCII.
Nat. Chem. **4**, 389–395 (2012).

[288] E. Thyrhaug, S. A. Bogh, M. R. Carro-Temboury, C. S. Madsen, T. Vosch, and D. Zigmantas.
Ultrafast coherence transfer in DNA-templated silver nanoclusters.
Nat. Commun. **8**, 15577 (2017).

[289] D. L. Andrews and T. Thirunamachandran.
On three-dimensional rotational averages.
J. Chem. Phys. **67**, 5026–5033 (1977).

[290] S. Schott, A. Steinbacher, J. Buback, P. Nuernberger, and T. Brixner.
Generalized magic angle for time-resolved spectroscopy with laser pulses of arbitrary ellipticity.
J. Phys. B: At. Mol. Opt. Phys. **47**, 124014 (2014).

[291] P. Malý, J. Ravensbergen, J. T. M. Kennis, R. van Grondelle, R. Croce, T. Mančal, and B. van Oort.
Polarization-controlled optimal scatter suppression in transient absorption spectroscopy.
Sci. Rep. **7**, 43484 (2017).

[292] V. Novoderezhkin, R. Monshouwer, and R. van Grondelle.
Disordered exciton model for the core light-harvesting antenna of Rhodopseudomonas viridis.
Biophys. J. **77**, 666–681 (1999).

[293] S. F. Völker, S. Uemura, M. Limpinsel, M. Mingebach, C. Deibel, V. Dyakonov, and C. Lambert.
Polymeric squaraine dyes as electron donors in bulk heterojunction solar cells.
Macromol. Chem. Phys. **211**, 1098–1108 (2010).

[294] Y. Ebihara and M. Vacha.
Relating conformation and photophysics in single MEH-PPV chains.
J. Phys. Chem. B **112**, 12575–12578 (2008).

[295] S. Habuchi, S. Onda, and M. Vacha.
Mapping the emitting sites within a single conjugated polymer molecule.
Chem. Commun. **-**, 4868–4870 (2009).

[296] C. Lambert, F. Koch, S. F. Völker, A. Schmiedel, M. Holzapfel, A. Humeniuk, M. I. S. Röhr, R. Mitric, and T. Brixner.
Energy transfer between squaraine polymer sections: From helix to zigzag and all the way back.
J. Am. Chem. Soc. **137**, 7851–7861 (2015).

[297] B. Kriete, A. S. Bondarenko, V. R. Jumde, L. E. Franken, A. J. Minnaard, T. L. C. Jansen, J. Knoester, and M. S. Pshenichnikov.
Steering self-assembly of amphiphilic molecular nanostructures via halogen exchange.
J. Phys. Chem. Lett. **8**, 2895–2901 (2017).

[298] C. Ramanan, A. L. Smeigh, J. E. Anthony, T. J. Marks, and M. R. Wasielewski.

Competition between singlet fission and charge separation in solution-processed blend films of 6,13-bis(triisopropylsilylethynyl)pentacene with sterically-encumbered perylene-3,4:9,10-bis(dicarboximide)s.
J. Am. Chem. Soc. **134**, 386–397 (2012).

[299] M. Brendel, S. Krause, A. Steindamm, A. K. Topczak, S. Sundarraj, P. Erk, S. Höhla, N. Fruehauf, N. Koch, and J. Pflaum.
The effect of gradual fluorination on the properties of F_nZnPc thin films and F_nZnPc/C60 bilayer photovoltaic cells.
Adv. Funct. Mater. **25**, 1565–1573 (2015).

[300] C. Y. Wong, B. D. Folie, B. L. Cotts, and N. S. Ginsberg.
Discerning variable extents of interdomain orientational and structural hetero-geneity in solution-cast polycrystalline organic semiconducting thin films.
J. Phys. Chem. Lett. **6**, 3155–3162 (2015).

[301] M. U. Rothmann, J. S. Kim, J. Borchert, K. B. Lohmann, C. M. O'Leary, A. A. Sheader, L. Clark, H. J. Snaith, M. B. Johnston, P. D. Nellist, and L. M. Herz.
Atomic-scale microstructure of metal halide perovskite.
Science **370**, eabb5940 (2020).

[302] B. J. Schwartz.
Conjugated polymers as molecular materials: How chain conformation and film morphology influence energy transfer and interchain interactions.
Annu. Rev. Phys. Chem. **54**, 141–172 (2003).

[303] T. Unger, F. Panzer, C. Consani, F. Koch, T. Brixner, H. Bässler, and A. Köhler.
Ultrafast energy transfer between disordered and highly planarized chains of poly[2-methoxy-5-(2-ethylhexyloxy)-1,4-phenylenevinylene] (MEH-PPV).
ACS Macro Lett. **4**, 412–416 (2015).

[304] V. May and O. Kühn.
Charge and energy transfer dynamics in molecular systems.
Second edition. Wiley-VCH Verlag GmbH, Weinheim (2004).

[305] E. Collini, H. Gattuso, Y. Kolodny, L. Bolzonello, A. Volpato, H. T. Frid-man, S. Yochelis, M. Mor, J. Dehnel, E. Lifshitz, Y. Paltiel, R. D. Levine, and F. Remacle.
Room-temperature inter-dot coherent dynamics in multilayer quantum dot ma-terials.
J. Phys. Chem. C **124**, 16222–16231 (2020).

[306] J. R. Caram, H. Zheng, P. D. Dahlberg, B. S. Rolczynski, G. B. Griffin, A. F. Fidler, D. S. Dolzhnikov, D. V. Talapin, and G. S. Engel.
Persistent interexcitonic quantum coherence in CdSe quantum dots.
J. Phys. Chem. Lett. **5**, 196–204 (2014).

[307] P. Akhtar, C. Zhang, T. N. Do, G. Garab, P. H. Lambrev, and H.-S. Tan.
Two-dimensional spectroscopy of chlorophyll a *excited-state equilibration in light-harvesting complex II.*
J. Phys. Chem. Lett. **8**, 257–263 (2017).

[308] T. Joo, Y. Jia, J.-Y. Yu, M. J. Lang, and G. R. Fleming.
Third-order nonlinear time domain probes of solvation dynamics.
J. Chem. Phys. **104**, 6089 (1996).

[309] L. Valkunas, Y.-Z. Ma, and G. R. Fleming.
Exciton-exciton annihilation in single-walled carbon nanotubes.
Phys. Rev. B **73**, 115432 (2006).

[310] H. Marciniak, X.-Q. Li, F. Würthner, and S. Lochbrunner.
One-dimensional exciton diffusion in perylene bisimide aggregates.
J. Phys. Chem. A **115**, 648–654 (2011).

[311] M. Vengris, D. S. Larsen, L. Valkunas, G. Kodis, C. Herrero, D. Gust, T. Moore, A. Moore, and R. van Grondelle.
Separating annihilation and excitation energy transfer dynamics in light harvesting systems.
J. Phys. Chem. B **117**, 11372–11382 (2013).

[312] E. E. Ostroumov, R. M. Mulvaney, J. M. Anna, R. J. Cogdell, and G. D. Scholes.
Energy transfer pathways in light-harvesting complexes of purple bacteria as revealed by global kinetic analysis of two-dimensional transient spectra.
J. Phys. Chem. B **117**, 11349–11362 (2013).

[313] P. Malý, A. T. Gardiner, R. J. Cogdell, R. van Grondelle, and T. Mančal.
Robust light harvesting by a noisy antenna.
Phys. Chem. Chem. Phys. **20**, 4360–4372 (2018).

[314] Y.-Z. Ma, R. J. Cogdell, and T. Gillbro.
Energy transfer and exciton annihilation in the B800-850 antenna complex of the photosynthetic purple bacterium Rhodopseudomonas acidophila (Strain 10050). A femtosecond transient absorption study.
J. Phys. Chem. B **101**, 1087–1095 (1997).

[315] V. Perlík, J. Hauer, and F. Šanda.
Finite pulse effects in single and double quantum spectroscopies.
J. Opt. Soc. Am. B: Opt. Phys. **34**, 430–439 (2017).

[316] A. Turkin, P. Malý, and C. Lambert.
Fluorescence band exchange narrowing in a series of squaraine oligomers: Energetic vs. structural disorder.
Phys. Chem. Chem. Phys. **23**, 18393–18403 (2021).

[317] C. You, A. Nellikka, I. Leon, and O. S. Magaña-Loaiza.
Multiparticle quantum plasmonics.
Nanophotonics **9**, 1243–1269 (2020).

[318] U. Bangert, L. Bruder, and F. Stienkemeier.
Pulse overlap ambiguities in multiple quantum coherence spectroscopy.
arXiv:2206.06740 (2022).

[319] A. Albrecht Ferro, J. D. Hybl, and D. M. Jonas.
Complete femtosecond linear free induction decay, Fourier algorithm for dispersion relations, and accuracy of the rotating wave approximation.
J. Chem. Phys. **114**, 4649–4656 (2001).

[320] E. Harel, A. F. Fidler, and G. S. Engel.
Single-shot gradient-assisted photon echo electronic spectroscopy.
J. Phys. Chem. A **115**, 3787–3796 (2011).

[321] T. Mirkovic, E. E. Ostroumov, J. M. Anna, R. van Grondelle, Govindjee, and G. D. Scholes.
Light absorption and energy transfer in the antenna complexes of photosynthetic organisms.
Chem. Rev. **117**, 249–293 (2017).

[322] L. Valkunas, I. H. M. van Stokkum, R. Berera, and R. van Grondelle.
Exciton migration and fluorescence quenching in LHCII aggregates: Target analysis using a simple nonlinear annihilation scheme.
Chem. Phys. **357**, 17–20 (2009).

[323] R. van Grondelle, J. P. Dekker, T. Gillbro, and V. Sundstrom.
Energy transfer and trapping in photosynthesis.
Biochim. Biophys. Acta - Bioenerg. **1187**, 1–65 (1994).

[324] G. R. Fleming and R. van Grondelle.
Femtosecond spectroscopy of photosynthetic light-harvesting systems.
Curr. Opin. Struct. Biol. **7**, 738–748 (1997).

[325] G. T. Oostergetel, H. van Amerongen, and E. J. Boekema.
The chlorosome: A prototype for efficient light harvesting in photosynthesis.
Photosynth. Res. **104**, 245–255 (2010).

[326] L. M. Günther, M. Jendrny, E. A. Bloemsma, M. Tank, G. T. Oostergetel, D. A. Bryant, J. Knoester, and J. Köhler.
Structure of light-harvesting aggregates in individual chlorosomes.
J. Phys. Chem. B **120**, 5367–5376 (2016).

[327] A. Gelzinis, V. Butkus, E. Songaila, R. Augulis, A. Gall, C. Büchel, B. Robert, D. Abramavičius, D. Zigmantas, and L. Valkunas.

Mapping energy transfer channels in fucoxanthin–chlorophyll protein complex.
Biochim. Biophys. Acta - Bioenerg. **1847**, 241–247 (2015).

[328] Z. Wang, N. Lenngren, E. Amarotti, A. Hedse, K. Žídek, K. Zheng, D. Zigmantas, and T. Pullerits.
Excited states and their dynamics in CdSe quantum dots studied by two-color 2d spectroscopy.
J. Phys. Chem. Lett. **13**, 1266–1271 (2022).

[329] J. Gierschner and S. Y. Park.
Luminescent distyrylbenzenes: Tailoring molecular structure and crystalline morphology.
J. Mater. Chem. C **1**, 5818–5832 (2013).

[330] S. I. Stupp and L. C. Palmer.
Supramolecular Chemistry and Self-Assembly in Organic Materials Design.
Chem. Mater. **26**, 507–518 (2014).

[331] F. Ishiwari, Y. Shoji, and T. Fukushima.
Supramolecular scaffolds enabling the controlled assembly of functional molecular units.
Chem. Sci. **9**, 2028–2041 (2018).

[332] A. Liess, A. Arjona-Esteban, A. Kudzus, J. Albert, A.-M. Krause, A. Lv, M. Stolte, K. Meerholz, and F. Würthner.
Ultranarrow bandwidth organic photodiodes by exchange narrowing in merocyanine H- and J-aggregate excitonic systems.
Adv. Funct. Mater. **29**, 1805058 (2019).

[333] A. P. H. J. Schenning and E. W. Meijer.
Supramolecular electronics; nanowires from self-assembled π-conjugated systems.
Chem. Commun. **-**, 3245–3258 (2005).

[334] T. Schembri, J. H. Kim, A. Liess, V. Stepanenko, M. Stolte, and F. Würthner.
Semitransparent layers of social self-sorting merocyanine dyes for ultranarrow bandwidth organic photodiodes.
Adv. Opt. Mater. **9**, 2100213 (2021).

[335] D. Bialas, F. Fennel, N. Noll, M. Holzapfel, A. Schmiedel, C. Lambert, and F. Würthner.
Supramolecular p/n-heterojunction of C60-functionalized bis(merocyanine) quadruple stack: A model system for charge carrier separation and recombination in organic solar cells.
Nat. Sci. **2**, e210430 (2022).

[336] H. Lin, R. Camacho, Y. Tian, T. E. Kaiser, F. Würthner, and I. G. Scheblykin.
Collective fluorescence blinking in linear J-aggregates assisted by long-distance exciton migration.
Nano Lett. **10**, 620–626 (2010).

[337] X. Zhan, A. Facchetti, S. Barlow, T. J. Marks, M. A. Ratner, M. R. Wasielewski, and S. R. Marder.
Rylene and related diimides for organic electronics.
Adv. Mater. **23**, 268–284 (2011).

[338] A. Nowak-Król and F. Würthner.
Progress in the synthesis of perylene bisimide dyes.
Org. Chem. Front. **6**, 1272–1318 (2019).

[339] B. E. Partridge, P. Leowanawat, E. Aqad, M. R. Imam, H.-J. Sun, M. Peterca, P. A. Heiney, R. Graf, H. W. Spiess, X. Zeng, G. Ungar, and V. Percec.
Increasing 3D supramolecular order by decreasing molecular order. A comparative study of helical assemblies of dendronized nonchlorinated and tetrachlorinated perylene bisimides.
J. Am. Chem. Soc. **137**, 5210–5224 (2015).

[340] A. Nowak-Król, M. I. S. Röhr, D. Schmidt, and F. Würthner.
A crystalline π-stack containing five stereoisomers: Insights into conformational isomorphism, chirality inversion, and disorder.
Angew. Chem. Int. Ed. **129**, 11936–11940 (2017).

[341] K. Menekse, P. Chen, B. Mahlmeister, O. Anhalt, A. Kudzus, M. Stolte, and F. Würthner.
Quinoidal dicyanomethylene-endcapped cyclopentadithiophenes as vacuum-processable n-type semiconductors.
J. Mater. Chem. C **8**, 15303–15311 (2020).

[342] D. Polli, G. Grancini, J. Clark, M. Celebrano, T. Virgili, G. Cerullo, and G. Lanzani.
Nanoscale imaging of the interface dynamics in polymer blends by femtosecond pump-probe confocal microscopy.
Adv. Mater. **22**, 3048–3051 (2010).

[343] M. Binz, L. Bruder, L. Chen, M. Gelin, W. Domcke, and F. Stienkemeier.
Effects of high pulse intensity and chirp in two-dimensional electronic spectroscopy.
Opt. Express **28**, 25806–25829 (2020).

[344] A. Liess, A. Lv, A. Arjona-Esteban, D. Bialas, A.-M. Krause, V. Stepanenko, M. Stolte, and F. Würthner.

Exciton coupling of merocyanine dyes from H- to J-type in the solid state by crystal engineering.
Nano Lett. **17**, 1719–1726 (2017).

[345] G. P. Kini, S. J. Jeon, and D. K. Moon.
Design principles and synergistic effects of chlorination on a conjugated backbone for efficient organic photovoltaics: A critical review.
Adv. Mater. **32**, 1906175 (2020).

[346] J. Gleick.
Chaos: Making a new science. Vintage, London, England (1998).

Individual Contributions

All co-authors of the publication below, which was reprinted in Chapter 7 in this thesis, have been informed about the specified own contributions, as stated below, and they agree to them.

Anisotropy in Fifth-Order Exciton–Exciton-Interaction Two-Dimensional Spectroscopy

J. Lüttig, T. Brixner, and P. Malý, *Journal of Chemical Physics* **154**, 154202 (2021)

Author	J.L.	T.B	P.M.	Σ (in percent)
Idea and method development	50 %		50 %	15 %
Derivation of mathematical expressions	75 %		25 %	20 %
Performing simulations	75 %		25 %	20 %
Discussion of results	34 %	33 %	33 %	20 %
Writing first version of the manuscript	100 %			10 %
Correction of the manuscript		70 %	30 %	10 %
Publication coordination		100 %		5 %
Sum	54 %	19 %	27%	100 %

Acknowledgments

It's an experience like no other experience I can describe, the best thing that can happen to a scientist, realizing that something that's happened in his or her mind exactly corresponds to something that happens in nature. [...] A great shock, and a great, great joy!
-Leo Kadanoff, in *Chaos, Chapter: The Experimenter* [346]

Always trouble, always problems!
-A colleague at the very first day in the lab

The two quotes describe quite perfect how my PhD thesis was: exciting because I could work on something that nobody else has done before but on the other hand frustrating because a lot of things do not work. I consider my self very lucky because friends, colleagues and my family made my PhD thesis so special and a time that I enjoyed a lot. With this thesis also my time in Würzburg ends and I want to use the chance to thank the people who made this time so special.

- **Prof. Dr. Tobias Brixner** for giving me the opportunity to work in the field of ultrafast spectroscopy and providing the perfect place for me - not only for the PhD thesis but for almost seven years now. You encouraged me early on by offering me the chance to go to Israel and Sweden and by giving me the freedom to switch between different projects which allowed me to enjoy all the beauty of the different labs. In particular, I would like to thank you for giving me the opportunity to develop and try new experiments without limits but with support and an open door whenever it was needed. I appreciated very much that I could be a part of your group and work with you for such a long time.

- **Dr. Pavel Malý** for endless help in the lab and in explaining everything (more than once) from excitons over spectroscopy to Feynman diagrams. I really appreciate not only the time spending on science but also the great time outside of the lab: terraforming Mars, running through the ages or listening to Smetana. Thanks a lot for answering the endless questions that I had during the last two weeks of writing this thesis! It is one thing to be a great teacher but another thing to be a good friend and I am very happy that you were both during my PhD thesis.

- **Stefan Müller** for the great time in lab 5, especially in the very first months during my Master thesis, and for all the good (and very funny) moments in and outside of the lab. I will miss the everyday quotes from Scrubs!

- **Simon Büttner** rounding up the lab 5 crew with even more enthusiasm and a critical mind. Whenever I could convince you of something I knew I am on the right track. All the best for your PhD thesis! Without you my time at the institute would have been completely different.

- The Lab 4 crew, **Lysanne Dietrich**, **Daniel Fersch**, **Sebastian Pres** and **Bernhard Huber** for the great start in the group and all the good advice and discussion over the years.

- **Prof. Dr. Christoph Lambert** and **Dr. Arthur Turkin** for a great collaboration with fruitful discussions.

- **Prof. Dr. Jacob J. Krich** and **Dr. Peter A. Rose** for the great work together on higher-order PP and 2D spectroscopy. A special thanks belongs to Peter for "guiding" me trough the combinatorical proof.

- **Prof. Dr. Donatas Zigmantas** for letting me join your group for five months and showing me the tricks of NOPAs as well as making perfect BBQ.

- All the rest of the people from the division of chemical physics in Lund for the nice welcome and the great time - especially **Romain Rouxel** and **Edoardo Amarotti**.

- The people that corrected this thesis: **Stefan Müller**, **Matthias Hensen**, **Joscha Hoche**, **Sebastian Pres**, **Luisa Brenneis** and **Pavel Malý**. Your comments were all very helpful! **Andrea Gehring** and **Susanne Pfarr** for their very friendly support and help in all organizational matters.

- **Joscha Hoche** for great discussion and evenings throughout the years and for the good discussions about exciton theory.

- **Elisabeth Ströle** for the great time living together (including the lockdown) and the good memories connected to the Kloster- and Neutorstraße.

- The **five and a half friends** for a perfect time together in Würzburg. Especially, my close friends **Mario** and **Kai** that made the whole time in Würzburg very special. We had a great time together starting from the very first day meeting you two guys in the Mensa, endless rounds of playing Skat during the bachelor studies, video chats over three continents, cooking together ("Betreutes Backen"), celebrating new year...the list goes on forever. The time with you as well as with **Lisa**, **Anne**, and now also **Jannes** was really special and I enjoyed every second. I am very thankful that I have so close friends that I know I can rely on.

- **Matthias Hensen** for being a very good friend - inside and outside of the lab. I just realized that we almost started simultaneously in the group and during the whole seven years you were always helping me with all the different questions during the day. I will very much miss the (daily) visits in your office. It was a good time with "rollercoaster-like" discussions starting with the political situation in North Ireland and ending with Benjamin Blümchen (and of course science in between).

- At the end I would like to thank my family, my two brothers **Felix** and **Philipp** as well as my Grandma **Gretel** for all their support. Most of all I want to thank my parents, **Martina** and **Peter**, for their help in good and bad times, their ongoing love during my whole life and for showing me that the most important thing is being there for each other.